The Dissertation Committee for Brennan Muir Coffey Certifies that this is the approved version of the following Dissertation:

Vacuum Ultraviolet Enhanced Atomic Layer Etching, and Area Selective Atomic Layer Deposition for Next Generation Nanofabrication

Committee:

John G. Ekerdt, Supervisor

James R. Engstrom

S.V. Sreenivasan

Delia J. Milliron

Gyeong S. Hwang

Vacuum Ultraviolet Enhanced Atomic Layer Etching, and Area Selective Atomic Layer Deposition for Next Generation Nanofabrication

by

Brennan Muir Coffey

Dissertation

Presented to the Faculty of the Graduate School of

The University of Texas at Austin

in Partial Fulfillment

of the Requirements

for the Degree of

Doctor of Philosophy

The University of Texas at Austin

December 2020

Dedication

To my family, loved ones, and friends - particularly my brother and father, who inspire me every day

Acknowledgements

Reflecting on my time at The University of Texas at Austin is humbling. This dissertation is the product of the tenacity, support, and guidance of a great number individuals. First and foremost, I would like to express my deepest gratitude to my advisor, Dr. John G. Ekerdt, for his patience, support, and guidance over the past five years. I can only hope to provide a fraction of the same unfaltering support, and patience to those I mentor throughout my career. His refusal to stray from encouragement, and support, after years of failure, has served as a haven in obscured times. The environment within his group has been a unique and rewarding experience, that I am truly thankful to have benefited from. I would also like to express my sincerest gratitude to Dr. James R. Engstrom, who over the course of his time at UT, provided mentorship and guidance for a number of tasks I was faced with. Through the thoughtful and caring support of Dr. Ekerdt, and Dr. Engstrom, I would not be where I am today.

I would like to convey my sincerest gratitude to Himmi Nallan, who, in the trenches with me on a number of occasions, helped define our labs. The involvement, and backup for imminent failure for tasks that were essentially exploratory is something I have the deepest gratitude for. Without his help, our cohort, and lab, would simply not be where it is today. Our constant banter, thoughtful discussion, critical assessment of ideas, and support for one another on all difficult tasks has been instrumental to the success of this work, and the engineer and scientist I have grown into. Additionally, I would like to express my sincerest thanks to Edward Lin, who has been a constant supportive figure through my graduate school experience. He has had an instrumental effect on this work through close collaboration experimentally. In addition to the support of Ed, I would like to thank Bryce Edmondson for his support and mentorship through the years, as well as

Pei-Yu Chen, who has been supportive, with our thoughtful and whimsical conversations in the office over the years. I am grateful to have had the opportunity to collaborate with and learn from both Bryce and Pei-Yu. In addition to the aforementioned, I would like to express my sincerest thanks to my committee members, Dr. S.V. Sreenivasan, Dr. Delia J. Milliron, and Dr. Gyeong S. Hwang, for their valuable insight, support, and guidance throughout my time at UT. Their involvement has enabled the research that I am been fortunate to have had the opportunity to explore.

In addition to the aforementioned, I would like to express my sincerest thanks to Erik Cheng, and Dr. Renqin Zhang for their valuable help in learning density functional theory. I also would like to thank Akhila Mallavarapu, who has been instrumental in all of the ALE work performed on Ru and Pd, and who has done excellent work in demonstrating MACE with Ru. In addition to Himmi, Ed, Bryce, and Pei-Yu, I also would not be where I am were it not for the support of several other Ekerdt group members. I would like to thank Sonali Chopra, Zizhuo Zhang, Xin Yang, Sam Johnson, Di Li, Chon Hei Lam, Thanh Tung Le, Brad Leonhardt, and Wen Liao. I am proud to call you all my friends and have learned from you. I am truly thankful for the experiences we have shared in Dr. Ekerdt's research group. I am also grateful for having had the chance to learn and explore new fields through collaborations with Dr. Feng Zou, Dr. Jianyu Li, Jayse Langdon, Julia Lamb, Dr. Rodrigo Rodriguez, and Austin Paul-Orecchio.

As all of the work in this dissertation involved prototyping, prototyping, design, and troubleshooting, I would like to express my sincerest thanks the current and former staff members of the chemical engineering and physics machine shops, particularly, Shallaco McDonald, David Gray, Allan Schroeder, Kenny Schneider, and Edwin Baez, who have been instrumental in almost every prototyped piece of equipment within our labs. Additionally, without the support of Jason Barborka, Randy Rife, Valerie Croft, Jim

Smitherman, Kevin Haynes, Kate Baird, Eloise Boisjoli, Melinda Heidendreich, Carrie Brown, Sara Lombard, and many more. Their assistances have been invaluable to my success at UT. I would also like to express my deepest thanks to all of the current and former staff within the Texas materials institute, particularly Dr. Raluca Gearba-Dolocan, Dr. Andrei Dolocan, Dr. Richard Piner, Dr. Steve Swinnea, and Dr. Hugo Celio, for their invaluable conversations, guidance, training, and numerous conversations throughout my time at UT. I would also like to express my deepest thanks to the current and former staff at the microelectronics research center, including William "Jesse" James, James Hitzfelder, Ricardo Garcia. I also owe my deepest gratitude to the current and former staff at NASCENT, including Dr. Shrawan Singhal, Dr. Oved Abed, Dr. Larry Dunn, Risa Hartman, Matt Weldon, Janet Monaco, and Dr. Darlene Yanez who all share a part in my accomplishments.

I would also like to thank the wonderful staff at the Texas Advanced Computing Center (TACC) at The University of Texas at Austin for their support, and for providing high performance computing that has contributed to the research results reported herein. I would also like to acknowledge NASCENT, the NSF graduate research fellowship program (National Science Foundation Grant Numbers 1610403, EEC-1160494), and the Thrust 2000 Doctoral Fellowship, for funding me through my times in graduate school.

I would also like to express my deepest gratitude to my friends and family through my graduate school experience. I would not be where I am without the constant guidance and support from my brother Aidan Coffey, father Dr. Randall Coffey, mother Dawn Coffey, and nana Joan Coffey. You all share in this success with me. Finally, words do not capture my gratitude for Emily Gordon, who has been a force of support and love through difficult and facile times.

Abstract

Vacuum Ultraviolet Enhanced Atomic Layer Etching, and Area Selective Atomic Layer Deposition for Next Generation Nanofabrication

Brennan Muir Coffey, Ph.D.

The University of Texas at Austin, 2020

Supervisor: John G. Ekerdt

Novel nanofabrication methods for area-selective (AS) deposition and atomic layer etching (ALE) are presented. The aims of these methods are to facilitate the integration of metal assisted chemical etching (MACE), and electroless Cu deposition into devices such as FinFETs, transparent conductive electrodes (TCEs), and patterned photonic structures, which are ubiquitous in next generation nanotechnology, and flexible electronics. MACE and electroless Cu deposition require high quality metal catalyst (e.g., Pd, and Ru) patterns for their implementation, however, ALE methods to remove metals are limited, and difficult to control on an atomic scale. Additionally, no ALE methods currently exist that offer selectivity to remove undesired metal deposition regions, while leaving desired regions largely untouched. Two solutions are presented to ameliorate these difficulties: the first demonstration of vacuum ultraviolet (VUV) enhanced ALE, which has the potential to remove one atomic layer of Pd and Ru at a time, while also being selective to undesired Pd and Ru deposition; and the second, is to control deposition using AS atomic layer deposition (ALD) for photonic devices to desired regions alone, circumventing the need for patterning the challenging to etch $BaTiO_3$, while still allowing surface phase epitaxy.

The first demonstration of VUV ALE is shown, where etching of Pd and Ru is achieved at 100 – 150 °C, with approximate material removal rates of 2.8, and 1.2 Å/cycle, respectively. Etching is accomplished using an oxidation half-cycle, consisting of co-exposure of the metal substrate to VUV and O_2 at 1 Torr for 2 – 5 min, followed by an etching half-cycle, consisting of exposure to 0.50 Torr of HCOOH for 30 sec. Density functional theory (DFT) is used to explore oxidation mechanisms on Pd and Ru. DFT results indicate all oxidants readily incorporate into the surface of both metals, however, a large of concentration of atomic O in the near surface region is required to form an oxide that can be removed by HCOOH exposure. Nudged elastic band (NEB) calculations indicate this is due to difficulty in forming subsurface oxides when a surface oxide is present on Pd, as well as Ru. True self-limiting behavior is predicted, and observed for Ru ALE, while the amount of Pd etched is controlled with the temperature and time of VUV/O_2 co-exposure. Additionally, selectivity in oxidation, and thus material etched, is observed on Pd, and Ru, where at co-exposure times less than 2 min, Pd will not oxidize if it is a continuous (low surface area) thin film, while discontinuous Pd will oxidize. Ru etch rate is decreases as etching is performed, indicating that as roughness decreases (with ALE cycles), longer oxidation times are required to achieve oxidation. This is amenable to the fabrication of the TCE, which requires selectivity between undesired and desired deposition, and patterning of Pd or Ru catalyst layers.

Finally, AS-ALD of difficult to pattern crystalline $BaTiO_3$ (BTO) is presented, where patterns are defined with one lithographic patterning step. Epitaxial crystallization to form a single crystal film with an out-of-plane *c*-axis orientation, should be observed after AS patterning. This process could eliminate the need for post-growth etching for devices in, for example, Si photonic device fabrication.

Table of Contents

List of Tables

List of Figures

Chapter 1: Introduction

1.1. Challenges and State of the Art in Device Fabrication

The state of the art in nanotechnology has been driven by a seemingly endless push to make device critical dimensions as small as possible. This is captured in the prediction by Gordon Moore, who hypothesized the density of transistors in a microchip would approximately double every two years to keep pace with demands of technology.[1] This has held true from the 1960s through the early 2010s, when devices began to reach physical limits owing to the fact that there are on the order of tens of atoms that constitute the critical dimension of a device. This fundamental limit poses a unique challenge to the semiconductor industry, where complex devices, three-dimensional structures, and exotic materials are allowing continued improvements – without the need to continually scale down dimensions.

Of interest in next generation nanofabrication are processes offering a high degree of control over deposition and removal of materials. One such method that could be important in novel memory and logic devices is metal assisted chemical etching (MACE).[2–6] MACE allows high fidelity features (aspect ratio >150) to be etched into Si[2,7] once patterning of a MACE-active catalyst (Pd, Co, Ni, Fe, Ru, Pt)[2,8,9] is completed. Another method of importance to nanofabrication is electroless Cu deposition, which deposits high quality Cu where a catalyst (Pd, Pt, Sn, Ag, etc.) is present.[10–13] Currently widely applied in the front end of the line interconnect fabrication, electroless deposition is amenable in roll-to-roll processing, low temperatures for flexible electronics,[14] and has applications ranging from fuel cells to interconnect fabrication.[15,16]

Devices whose fabrication is complemented by MACE and electroless Cu deposition are shown in Figure 1.1. MACE is suited to creating high aspect ratio Si features,

such as those that comprise logic and memory devices such as FinFETs,[2,3] and 3D NAND memory[5] (Figure 1.1(a)). Despite its potential, MACE has not been adopted industrially, as Au is the most widely used catalyst, which is not CMOS compatible. Recent work has shown that CMOS compatible Ru and Pd are alternative MACE active catalysts, which may be important to industrial incorporation of MACE processing.[8,17,18] Similarly, electroless deposition of Cu typically uses a metal catalyst to create high quality Cu patterns. These patterns are important in wearable electronics, and flexible display technologies, such as the transparent conductive electrode (TCE) as seen in Figure 1.1(b) (taken from Ref 14). Because Cu nucleates on all catalyst present, fine control over desired, and undesired catalyst growth regions is necessary. As both MACE and electroless deposition necessitate well-defined metal catalyst patterns, etching of the platinum group catalysts, Pd, and Ru, is required.

An alternative to challenges associated with patterning is the direct deposition of material in desired growth regions, with high selectivity against growth in undesired regions. This is amenable to devices such as the TCE, or those containing materials sensitive to patterning methods (i.e., plasmas),[19] or have etch products with low volatility. One such application of direct deposition is for Si photonics, such as wave guides, which is shown in Figure 1.1(c) using SiN, taken from Ref 20. Si wave guides are fabricated using optoelectronic perovskites such as $BaTiO_3$ (BTO), which must be monolithically integrated onto Si,[21,22] and have excellent crystalline quality for ferroelectric behavior.[23] Patterning of BTO typically uses Cl or F containing plasmas.[24] However, patterning of both produces halogenated products that have low volatility and remain on the surface,[25,26] which makes pattern definition, and selectivity during the etch, challenging. Thus methods to circumvent patterning challenges, such as area-selective (AS) deposition, are of great interest not only

to catalyst pattern definition in MACE, and electroless Cu deposition, but Si wave guide fabrication as well.

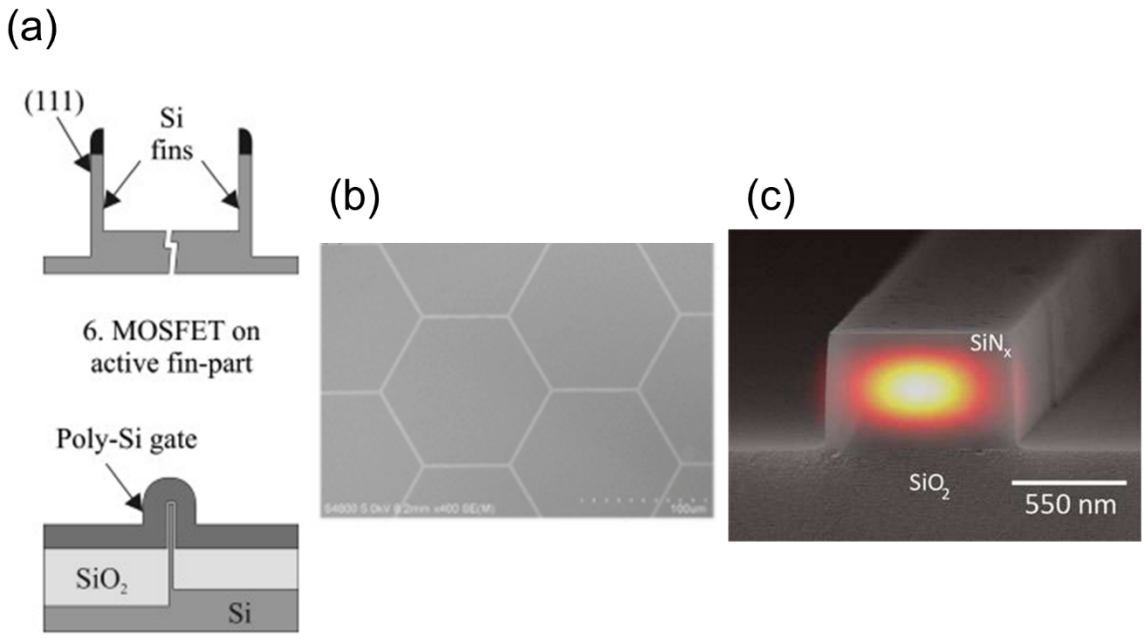

Figure 1.1. Applications for MACE, electroless Cu deposition, and AS deposition are shown. (a) is a FinFET, showing the Si fin beforehand that could be developed with MACE, (b) is a hexagonal transparent conductive electrode, where Cu contacts are lighter on the darker background, (c) is a SiN waveguide fabricated on an SiO_2 substrate, where the intensity of a light wave propagating in the material is indicated in the SiN with color. (a), (b), and (c), are taken from 2, 14, and 20, respectively.

While there are many opportunities for MACE, electrodeposition, and AS deposition, there are numerous barriers to their eventual implementation in fabrication of FinFETs, TCE devices, and wave guides. One challenge with MACE is removing the

platinum group metal catalyst after MACE has been performed, and minimizing porosity in the resulting Si, and eventual device.[27] There is a similar difficulty with electroless Cu deposition, which requires all undesired Pd nucleation sites to be removed before deposition occurs, to minimize Cu growth in undesired regions. It is crucial to have selectivity to remove the undesired deposition, while leaving desired deposition regions relatively unaffected. However, highly controlled patterning of metals remains challenging, methods are limited, and patterning is typically accomplished using plasmas that create strongly oxidative environments. Ion milling may also be used, however, redeposition of masking material, and selectivity issues due to its non-chemical nature must be dealt with. Additionally, as nanofeatures become increasingly complex, patterning often involves multistep lithographic, or complex etch-back schemes to realize complex structures, which can be prohibitive from a cost perspective. This point is a challenge for the state of the art in etching platinum group metals, such as Pd, and Ru.

Area-selectivity (in etching) to desired and undesired regions is not limited to controlling Cu plating for TCE fabrication, as limiting growth to desired growth regions is also a significant challenge for many materials. AS deposition is attractive for devices that are comprised of difficult to etch materials, or require complex etch-back, or sacrificial layer schemes, like those required to fabricate BTO photonics.[28–31] There is another challenge associated with AS methods, specifically for photonics, that require pristine films and template layers for crystallization of the functional material.[29,32] Effects of the AS process on epitaxial crystallization must be understood as deposition, and removal, of blocking layers has an unknown effect on the resulting functional material. Generally, these needs have led to an ever-expanding interest in AS deposition methods that exploit surface modification to render regions of the surface inert toward reagents used to grow a film or layer.

Overall this work focuses on nanofabrication methods for the etching and deposition processes to ameliorate difficulties with the current state of the art. Specifically, methods focus on the controlled etching of Pd, and Ru, as well as demonstrating etch selectivity to desired/undesired growth regions. Additionally, AS deposition for difficult to etch materials like BTO is a focus, where crystallization of the resulting film is investigated after subjecting substrates to AS patterning methods.

1.2. Catalyst Patterning for Nanofabrication

Patterning of features, specifically etching or depositing a material with selectivity, is a significant obstacle in realizing many next generation devices. MACE is one technique that has the potential to define high fidelity nanostructures with high aspect ratios, particularly useful in FinFETs and 3D NAND memory devices. MACE, as discussed above, is a wet chemical etch, that oxidizes Si immediately beneath a catalytic metal layer. The proposed mechanism for MACE is shown in Figure 1.2 (taken from Ref. 9), where the relative potentials of each half reaction, and band positions of the Au and Si layers are indicated in (a), (b), and (c), while the mechanistic etching reactions are shown in (d), and (e) for n-Si, and p-Si, respectively. The metal catalyst in MACE facilitates reduction of an oxidant in the solution phase, typically H_2O_2. Reduction of the oxidant species injects holes (h^+) in the metal layer that are then are trapped at, or transported away from, the interface of the metal and underlying Si (Figure 1.2(d), and (e), respectively). Si in contact with the catalytic layer is oxidized in a reduction-oxidation reaction to form SiO_2. Once SiO_2 is formed beneath the catalyst layer, HF_2^- (or H_2SO_4 depending on the demonstration) etches SiO_2, forming the etch product. The metal catalyst is then exposed to Si beneath the removed SiO_2 layer to continue the etch. MACE results in a continuous etch, that, with fine

control over which surfaces are oxidized, can yield high aspect ratio features for FinFETs or other devices. As the metal catalyst dictates what is oxidized in the MACE mechanism, high control over catalyst patterning is required. However, the two MACE catalysts of interest (that are also CMOS compatible) are Pd and Ru, whose patterning is especially challenging.

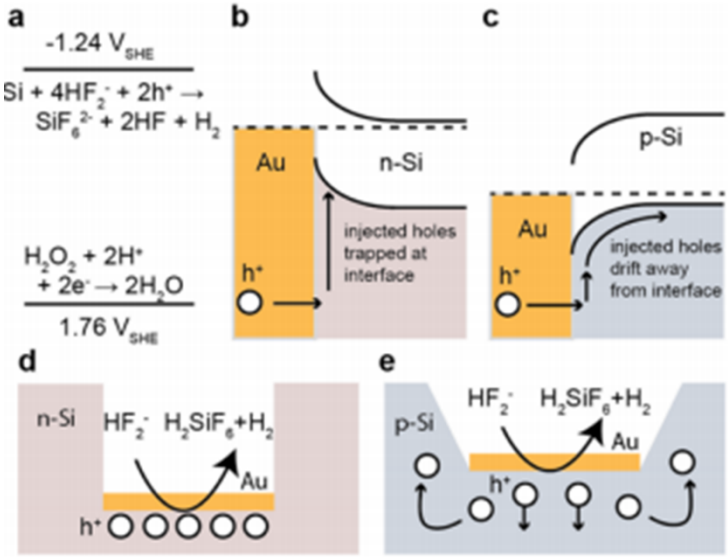

Figure 1.2. (a) Schematic of reduction potentials of the two MACE half-reactions relative to the standard hydrogen electrode, VSHE. (b, c) Band-diagram of Au–Si interface for n-type and p-type Si, respectively, showing the behavior of hole carriers injected by the reduction of H_2O_2. (d, e) Schematic of the resulting morphology of MACE for n-type and p-type Si, respectively. Taken from Ref. 9.

Similar to the requirement of a catalyst for MACE, electroless Cu deposition also requires a Pd catalyst to facilitate deposition, where Cu is known to nucleate on Pd before other surfaces.[10,15] Therefore, in the scheme enabling the TCE with electroless Cu deposition, clearing all non-growth areas of Pd is central to creating a TCE with well-defined geometries to yield good optical properties (e.g., haze, and transparency).[33]

Wet etching of platinum group metals has been demonstrated for Pd, using $FeCl_3$ solutions,[34] acetylacetone (acac), and hexafluoroacetylacetone (hfac), [35] and acidic Ce^{4+} solutions for Ru.[36] While wet etching methods can yield high quality structures, the etch rate is difficult to control on an atomic scale. Dry etching methods are an alternative that can offer atomic level control via surface reactions, that can be self-limiting. Dry etching of Pd, and Ru are known to proceed by combining strong oxidants, such as O, with vapor phase etchants.[37] Atomic O is produced using a plasma (usually either capacitive or inductive plasma), where the oxides formed are usually PdO_x, RuO_2, or RuO_4. PdO_x and RuO_2 can be etched by exposure to Cl or F containing plasmas,[34,38–40] CHF_3/Ar,[40] ethanol,[41] or acac, and hfac,[35] while is RuO_4 (formed by O_3) is volatile, and will sublime thermally.[42] Despite the prevalence of plasma-based etching methods, use of certain plasmas may not be compatible with certain materials/structures,[43] photoresist can be damaged, or poor selectivity is observed due to the production of etch products with low volatility (such as those produced in etching BTO).[25,26] Additionally, O_2 plasmas have an anomalous effect on MACE, where the structures are more porous after plasma exposure, which can impede device function, and yield.[18] These difficulties imply a need for a non-plasma oxidation scheme that allow the controlled etching of platinum group metals. An additional benefit would be the selectivity to desired and undesired growth regions.

The current state of the art also uses ion milling to generate patterns, like those observed in the Si wave guide. Ion milling can offer good anisotropy and pattern definition at the atomic level using EUV,[19] or electron beam lithography.[44] However, ion milling is a physical etching process that sputters material non-selectively. While ion milling is a staple of pattern definition in lithography, redeposition of sputtered material, difficult scalability (if using an electron beam for pattern definition), and no chemical selectivity, make it a difficult technique to conform to the requirements of next generation devices alone.

1.3. Atomic Layer Etching

Similar to the plasma-based methods that continuously remove Pd, and Ru, self-limiting control via surface chemical reactions has also been demonstrated. Control is obtained by cycling reactants, wherein each cycle a self-limiting saturation step is achieved. In this way only the layer that is modified in the self-limiting step is etched. This process is known as atomic layer etching (ALE), and is seen in Figure 1.3. ALE is named due to the fact that, in a perfect demonstration, half-steps would saturate at a monolayer, and the maximum amount of material removed would be limited to the monolayer that is modified. This offers greater control over the removal of, for instance Pd or Ru, however, there is difficulty in achieving large etch rates, and maintaining selectivity to the to-be-etched material over side reactions, and metal etching techniques are limited.[35] Typically, ALE is accomplished by activating the surface or near surface layer with a chemical treatment, reactant A, capable of changing the oxidation state of the metal (i.e., making the metal more reactive) (Figure 1.3(a), and (b)). Once surface sites are occupied, no further reaction can proceed. Following an inert gas purge, the activated layer is then removed using an energetic impetus, reactant B (Figure 1.3(c), and (d)) which is usually a plasma. A combination of ion energy, and reactive gas species complete the reaction on the surface to produce a volatile etch product. The modified layer created by exposure to reactant A (typically a metal halogen species) cannot sublime thermally, and requires B to be removed from the surface.

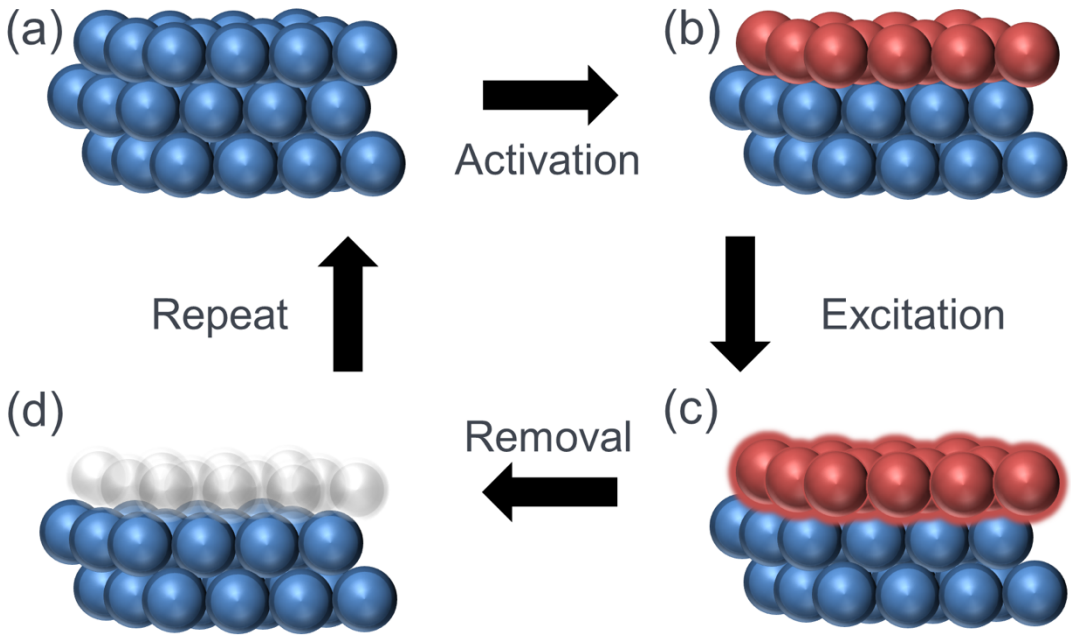

Figure 1.3. A general ALE scheme is shown where four steps comprise one ALE cycle: (a) the bare surface before etching is performed is shown where unmodified atoms are shown in blue, (b) the modified surface is shown in red atop unmodified substrate with some activation step, (c) through some excitation step, the modified surface is made to sublime from the surface, which results in (d), removal of the modified surface, and establishing a surface of the same starting quality for continued ALE cycles.

Recent advances within ALE have demonstrated that etching does not necessarily have to proceed using an energetic impetus in the form of a plasma, and that thermal ALE is possible with careful choice of reactants and etching conditions. Seminal work demonstrating the ALE of Al_2O_3 using sequential exposures to a fluorinating species, HF-Pyridine, and a molecule to participate in ligand exchange with the fluorinated surface species, a metal β-diketonate, (tin(II) acetylacetonate, $Sn(acac)_2$)[45,46] has spurred many thermal ALE studies. There have also been limited demonstrations of the amalgamation of plasma and thermal ALE to etch more challenging materials, such as AlN, where the etch

is facilitated by the use of an H_2 plasma to help sublime the etch product, AlF_3, from the surface.[47]

In demonstrations of ALE of noble metals, an O_2 plasma is always used. The plasma causes oxidation of the difficult to oxidize species (Pd, or Ru), which can then be removed with a vapor etchant, such as acetylacetone, hexafluoroacetylacetone, or, as has been demonstrated on Pd, formic acid (HCOOH).[48] A key point with these studies is that HCOOH will etch the base or noble metal that is oxidized,[48] so fine control over the oxidation step is crucial. This is also important in that it is clear HCOOH is capable of etching several base and noble metal oxides. However, the use of an O_2 plasma is undesired for fabrication of the previously discussed devices due to the large amount of material removed per cycle (1.2 nm Pd/cycle) and no potential to limit etching to desired/undesired growth regions.

1.4. Vacuum Ultraviolet-Enhanced Atomic Layer Etching

There is significant potential for thermal ALE, especially if it is complemented with other methods, such as a plasma, as discussed in the ALE of AlN using a H_2 plasma.[47] One such method is at the intersection of vacuum ultraviolet (VUV) light treatment with ALE. VUV light, while well known as an organic cleaning treatment,[49] and widely used in advanced oxidation processes for removal of volatile organic compounds (VOCs),[50–52] is only starting to see use within nanofabrication. Specifically, VUV enhancement has been employed in atomic layer deposition (ALD) to deposit conformal oxide films such as Al_2O_3,[53] and TiO_2,[54,55] and at low temperatures. However, its use within ALE is yet to be realized. The work presented herein is the first demonstration of VUV enhanced ALE.

The use of VUV enhancement is effectively a method to deliver energetic species to a surface, similar to how an inert gas plasma delivers high energy molecules to facilitate

a reaction. VUV photons correspond to wavelengths of $110 < \lambda < 400$ nm ($6.2 < h\nu < 11.3$ eV), where the selected wavelength range can be chosen based on the window material. If a SiO_2 window is used, photons with $\lambda < 220$ nm are attenuated. If a MgF_2 window is used, the allowed wavelength range is 110 – 180 nm. VUV light can be produced a number of ways, not limited to, excimer lasers, Xe arc lamps, Hg arc lamps, or the method used within this discussion, D_2 lamps.[56]

VUV is widely used for advanced oxidation processes due to the large absorption cross-section of many molecules in the 110 – 180 nm wavelength range. Of interest in my research is the interaction of VUV with O_2 gas, which has an absorption cross section of 12 cm^{-1} in the VUV, [57] which gives an attenuation length of 1.8 cm. The co-exposure of VUV and O_2 yields atomic O, O_2, and O_3,[58] which are all good oxidizing agents. These oxidizing species can then be used to cause low temperature oxidation of difficult to oxidize metals, Pd, and Ru. Once oxidized, the metal can be removed with HCOOH, which completes an ALE cycle. The VUV enhanced ALE process is shown in Figure 1.4.

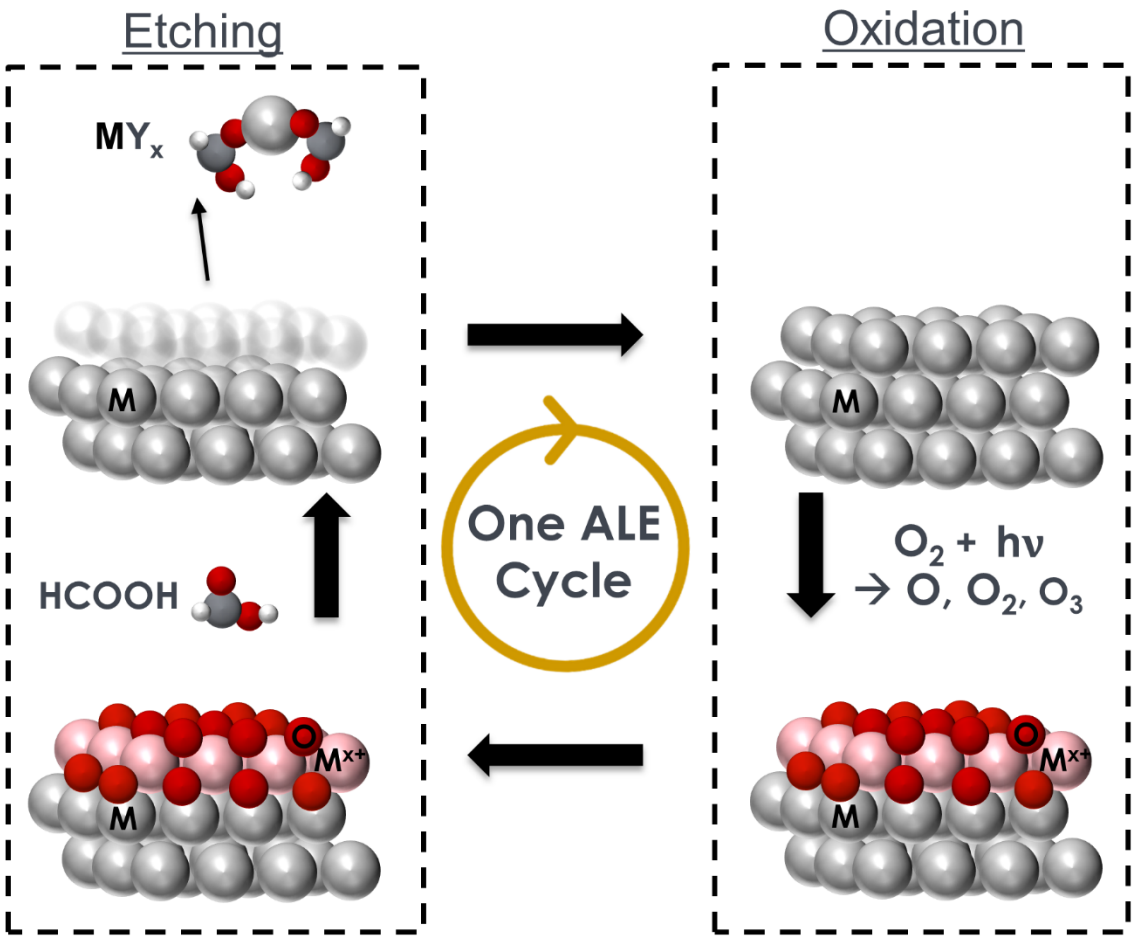

Figure 1.4. A schematic for VUV enhanced ALE is shown, where one ALE cycle is comprised of an etching and oxidation half cycle, shown on the left, and right, respectively. Oxidation is comprised of exposing the metal, M, with O_2 and light, hν, which produces O, O_2, and O_3. These oxidants change the valency of the surface atomic layer of M to M^+. The etching half cycle is comprised of a vapor dose of HCOOH, which adsorbs, and removes, the modified M^+ layer. The surface is then returned to its starting quality for more ALE cycles.

Owing to the novelty of VUV enhanced ALE, it is worthwhile to explore the limits of the technique in the context of removing undesired deposition for TCE fabrication, and removing the MACE catalyst after MACE has been performed. Eventually, depending on the active oxidant molecules, selectivity in oxidation could be achieved (i.e., through a

shadow mask or with lift-off), which could lead to anisotropy in ALE. An additional benefit is the potential to adsorb a monolayer of reactive gases, that, once illuminated with VUV light, could react to form oxidizing (H_2O_2, NO_2, etc.), nitriding (NH_3, N_2, etc.), fluorinating (NF_3, HF, SF_6, CH_3F, etc.), or phosphiding (HP, PH_3, etc.) species locally on the surface. These species may then be able to cause a surface reaction of the substrate material. The fine control of decomposing a monolayer of adsorbing reactant molecules could lead to the self-limiting generation of reactants with VUV for a broad range of materials, and limit reaction to surface and near surface layers. This benefit could be a great addition to the VUV enhanced ALE technique.

1.5. Area-Selective Atomic Layer Deposition

Heroic efforts have been made to enable the low temperature removal of Pd and Ru, however, an alternative to etching to define a pattern is AS deposition. Atomic layer deposition (ALD) is well-suited to AS deposition, as fine control over surface chemistry can limit or promote growth in certain regions, thus defining a pattern.[59] The general ALD scheme is related to ALE in that deposition is performed by saturating a surface with an activation step, which then reacts with a co-reactant to leave behind the deposited material. The process flow of ALD of an oxide is shown in Figure 1.5. The first reactant, A, adsorbs to the surface in a self-limiting fashion. Following an inert gas purge, the second reactant, B, is introduced, which reacts with A and nothing else. By repeating cycles of A, followed by B, with an inert gas purge in between half-cycles, a material can be deposited in a conformal, and highly controlled manner at low temperatures (< 400 °C). In this demonstration, the co-reactant is water, which results in deposition of an oxide material.

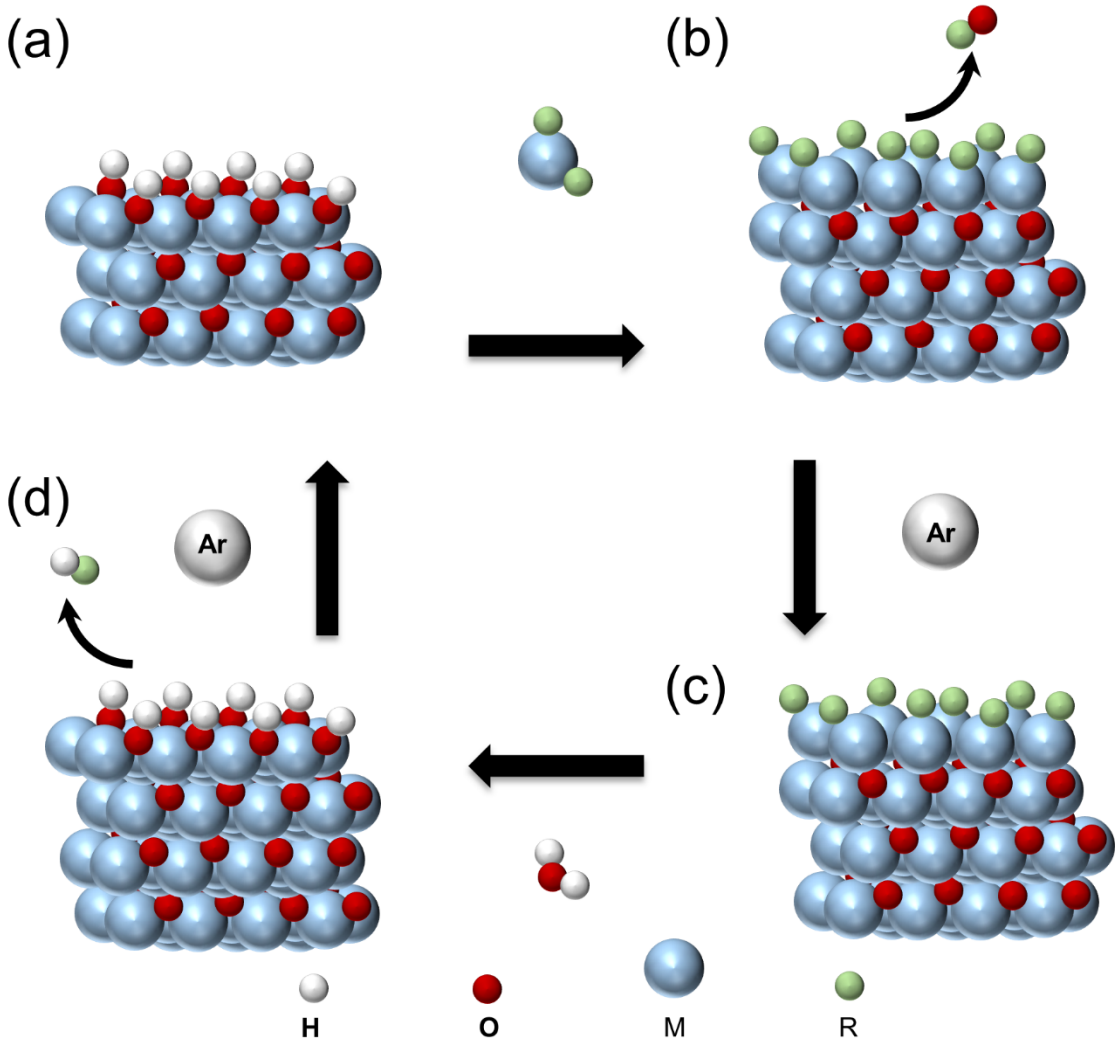

Figure 1.5. ALD of an oxide material is shown. (a) is the starting oxide, where the material to be deposited, M, is shown in blue, and oxygen is shown in red. The starting surface is passivated with the white species, H, which can only react with green atoms, R, and O atoms. (b) shows the saturation of M, where only OR species form on the surface to leave M-O surface bonds. (c) indicates an Ar purge to remove all MR species. (d) shows the removal of R surface atoms by H_2O addition, which reproduces the starting oxide surface for the next step, (a). (a), (b), (c), and (d), comprise one ALD cycle.

As patterned photonic devices (Si wave guides), are a focus of this work, several oxide perovskites are of particular interest owing to their favorable ferroelectricity. BTO is one such material, and is being studied heavily due to its relatively large linear response in the index of refraction to an applied electric field.[60] This behavior is captured in a parameter called the Pockels coefficient.[61,62] Additionally, BTO has recently been monolithically integrated onto Si by using an oxide perovskite with similar lattice parameters, $SrTiO_3$ (STO), as a buffer layer.[29,32,63] However, growth of BTO for ferroelectric applications is difficult, as epitaxial crystallization, and thus ferroelectricity is strongly dependent on interface quality of the BTO film.[29,32] To add to the challenge of creating BTO photonic structures, Ba and Ti etch products have low volatility (e.g., BaF, and TiF),[25,26] which makes top-down patterning of BTO for Si wave guides difficult. Therefore, it is desired to develop an AS-ALD method that facilitates controlled deposition, and thus feature creation, for photonic structures, and does not hinder BTO crystalline quality.

Area-selectivity can be imparted during growth by limiting where reactants A and B adsorb onto a surface. In this demonstration, oxide precursors are hydrophilic, indicating that they will adsorb, and grow, in surface regions with a large OH density, while growth will be limited in hydrophobic surface regions without large OH densities.[28–30] Area-selective ALD by controlling surface hydrophobicity is shown in Figure 1.6. While this method has potential to yield area selective ALD of BTO, the process to deposit and remove the polymer resist layer has unknown consequences on the interface, and resulting epitaxial crystallization of BTO. Thus it is important to understand the implications that depositing, and removing a polymer blocking layer have on epitaxial crystallization of BTO.

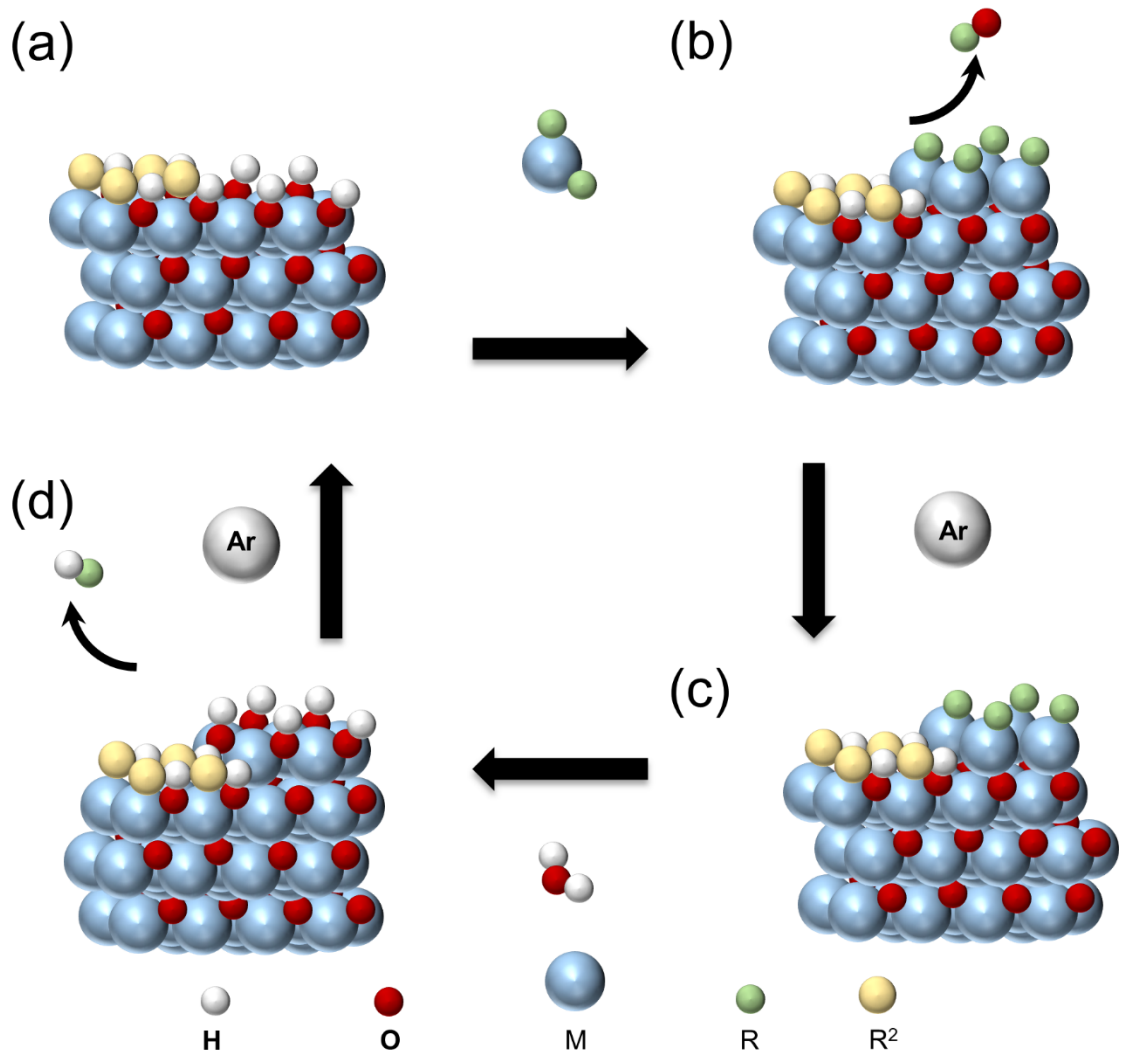

Figure 1.6. ALD of an oxide material is shown. (a) is the starting oxide, where the material to be deposited, M, is shown in blue, oxygen is shown in red, and a hydrophobic species R^2 is shown in light yellow. The starting surface is passivated with the hydrophobic species, R^2, which resists adsorption of M atoms. (b) shows the saturation of M, where only OR species form on the surface to leave M-O surface bonds, where no surface reactions are formed on the area blocked with R^2. (c) indicates an Ar purge to remove all MR species. (d) shows the removal of R surface atoms by H_2O addition, which reproduces the starting oxide surface for the next step, (a). (a), (b), (c), and (d), comprise one ALD cycle, where material has only grown on the areas without R^2.

1.6. Research Objectives and Overview

Nanofabrication is comprised of many carefully designed etching and deposition steps to yield the desired structure. Discussed thus far are methods that require complementary etching and deposition techniques to facilitate the eventual device application. Specifically, an ALE method to aid in removal of catalyst material before or after processing (MACE, or electroless Cu deposition) has been completed, and an AS-ALD method that minimizes patterning steps (Si waveguides). Demonstration of low-temperature, non-plasma ALE methods for metals have not been shown, and AS-ALD of crystalline perovskites has yet to be demonstrated. These aims are outlined in Figure 1.7, where a process flows utilizing the ALE of Pd and Ru for the TCE, FinFET are shown in (a), and a process flow for AS-ALD of photonic structures is shown in (b).

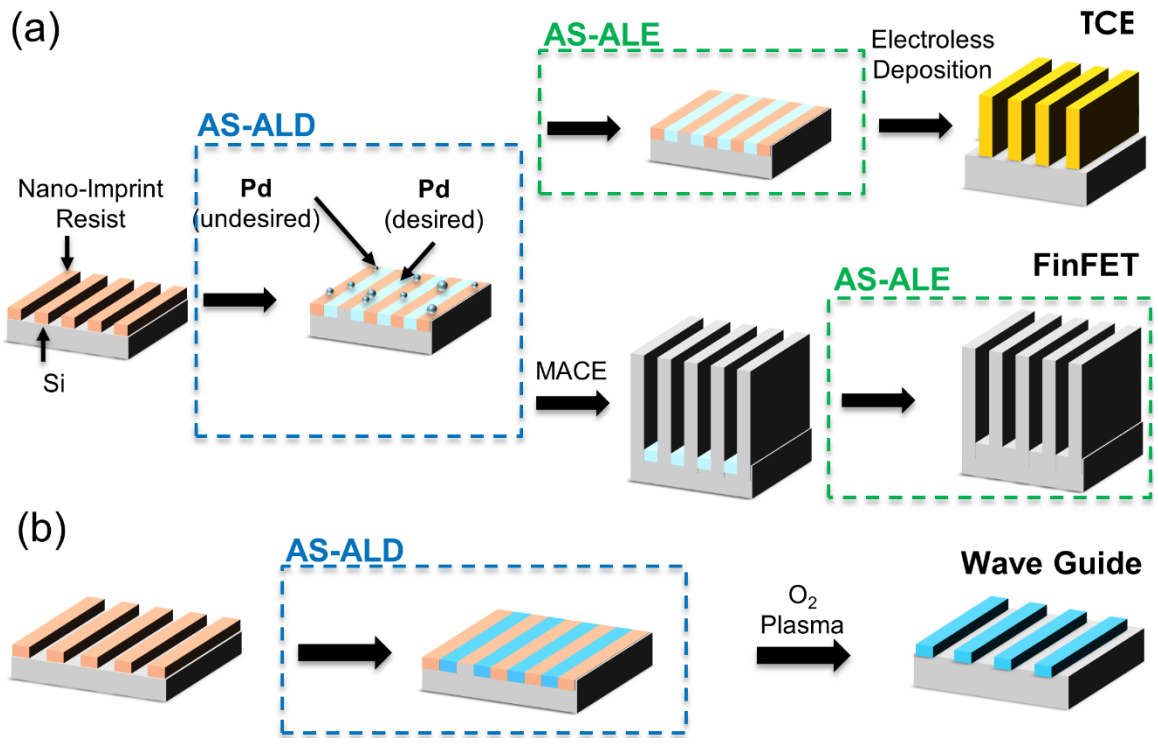

Figure 1.7. Process flow for the production of the TCE and FinFET devices involving ALE and ALE with selectivity to undesired Pd deposition is shown in (a). A process flow for the AS-ALD production of photonic wave guides is shown in (b). ALE steps are shown in green dashed boxes, while ALD steps are shown in blue dashed boxes in each process flow.

The aim of this dissertation is to present methods to aid with the difficulties in enabling technologies defined previously. Specifically, the first demonstration of VUV-enhanced ALE, as well as the first demonstration of AS-ALD to yield epitaxial crystalline structures. VUV-enhanced ALE is presented as a low-temperature, non-plasma, method to remove Pd in Chapter 3, where density functional theory (DFT) analysis is used in conjunction with experiments to assess the oxidation characteristics of irradiating a Pd thin film with VUV photons in an O_2 environment. Chapter 4 demonstrates VUV-ALE for removal of Pd and explores the kinetics of oxidation for low and high surface area features in the context of removing undesired Pd deposition for TCE fabrication. Chapter 5 expands the methods developed on Pd to Ru, another CMOS compatible MACE catalyst. VUV-enhanced ALE of Ru is studied using density functional theory and experiments.

Chapter 6 explores the AS-ALD of BTO to fabricate patterns while minimizing lithographic steps. Crystallization of BTO via surface phase epitaxy is explored after subjecting the surface to the AS patterning process. Thus the aim is to demonstrate the first AS-ALD of crystalline oxide perovskites.

1.7. REFERENCES

(1) Mack, C. A. Fifty Years of Moore's Law. *IEEE Transactions on Semiconductor Manufacturing* **2011**, *24* (2), 202–207.

(2) Jovanović, V.; Suligoj, T.; Poljak, M.; Civale, Y.; Nanver, L. K. Ultra-High Aspect-Ratio FinFET Technology. *Solid-State Electronics* **2010**, *54* (9), 870–876.

(3) Nagy, D.; Indalecio, G.; GarcíA-Loureiro, A. J.; Elmessary, M. A.; Kalna, K.; Seoane, N. FinFET Versus Gate-All-Around Nanowire FET: Performance, Scaling, and Variability. *IEEE Journal of the Electron Devices Society* **2018**, *6*, 332–340.

(4) Ishikawa, K.; Karahashi, K.; Ichiki, T.; Chang, J. P.; George, S. M.; Kessels, W. M. M.; Lee, H. J.; Tinck, S.; Um, J. H.; Kinoshita, K. Progress and Prospects in Nanoscale Dry Processes: How Can We Control Atomic Layer Reactions? *Jpn. J. Appl. Phys.* **2017**, *56* (6S2), 06HA02.

(5) Ishikawa, K.; Karahashi, K.; Ishijima, T.; Cho, S. I.; Elliott, S.; Hausmann, D.; Mocuta, D.; Wilson, A.; Kinoshita, K. Progress in Nanoscale Dry Processes for Fabrication of High-Aspect-Ratio Features: How Can We Control Critical Dimension Uniformity at the Bottom? *Jpn. J. Appl. Phys.* **2018**, *57* (6S2), 06JA01.

(6) Huang, Z.; Geyer, N.; Werner, P.; de Boor, J.; Gosele, U. Metal-Assisted Chemical Etching of Silicon: A Review. *Adv. Mater.* **2010**, *23* (2), 285–308.

(7) Dimaggio, E.; Narducci, D.; Pennelli, G. Fabrication of Silicon Nanowire Forests for Thermoelectric Applications by Metal-Assisted Chemical Etching. *J. of Materi Eng and Perform* **2018**, *27* (12), 6279–6285.

(8) Han, H.; Huang, Z.; Lee, W. Metal-Assisted Chemical Etching of Silicon and Nanotechnology Applications. *Nano Today* **2014**, *9* (3), 271–304.

(9) Lai, R., A.; Hymel, T., M.; Narasimhan, V., K.; Cui, Y. Schottky Barrier Catalysis Mechanism in Metal-Assisted Chemical Etching of Silicon | ACS Applied Materials & Interfaces. **2016**, *8* (14), 8875–8879.

(10) Matthey, J. Tin-Palladium Catalysts for Electroless Plating (accessed Sep 24, 2020).

(11) Sard, R. The Nucleation, Growth, and Structure of Electroless Copper Deposits. *J. Electrochem. Soc.* **1970**, *117* (7), 864.

(12) Uzunlar, E.; Wilson, Z.; Kohl, P. A. Electroless Copper Deposition Using Sn/Ag Catalyst on Epoxy Laminates. *J. Electrochem. Soc.* **2013**, *160* (12), D3237.

(13) Vukmirovic, M. B.; Bliznakov, S. T.; Sasaki, K.; Wang, J. X.; Adzic, R. R. Electrodeposition of Metals in Catalyst Synthesis: The Case of Platinum Monolayer Electrocatalysts. *Electrochem. Soc. Interface* **2011**, *20* (2), 33.

(14) Chen, X.; Guo, W.; Xie, L.; Wei, C.; Zhuang, J.; Su, W.; Cui, Z. Embedded Ag/Ni Metal-Mesh with Low Surface Roughness As Transparent Conductive Electrode for Optoelectronic Applications. *ACS Appl. Mater. Interfaces* **2017**, *9* (42), 37048–37054.

(15) Xiang, C.; Kung, S.-C.; Taggart, D. K.; Yang, F.; Thompson, M. A.; Güell, A. G.; Yang, Y.; Penner, R. M. Lithographically Patterned Nanowire Electrodeposition: A Method for Patterning Electrically Continuous Metal Nanowires on Dielectrics. *ACS Nano* **2008**, *2* (9), 1939–1949.

(16) Deckert, C. A. Electroless Copper Plating A Review: Part I. *Plating and Surface Finishing* **1995**, 48–55.

(17) Yae, S.; Morii, Y.; Fukumuro, N.; Matsuda, H. Catalytic Activity of Noble Metals for Metal-Assisted Chemical Etching of Silicon. *Nanoscale Res Lett* **2012**, *7* (1), 352.

(18) Mallavarapu, A.; Sreenivasan, S. V. Metal Assisted Chemical Etching of Ru for Si Nanowires. *Unpublished* **2020**.

(19) Harwell, J.; Burch, J.; Fikouras, A.; Gather, M. C.; Di Falco, A.; Samuel, I. D. W. Patterning Multicolor Hybrid Perovskite Films via Top-Down Lithography. *ACS Nano* **2019**, *13* (4), 3823–3829.

(20) Agha, I.; Davanço, M.; Thurston, B.; Srinivasan, K. Low-Noise Chip-Based Frequency Conversion by Four-Wave-Mixing Bragg Scattering in SiN_x Waveguides. *Opt. Lett., OL* **2012**, *37* (14), 2997–2999.

(21) Hu, S.; McDaniel, M. D.; Posadas, A.; Hu, C.; Wu, H.; Yu, E. T.; Smith, D. J.; Demkov, A. A.; Ekerdt, J. G. Monolithic Integration of Perovskites on Ge(001) by Atomic Layer Deposition: A Case Study with $SrHf_xTi_{1-x}O_3$. *MRS Communications* **2016**, *6* (3), 125–132.

(22) Lin, E. L.; Hu, S.; Ekerdt, J. G. Monolithic Integration of Metal-Ferroelectric-Semiconductor Heterostructure Using Atomic Layer Deposition. In *Oxide-based Materials and Devices VIII*; International Society for Optics and Photonics, 2017; Vol. 10105, p 1010519.

(23) Abel, S.; Fompeyrine, J. Electro-Optically Active Oxides on Silicon for Photonics. In *Thin Films on Silicon*; Materials and Energy; World Scientific, 2015; Vol. Volume 8, pp 455–501.

(24) Shoron, O. F.; Raghavan, S.; Freeze, C. R.; Stemmer, S. $BaTiO_3/SrTiO_3$ Heterostructures for Ferroelectric Field Effect Transistors. *Appl. Phys. Lett.* **2017**, *110* (23), 232902.

(25) Dai, L.; Wang, S.; Shu, P.; Zhong, Z.; Wang, G.; Zhang, G. Etching Mechanism of Barium Strontium Titanate (BST) Thin Films in CHF_3/Ar Plasma. *Chin. Sci. Bull.* **2011**, *56* (21), 2267–2271.

(26) Li, Y.; Wang, C.; Yao, Z.; Kim, H.-K.; Kim, N.-Y. Comparative Analysis of Barium Titanate Thin Films Dry Etching Using Inductively Coupled Plasmas by Different Fluorine-Based Mixture Gas. *Nanoscale Res Lett* **2014**, *9* (1), 530.

(27) Chen, C.-Y.; Wei, T.-C.; Lin, C.-T.; Li, J.-Y. Enhancing Formation Rate of Highly-Oriented Silicon Nanowire Arrays with the Assistance of Back Substrates. *Scientific Reports* **2017**, *7* (1), 3164.

(28) Torgersen, J.; Acharya, S.; Dadlani, A. L.; Petousis, I.; Kim, Y.; Trejo, O.; Nordlund, D.; Prinz, F. B. Relating Electronic and Geometric Structure of Atomic

Layer Deposited $BaTiO_3$ to Its Electrical Properties. *J. Phys. Chem. Lett.* **2016**, *7* (8), 1428–1433.

(29) Ngo, T. Q.; Posadas, A. B.; McDaniel, M. D.; Hu, C.; Bruley, J.; Yu, E. T.; Demkov, A. A.; Ekerdt, J. G. Epitaxial C-Axis Oriented $BaTiO_3$ Thin Films on $SrTiO_3$-Buffered Si(001) by Atomic Layer Deposition. *Appl. Phys. Lett.* **2014**, *104* (8), 082910.

(30) Chen, Z.; Wang, H.; Wang, X.; Chen, P.; Liu, Y.; Zhao, H.; Zhao, Y.; Duan, Y. Low-Temperature Remote Plasma Enhanced Atomic Layer Deposition of ZrO_2/Zircone Nanolaminate Film for Efficient Encapsulation of Flexible Organic Light-Emitting Diodes. *Scientific Reports* **2017**, *7*, 40061.

(31) Zhang, Z.; Dwyer, T.; Sirard, S. M.; Ekerdt, J. G. Area-Selective Atomic Layer Deposition of Cobalt Oxide to Generate Patterned Cobalt Films. *Journal of Vacuum Science & Technology A* **2019**, *37* (2), 020905.

(32) Lin, E. L.; Posadas, A. B.; Wu, H. W.; Smith, D. J.; Demkov, A. A.; Ekerdt, J. G. Epitaxial Growth of Barium Titanate Thin Films on Germanium via Atomic Layer Deposition. *II-VI Compd 1987, Proc of the Third Int Conf on II-VI Compd* **2017**, *476*, 6–11.

(33) Nian, Q.; Callahan, M.; Look, D.; Efstathiadis, H.; Bailey, J.; Cheng, G. J. Highly Transparent Conductive Electrode with Ultra-Low HAZE by Grain Boundary Modification of Aqueous Solution Fabricated Alumina-Doped Zinc Oxide Nanocrystals. *APL Materials* **2015**, *3* (6), 062803.

(34) Williams, K. R.; Gupta, K.; Wasilik, M. Etch Rates for Micromachining Processing-Part II. *Journal of Microelectromechanical Systems* **2003**, *12* (6), 761–778.

(35) Chen, J. K.-C.; Altieri, N. D.; Kim, T.; Lill, T.; Shen, M.; Chang, J. P. Directional Etch of Magnetic and Noble Metals. I. Role of Surface Oxidation States. *Journal of Vacuum Science & Technology A: Vacuum, Surfaces, and Films* **2017**, *35* (5), 05C304.

(36) Philipsen, H.; Mouwen, N.; Teck, S.; Monnens, W.; Le, Q. T.; Holsteyns, F.; Struyf, H. Wet-Chemical Etching of Metals for Advanced Semiconductor Technology Nodes: Ru Etching in Acidic Ce^{4+} Solutions. *Electrochimica Acta* **2019**, *306*, 285–298.

(37) Sang, X.; Chang, J. P. Physical and Chemical Effects in Directional Atomic Layer Etching. *J. Phys. D: Appl. Phys.* **2020**, *53* (18), 183001.

(38) Hsu, C. C.; Coburn, J. W.; Graves, D. B. Etching of Ruthenium Coatings in O2- and Cl2-Containing Plasmas. *Journal of Vacuum Science & Technology A* **2005**, *24* (1), 1–8.

(39) Kim, H. W.; Ju, B.-S.; Kang, C.-J. Patterning of Ru Electrode in O2/Cl2 Gas Using Reactive Ion Etcher. *Vacuum* **2003**, *71* (4), 481–486.

(40) Fracassi, F.; d'Agostino, R.; Cacucci, A. Dry Etching of Palladium Thin Films in Fluorine Containing Plasmas: X-ray Photoelectron Spectroscopy Investigation. *Journal of Vacuum Science & Technology A: Vacuum, Surfaces, and Films* **1998**, *13* (1), 63–66.

(41) Hwang, S. M.; Garay, A. A.; Lee, W. I.; Chung, C. W. High Density Plasma Reactive Ion Etching of Ru Thin Films Using Non-Corrosive Gas Mixture. *Thin Solid Films* **2015**, *587*, 28–33.

(42) Nakahara, M.; Tsunekawa, S.; Watanabe, K.; Arai, T.; Yunogami, T.; Kuroki, K. Etching Technique for Ruthenium with a High Etch Rate and High Selectivity Using Ozone Gas. *Journal of Vacuum Science & Technology B: Microelectronics and Nanometer Structures Processing, Measurement, and Phenomena* **2001**, *19* (6), 2133–2136.

(43) Wan, D.; Paolillo, S.; Rassoul, N.; Kotowska, B. K.; Blanco, V.; Adelmann, C.; Lazzarino, F.; Ercken, M.; Murdoch, G.; Bömmels, J.; Wilson, C. J.; Tökei, Z. Subtractive Etch of Ruthenium for Sub-5nm Interconnect. In *2018 IEEE International Interconnect Technology Conference (IITC)*; 2018; pp 10–12.

(44) Chen, Y. Nanofabrication by Electron Beam Lithography and Its Applications: A Review. *Microelectronic Engineering* **2015**, *135*, 57–72.

(45) Lee, Y.; George, S. M. Atomic Layer Etching of Al_2O_3 Using Sequential, Self-Limiting Thermal Reactions with $Sn(Acac)_2$ and Hydrogen Fluoride. *ACS Nano* **2015**, *9* (2), 2061–2070.

(46) Lee, Y.; DuMont, J. W.; George, S. M. Trimethylaluminum as the Metal Precursor for the Atomic Layer Etching of Al_2O_3 Using Sequential, Self-Limiting Thermal Reactions. *Chem. Mater.* **2016**, *28* (9), 2994–3003.

(47) Johnson, N. R.; Sun, H.; Sharma, K.; George, S. M. Thermal Atomic Layer Etching of Crystalline Aluminum Nitride Using Sequential, Self-Limiting Hydrogen Fluoride and $Sn(Acac)_2$ Reactions and Enhancement by H_2 and Ar Plasmas. *Journal of Vacuum Science & Technology A: Vacuum, Surfaces, and Films* **2016**, *34* (5), 050603.

(48) Chen, J. K.-C.; Altieri, N. D.; Kim, T.; Chen, E.; Lill, T.; Shen, M.; Chang, J. P. Directional Etch of Magnetic and Noble Metals. II. Organic Chemical Vapor Etch. *Journal of Vacuum Science & Technology A: Vacuum, Surfaces, and Films* **2017**, *35* (5), 05C305.

(49) Falkenstein, Z. Surface Cleaning Mechanisms Utilizing VUV Radiation in Oxygen-Containing Gaseous Environments; Kley, E.-B., Herzig, H. P., Eds.; San Diego, CA, **2001**; pp 246–255.

(50) Ameta, R.; Solanki, M. S.; Benjamin, S.; Ameta, S. C. Chapter 6 - Photocatalysis. In *Advanced Oxidation Processes for Waste Water Treatment*; Academic Press, **2018**; pp 135–175.

(51) Johnson, M. S.; Nilsson, E. J. K.; Svensson, E. A.; Langer, S. Gas-Phase Advanced Oxidation for Effective, Efficient in Situ Control of Pollution. *Environ. Sci. Technol.* **2014**, *48* (15), 8768–8776.

(52) Munter, R. Advanced Oxidation Processes - Current Status and Prospects. *Proceedings from the Estonian Academy of Sciences, Chemistry* **2008**, *50* (2), 59–80.

(53) Chalker, P. R.; Marshall, P. A.; Dawson, K.; Brunell, I. F.; Sutcliffe, C. J.; Potter, R. J. Vacuum Ultraviolet Photochemical Selective Area Atomic Layer Deposition of Al_2O_3 Dielectrics. *AIP Advances* **2015**, *5* (1), 017115.

(54) Chalker, P. R.; Marshall, P. A.; Dawson, K.; Sutcliffe, C. J.; Brunell, I. F.; Sedghi, N.; Hall, S.; Potter, R. J. Vacuum Ultraviolet Photochemical Atomic Layer Deposition of Alumina and Titania Films. *ECS Transactions* **2015**, *69* (7), 139–145.

(55) Miikkulainen, V.; Väyrynen, K.; Mizohata, K.; Räisänen, J.; Vehkamäki, M.; Ritala, M. Photoassisted Atomic Layer Deposition of Oxides Employing Alkoxides as Single-Source Precursors. *Journal of Vacuum Science & Technology A* **2019**, *37* (6), 060911.

(56) Chalker, P. R. Photochemical Atomic Layer Deposition and Etching. *Surface and Coatings Technology* **2016**, *291* (Supplement C), 258–263.

(57) Huffman, R. E. Absorption Cross-Sections of Atmospheric Gases for Use in Aeronomy. *Can. J. Chem.* **1969**, *47* (10), 1823–1834.

(58) Slanger, T. G.; Cosby, P. C. Oxygen Spectroscopy below 5.1 EV. *J. Phys. Chem.* **1988**, *92* (2), 267–282.

(59) Parsons, G. N.; George, S. M.; Knez, M. Progress and Future Directions for Atomic Layer Deposition and ALD-Based Chemistry. *MRS Bulletin* **2011**, *36* (11), 865–871.

(60) Martin, L. W.; Rappe, A. M. Thin-Film Ferroelectric Materials and Their Applications. *Nature Reviews Materials* **2016**, *2* (2), 1–14.

(61) Abel, S.; Eltes, F.; Ortmann, J. E.; Messner, A.; Castera, P.; Wagner, T.; Urbonas, D.; Rosa, A.; Gutierrez, A. M.; Tulli, D.; Ma, P.; Baeuerle, B.; Josten, A.; Heni, W.; Caimi, D.; Czornomaz, L.; Demkov, A. A.; Leuthold, J.; Sanchis, P.; Fompeyrine, J. Large Pockels Effect in Micro- and Nanostructured Barium Titanate Integrated on Silicon. *Nature Materials* **2019**, *18* (1), 42–47.

(62) Kormondy, K. J.; Abel, S.; Fallegger, F.; Popoff, Y.; Ponath, P.; Posadas, A. B.; Sousa, M.; Caimi, D.; Siegwart, H.; Uccelli, E.; Czornomaz, L.; Marchiori, C.;

Fompeyrine, J.; Demkov, A. A. Analysis of the Pockels Effect in Ferroelectric Barium Titanate Thin Films on Si(001). *Microelectronic Engineering* **2015**, *147*, 215–218.

(63) McDaniel, M. D.; Posadas, A.; Ngo, T. Q.; Dhamdhere, A.; Smith, D. J.; Demkov, A. A.; Ekerdt, J. G. Epitaxial Strontium Titanate Films Grown by Atomic Layer Deposition on $SrTiO_3$-Buffered Si(001) Substrates. *Journal of Vacuum Science & Technology A* **2012**, *31* (1), 01A136.

Chapter 2: Experimental and Computational Methods

Pd and Ru samples are evaporated using electron beam evaporation (CHA industries), or sputtered using a DC sputtering system (EMS-Quorum, EMS300TD), respectively. Film thickness is monitored using an in situ quartz crystal microbalance (QCM). Evaporation targets are > 99.99% Pd, and Ru (Plasmaterials Inc.), while Si substrates are single side polished p-Si(100) wafers (1 – 10 Ω cm, University Wafer Inc. and Nova Electronics Inc.). $SrTiO_3$(001) single crystals are purchased from MTI electronic and are used as the substrate in all epitaxial crystallization studies with BTO. All samples are prepared with a standard degreasing procedure that includes sonicating in acetone, isopropyl alcohol, and water (>18 MΩ cm), for 10 min each, followed by drying under a stream of N_2 (research grade).

2.1. Ultra-High Vacuum Facilities – Atomic Layer Etching

ALE of Pd and Ru is performed in a custom ultra-high vacuum reactor and analysis system. A computer aided design drawing of the UHV system built for ALE is shown in Figure 2.1. All chambers are connected to one another via a UHV transfer line that is maintained at 1×10^{-7} Torr by a turbomolecular pump. Samples enter the system from the load lock (Figure 2.1(a), blue), which has the capacity to store/load up to five samples at once. Once the pressure inside the loadlock chamber is acceptable ($< 9 \times 10^{-7}$ Torr), samples are moved into the transfer line, where they are loaded onto a cart that spans the length of the transfer line. The transfer line cart can hold up to eight samples for transportation or storage. Further details of the transfer line, and the design of the transfer line cart can be found in Appendix A. Also depicted in Figure 2.1 is the vacuum furnace (b), the X-ray photoelectron spectrometer (c), and the ALE chamber (d).

Once in the load lock chamber, samples are loaded directly into the UHV furnace, which is indicated in Figure 2.1(b) in red. The furnace is a quartz tube that is surrounded by an insulated metal coil that has the capability to anneal samples to 1000 °C. Samples are raised on a Langmuir probe, that has monitoring feedthroughs installed at the end of the probe (thermocouple). The top of the furnace is isolated from ambient, as it was found temperature setpoints are not repeatable if convection near the top of the quartz tube is not mitigated. There is also a gas line to supply H_2 during annealing, allowing the reduction of oxide materials.

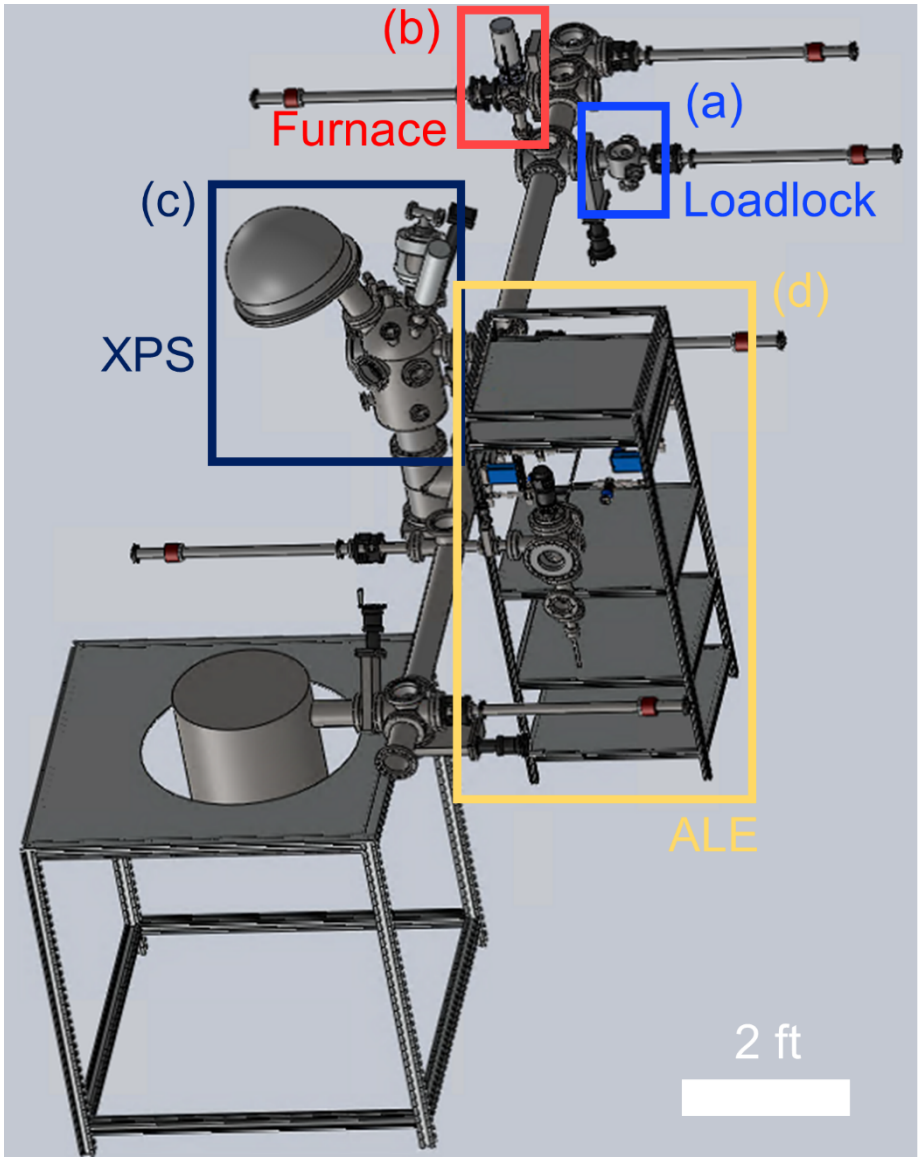

Figure 2.1. A perspective view of the custom UHV treatment and analysis facility used for ALE studies. The loadlock is shown in (a), while the furnace is shown in (b), and the XPS is shown in dark blue (c), and finally the ALE chamber is shown in yellow, in (d). A scale bar is inset as well. Unlabeled near the bottom of the figure is the plasma enhanced ALD chamber.

2.1.1. X-RAY PHOTOELECTRON SPECTROSCOPY CHAMBER

The X-ray photoelectron spectroscopy (XPS) chamber is used for surface sensitive (i.e., within the topmost 5 nm of a surface) chemical analysis of samples and is seen in Figure 2.2. In situ analysis allows sensitive samples to be analyzed without exposure to ambient conditions. The X-ray photoelectron (XP) spectrometer is a PHI 5600 system, maintained at 1×10^{-9} Torr with a turbomolecular pump, and an ion pump. There is a IR lamp installed internal to the chamber allowing rapid overnight bakeouts to be performed. The XPS detector is a 16 channel detector, while the X-ray source is a dual Mg, Al anode. All XP spectra presented in this dissertation are generated using Mg Kα photons (1253.4 eV), with 15 kV, and 250 W power. The stage is electrically isolated, which allows the sample current to be read on a BNC feedthrough on the 5-axis manipulator. These conditions typically yield a sample current of 40-60 nA. The Mg anode is used as that allows the highest resolution to be achieved on a non-monochromated system. The chamber is also equipped with a PHI 11-068 ion gun, which has the capability to sputter with either of the two gases, Ar or He, on the chamber. Sputtering is performed by accelerating Ar ions through 3 kV, while maintaining 25 mA of emission current, and 15 mPa extractor pressure. The raster is kept at 5×5 mm^2. Ar is used for sputtering and depth profiling, while He is used for ion scattering spectroscopy. There is a camera mounted via a custom gimbal mount that allows viewing of the area being analyzed during acquisition. The camera is behind a 12X zoom microscope (Navitar), with a 0.5X lens attachment (Navitar, 1-50012) and 2X adapter. This configuration yields a working distance of 165 mm. The camera (MiniVID 3.0 6.3MP, LWScientific) is operated using Toupview software. A fiber optic illumination source is used to light the chamber for viewing via the camera using a 150 W halogen lamp (Fostec), and a fiber optic cable attached to the XPS chamber. The camera, and ion gun are both aligned to the analyzer plane, which allows for

repeatable focusing and sputtering once the image in the camera is in focus. The sample is mounted on a dual-stage differentially pumped 5-axis manipulator, allowing *x, y, z*, theta, and psi, rotation. Retard linearity is corrected with low and high pass energy XP scans. Peak positions are calibrated to Cu 2*p*, and Au 4*f* at 932.7, and 84.0 eV, respectively. Alignment to the analyzer focal plane is completed using a Ag slotted sample, which allows for focusing by minimizing counts through the slots in the alignment sample. The ion gun is aligned by maximizing the low energy electron peak ~1250 eV, and verified using a phosphorous sheet, which phosphoresces when struck with energetic Ar ions.

XP spectra are analyzed using CasaXPS (v2.6.13), where fitting of spectra is commonly employed to yield information on the thickness, as well as the chemical species present in the analysis volume.

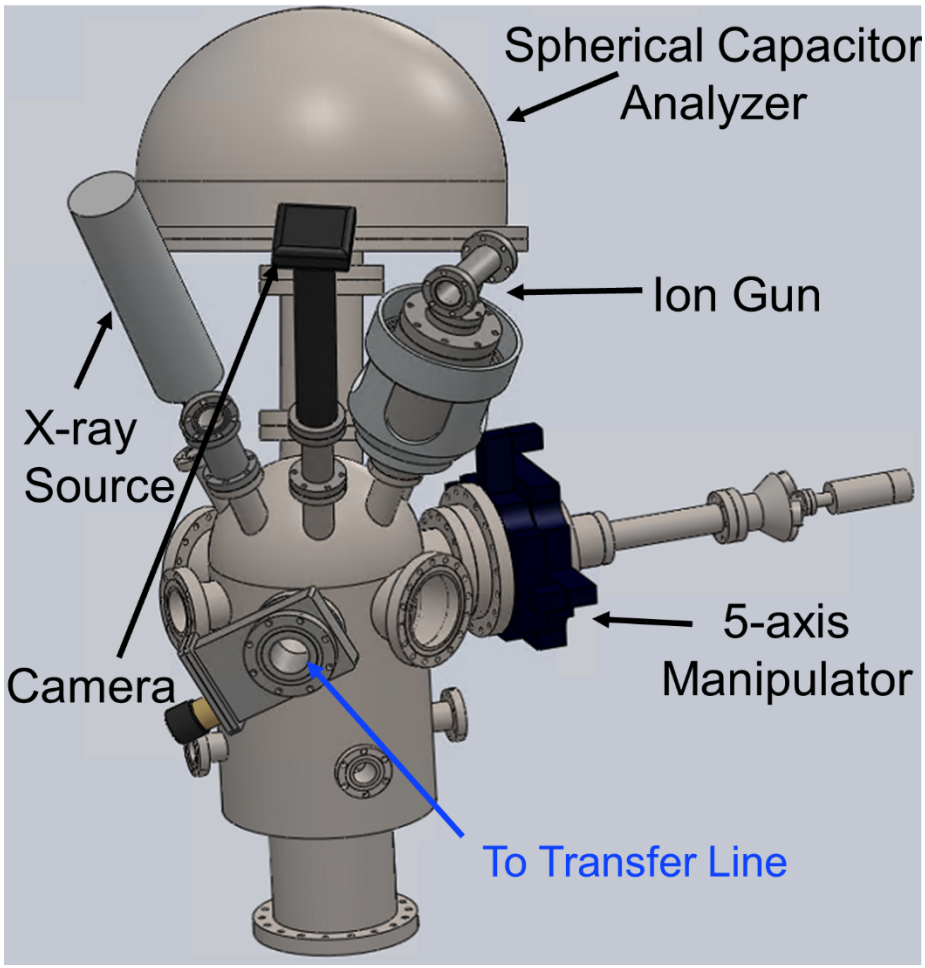

Figure 2.2. A CAD drawing of the XPS chamber is shown. Indicated are the X-ray source (dual source anode), the spherical capacitor analyzer (SCA), the camera mounted behind the microscope, the ion gun, and 5-axis manipulator. Also indicated is the flange that makes the connection to the UHV transfer line in blue.

2.1.2. VACUUM ULTRAVIOLET ENHANCED ATOMIC LAYER ETCHING

The ALE chamber, shown in Figure 2.3, is also attached to the transfer line, allowing in situ sample treatment and analysis. The ALE chamber is a custom six-way stainless steel cross, backed by a dual stage rotary vane roughing pump for low vacuum etching treatments, and a turbomolecular pump for UHV transfer. The ALE chamber pressure is 1×10^{-7} Torr, while the walls are maintained at 80 °C for compatibility with Viton seals on the chamber. The ALE is maintained in a warm-wall configuration to minimize adsorption (and pumping times) after etching is performed. Samples are mounted on a Langmuir probe feedthrough (stroke length 25.4 cm), with a combination thermocouple and power feedthrough with a custom machinable ceramic (Macor) and stainless steel stage that also electrically isolates the sample from ground. The stage is designed for compatibility with remote ion etching (RIE) processes from an inductively coupled plasma (ICP) source, where the stage can be held > 1kV during plasma treatments. The remote plasma source must occupy the slot that the D_2 VUV lamp occupies.

While not installed at the time of writing this dissertation, the ALE chamber is capable of remote plasma exposures as well. The RIE ICP source is RF plasma source equipped with an alumina chamber (Litmas RPS 1501, Advanced Energy) allowing for processing of fluorinated gases up to 1.5 kW. The plasma source has an auto tuned RF matching network, and is controlled using the virtual front panel software from Advanced Energy. ChemRaz gaskets are used at all connections to the ALE chamber to compatibility with plasma environments, and high temperatures. Building water is used to cool the plasma during operation (T < 35 °C, at 1 gpm). Care must be taken when using the ICP plasma, as too low/high gas flowrate, too low/high pressure, and too low/high power will cause the plasma to function in capacitive mode. This is not recommended long term as the voltage differential is sunk in the plasma sheath of a capacitive plasmas as opposed to

producing ions from the gas. This results in high energy ions sputtering in the sheath of the alumina chamber. Ions are accelerated to the sample using a high voltage supply (1 kV), connected to the chamber with a safe high voltage (SHV) connector that transmits power into the vacuum chamber.

Gases are introduced into the ALE through the manifold, which is a custom 0.25" VCR Swagelok welded section with six precursor slots. Each slot is equipped with its own high-speed pneumatic valve (ALD Valve, Swagelok), and mass flow controller, which allows for controlled gas introduction into the chamber during cycles. The second gas inlet is on a 2.75" conflat (CF) flange, which has reactive gases behind a mass flow controller and pneumatic valve. O_2 (research grade) is introduced using this feedthrough. The VUV light source is a D_2 lamp (Hamamatsu, L11798) with a MgF_2 window mounted on the top of the ALE reactor. Samples are raised to the VUV light source within 0.5 cm of the MgF_2 window during exposures, and lowered 15 cm to the gas manifold inlet during etching cycles. The attenuation length of VUV photons in Ar is ~ 2 cm, which mitigates their interaction during etching half-cycles. Ar is continuously flowing through all exposures, to yield a background pressure of 0.1 Torr in the ALE chamber. Actuation of the pneumatic valves is accomplished manually using LabView (Version 19). The valve control circuit is shown in Appendix B. Pressure is monitored using a 10 Torr Baratron gauge mounted on the exhaust of the ALE chamber. Gases leaving the exhaust are scrubbed through a heated scrubber section comprised of a 20" CF nipple, wrapped in resistive heating tape to achieve a temperature > 400 °C. The CF scrubber section is packed with stainless steel metal wool to provide high surface area to thermally crack any unreacted gases leaving the ALE chamber. There is also an exhaust line installed for exhausting fluorinated gases (i.e., NF_3) to a commercial scrubber (Thermo Scientific), for greater gas variety.

The sample temperature inside the ALE chamber is achieved by heating the sample with a 24 V halogen light bulb from below (Osram) in a warm-wall, hot-substrate configuration. The lightbulb housing is a custom high temperature stainless steel housing, with a rapid response thermocouple floating above the light bulb, which is the control temperature for samples inside the ALE reactor. The electrical connections are fixed inside the ALE chamber, so that there is minimal risk to lose electrical contact with any equipment when raising and lowering the sample during oxidation and etching half cycles.

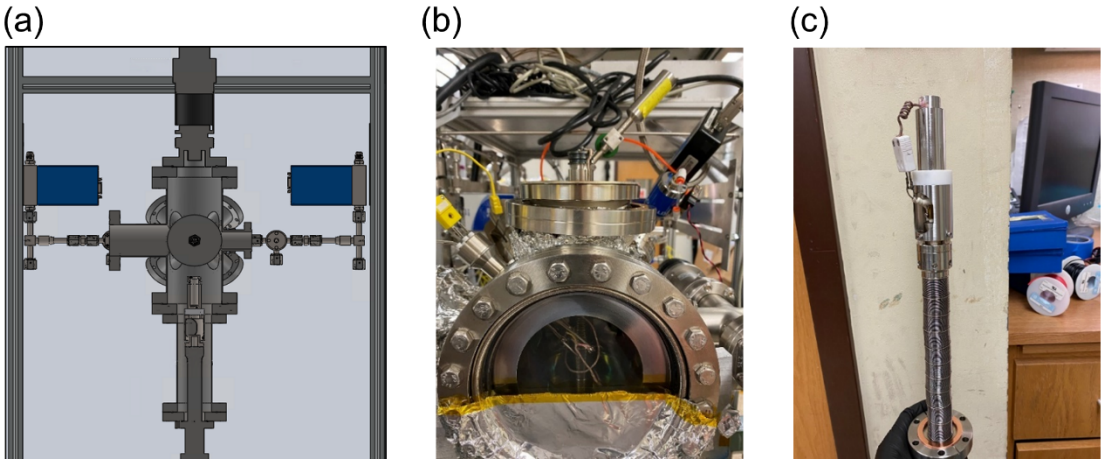

Figure 2.3. A cross sectional view of the ALE chamber is seen in (a), where the D_2 lamp is at the top of the reactor, precursor manifold is behind the reactor, and the sample stage is fully retracted at the bottom of the reactor. (b) shows the full stroke length of the sample holder, where the D_2 lamp is removed from the ALE reactor and the sample is seen protruding from the top 6" flange. (c) the sample holder, mounted to the end of the Langmuir probe, where the lightbulb housing is on the top, and it is electrically isolated from the feedthrough with a custom Macor adapter, seen in white.

While this description is used for all etching performed in this thesis, there are several improvements that should be made to the chamber. More discussion of the design

recommendations, and a CAD drawing of the recommendations, can be found in Appendix C.

2.2. Ultra-High Vacuum Facilities – Atomic Layer Deposition

ALD is performed in a separate UHV facility consisting of a molecular beam epitaxy (MBE) system (DCA M600 MBE system), custom hot-wall ALD chamber, and an XPS chamber, equipped with a quartz crystal monochromator. Similar to the system used in etching experiments, the system used for studying ALD of perovskites allows for the in situ vacuum transfer of samples without exposing them to ambient conditions. An overview of the system is seen in Figure 2.4, which is taken from Ref. 1.

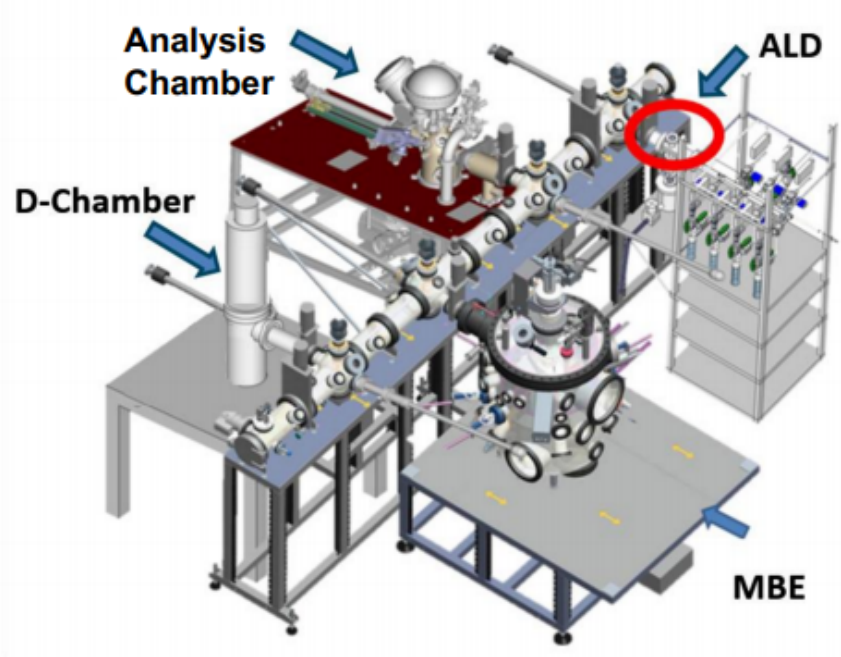

Figure 2.4. Drawing of the UHV system that is used to perform ALD of BTO. The ALD chamber is indicated in a red circle, while the MBE, and analysis chamber (XP analysis) are also shown with arrows. Low temperature reduction can be accomplished using the D chamber indicated as well.

2.2.1. ATOMIC LAYER DEPOSITION

The ALD chamber is a custom rectangular hot-wall stainless steel reactor connected to a similar manifold as previously described, is seen in Figure 2.5, which is taken from Ref. 1. The ALD reactor is backed by a dual stage rotary vane pump during ALD cycles, where all six manifold mass flow controllers deliver Ar (research purity) at a rate of 20 sccm during all ALD cycles. The pressure inside the ALD chamber when it is pumped on by the turbomolecular pump is 5×10^{-7} Torr, at a temperature of 150 °C. ALD is performed by exposing substrates to half-cycles of precursor vapors inside the ALD chamber. Precursor dose is controlled again by a pneumatic ALD valve with a 3-way pneumatic valve, and a dedicated mass flow controller. Ar is used as the carrier gas, which is diverted into the precursor saturator when it is desired to dose via actuating the 3-way pneumatic valve. ALD cycles are performed by exposing substrates to one cycle of precursor A, followed by an Ar purge, dosing the vapor of precursor B, followed by an Ar purge. Oxide materials are the focus of this discussion, therefore, H_2O is the co-reactant for all conditions discussed herein. Precursor dosing time is controlled using LabView (Version 19).

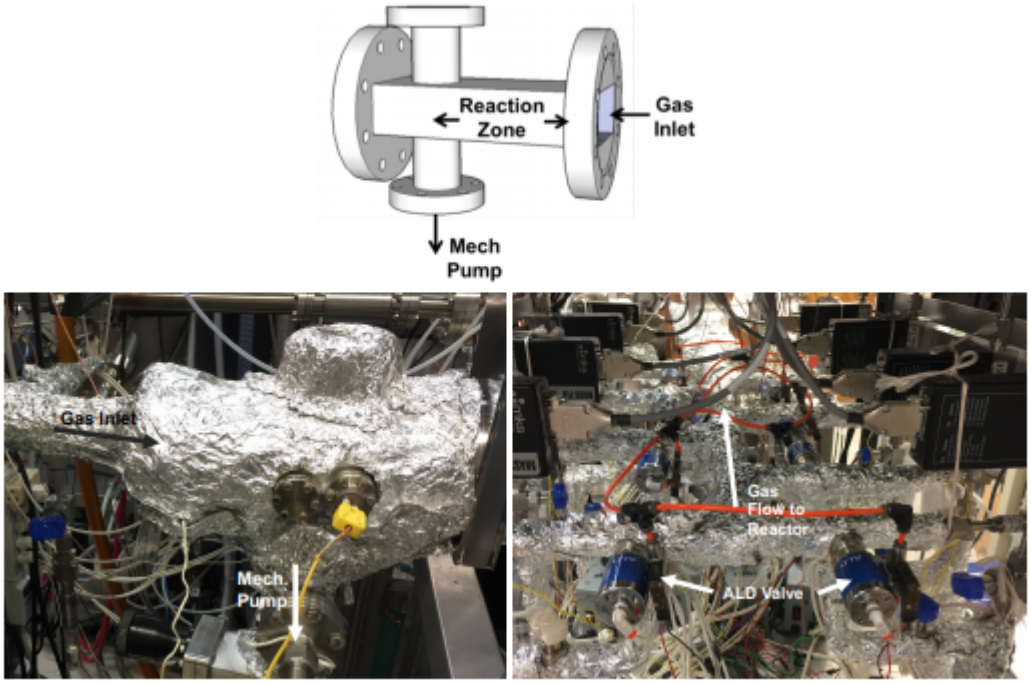

Figure 2.5. CAD drawing of the ALD reactor on top, where the gas inlet, and pumping flanges are shown below on the left. The view down the manifold is shown in the lower right image, where gas flow into the reactor is indicated.

ALD of $BaTiO_3$ is performed using three precursors, as outlined in Table 2.1. One cycle of Ba or Ti consists of a 1 sec dose of the Ba/Ti precursor, followed by a 15 sec purge with Ar, followed by a 1 sec dose of H_2O, and finally a 15 sec Ar purge. This is indicated with the following shorthand 15/1/15/1 for a given precursor. As this is a perovskite, the ratio of Ba:Ti must be tuned to be as close to 1 as possible. Composition is calculated from in situ XPS measurements, where the stoichiometry of 1 is achieved by dosing 3 Ba: 4 Ti cycles. All ALD growths are at 225 °C.

Table 2.1. Precursors used for the ALD of $BaTiO_3$ are shown. The temperature of the saturator is also indicated in the far right column.

Element	Precursor	Temperature
Ba	Barium Bis(triisopropylcyclopentadienyl)	150 °C
Ti	Titanium Tetraisopropoxide	35 °C
O	Water	20 °C

2.2.2. X-RAY PHOTOELECTRON SPECTROSCOPY AND MOLECULAR BEAM EPITAXY

Film composition is analyzed in situ using XPS, in a similar manner to that described previously. The XP spectra for ALD are collected with monochromated Al Kα (1486.6 eV) radiation. This yields higher resolution spectra than those collected using the non-monochromated Mg source.

The DCA M600 MBE system has a base pressure of 1×10^{-9}, which is maintained by a cryopump. The MBE system is equipped with a heater and manipulator that allows annealing of samples to 1000 °C, while rotating them as well. There are six Knudsen (effusion) cells, and four electron beam evaporators, which are used for finely controlled molecular beam deposition. The system also has O_2 and N_2 atomic sources as remote RF plasmas. Film thicknesses are characterized using an in situ QCM, where composition and growth are controlled with pneumatically actuated shutters (RF plasmas), temperature (Knudsen cells), or emission current (electron beam evaporation cells). Surface crystallinity is monitored using reflective high energy electron diffraction (RHEED) as annealing or deposition occurs.

2.3. Area – Selective Patterning

Hydrophobic patterns are generated using polystyrene (PS, Sigma-Aldrich), which are filtered, and then deposited with spin coating onto the substrates. Patterns are produced by exposing PS to UV light with a shadowmask to block regions of the surface from illumination. The shadowmask consists of a series of squares in a grid pattern, where the side of the square ranges from 50 μm to 1 mm. The exposure chamber is evacuated of O_2 by flowing N_2 for 60 min prior to turning on the UV lamp. PS exposed to the UV lamp is crosslinked, while PS that is shadowed from the UV light is uncrosslinked. Toluene is used to rinse the uncrosslinked PS from the surface, which transfers the shadowmask pattern into the PS. Crosslinked PS is removed with an O_2 plasma etch (Oxford Plasma). This follows the procedure outlined in Refs. 2, and 3.

2.4. Film Metrology and Characterization

Samples for studying the ALE of Ru and Pd are characterized in situ using XPS as previously described. Ex situ characterization is performed with scanning electron microscopy (SEM), X-ray diffraction (XRD), X-ray reflectivity (XRR), and atomic force microscopy (AFM). Details of etching can be found in Chapters 3, 4, 5, and 6.

ALD samples are characterized in situ using XPS and RHEED to monitor surface crystallization. Ex situ characterization is performed with SEM, AFM, XRD, XRR, and time of flight secondary ion mass spectroscopy (TOF-SIMS). BTO is amorphous as deposited unless grown in a pristine template layer prepared using MBE.[4] Crystallization of BTO is achieved through a post-deposition anneal in the MBE chamber in an oxygen environment, where the O_2 partial pressure is 1×10^{-6} Torr. The onset of crystallization is monitored in situ using RHEED. Thin films of BTO that are grown in bare STO(001) substrates are observed to crystallize at 650 °C. The onset of crystallization is higher for

films that are grown on STO substrates subjected to AS patterning with PS.[1] Details of AS-ALD are found in Chapter 7.

2.5. Computational Methods

Simulations are used to understand characteristics and mechanistic details of oxidation on Pd and Ru. Ab initio simulations are performed within the approximations of density functional theory (DFT). DFT simulations are performed using the plane-wave basis code Quantum Espresso (v6.4.1).[5,6] Ex situ XRD measurements inform the facet of the slab models that are analyzed using DFT. DFT is performed within the generalized gradient approximation (GGA) with the Perdew-Burke-Ernzerhof (PBE) exchange functional and correlation.[7,8] As Pd and Ru are relatively light transition metals, non-relativistic, ultrasoft pseudopotentials are used to describe the valence structure of each atom. The effects of dispersion are found to be important to characterizing the system, therefore all DFT models account for dispersion with the Grimme-D3 correction[9] and Becke-Johnson damping.[10] This description of the system was chosen using a figure of merit that weights the predicted geometry of resulting structures, and comparing adsorption energies, fermi energy levels, and cohesive energies with published reports. Van der Waals D2, D3, Cooper, and several combinations of various functionals and exchange correlations were explored, as well as revised pseudopotentials, projector augmented wave (PAW) pseudopotentials, high accuracy pseudopotentials among others were evaluated. More detail on exchange functionals, exchange correlations, and pseudopotentials that were evaluated can be found in Appendix D, which also includes a sample input file for an optimization calculation, and a NEB calculation.

Pd and Ru slabs are simulated with either four or six atomic layers, depending on the aim of the simulation. Thicker slabs are used to allow more atomic planes to relax in

simulations that involve deeper incorporation of O into the substrate slab. These slabs are used to understand the effect of subsurface O incorporation on O diffusion, as well as adsorption of oxidants onto the slab surface. The nudged elastic band method (NEB) is used to estimate the minimum energy path (MEP) for a given reaction. Density of state (DOS) and projected density of state (PDOS) calculations are used to assess oxidant bonding on Pd. All DOS and PDOS calculations are performed by raising the number of k-points used to sample the irreducible Brillouin zone from 5×5×1, to 10×10×1, and finally 30×30×1 for the optimization, self-consistent field (SCF), and non-self-consistent field (NSCF) calculations, respectively. Convergence of k-point was also verified by raising the number of k-points to 8×8×1, 30×30×1, and 50×50×1, for the optimization, SCF, and NSCF calculations, respectively. The wavefunction cutoff energy and charge density cutoff energy is 45, and 450 Ry, respectively. Convergence of the wavefunction and charge density cutoff energy is verified by raising them to 60, and 600 Ry, respectively. The NSCF calculation is used to determine the charge density of the solid. Differential charge density ($\Delta\rho$) is used to assess localization of electrons after an adsorption/reaction event. More detail on DFT, DOS, PDOS, and $\Delta\rho$ can be found in Chapters 3, and 4.

All simulations are performed using the Lonestar5 resource at the Texas Advanced Computing Center (TACC), while structures are analyzed and visualized using XCrysDen (Version 1.6.2).[11]

2.6. REFERENCES

(1) Lin, E. L. Atomic Layer Deposition of Epitaxial Perovskites for Electronic and Photonic Applications. *Thesis* **2018**.

(2) Zhang, Z.; Dwyer, T.; Sirard, S. M.; Ekerdt, J. G. Area-Selective Atomic Layer Deposition of Cobalt Oxide to Generate Patterned Cobalt Films. *Journal of Vacuum Science & Technology A* **2019**, *37* (2), 020905.

(3) Zhang, Z.; Nallan, H. C.; Coffey, B. M.; Ngo, T. Q.; Pranamik, T.; Ekerdt, J. G.; Banerjee, S. Atomic Layer Deposition of Cobalt Oxide on Oxide Substrates and Low Temperature Reduction to Form Ultrathin Cobalt Metal Films. *Journal of Vacuum Science & Technology A* **2019**, *37* (1), 010903.

(4) Ngo, T. Q.; Posadas, A. B.; McDaniel, M. D.; Hu, C.; Bruley, J.; Yu, E. T.; Demkov, A. A.; Ekerdt, J. G. Epitaxial C-Axis Oriented BaTiO3 Thin Films on SrTiO3-Buffered Si(001) by Atomic Layer Deposition. *Appl. Phys. Lett.* **2014**, *104* (8), 082910.

(5) Giannozzi, P.; Baroni, S.; Bonini, N.; Calandra, M.; Car, R.; Cavazzoni, C.; Ceresoli, D.; Chiarotti, G. L.; Cococcioni, M.; Dabo, I.; Corso, A. D.; Gironcoli, S. de; Fabris, S.; Fratesi, G.; Gebauer, R.; Gerstmann, U.; Gougoussis, C.; Kokalj, A.; Lazzeri, M.; Martin-Samos, L.; Marzari, N.; Mauri, F.; Mazzarello, R.; Paolini, S.; Pasquarello, A.; Paulatto, L.; Sbraccia, C.; Scandolo, S.; Sclauzero, G.; Seitsonen, A. P.; Smogunov, A.; Umari, P.; Wentzcovitch, R. M. QUANTUM ESPRESSO: A Modular and Open-Source Software Project for Quantum Simulations of Materials. *J. Phys.: Condens. Matter* **2009**, *21* (39), 395502.

(6) Giannozzi, P.; Andreussi, O.; Brumme, T.; Bunau, O.; Nardelli, M. B.; Calandra, M.; Car, R.; Cavazzoni, C.; Ceresoli, D.; Cococcioni, M.; Colonna, N.; Carnimeo, I.; Corso, A. D.; Gironcoli, S. de; Delugas, P.; DiStasio, R. A.; Ferretti, A.; Floris, A.; Fratesi, G.; Fugallo, G.; Gebauer, R.; Gerstmann, U.; Giustino, F.; Gorni, T.; Jia, J.; Kawamura, M.; Ko, H.-Y.; Kokalj, A.; Küçükbenli, E.; Lazzeri, M.; Marsili, M.; Marzari, N.; Mauri, F.; Nguyen, N. L.; Nguyen, H.-V.; Otero-de-la-Roza, A.; Paulatto, L.; Poncé, S.; Rocca, D.; Sabatini, R.; Santra, B.; Schlipf, M.; Seitsonen, A. P.; Smogunov, A.; Timrov, I.; Thonhauser, T.; Umari, P.; Vast, N.; Wu, X.; Baroni, S. Advanced Capabilities for Materials Modelling with Quantum ESPRESSO. *J. Phys.: Condens. Matter* **2017**, *29* (46), 465901.

(7) Perdew, J. P.; Burke, K.; Ernzerhof, M. Generalized Gradient Approximation Made Simple. *Phys. Rev. Lett.* **1996**, *77* (18), 3865–3868.

(8) Perdew, J. P.; Burke, K.; Ernzerhof, M. Generalized Gradient Approximation Made Simple [Phys. Rev. Lett. 77, 3865 (1996)]. *Phys. Rev. Lett.* **1997**, *78* (7), 1396–1396.

(9) Grimme, S.; Antony, J.; Ehrlich, S.; Krieg, H. A Consistent and Accurate Ab Initio Parametrization of Density Functional Dispersion Correction (DFT-D) for the 94 Elements H-Pu. *J. Chem. Phys.* **2010**, *132* (15), 154104.

(10) Grimme, S.; Ehrlich, S.; Goerigk, L. Effect of the Damping Function in Dispersion Corrected Density Functional Theory. *Journal of Computational Chemistry* **2011**, *32* (7), 1456–1465.

(11) Kokalj, A. XCrySDen—a New Program for Displaying Crystalline Structures and Electron Densities. *Journal of Molecular Graphics and Modelling* **1999**, *17* (3), 176–179.

Chapter 3: Theoretical and Experimental Analysis of VUV Enhanced Oxidation of Pd

Contents for this chapter are published as: B. M. Coffey, H. C. Nallan. J. R. Engstrom, J. G. Ekerdt. Accepted, Applied Materials and Interfaces. 2020.

Supplementary information is found in Appendix E.

3.1. Introduction

Continued progress of nanotechnology hinges on methods that allow cyclic modification to remove or deposit material one atomic layer at a time using self-limiting chemical reactions. Of interest is the atomic layer etching (ALE) of noble metals, such as Pt, Ru, and Pd. Pd is widely used as a catalyst for oxygen evolution,[1] oxygen reduction,[2] and, of particular interest to the nanotechnology community, for metal assisted chemical etching.[3–6] Additionally, Pd ALE methods are instrumental in the development of MRAM devices,[7] and Si nanostructures.[8] Etching of Pd is typically performed using Ar/CF_4 or $Ar/CF_4/O_2$ plasmas,[9] or O_2 plasma followed by vapor exposure of HCOOH, hexafluoroacetylacetone (hfac), or acetylacetone (acac).[7] In addition to dry etching, Pd may also be etched using wet methods consisting of $FeCl_3$,[10] or hfac and acac.[11]

ALE of Pd has been elusive thus far as it is difficult to limit oxidation to the topmost layer of Pd (~2-4 Å) using conventional O_2 plasma exposures. We demonstrated, and discuss in Chapter 4, that co-exposure of vacuum ultraviolet (VUV) light and O_2 gas leads to PdO_x formation, wherein the Pd 3*d* X-ray photoelectron (XP) feature for Pd^{2+} at 336.7 eV develops as oxidation proceeds.[12] After sufficiently short exposures to VUV at low

enough temperatures PdO_x formation is limited to the near-surface region. Removal of this PdO_x by exposure to HCOOH vapor results in Pd metal etch rates of 2.8 Å/cycle, which is approximately the minimum bulk Pd-Pd distance, 2.7 A.[13,14] However, key to fully exploiting this approach to ALE is a better understanding of PdO_x and its formation from VUV/O_2 co-exposure.

VUV irradiation of O_2 yields singlet atomic oxygen, $O(^1D)$, triplet atomic oxygen, $O(^3P)$, and O_3, according to Equations (3.1) – (3.3)[15]

$$O_2 \rightarrow O(^3P) + O(^3P);\ 185\ nm < \lambda < 240\ nm \quad (3.1)$$

$$O_2 \rightarrow O(^1D) + O(^3P);\ \lambda < 185\ nm \quad (3.2)$$

$$O(^3P) + O_2 + M \rightarrow O_3 + M \quad (3.3)$$

where production of O_3 proceeds *via* recombination in the presence of a third body, M.[16] Thermal treatment of Pd with O_2 does not form PdO_x for substrate temperatures up to 200 °C.[12] Therefore, formation of PdO_x at temperatures T < 200 °C under VUV and O_2 co-exposure is attributed to the presence of O_3, $O(^1D)$, and $O(^3P)$. $O(^1D)$, and $O(^3P)$ are collectively referred to as atomic O. The relative abundances of O_3 and atomic O depend on the rates of production (Eqns. 1-3) and rates of various loss reactions. The mean free path of O_2 at 1 Torr is on the order of 0.01 cm, and the gap between the light source and the substrate surface is 0.5 cm, so intermolecular and surface collisions contribute to loss reactions. Atmospheric photochemical processes of UV and O_2 offer insight into the kinetics and rates of formation of the species in Equations (1) – (3). Gas phase reactions in the stratosphere at comparable pressures to the experimental setup used herein (1 Torr) predict O_3 to have a lifetime (*viz.*, the abundance/total loss rate) of approximately 1000 s

while atomic O has a lifetime of about 0.002 s.[17,18] Measurements of O_3 (96% pure) decomposition to O_2 ($2O_3 \rightarrow 3O_2$) indicate a half-life ranging between 9×10^3 s and 1.3×10^5 s at 300K and 4 Torr; the half-life increases due to passivation of surfaces from continued O_3 exposure.[19] The lifetime of atomic O produced by VUV/O_2 co-exposure[12] is unknown, as is the relative abundance of O and O_3; however, it is reasonable to assume that O is short-lived, relative to O_3. We hypothesize that a gas composition consisting of mainly atomic O, O_3 and O_2 is incident on a Pd sample when the surface is illuminated by the VUV light source; and a gas comprised of O_3 and O_2 is incident on a Pd sample shadowed from the VUV light source.

Density functional theory (DFT) is well suited to aid in answering mechanistic questions of how PdO_x is formed using VUV/O_2, and which oxidants participate in the oxidation reactions. Interactions of Pd metal with O_2 is characterized theoretically and experimentally, as there is a wealth of literature reporting oxidation of Pd(111)[20–23] and Pd(100)[24] surfaces with O and O_2. Others have shown that a coverage of 0.25 monolayer (ML) of O is produced upon exposing Pd to O_2 at 0.5 Torr.[21,25–27] Thus assessment of adsorption and bonding with DFT at 0.25 ML of O coverage approximates the experimental conditions explored herein, and represents an important intermediate state for continued oxidation. However, while DFT studies of O_2 and O interactions on Pd surfaces are widely available, little information is available probing the surface interactions of O_3 on Pd.

This study aims to elucidate the surface-adsorbate interaction between Pd and oxidants produced from co-exposure of VUV and O_2 using experimental and DFT analysis.

Of particular interest is gaining insight into the molecular scale events concerning the reactions of O_3 and O with a Pd surface, specifically in limiting oxidation to near-surface Pd layers, and determining barriers to the growth of a surface oxide, and if it is self-limiting in any way. This mechanistic information can then be used to offer further insight into the VUV-enhanced ALE of Pd,[12] and potential avenues to further control VUV-enhanced ALE.

3.2. METHODS

3.2.1. EXPERIMENTAL METHODS

Sample preparation and equipment used follows methods described elsewhere.[12] Pd metal thin films are deposited using an electron beam evaporation tool (CHA Industries) where thickness is monitored *in situ* using a quartz crystal microbalance (QCM, Inficon). Pd evaporation targets are >99.95% purity and Ti evaporation targets are >99.995% purity (Kurt J. Lesker). Substrates are double side polished B-doped Si (100) (University Wafer, 1 – 10 Ω cm), and are used as received. Ti adhesion layers are evaporated onto the substrate *in situ* prior to evaporation of Pd and are nominally 10 nm. Adhesion layers are used to prevent the "peeling" of Pd from Si substrates that we have observed. The substrate Si has a native oxide present before evaporation. Pd film thickness and crystallinity is characterized *ex situ* using X-ray diffraction (XRD), and X-ray reflectivity (XRR) with a Rigaku Ultima IV diffractometer, which uses Cu Kα radiation. Pd film thickness is calculated by fitting XRR spectra using GenX (v2.4.10).[28] Evaporated nominal thicknesses of 20 nm Pd are measured to be between 22 – 24 nm, while 10 nm Ti is ~5-8 nm.

Samples are degreased by sonicating in acetone, isopropanol, and water (>18 MΩ cm), for 10 min each, and drying with N_2 prior to loading into the analysis and reaction system. All etching and X-ray photoelectron (XP) characterizations are completed in a custom-built ultra-high vacuum system consisting of a transfer line (base pressure 1×10^{-7} Torr), which connects an XP spectrometer (PHI 5600, base pressure 1×10^{-9} Torr), custom-built vacuum furnace, load-lock chamber, and ALE chamber. XP spectroscopy (XPS) is performed without breaking vacuum. The XP spectra are collected using Mg Kα radiation. Curve fitting and analysis of XP spectra is done using CasaXPS (v.2.3.16).

All oxidation exposures are done in the ALE chamber, which is described in more detail elsewhere.[12] Briefly, the ALE chamber is a custom stainless steel chamber equipped with a VUV lamp (H2D2 Hamamatsu, L11798), which is a 110 W lamp, with a broad emission spectrum from $115 < \lambda < 400$ nm, and the strongest lines at 128, and 160 nm, ($6.5 < h\nu < 11.3$ eV). The reactor is maintained at 50 °C, in a warm wall configuration, while the sample is heated to the reaction temperature *via* a halogen bulb underneath the sample. Substrate heating is maintained with a temperature controller, which regulates power delivery to the bulb by measuring the temperature beneath the substrate.

Co-exposure of VUV and O_2 is performed at 1 Torr, where the sample is held 0.5 cm from the MgF_2 window of the VUV light source so reactive species will reach the substrate surface. Ar (Matheson, 99.9999%) is introduced to give a background pressure of 0.100 Torr. O_2 (Matheson, >99.999%) is introduced into the ALE chamber to yield an O_2 partial pressure of 1 Torr. Caution is required when working with the VUV lamp, as

UV light is damaging to biological tissue. Protective eyewear is used at all times when using the VUV lamp.

20 nm Pd films are used to elucidate the dominant oxidant present in the gas phase by irradiating samples at ALE reaction conditions of 1 Torr O_2 co-exposed with VUV light for 3 min. Two conditions are explored to discern oxidation arising from O or O_3: one with a Pd film positioned such that the surface normal vector is facing VUV light (illuminated), and the second is mounted face down, so that the surface normal vector is pointing 180° away from the VUV light (shadowed). In this way, O and O_3 may impinge on the surface in the illuminated configuration, whereas O_3 can diffuse to the surface in the shadowed configuration as O will recombine before reaching the shadowed surface. 20 nm Pd is also used to explore temperature and time effects of VUV/O_2 co-exposure on PdO_x formation.

3.2.2. THEORETICAL METHODS

Ab initio calculations are performed using the plane wave basis code Quantum Espresso (version 6.4.1).[29,30] Pd crystal structures are well-known to be fcc, with a lattice constant a = 3.859 Å.[20] Bulk Pd is optimized before surfaces are constructed to minimize stresses within the cell. Pd surfaces (111) and (100) are modeled using this bulk Pd crystal structure, which is in agreement with interplanar spacing measured experimentally using XRD. Pd(111) and Pd(100) are modeled by 2×2 surface cells. This corresponds to a coverage of θ = 0.25 ML, which is the nominal coverage for PdO_x formation at experimental conditions herein.[21,22,25–27] Pd is modeled using four and six atomic layers for initial oxidation of clean Pd, and PdO_x growth, respectively. For calculations where O

incorporation increases, 1 O layer indicates a surface O layer, while 2 O layers indicates O placed on the surface, as well as in between the $n = 2$, and $n = 3$ atomic Pd planes, and 3 O layers indicates O placed on the surface, and in between the $n = 2$, $n = 3$, and $n = 4$ atomic planes. PdO_x layered structures are created by placing O in the interstitial hollow sites, optimizing the structure, and using the optimized structure in calculations. Structures are chosen this way to allow at least two atomic layers to relax freely as O is incorporated into the Pd substrate, while keeping the bottom two atomic Pd layers fixed at the bulk position. Periodic images orthogonal to the slab are separated by 20 Å of vacuum.

All DFT calculations use the Perdew-Burke-Ernzerhof (PBE)[31,32] exchange-correlation functional, and Grimme-D3[33] van der Waals correction with Becke-Johnson damping.[34] Van der Waals forces are necessary to capture the free molecular parameters of O_3 (i.e., bond angle, and bond distance, $d_{O\text{-}O}$), and thus are included in all simulations. Ultrasoft pseudopotentials are employed as well, where the valence structure of Pd is $4s^2 5s^2 4p^6 4d^8$, and O is $2s^2 2p^4$. Pd slabs are optimized using a 5×5×1 Monkhorst-Pack grid with charge density and wavefunction energy cut-off 600 Ry and 60 Ry, respectively. Convergence of *k*-points and atomic layers is verified by varying the *k*-point mesh from 5×5×1 to 8×8×1, and increasing the number of atomic layers from four to six, which results in an energy difference <2 meV/atom. The choice of unit cell (i.e., 100, vs. 111, and four or six atomic layers) for free molecular calculations of oxidants are < 2 meV of one another. Marzari-Vanderbilt "cold-smearing" is used with a smearing width of 0.002 Ry. Spin-polarized calculations are only employed for free molecular oxidant species (O_2, and O_3), as ferromagnetic effects can arise on Pd surfaces that are spin-polarized.[20,35] Density of

state (DOS) and projected density of state (PDOS) calculations are used to examine bonding, while nudged elastic band[36] (NEB) calculations are used to identify transition states.

Adsorption energy, E_{ads}, is calculated according to Equation (3.4),

$$E_{ads} = E_{surf} + E_{Ox} - E_{Ox/surf} \quad (3.4)$$

where E_{surf} is the energy of the optimized surface, E_{Ox} is the energy of the optimized oxidant O, O_2, or O_3, and $E_{Ox/Surf}$ is the energy of the optimized Pd surface with the oxidant adsorbed. E_{Ox} is calculated as described in detail in Supporting Information (Figure E.1). All oxidant energies, E_{Ox}, are referenced to the energy of a free O_2 molecule according to the following: $E_O = ½ \times (E_{O2} + \Delta E_{O\text{-}O})$, where $\Delta E_{O\text{-}O}$ is the bond energy of an O_2 molecule, 498 kJ/mol; E_{O2} is the calculated energy of a free molecular O_2 species; and $E_{O3} = E_{O2} + E_O - \Delta U_r$, where ΔU_r is the change in internal energy for the reaction $O_3 \rightarrow O_2 + O$, which is 102.4 kJ/mol.[37] In this convention a positive adsorption energy indicates exothermic adsorption, while a negative value is endothermic. It is also important to note that all adsorption energies reported are for adsorbed O, O_2, or O_3, and are not normalized to the number of O atoms involved in adsorption. All adsorbing oxidants species are relaxed from an initial position 3 Å above the surface atomic plane.

Differential charge density, $\Delta\varrho$, is calculated according to Equation (3.5),

$$\Delta\varrho = \varrho_{A/surf} - \varrho_A - \varrho_{surf} \quad (3.5)$$

where $\varrho_{A/surf}$ is the charge density of the optimized geometry of the Pd with adsorbate, ϱ_A is the charge density of the adsorbate in the same geometric configuration on the surface, without any Pd atoms present, and ϱ_{surf} is the charge density of the optimized Pd surface

without any adsorbate. All $\Delta\rho$ plots have the same contour cut-off point (0.031 e/bohr^3) to allow comparison between oxidant/Pd systems.

Pd structure images and analysis is completed using XCrysDen (Version 1.6.2),[38] and VESTA (Version 1.1.0),[39] where charge density images are generated using VESTA.

3.3. Results

3.3.1. Proposed Oxidation Mechanism

A proposed oxidation mechanism is presented in Figure 3.1 to contextualize the results. Based on experimental results and DFT calculations, the proposed oxidation of Pd consists of four steps: (1) All oxidizing species adsorbing on a clean Pd surface (O, O_2, and O_3); (2) a 2D surface oxide forming from adsorbed O originating from gas phase O, dissociation of O_2 on Pd, and dissociation of O_3 on Pd; (3) adsorbed atomic O diffusing subsurface; and (4) oxidation of subsurface layers from adsorbed atomic O for continued growth of PdO_x. While gas phase O and O_3 adsorb to produce a 2D surface oxide, the results presented herein point to gas phase atomic O as the species responsible for subsurface oxidation.

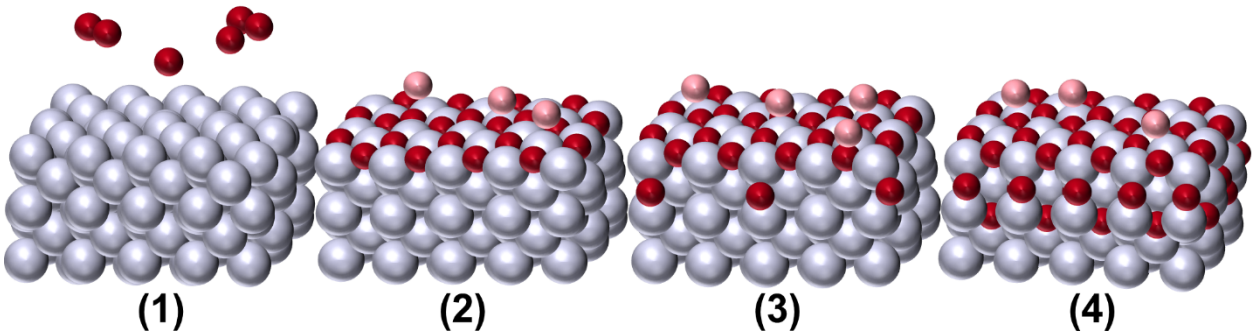

Figure 3.1. A schematic representation of oxidation of Pd by co-exposure to VUV/O_2. Clean Pd is shown in panel (1), where O, O_2, and O_3, adsorb and dissociate. Panel (2) shows a Pd surface that forms a 2D surface oxide from dissociation arising from O_2, and O_3, as well as gas phase O. Panel (3) shows O atoms beginning to diffuse subsurface, while more atomic O is added to the surface originating from the gas phase. Panel (4) shows the self-limiting nature of the subsurface PdO_x oxide. Gray atoms indicate Pd, while dark red indicates O, and light red indicates an adsorbed O species that has not yet incorporated into Pd. The structure depicted in all four panels is fcc Pd.

3.3.2. PD SURFACE OXIDATION

20 nm Pd is used to establish the surface that is oxidized in VUV/O_2 oxidation experiments, as well as if the film crystal structure changes with thermal annealing in O_2. XRD of the initial surface is shown in Figure 3.2, where an untreated 20 nm Pd surface is shown on the bottom in blue, and a Pd surface heated in O_2 for 60 min at 100 °C, and 200 °C, is shown in the middle in green, and top in red, respectively. XRD reveals two features at 2θ of 40.10° and 46.44°, which are attributed to Pd(111) and Pd(200), respectively. Overlapping Ti(111) in the region of Pd(111) is not detectable, likely due to the thickness of the Ti layer, which is estimated to be ~5 nm from fits of XRR data (not shown). Fitting of the features in Figure 3.2 yield the Pd(111) and Pd(100) interplanar spacing, d_{111} = 2.248 ± 0.001 Å, and d_{100} = 1.955 ± 0.003 Å, respectively. The position of the two features do not change if annealed up to 200 °C.

The Pd surface that results after repeated etch cycles is also investigated, as VUV-enhanced oxidation is studied with ALE in mind. ALE is performed as described elsewhere.[12] After 5, 10, and 20 ALE cycles, Pd(111) and Pd(200) are the only features detectable by XRD (not shown). Therefore, the surface consisting of Pd(111) and Pd(100) is a reasonable representation of the Pd surface. The use of Pd(111) and Pd(100) also allows

for comparison between simulation reported herein and the literature.[20–27] However, it is important to note that the surfaces investigated herein are not atomically smooth, and, as we have shown, Pd surface roughness decreases as ALE is performed, and the rate of oxidation depends on surface area.[12] This implies high order facets are likely present for the initial ALE cycles, and oxidation occurs more rapidly. Thus we expect experimental oxidation to be more facile compared to the atomically smooth surfaces used herein for the DFT simulations owing to a larger number of adsorption sites present on higher order surfaces, and longer oxidation times may be required as ALE is progresses into the film.

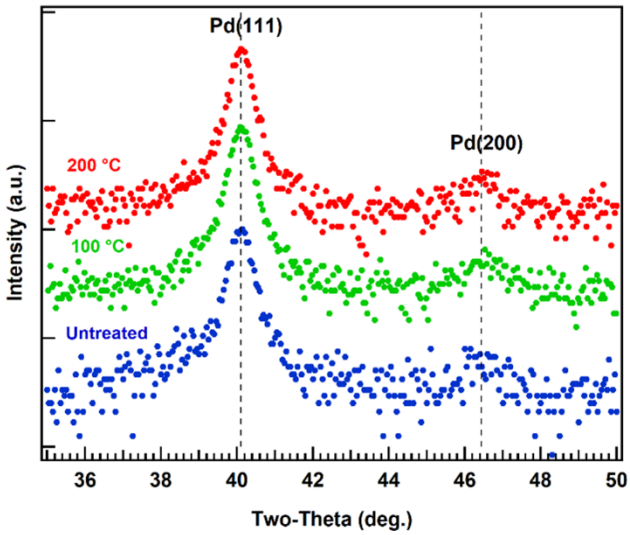

Figure 3.2. XRD of 20 nm Pd on 10 nm Ti on p-Si(100) without being exposed to any treatment (blue, bottom), a second film exposed to O_2 at 100 °C for 60 min (green, middle), and a third film exposed to O_2 at 200 °C for 60 min (red, top). Two features are indicated with vertical dashed lines corresponding to Pd(111), and Pd(200) reflections.

20 nm Pd is used to elucidate the oxidant (*e.g.*, O, O_2, or O_3) responsible for forming PdO_x by co-exposing samples at 1 Torr and 50 °C to VUV/O_2, where one sample is facing

up (illuminated), exposing the Pd surface to O, O_2 and O_3; and another facing down (shadowed), exposing the Pd surface to O_2 and O_3. Owing to the long lifetime and half-life of O_3,[17–19] O_3 is likely capable of diffusing to the Pd surface that is shadowed. The ratio of the lifetime of atomic O to O_3 is approximately 2×10^{-6}, indicating it is highly unlikely atomic O diffuses to the Pd surface when it is shadowed. Oxidation arising from O_2 is very unlikely, as thermal exposures to O_2 up to 200 °C do not form PdO_x,[12] which is in agreement with previous studies.[27]

Figure 3.3(a) shows the 3*d* XP region after co-exposure to VUV/O_2 for the illuminated and shadowed configurations. There are two visible XP features before oxidation (Figure 3.3(c), top), which are attributed to Pd $3d_{5/2}$ and Pd $3d_{3/2}$ at 335.0 eV, and 342.0 eV, respectively. After co-exposure to VUV/O_2, the illuminated sample displays a second Pd $3d_{5/2}$ feature at 336.7 eV (+1.7 eV relative to Pd^0), which is due to Pd^{2+} in the form PdO.[40,41] There is no observable Pd^{2+} character in the sample shadowed after 3 min co-exposure to VUV/O_2 (Figure 3.3(a)). These observations are consistent with gas phase atomic O as the dominant oxidant. O_3 forms Pd^{2+}, however, the time of exposure must be longer than 3 min. PdO_x is observed in the shadowed sample after VUV/O_2 co-exposure for 15 min at 50 °C (not shown). Therefore, while O_3 will oxidize Pd^0 to PdO_x, atomic O forms PdO_x more quickly.

All samples are illuminated in the following results. Growth of PdO_x is monitored using XPS while increasing the temperature, and time of co-exposure to VUV/O_2 in Figures 3.3(b), and (c). In Figure 3.3(b), 20 nm Pd is co-exposed to 1 Torr of O_2 and VUV light for 3 min at 50 °C, 100 °C, and 200 °C. For reference, the effective attenuation length of Pd

3*d* electrons is 11 Å, which means an increase in PdO_x thickness above Pd^0 of 10 Å results in approximately a 59% reduction in measured XP signal.[42] A Pd^0 signal persists at 335.0 eV in all Figure 3.3 spectra, and an ~3.5 nm PdO_x overlayer would be needed to fully attenuate the signal. The ratio Pd^{2+}/Pd^0 is 1.13, 1.05, 2.29, at 50 °C, 100 °C, and 200 °C, respectively, indicating that, for an equivalent exposure, more PdO_x forms as the temperature is raised. The oxide thickness approximately doubles as the temperature increases from 100 °C to 200 °C. In Figure 3.3(c), 20 nm Pd is co-exposed to 1 Torr of VUV/O_2 at 100 °C for 0.5, 1, 3, 30, and 40 min. The Pd^{2+}/Pd^0 ratio is 1.11, 1.80, and 2.77 for 3, 30, and 40 min co-exposure. Increasing VUV/O_2 co-exposure time from 3 min to 40 min at 100 °C increases the PdO_x thickness by approximately 150%. It is also important to note that the Pd^{2+}/Pd^0 ratios reported here vary by 5-10% when compared against previous work.[12] Therefore we expect a variation in oxidation, and etch rate, of approximately 10% for a given exposure condition.

We reported etching of 2.8 Å/cycle for 3 min co-exposures at 100 °C,[12] which is expected for the removal of between 1 and 2 Pd layers. The estimate of 2.8 Å/cycle is found by measuring the thickness of a Pd thin film before and after etching (5, 10, and 20 ALE cycles) using X-ray reflectivity, and plotting the thickness change as a function of number of ALE cycles performed. We find that the line of best fit to the data has a slope of 2.8 Å/cycle, which is the etch rate reported. Below we argue the formation of PdO_x is limited by diffusion of O into the subsurface under the exposure temperature and time conditions of this study. Slow diffusion below 100 °C could explain the similar amounts of PdO_x for 50 °C and 100 °C, which is observed herein.

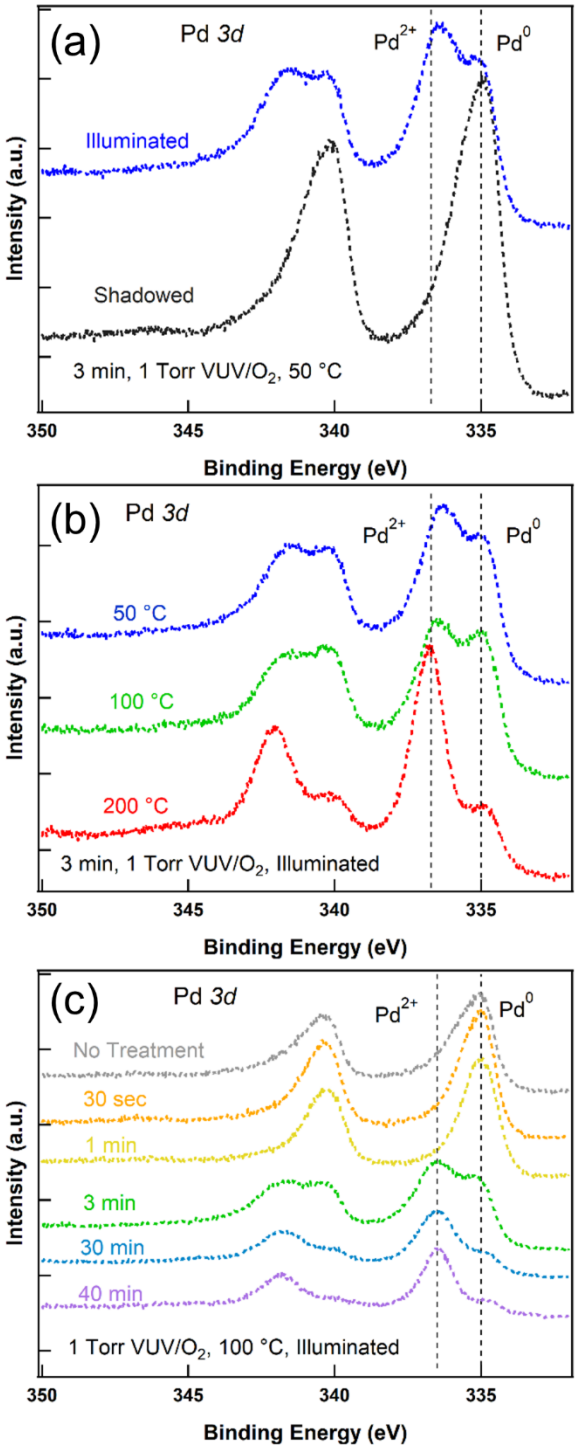
(a)
Pd 3d
Pd2+
Pd0
Illuminated
Shadowed
3 min, 1 Torr VUV/O2, 50 °C
Intensity (a.u.)
350
345
340
335
Binding Energy (eV)
(b)
Pd 3d
Pd2+
Pd0
50 °C
100 °C
200 °C
3 min, 1 Torr VUV/O2, Illuminated
Intensity (a.u.)
350
345
340
335
Binding Energy (eV)
(c)
Pd 3d
Pd2+
Pd0
No Treatment
30 sec
1 min
3 min
30 min
40 min
1 Torr VUV/O2, 100 °C, Illuminated
Intensity (a.u.)
350
345
340
335
Binding Energy (eV)

Figure 3.3. Pd 3*d* XP spectra of 20 nm Pd co-exposed to VUV/O_2 at 1 Torr. (a) Substrates where the sample is illuminated during co-exposure to VUV/O_2 for 3 min at 50 °C (top, blue curve), and shadowed (bottom, black curve), where the configuration of each sample is indicated on the far left above each trace (b) Pd illuminated for 3 min by VUV/O_2 at 50 °C, 100 °C, and 200 °C, in the blue, green, and red curves, respectively where the temperature is indicated above each curve on the far left (c) Pd illuminated by VUV/O_2 for 0.5, 1, 3, 30, and 40 min at 100 °C, with an untreated sample shown in gray at the top for comparison, and time labels shown above each curve on the far left. Positions for oxidation states Pd^0 and Pd^{2+} are indicated with vertical dashed lines as well. Experimental conditions for all figures are shown inset, in the lower left corner.

3.3.3. DFT Simulations of Pd Surfaces with Adsorbed Oxidants

Structural parameters (interplanar Pd distances between the *n*th and (*n* + 1)th layer, $d_{n(n+1),}$ Pd-O distances, $d_{Pd\text{-}O}$, O-O distances, $d_{O\text{-}O}$, and adsorbed O height, *z*) of free/adsorbed O, O_2, and O_3 on Pd(111), and Pd(100) are presented in Table E.1. The structure of O_3 adsorbed onto Pd(111), and Pd(100) is shown in Figure 3.4. Parameters of adsorbed oxidants O, and O_2 onto Pd(111), and Pd(100) are similar to previous reports of adsorption site, height, and interplanar expansion to accommodate oxidants on the surface.[20,23,27,43–45] Atomic O on Pd(111) does not reach the nominal bond distance of PdO $1.96 < d_{Pd\text{-}O} < 1.98$ Å; however, on Pd(100), $d_{Pd\text{-}O}$ is 1.98 Å. This is likely similar to the 2D Pd_5O_4 that is known to result from O_2 exposures on Pd(100),[27] and is consistent with other reports of $d_{Pd\text{-}O}$.[23] However, we note that this 2D surface oxide lacks the $3d_{5/2}$ XP feature at 336.7 eV we observe is required for ALE of $PdO_{x,}$[12] and instead likely has an XP spectral feature at 335.5 eV.[27]

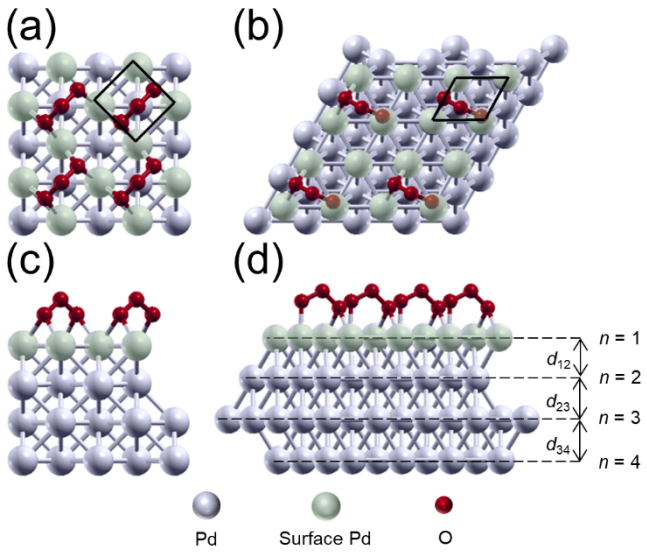

Figure 3.4. Pd surfaces (111) and (100) with adsorbed O_3 are shown with two unit cells shown in the *x* and *y* directions (in-plane). (a) is the top-view of a Pd(100) (2×2) surface, with O_3 occupying the hollow site. (b) is the top-view of a Pd(111) (2×2) surface with O_3 occupying the hollow hcp site. O_3 adsorbed onto Pd(100) and Pd(111) from the viewed from the side is seen in (c) and (d), respectively. Interplanar distances of the substrate corresponding to measurements in the text are also indicated, where the subscript indicates which two planes the interplanar spacing refers. The unit cell is shown with a black solid line, while surface Pd atoms are light green, as indicated in the bottom of the figure.

Adsorption energies, E_{ads}, of O, O_2 and O_3 on Pd(111), Pd(100), and PdO(101), are listed in Table 3.1. PdO(101) is presented here as an analogue to fully-oxidized Pd, as the PdO(101) surface is observed when Pd(111) or (100) is oxidized with O_2,[24] and thus represents the final PdO_x structure. Adsorption onto the "fully formed" structure of PdO_x is used to offer insight into the likelihood of continued growth of PdO_x once a fully oxidized

surface PdO_x is produced, and how further oxidation may proceed in an ALE scheme using VUV/O_2,

DFT reports estimate E_{ads} of atomic O as 3.62 eV[22] to 3.90 eV.[23] We calculate E_{ads} to be 4.37 eV, and 4.52 eV, on Pd(100), and Pd(111), respectively. The heat of adsorption of O_2 is measured experimentally to be 2.38 eV on polycrystalline Pd,[46] and 2.12 eV on Pd(111).[22] We calculate E_{ads} of O_2* to be 2.44 eV, and 2.09 eV on Pd(100), and Pd(111), respectively. DFT calculations herein estimate E_{ads} for atomic O onto Pd(111) is greater than Pd(100) by 0.15 eV. Molecular O_2 adsorbs more strongly to Pd(100) than to Pd(111) by 0.35 eV. The Pd(100) surface restructures to accommodate O_2 (Supporting Information, Table E.1), and is likely facile compared to Pd(111), resulting in a lower E_{ads}. Similar behavior is seen in O_3 adsorbing onto Pd(111) and Pd(100), where adsorption onto Pd(100) is stronger by 0.23 eV, which is most likely due to the favorable size of the hollow site on Pd(100). This interpretation is consistent with the relative heights of O adsorption onto Pd(100) and Pd(111), as adsorbed O is most stable at a height -0.427 Å on Pd(100) than on Pd(111).

E_{ads} of atomic O adsorption onto PdO(101) is markedly lower than that on Pd(100), and Pd(111), changing by -1.65 eV, and -1.80 eV, respectively. However, E_{ads} for O_2, and O_3 changes less between PdO(101), and Pd(111)/Pd(100), suggesting that, although PdO is present, adsorption of O, O_2, and O_3 is still likely, where O and O_3 adsorb the most strongly (per O atom).

Table 3.1. DFT results of adsorption energy (E_{ads}) for O, O_2 and O_3 adsorbing onto Pd(100) and Pd(111). PdO(101) is also presented for comparison to a fully-oxidized Pd surface.

Species	Surface	Cell	E_{ads} (eV)	Reaction
Pd/O	100	2×2	4.37	O-g + Pd(100) → O/Pd(100)
[1]Pd/O_2	100	2×2	2.44	O_2-g + Pd(100) → O_2*/Pd(100)
Pd/O + O	100	2×2	1.92	O_2-g + Pd(100) → O + O/Pd(100)
[1]Pd/O_3	100	2×2	3.98	O_3-g + Pd(100) → O_3*/Pd(100)
Pd/O	111	2×2	4.52	O-g + Pd(111) → O/Pd(111)
[1]Pd/O_2	111	2×2	2.09	O_2-g + Pd(111) → O_2*/Pd(111)
Pd/O + O	111	2×2	2.41	O_2-g + Pd(111) → O + O/Pd(111)
[1]Pd/O_3	111	2×2	3.76	O_3-g + Pd(111) → O_3*/Pd(111)
Pd/O_3	111	2×2	4.60	O_3-g + Pd(111) → O_2* + O/Pd(111)
PdO/O	101		2.72	O-g + PdO(101) → O/PdO(101)
PdO/O_2	101		1.62	O_2-g + PdO(101) → O_2*/PdO(101)
PdO/O_3	101		3.44	O_3-g + PdO(101) → O_3*/PdO(101)
[1]The oxidant is adsorbed in an intermediate state (*i.e.*, O_2*, O_3*) onto the Pd(111) and Pd(100) surface				

PDOS, and $\Delta\rho$ calculations are used to offer insight into the nature of the surface-adsorbate interaction. Results for O, O_2, and O_3 adsorbed onto Pd(100) are shown in Figure

3.5. The PDOS and $\Delta\varrho$ are comprised of states contributed mainly from O *p* electrons, and Pd *d* electrons. In the case of O adsorbing onto Pd(100) (Figure 3.5(c)), there is a large $\Delta\varrho$ in the surface Pd layer, with minimal change in subsurface Pd layers as seen in Figure 3.5(d). This indicates a negatively charged $O^{\delta-}$ surface species, complemented by formation of $Pd^{\delta+}$. The majority of the O *p* states are contributed around E_f, which is also accompanied by an increase in Pd *d*-band resonance.

Similar behavior is observed for O_2/Pd(100), however more O *p* states are contributed in the Pd *d*-band region compared to O/Pd(100) (Figure 3.5(e)) indicating *pd*-hybridization. Adsorbed O_2 onto Pd(100) interacts with subsurface electrons, as evidenced by the large $\Delta\varrho$ below the surface (layer $n = 2$) compared to $\Delta\varrho$ in Figure 3.5(d). The magnitude of $\Delta\varrho$ for O_2/Pd(100) is also less than for O/Pd(100).

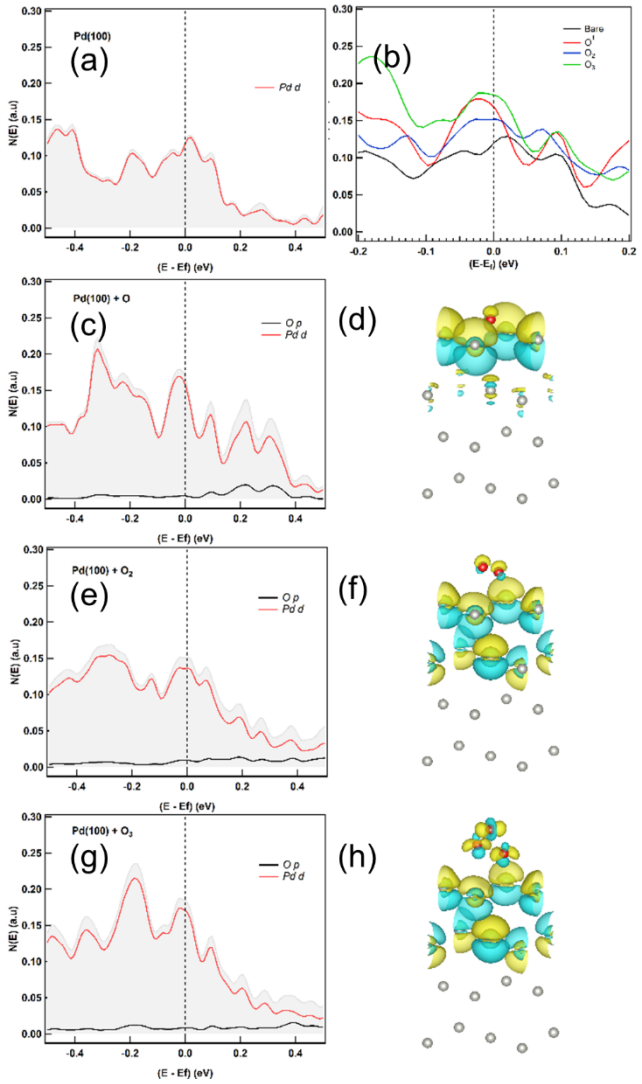

Figure 3.5. PDOS for O, O_2, and O_3 adsorbing onto (2×2) Pd(100) in (a), (c), (e) and (g). Total DOS are shown in gray in the background of each PDOS image. Red indicates states attributed to Pd electrons, while black indicates states attributed to O electrons. Each PDOS has been corrected so that E_f is at 0 eV. The region surrounding E_f is shown in detail in (b). Δρ is shown for each adsorbed configuration in the PDOS in (d), (f), and (h). All Δρ contours are at the same value of 0.031 e/bohr^3. Regions with higher electron density are shown in yellow (δ^-), while regions of lower electron density are shown in blue (δ^+). Red spheres are O atoms and gray spheres are Pd atoms.

Finally, O_3 adsorbing onto Pd(100) shares similarities with the O/Pd(100) system (Figure 3.5(g)), showing an increase in *d*-band resonance when compared to the clean Pd(100) surface. A large number of O *p* states are contributed at all energy levels of the *d*-band as well, indicating *pd* hybridization with Pd(100) and adsorbed O_3. This is also evidenced by the comparatively large $\Delta\rho$ for the hybridized *sp* orbitals that are visible in adsorbed O_3/Pd(100) (Figure 3.5(h)), which has similar character to the final bond observed in O/Pd(100), and markedly different than O_2/Pd(100). O_3 adsorbing onto Pd(100) also has the most states available, as seen in Figure 3.5(b). This suggests decomposition of O_3 is probable and that, while it was not observed in this study, O_3 would likely dissociatively adsorb on a larger surface cell of Pd(100), as repulsive effects would be lower. This is confirmed in 4×4 simulations of O_3 adsorbing onto Pd(100), where O_3 dissociatively adsorbs to form O_2* and O* (not shown).

Similar behavior is seen in oxidants adsorbed onto Pd(111), which is shown in Figure 3.6; however, there are notable differences. All oxidants interact with more electrons from subsurface Pd layers, whereas only O_2 and O_3 recruit Pd(100) subsurface electrons, indicating stronger adsorption. Additionally, the number of states in the vicinity of E_f, as seen in Figure 3.6(b), does not vary as much as it does on Pd(100), though O_3 has the most available states, which is also clear from $\Delta\rho$ around the adsorbed oxidant in Figures 3.6(d), (f), and (h). These results suggest that Pd(111) is less active towards O_3 decomposition than Pd(100), which is consistent with the weaker adsorption energies of 3.39 eV and 3.62 eV on Pd(111) and Pd(100), respectively. O_2 is similarly reported to adsorb more strongly to Pd(100) than to Pd(111).[23]

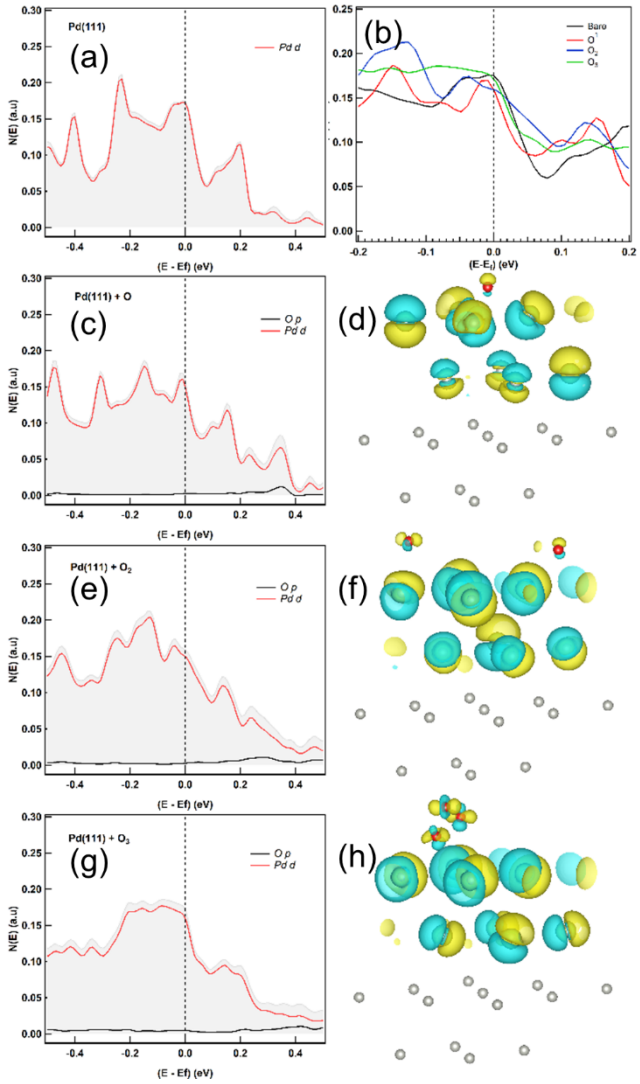

Figure 3.6. PDOS for O, O_2, and O_3 adsorbing onto (2×2) Pd(111) in (a), (c), (e) and (g). Total DOS are shown in gray in the background of each PDOS image. Red indicates states attributed to Pd electrons, while black indicates states attributed to O electrons. Each PDOS has been corrected so that E_f is at 0 eV. The region surrounding E_f is shown in detail in (b). Δρ is shown for each adsorbed configuration in the PDOS in (d), (f), and (h). All Δρ contours are at the same value of 0.031 e/bohr^3. Regions with higher electron density are shown in yellow (δ^-), while regions of lower electron density are shown in blue(δ^+). Red spheres are O atoms and gray spheres are Pd atoms.

3.4. DISCUSSION

3.4.1. EFFECTS OF 2D SURFACE OXIDE ON ADSORPTION AND REACTION

Calculations indicate atomic O adsorption is reduced when a 2D surface oxide is formed, and dissociative adsorption is not predicted for a (2×2) 100 unit cell, which is smaller than the 111 unit cell. Therefore, oxidant bonding and adsorption onto Pd with increasing O content (i.e., surface O layer, subsurface O, etc.) is also explored. Structures of the O layered surfaces are shown in Figure E.3. Adsorption energies are reported in Table 3.2 for varying amounts of O incorporated into the Pd substrate. Experimentally, the 2D surface oxide that is formed on Pd is not complete (*i.e.,* $Pd^{2-\epsilon}$ is formed).[27] In experiments, 20 nm Pd is exposed to five ALE cycles consisting of 3 min co-exposure of VUV and O_2 at 1 Torr, and 100 °C followed by HCOOH vapor exposure. Separately, 20 nm Pd is exposed to five ALE cycles consisting of 3 min of O_2 exposure at 100 °C and HCOOH vapor exposure. The corresponding XRR curves before and after etching are presented in Figure E.4. The film exposed only to thermal O_2 presumably formed a 2D surface Pd_5O_4-like oxide, and is not etched; while the film co-exposed to VUV and O_2 is etched at a rate of 3.2 Å/cycle. Therefore, the transformation of $Pd^{2-\epsilon}$ to Pd^{2+}, which does not occur with 1 O layer on Pd, is important to achieving the ALE of PdO_x.

Atomic O adsorption is lower for all amounts of O incorporated into Pd(100), as E_{ads} changes by -1.14 eV, -0.54 eV, and -2.28 eV, for 1, 2, and 3 O layers, respectively. E_{ads} for O adsorbing onto Pd(111) decreases in a similar fashion. Despite lower E_{ads} for atomic O, which suggests repulsion from O on the surface restricts adsorption, atomic O is still

adsorbs the strongest per O atom. Adsorption of O_3 is comparable to Pd metal without O incorporation, with a slightly lower E_{ads}, however, E_{ads} for O_2 decreases the most on Pd(100) and Pd(111). Thus it appears O, O_2, and O_3 adsorb strongly, yet only O is observed to cause Pd oxidation to PdO_x experimentally at short enough times (Figure 3.3(a)).

Table 3.2. DFT results of adsorption energy calculations of the most stable configuration for O, O_2 and O_3 adsorbing to Pd(111) and Pd(100) that has O layers placed on the surface (1 O layer), between the n = 1 and 2 Pd atomic planes (2 O layer), and between the n = 2 and 3 Pd atomic planes (3 O layer).

	Pd(100)		Pd(111)	
Species	n O layers	E_{ads} (eV)	n O layers	E_{ads} (eV)
Pd/O	1	3.23[1]	1	3.05[1]
Pd/O_2	1	0.68	1	1.51
Pd/O_3	1	2.45	1	3.23
Pd/O	2	3.83	2	2.29
Pd/O_2	2	1.38	2	1.78
Pd/O_3	2	3.19	2	3.94
Pd/O	3	2.09	3	2.17
Pd/O_2	3	1.72	3	1.91
Pd/O_3	3	3.47	3	3.65

[1]E_{ads} is shown for the intermediate state, O_2*, while E_{ads} is calculated for the dissociated state on Pd(111), O + O/Pd(111) as energy is lowered for two occupied neighboring hcp, fcc, surface sites.

Additional bonding information is gained by examining the PDOS and $\Delta\varrho$ for O, O_2, and O_3 adsorbing onto Pd(100) and Pd(111) with 1, 2, and 3 O layers incorporated, which are seen in Figures E.5 – E.10. The PDOS and $\Delta\varrho$ reveal that, as O is incorporated into the substrate, an increasing number of deep substrate electrons participate in adsorption (i.e., $\Delta\varrho \neq 0$ for the Pd atomic layers $n > 3$). This indicates that the molecular species O_2 and O_3 interact with more substrate electrons. An effective potential is built up at the surface due to formation of PdO_x, which facilitates adsorption and charge transfer. This is also evidenced by the largest number of states observed in the 3 O layer system for both Pd(111), and Pd(100).

Examining all three oxidants on both Pd(111) and Pd(100) reveals all oxidants perturb a large number of substrate Pd electrons, indicating the tendency to form covalent bonds. When this information from the PDOS and $\Delta\rho$ is taken into context with experimental results, it is clear that all oxidants, O, O_2, and O_3, dissociate on Pd surfaces. Thus dissociation is not the limiting factor for continued PdO_x growth. Due to the presence of O, and resulting oxidation that is observed, it can be concluded that atomic O causes oxidation, and a high concentration of O is required for PdO_x growth.

3.4.2. ATOMIC O DIFFUSION THROUGH OXIDIZED AND CLEAN PD

Diffusion of O through Pd metal and Pd with 0.25 ML of O is followed with the NEB method, where the approximate minimum energy path, and selected images along the energy path for the two conditions are shown in Figure 3.7. Atomic O diffusion into a clean Pd(111) surface is shown in the blue curve, while diffusion through Pd with 0.25 ML of O is shown in the red curve. The reaction coordinate is the depth of O into the Pd substrate relative to the initial adsorption site on the surface. The energy of a free O atom is shown at the top of Figure 3.7 for comparison. All energies are downhill relative to atomic O, and the change in energy between the free O atom and the highest energies in Figure 3.7 and O is 0.34 eV for both surfaces, again confirming the difficulty in forming PdO_x. Image positions in Figure 3.7 ("2", "3", etc.) do not line up due to restructuring that occurs with different transition states for each system (*i.e.*, Pd with surface O, vs. bare Pd). It is clear that the most stable position for O is on the surface, as that is the lowest energy of all configurations. The energy of the system increases as O moves subsurface, where the transition state is for O moving through a plane of Pd atoms. This step has an activation energy, E_a, of 2.87 eV. O achieves stability in a local minimum in the subsurface hollow site, Point 3 on the NEB curve. However, once O is subsurface, the activation energy to diffuse to the surface is small in comparison, at 0.51 eV.

The same pathway is shown for an atomic O coverage of $\theta = 0.25$ ML in the red curve in Figure 3.7. Initial O migration to subsurface Pd has an E_a that is reduced by 1.07 eV relative to clean Pd. Diffusion towards the surface is approximately the same for clean Pd and $\theta = 0.25$ ML O at 0.51 eV, and 0.52 eV, respectively. Diffusion of O through bulk

PdO_x becomes easier, where E_a decreases by 0.41 eV to 1.43 eV. The E_a of O diffusion through Pd is measured experimentally to be 1.26 eV.[47] It is suspected that increased O incorporation would continue to decrease E_a. Growth of PdO_x therefore requires an abundance of atomic O to act as the driving force for O diffusion into Pd, as well as PdO_x. Experimentally, the abundance of O arises from atomic O (and O_3, at longer times) produced by co-exposure to VUV/O_2. Note that this description of diffusion is likely overly simplified, where in reality it is complicated by other diffusive processes (vacancies, defects, higher O content, place exchange, restructuring with oxidation, *etc*.).

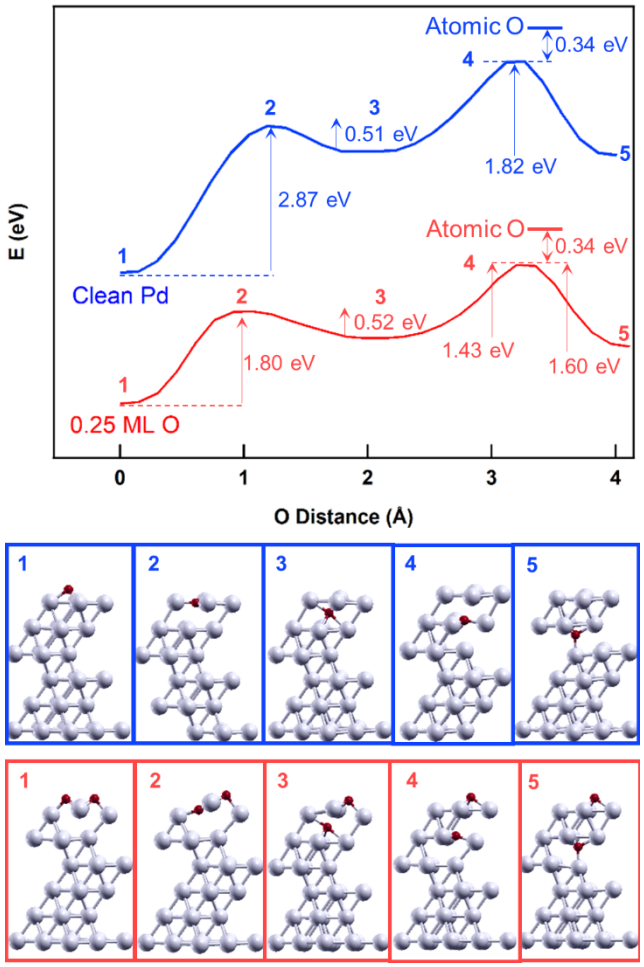

Figure 3.7. NEB calculations for O diffusing through a six-layered Pd(111) slab. The energy paths of the systems are shown as a function of O depth into the substrate. Two conditions are shown: O diffusion through a clean Pd(111) slab (blue); and O diffusion through a Pd(111) slab with 1 O layer ($\theta = 0.25$ ML) on the surface (red). Energy differences and selected images are annotated in the NEB diagram, where selected images showing the unit cell are shown beneath. The energy of free atomic O is shown above each curve as well.

3.4.3. OXIDATION MECHANISM

Overall, four steps are proposed in the mechanism using co-exposure of VUV and O_2 (Figure 3.1) to form the PdO_x that is etched during the ALE process. We define PdO_x to correspond to Pd that has the Pd^{2+} $3d_{5/2}$ XP feature at 336.7 eV. Clean Pd clearly dissociates O_2, and O_3, while O readily incorporates into the surface Pd, which all strongly adsorb onto the Pd surface. This is consistent with experimental results, where the 2D surface oxide is known to approximate a Pd_5O_4 structure[27] and forms easily. However, this 2D surface oxide results in incomplete oxidation of Pd with no discernable XP feature at 336.7 eV, and is unable to be removed by HCOOH exposure.

PdO_x is not detectable by XPS for co-exposures to VUV/O_2 at 100 °C for times < 1 min, which indicates growth of PdO_x past the 2D surface oxide is difficult, and must overcome an energetic barrier due to repulsion from O on the surface. This is clear in the Pd^{2+}/Pd^0 ratio for samples at 50 °C and 100 °C, which are approximately the same; and samples exposed for 40 min at 100 °C, and those exposed for 3 minutes at 200 °C, which are approximately the same as well. This is also shown by the minimal increase in Pd^{2+}/Pd^0 ratio when the time of co-exposure is increased from 3 to 30 min; and clearly demonstrated by E_{ads}, where adsorption is hindered once O is incorporated into the substrate. Molecular O_2 adsorption suffers the most with some oxidation present on the Pd surface, which is likely why O_2 is not observed to form PdO_x at low temperatures. Additionally, the intermediate O_2* state is more stable than dissociated O_2 at 0.25 ML O coverage on Pd(100) (Table 3.1 and Figure E.1). E_{ads} for atomic O and O_3 adsorbing onto Pd surfaces with O

incorporated are reduced, but not to the same extent that O_2 is. Atomic O diffusion is probed in more depth in NEB calculations, where E_a for O diffusion into Pd is 2.87 eV for clean Pd(111) and 1.60 eV for a surface O coverage of $\theta = 0.25$ ML, which is a large energetic barrier to overcome. We note the amount of material removed is limited by how much PdO_x is formed. While VUV/O_2 PdO_x growth is not self-limiting, the amount of PdO_x formed, and thus etched by HCOOH exposure. can be controlled by the time temperature of VUV exposure.

Increased O content restricts oxidant adsorption, growth of PdO_x beyond 2D surface oxide formation, and O diffusion through Pd. Recruitment of subsurface electrons increases as O is incorporated, which indicates O_2 and O_3 adsorb more strongly as more O is incorporated into the substrate. This is observed in E_{ads} increasing from $1 < 2 < 3$ O layers incorporated for O_2 on Pd(100), and Pd(111), and for O_3 on Pd(100). Greater recruitment of subsurface electrons facilitates adsorption of O_3, and O (over O_2 which has the weakest adsorption). Overall, growth of PdO_x is caused by a high concentration of O on the surface, arising from O in the gas phase. We also report (Figure 3.3(a)) on the formation of PdO_x with atomic O at short times when a surface is illuminated, whereas O_3 does not form PdO_x for an equivalent exposure when the substrate is shadowed (O_3 forms PdO_x after 15 min). As the illuminated and shadowed configurations illustrate, selectivity in the species responsible for oxidation could be potentially achieved and an anisotropic oxidation and etching benefit may be achievable; however, this point warrants further investigation.

Taken as a whole, these data support a picture of PdO_x formation that is driven by atomic O in the gas phase to facilitate growth of PdO_x past a 2D surface oxide.

Additionally, these mechanistic details explain the observed etch rate of 2.8 Å/cycle, which corresponds to 1-2 Pd layers. VUV/O_2 co-exposure lends itself well to oxidizing near surface Pd – particularly useful for the ALE of noble metals that are difficult to oxidize, such as Pt and Ru.

3.5. CONCLUSIONS

The oxidation of Pd metal via co-exposure to VUV and O_2 is demonstrated experimentally, and a mechanistic picture of oxidation is constructed. DFT, PDOS, and $\Delta\varrho$ calculations coupled with experimental results show O_3 is an able oxidant, with similar reactivity to O on Pd(111) and Pd(100). Once 1 O layer is formed on the surface of Pd(100) or Pd(111), continued oxidation is difficult due to increased O content. While O_3 is well suited to overcome the transition from 2D surface oxide to subsurface PdO_x due to its comparatively large E_{ads} relative to O_2, the fact that no oxidation is observed for equivalent co-exposure times of atomic O (illuminated Pd substrates) and O_3 (shadowed Pd substrates) indicates atomic O drives PdO_x formation. Atomic O has the largest E_{ads} for all structures investigated, while O_2, and O_3 adsorb more strongly as O is incorporated into the substrate Pd. This indicates oxidation is associated with a large reservoir of atomic O in the gas phase arising from VUV/O_2, and may be made easier as O is incorporated. Continued growth of PdO_x past the 2D surface oxide is dominated by subsurface diffusion, which, from NEB calculations, has an E_a of 1.80 eV. Subsurface diffusion E_a decreases as more O is incorporated into Pd. Thus, VUV/O_2 co-exposure is an excellent candidate to allow controlled etching of Pd. Additionally the potential for selectivity in oxidation is suggested.

Further control over selectivity in oxidation, by perhaps illuminating an adsorbed layer of reactive gas species, may offer additional avenues to control ALE of a variety of materials with VUV. We suspect this mechanistic picture of oxidation of Pd could similarly be applied to other noble metals, such as Pt and Ru, which is discussed in more detail in Chapter 5.

3.6. REFERENCES

(1) McCrory, C. C. L.; Jung, S.; Peters, J. C.; Jaramillo, T. F. Benchmarking Heterogeneous Electrocatalysts for the Oxygen Evolution Reaction. *J. Am. Chem. Soc.* **2013**, *135* (45), 16977–16987.

(2) Sha, Y.; Yu, T. H.; Merinov, B. V.; Goddard, W. A. DFT Prediction of Oxygen Reduction Reaction on Palladium–Copper Alloy Surfaces. *ACS Catal.* **2014**, *4* (4), 1189–1197.

(3) Sun, J. B.; Almquist, B. D. Interfacial Contact Is Required for Metal-Assisted Plasma Etching of Silicon. *Advanced Materials Interfaces* **2018**, *5* (24), 1800836.

(4) Han, H.; Huang, Z.; Lee, W. Metal-Assisted Chemical Etching of Silicon and Nanotechnology Applications. *Nano Today* **2014**, *9* (3), 271–304.

(5) Huang, Z.; Geyer, N.; Werner, P.; de Boor, J.; Gosele, U. Metal-Assisted Chemical Etching of Silicon: A Review. *Adv. Mater.* **2010**, *23* (2), 285–308.

(6) Li, X.; Bohn, P. W. Metal-Assisted Chemical Etching in HF/H_2O_2 Produces Porous Silicon. *Appl. Phys. Lett.* **2000**, *77* (16), 2572–2574.

(7) Chen, J. K.-C.; Altieri, N. D.; Kim, T.; Chen, E.; Lill, T.; Shen, M.; Chang, J. P. Directional Etch of Magnetic and Noble Metals. II. Organic Chemical Vapor Etch. *Journal of Vacuum Science & Technology A: Vacuum, Surfaces, and Films* **2017**, *35* (5), 05C305.

(8) Tamarov, K.; Swanson, J. D.; Unger, B. A.; Kolasinski, K. W.; Ernst, A. T.; Aindow, M.; Lehto, V.-P.; Riikonen, J. Controlling the Nature of Etched Si Nanostructures: High- versus Low-Load Metal-Assisted Catalytic Etching (MACE) of Si Powders. *ACS Appl. Mater. Interfaces* **2020**, *12* (4), 4787–4796.

(9) Fracassi, F.; d'Agostino, R.; Cacucci, A. Dry Etching of Palladium Thin Films in Fluorine Containing Plasmas: X-ray Photoelectron Spectroscopy Investigation. *Journal of Vacuum Science & Technology A: Vacuum, Surfaces, and Films* **1998**, *13* (1), 63–66.

(10) Williams, K. R.; Gupta, K.; Wasilik, M. Etch Rates for Micromachining Processing-Part II. *Journal of Microelectromechanical Systems* **2003**, *12* (6), 761–778.

(11) Chen, J. K.-C.; Altieri, N. D.; Kim, T.; Lill, T.; Shen, M.; Chang, J. P. Directional Etch of Magnetic and Noble Metals. I. Role of Surface Oxidation States. *Journal of Vacuum Science & Technology A: Vacuum, Surfaces, and Films* **2017**, *35* (5), 05C304.

(12) Coffey, B. M.; Nallan, H. C.; Engstrom, J. R.; Lam, C. H.; Ekerdt, J. G. Vacuum Ultraviolet Enhanced Oxidation - A Route to the Atomic Layer Etching of Palladium Metal. *Chem. Mater.* **2020**, *32* (14), 6035–6042.

(13) Janthon, P.; Luo, S. (Andy); Kozlov, S. M.; Viñes, F.; Limtrakul, J.; Truhlar, D. G.; Illas, F. Bulk Properties of Transition Metals: A Challenge for the Design of Universal Density Functionals. *J. Chem. Theory Comput.* **2014**, *10* (9), 3832–3839.

(14) Lejaeghere, K.; Speybroeck, V. V.; Oost, G. V.; Cottenier, S. Error Estimates for Solid-State Density-Functional Theory Predictions: An Overview by Means of the Ground-State Elemental Crystals. *Critical Reviews in Solid State and Materials Sciences* **2014**, *39* (1), 1–24.

(15) Huffman, R. E. Absorption Cross-Sections of Atmospheric Gases for Use in Aeronomy. *Can. J. Chem.* **1969**, *47* (10), 1823–1834.

(16) Slanger, T. G.; Cosby, P. C. Oxygen Spectroscopy below 5.1 EV. *J. Phys. Chem.* **1988**, *92* (2), 267–282.

(17) Bakhtchadjian, R. *Bimodal Oxidation: Coupling of Heterogeneous and Homogeneous Reactions*; CRC Press, **2019**.

(18) Dessler, A. *Chemistry and Physics of Stratospheric Ozone*; Elsevier, **2000**.

(19) Zhukov, V.; Popova, I.; Yates, J. T. Delivery of Pure Ozone in Ultrahigh Vacuum. *Journal of Vacuum Science & Technology A* **2000**, *18* (3), 992–994.

(20) Honkala, K.; Laasonen, K. Ab Initio Study of O2 Precursor States on the Pd(111) Surface. *J. Chem. Phys.* **2001**, *115* (5), 2297–2302.

(21) Parker, D. H.; Koel, B. E. Chemisorption of High Coverages of Atomic Oxygen on the Pt(111), Pd(111), and Au(111) Surfaces. *Journal of Vacuum Science & Technology A* **1990**, *8* (3), 2585–2590.

(22) Peter, M.; Adamovsky, S.; Camacho, J. M. F.; Schauermann, S. Energetics of Elementary Reaction Steps Relevant for CO Oxidation : CO and O_2 Adsorption on Model Pd Nanoparticles and Pd(111). *Faraday Discussions* **2013**, *162* (0), 341–354.

(23) Plauck, A.; Stangland, E. E.; Dumesic, J. A.; Mavrikakis, M. Active Sites and Mechanisms for H_2O_2 Decomposition over Pd Catalysts. *PNAS* **2016**, *113* (14), E1973–E1982.

(24) Seriani, N.; Harl, J.; Mittendorfer, F.; Kresse, G. A First-Principles Study of Bulk Oxide Formation on Pd(100). *J. Chem. Phys.* **2009**, *131* (5), 054701.

(25) Sjövall, P.; Uvdal, P. Adsorption of Oxygen on Pd(111): Precursor Kinetics and Coverage-Dependent Sticking. *Journal of Vacuum Science & Technology A: Vacuum, Surfaces, and Films* **1998**, *16* (3), 943.

(26) Rose, M. K.; Borg, A.; Dunphy, J. C.; Mitsui, T.; Ogletree, D. F.; Salmeron, M. Chemisorption and Dissociation of O_2 on Pd(111) Studied by STM. *Surface Science* **2003**, *547* (1), 162–170.

(27) Gabasch, H.; Unterberger, W.; Hayek, K.; Klötzer, B.; Kleimenov, E.; Teschner, D.; Zafeiratos, S.; Hävecker, M.; Knop-Gericke, A.; Schlögl, R.; Han, J.; Ribeiro, F. H.; Aszalos-Kiss, B.; Curtin, T.; Zemlyanov, D. In Situ XPS Study of Pd(111) Oxidation at Elevated Pressure, Part 2: Palladium Oxidation in the 10−1mbar Range. *Surface Science* **2006**, *600* (15), 2980–2989.

(28) Björck, M.; Andersson, G. GenX: An Extensible X-Ray Reflectivity Refinement Program Utilizing Differential Evolution. *J Appl Cryst* **2007**, *40* (6), 1174–1178.

(29) Giannozzi, P.; Baroni, S.; Bonini, N.; Calandra, M.; Car, R.; Cavazzoni, C.; Ceresoli, D.; Chiarotti, G. L.; Cococcioni, M.; Dabo, I.; Corso, A. D.; Gironcoli, S. de; Fabris, S.; Fratesi, G.; Gebauer, R.; Gerstmann, U.; Gougoussis, C.; Kokalj, A.; Lazzeri, M.; Martin-Samos, L.; Marzari, N.; Mauri, F.; Mazzarello, R.; Paolini, S.; Pasquarello, A.; Paulatto, L.; Sbraccia, C.; Scandolo, S.; Sclauzero, G.; Seitsonen, A. P.; Smogunov, A.; Umari, P.; Wentzcovitch, R. M. QUANTUM ESPRESSO: A Modular and Open-Source Software Project for Quantum Simulations of Materials. *J. Phys.: Condens. Matter* **2009**, *21* (39), 395502.

(30) Giannozzi, P.; Andreussi, O.; Brumme, T.; Bunau, O.; Nardelli, M. B.; Calandra, M.; Car, R.; Cavazzoni, C.; Ceresoli, D.; Cococcioni, M.; Colonna, N.; Carnimeo, I.; Corso, A. D.; Gironcoli, S. de; Delugas, P.; DiStasio, R. A.; Ferretti, A.; Floris, A.; Fratesi, G.; Fugallo, G.; Gebauer, R.; Gerstmann, U.; Giustino, F.; Gorni, T.; Jia, J.; Kawamura, M.; Ko, H.-Y.; Kokalj, A.; Küçükbenli, E.; Lazzeri, M.; Marsili, M.; Marzari, N.; Mauri, F.; Nguyen, N. L.; Nguyen, H.-V.; Otero-de-la-Roza, A.; Paulatto, L.; Poncé, S.; Rocca, D.; Sabatini, R.; Santra, B.; Schlipf, M.; Seitsonen, A. P.; Smogunov, A.; Timrov, I.; Thonhauser, T.; Umari, P.; Vast, N.; Wu, X.; Baroni, S. Advanced Capabilities for Materials Modelling with Quantum ESPRESSO. *J. Phys.: Condens. Matter* **2017**, *29* (46), 465901.

(31) Perdew, J. P.; Burke, K.; Ernzerhof, M. Generalized Gradient Approximation Made Simple. *Phys. Rev. Lett.* **1996**, *77* (18), 3865–3868.

(32) Perdew, J. P.; Burke, K.; Ernzerhof, M. Generalized Gradient Approximation Made Simple [Phys. Rev. Lett. 77, 3865 (1996)]. *Phys. Rev. Lett.* **1997**, *78* (7), 1396–1396.

(33) Grimme, S.; Antony, J.; Ehrlich, S.; Krieg, H. A Consistent and Accurate Ab Initio Parametrization of Density Functional Dispersion Correction (DFT-D) for the 94 Elements H-Pu. *J. Chem. Phys.* **2010**, *132* (15), 154104.

(34) Grimme, S.; Ehrlich, S.; Goerigk, L. Effect of the Damping Function in Dispersion Corrected Density Functional Theory. *Journal of Computational Chemistry* **2011**, *32* (7), 1456–1465.

(35) Chen, Z.-X.; Neyman, K. M.; Lim, K. H.; Rösch, N. CH_3O Decomposition on PdZn(111), Pd(111), and Cu(111). A Theoretical Study. *Langmuir* **2004**, *20* (19), 8068–8077.

(36) Henkelman, G.; Uberuaga, B. P.; Jónsson, H. A Climbing Image Nudged Elastic Band Method for Finding Saddle Points and Minimum Energy Paths. *J. Chem. Phys.* **2000**, *113* (22), 9901–9904.

(37) Taniguchi, N.; Takahashi, K.; Matsumi, Y.; Dylewski, S. M.; Geiser, J. D.; Houston, P. L. Determination of the Heat of Formation of O3 Using Vacuum Ultraviolet Laser-Induced Fluorescence Spectroscopy and Two-Dimensional Product Imaging Techniques. *J. Chem. Phys.* **1999**, *111* (14), 6350–6355.

(38) Kokalj, A. XCrySDen—a New Program for Displaying Crystalline Structures and Electron Densities. *Journal of Molecular Graphics and Modelling* **1999**, *17* (3), 176–179.

(39) Momma, K.; Izumi, F. VESTA 3 for Three-Dimensional Visualization of Crystal, Volumetric and Morphology Data. *J Appl Cryst* **2011**, *44* (6), 1272–1276.

(40) Militello, M. C.; Simko, S. J. Palladium Oxide (PdO) by XPS. *Surface Science Spectra* **1998**, *3* (4), 395–401.

(41) Moulder, J. F.; Stickle, W. F.; Sobol, P. E.; Bomben, K. D. *Handbook of X-Ray Photoelectron Spectroscopy*; Chastain, J., Ed.; Perkin-Elmer: Eden Prarie, Minnesota, **1992**.

(42) Powell, C. J.; Jablonski, A. *NIST Electron Effective-Attenuation-Length Database Version 1.3*; National Institute of Standards and Technology: Gaithersburg, MD, **2011**.

(43) Todorova, M.; Reuter, K.; Scheffler, M. Oxygen Overlayers on Pd(111) Studied by Density Functional Theory. *J. Phys. Chem. B* **2004**, *108* (38), 14477–14483.

(44) Linstrom, P. NIST Chemistry WebBook, NIST Standard Reference Database 69, **1997**.

(45) Naito, K.; Nakamura, M.; Sakata, O.; Hoshi, N. Surface X-Ray Scattering of Pd(111) and Pd(100) Electrodes during the Oxygen Reduction Reaction. *Electrochemistry* **2011**, *79* (4), 256–260.

(46) Toyoshima, I.; Somorjai, G. A. Heats of Chemisorption of O_2, H_2, CO, CO_2, and N_2 on Polycrystalline and Single Crystal Transition Metal Surfaces. *Catal. Rev.-Sci. Eng.* **1979**, *19* (1), 105–159.

(47) Wang, D.; Flanagan, T. B. Diffusion of Oxygen in Pd. *Scripta Materialia* **2005**, *52* (7), 599–601.

Chapter 4: Vacuum Ultraviolet Enhanced Atomic Layer Etching of Pd Metal

Contents for this chapter are published as: B. M. Coffey, H. C. Nallan. J. R. Engstrom, J. G. Ekerdt, Vacuum Ultraviolet Enhanced Oxidation - A Route to the Atomic Layer Etching of Palladium Metal. Chem. Mater. ***2020****, 32 (14), 6035–6042.*

Supporting information is found in Appendix F.

4.1. Introduction

Atomic layer modification is a crucial nanofabrication tool enabling progress of nanotechnology. Atomic level methods are particularly important in facilitating the selective removal of base and noble metals, such as Pd. Removal of Pd is important in developing next generation MRAM technologies[1] and facilitating the development of metal assisted etching techniques.[2–5] Atomic layer etching (ALE) can potentially enable these applications; however, ALE methods for metals are very limited, and most are predicated on oxidation with an O_2 plasma.[6] Demonstrations of dry etching of Pd have used Ar/CF_4 and $Ar/CF_4/O_2$ plasmas,[7] O_2 plasma treatment followed by vapor exposure to formic acid, hexafluoroacetylacetone, and acetylacetone,[1] or wet etching involving $FeCl_3$[8] or acetylacetone and hexafluoroacetylacetone.[9] However, as device architectures continue to decrease in size and increase in complexity, use of plasmas is challenging, as maintaining uniformity across substrates, creating defect-free devices, and avoiding non-selective material removal are difficult. Highly selective chemical etching methods to retain feature fidelity are thus complementary in developing the next generation of nanotechnology.

A complement to plasma ALE is thermal ALE, which sublimes a chemically activated surface layer *via* heat as opposed to ions or radicals. Thermal ALE has been shown on a variety of materials, including SiO_2,[10] TiN,[11] and Al_2O_3.[12,13] In other demonstrations using thermal ALE chemistries, a plasma is required to complete the etch cycle, as is demonstrated in plasma enhanced thermal ALE of AlN with a H_2 plasma.[14] Thermal ALE, while in theory being applicable to many materials, to date has required fluorination and ligand exchange steps (to create a Lewis acid/base pair). This indicates thermal ALE cannot be directly employed on surfaces where fluorination is not facile thermally < 200 °C. Consequently, thermal ALE is demonstrated on materials in an oxidized state (*e.g.* Si^{4+}, Ti^{2+}, Al^{1+}, Al^{3+}). Thus a tool that offers controlled oxidation of the to-be-etched material is amenable to thermal ALE. The amalgamation of thermal ALE and controlled oxidation state change, would provide an important new technique for the development of next generation nanotechnology.

An alternative to plasma etching is photo-assisted etching, which can deliver the energy to cause surface reactions while minimizing undesired chemical changes or physical material removal. Photo-assisted chemical etching is reported for wet and dry etching of semiconducting substrates, in reducing roughness imparted to the surface of GaN during dry etching,[15] etching GaN using KOH and H_3PO_4 irradiated with a He-Cd laser,[16] etching deep structures in Si for quantum wires,[17] and photon-plasma-enhanced etching of Si.[18] Additional dry etching demonstrations utilize photo-enhancement by a KrF excimer laser to perform ALE of GaAs[19] and Si(111)[20] *via* Cl_2 adsorption and photogeneration of

electron-hole pairs that participate in the surface reaction. However, most, if not all, photochemical etching methods require a semiconductor substrate to photo-generate carriers that participate in the surface reaction, which limits widespread use.

The idea of supplementing chemical reactions with light in the vacuum ultra-violet region (VUV, λ<160 nm) has been explored in atomic layer deposition (ALD) schemes involving Al_2O_3, where VUV photons interact with O_3 to deposit Al_2O_3 at 60 °C,[21] as well as in the room temperature deposition of Al_2O_3 and TiO_2.[22,23] While the benefit of VUV exposure has been demonstrated in ALD and photo-dissociation for etching is possible, the potential utility of VUV-enhanced ALE has yet to be realized. Additionally, while many ALE techniques have been developed, few exist for many base or noble metals.[6]

Irradiation with VUV light, while rarely used for deposition or etching of materials, has been used within a variety of fields for cleaning purposes. VUV radiation arises from D_2 discharges, as well as Xe, and Hg arc lamps.[24] It is of interest due to the high energy of photons, and favorable absorption coefficients of H_2O, O_2, and many organic compounds in the context of advanced oxidation processes for volatile organic compound scrubbing.[25,26] O_2 is of particular interest in the current study. The absorption coefficient of O_2 in the VUV is 12 cm^{-1},[27] which gives an attenuation length of 1.8 cm at reaction conditions investigated herein. The photochemical interaction of VUV irradiation with O_2 is summarized below in Equations (4.1) – (4.3)[24,27]

$$O_2 \rightarrow O(^3P) + O(^3P);\ 185\ nm < \lambda < 240\ nm;\ (4.1)$$

$$O_2 \rightarrow O(^1D) + O(^3P); \lambda < 185 \text{ nm}; (4.2)$$

$$O(^3P) + O_2 + M \rightarrow O_3 + M; (4.3)$$

VUV interaction is dominated by the production of singlet oxygen, $O(^1D)$, (Eqn. 4.2), and triplet oxygen, $O(^3P)$, (Eqns. 4.1 and 4.2). Triplet oxygen can interact with O_2 and a third body, M, to produce O_3 (Eqn. 4.3).[28] It is proposed that O_3, $O(^1D)$, and $O(^3P)$ are the reactive species in VUV-enhanced demonstrations.[21,24] This work also aims to produce these highly oxidizing species and demonstrate controlled oxidation in an ALE scheme by co-exposing VUV with O_2.

This article presents the first demonstration of VUV-enhanced ALE, that allows for etching metals using VUV-photooxidation combined with exposure to vapor phase etchants. In this demonstration, Pd^0 is etched by co-exposure to VUV light and O_2 gas followed by a vapor exposure of formic acid (HCOOH). However, these ALE methods are likely not limited to Pd provided the extent of metal oxidation can be controlled with VUV.

4.2. Experimental Methods

Pd metal thin films are deposited using an electron beam evaporation tool (CHA Industries) where thickness is monitored *in situ* using a quartz crystal microbalance (QCM, Inficon). Pd evaporation targets are >99.95% purity and Ti evaporation targets are >99.995% purity (Kurt J. Lesker). Substrates are double side polished B-doped Si (100) (University Wafer, 1 – 10 Ωcm), where no treatment is done prior to evaporation of thin films. Ti adhesion layers are evaporated onto the substrate *in situ* prior to evaporation of

Pd. Films are described using a shorthand listing the thickness of each film (in nm) in the multilayer is in parentheses after the metal layer (*e.g.*, Pd(20)/Ti(10)/p-Si). The substrate is p-Si (100), which has a native oxide present. Pd film thickness and crystallinity is characterized *ex situ* using X-ray reflectivity (XRR) using a Rigaku Ultima IV diffractometer, which uses Cu Kα radiation. Pd film thickness is calculated using GenX (v2.4.10).[29] Evaporated thicknesses of Pd for the nominal Pd(20)/Ti(10)/p-Si films are measured to be 22 nm – 24 nm prior to etching.

Pd(2)/p-Si is also used in this demonstration. Pd(2)/p-Si is evaporated using the same apparatus mentioned for Pd(20)/Ti(10)/p-Si, however, the thickness is such that a measurement cannot be made *ex situ* with XRR. Pd(2)/p-Si is characterized *in situ* using X-ray photoelectron (XP) spectroscopy (XPS). Owing to the roughness of the as-deposited films as measured by atomic force microscopy (AFM), they are likely discontinuous before any ALE has been performed.[30]

Samples are degreased by sonicating in acetone, isopropanol, and water (>18 MΩs), for 10 min each, and drying with N_2 prior to loading into the analysis and reaction system. All etching and XP characterization are completed in a custom-built ultra-high vacuum system consisting of a transfer line (base pressure 1×10^{-7} Torr), which connects an XP spectrometer (PHI 5600, base pressure 1×10^{-9} Torr), custom-built vacuum furnace, load-lock chamber, and ALE chamber. The XP spectra are collected using Mg Kα radiation, which is produced using 15 kV, 4.2 A filament current, and results in 17 mA of emission current, yielding 40-60 nA of sample current. Curve fitting and analysis of XP spectra is done using CasaXPS (v.2.3.16).

All etching experiments are done in the ALE chamber. The ALE chamber is a custom stainless steel 6-way cross with four oblique ports attached around the gas inlet flange. The total volume of the chamber reactor is ~2 L, and is equipped with a high temperature stainless steel stage where the sample is heated from below using a 24 V halogen light bulb (Osram). The walls of the ALE reactor are maintained at 80 °C during all experiments. The sample stage has a stroke length of 25.4 cm, so the sample can span the entire vertical height of the ALE reactor. Light exposures within the ALE reactor involved irradiation with VUV photons from the sample normal using a Hamamatsu high brightness deuterium lamp (H2D2 Hamamatsu, L11798), which has a broad emission spectrum from 115 nm < λ < 400 nm. The strongest emission lines from the VUV light source are at 115 nm and 160 nm, corresponding to photons with energy 6.5 eV < hν < 11.3 eV, which results in an irradiance of 2.46 μW/cm^2/nm at 50 cm.

In normal oxidation conditions within the ALE reactor, under an O_2 atmosphere at 1 Torr, the attenuation length of VUV radiation at 115 nm is 1.8 cm, therefore the sample is held ~5 mm from the MgF_2 window of the VUV light source for all irradiation. Oxidation is completed by first loading the sample into the UHV chamber, switching to rough vacuum, which is maintained by a dual stage rotary vane pump, turning on the VUV light source, and setting the temperature of the reaction. The reaction temperature is maintained *via* an auto-tuned PID controller (Eurotherm 2450) with on-process monitoring, which allows the temperature of the substrate to be maintained within ± 1 °C of the reported temperature. Ar (Matheson, 99.9999%) is introduced at 80 sccm with mass flow controllers (MKS, type 147), which yields a background pressure of 0.100 Torr and

supplied for the duration of every experiment. The sample is moved into the VUV light exposure position, and equilibrates for 30 min prior to O_2 dosing. O_2 (Matheson, >99.999%) is introduced into the ALE chamber using a mass flow controller (MKS, type 147) at a flow rate of 150 sccm. This results in a pressure over the background Ar pressure of 1 Torr. The time of co-exposure to O_2 and VUV light is controlled by removing the sample from the light source after the time reported (*e.g.* 1 min, 2 min, 5 min *etc.*), and the VUV light source is left on. Due to the attenuation length of VUV photons at the reaction conditions (1 Torr O_2) the sample is moved 15.2 cm away from the light source, which is enough to avoid any VUV irradiation. As UV light is damaging to biological tissue, protective eyewear is used at all times. All control experiments are conducted in this configuration. Formic acid (HCOOH, Sigma-Aldrich, 99%) is introduced using a glass saturator tube isolated with a manual valve, and the vapor dose is controlled using a needle valve. The dose of formic acid results in a pressure rise of 0.46-0.50 Torr over the baseline Ar pressure. The manifold is described in detail elsewhere.[31] One ALE cycle consists of one oxidation step and Ar purge, which is then followed by one dose of formic acid and Ar purge. A shorthand is used as followed to denote ALE cycle parameters: O_2 gas dose time/purge time/formic acid dose time/purge time where all units are s (*i.e.*, A/B/C/D).

AFM (Asylum Research) images are obtained in tapping mode, and height images are obtained using Si cantilevers (HQ:NSC15/Al BS, μmasch). Images are analyzed using Gwyddion (v2.47). Data plots are made using Igor Pro (v2.6).

4.3. Results and Discussion

4.3.1. Initial Surfaces of 2 nm Pd and 20 nm Pd

A shorthand is used to describe samples for clarity. If a material is followed by a number in parentheses it indicates the thickness (in nm) of that material (*e.g.* a multilayered film consisting of 20 nm Pd on 10 nm Ti on p-Si(100) is described as Pd(20)/Ti(10)/p-Si). These thickness values are the values monitored in an electron beam evaporation tool using a QCM. The starting surface of Pd(2)/p-Si is characterized using XPS and AFM. Pd 3*d* and Si 2*p* XP spectra are shown in Figure 4.1(a). Pd has two features, $3d_{5/2}$ at 335.0 eV and $3d_{3/2}$ at 340.3 eV. Fitting the Pd $3d_{5/2}$ XP feature indicates only Pd^0 is present.[32] The XP spectra of Si 2*p* has two features at 103.0 eV and 99.0 eV corresponding to Si^{4+}, (nominally at 103.5 eV but includes a contribution from the Pd 4*s* XP feature[33]) and Si^0, respectively. Si^{4+} arises from the native oxide present on p-Si(100) wafers before metal evaporation. The 20 × 20 μm^2 AFM micrograph of the Pd(2)/p-Si in Figure 4.1(b) reveals a non-uniform surface, with roughness, R_a = 23.5 Å. The mass of Pd accumulated was measured using a QCM and corresponds to 2 nm of Pd if it were uniformly thick, however, clearly there are islands in the AFM micrograph, and the roughness is of the same order of magnitude of the nominal film thickness. The combination of AFM and XPS measurements indicate Pd(2)/p-Si is discontinuous and contains voids, as R_a is greater than the nominal film thickness, ~20 Å. This is consistent with previous observations of ultra-thin films with large R_a.[30]

XPS and AFM results for the initial surface of Pd(20)/Ti(10)/p-Si are shown in Figure 4.1(c) and (d), respectively. The Pd $3d_{5/2}$ XP feature at 335.0 eV indicates only Pd^0. Ti cannot be detected by XPS, as the Ti 2*p* XP feature that occurs at ~458.8 eV is fully attenuated by the Pd^0 overlayer. The 20×20 μm^2 AFM micrograph reveals a roughness of R_a = 11.4 Å. AFM and XPS indicate Pd(20)/Ti(10)/p-Si is a continuous film.

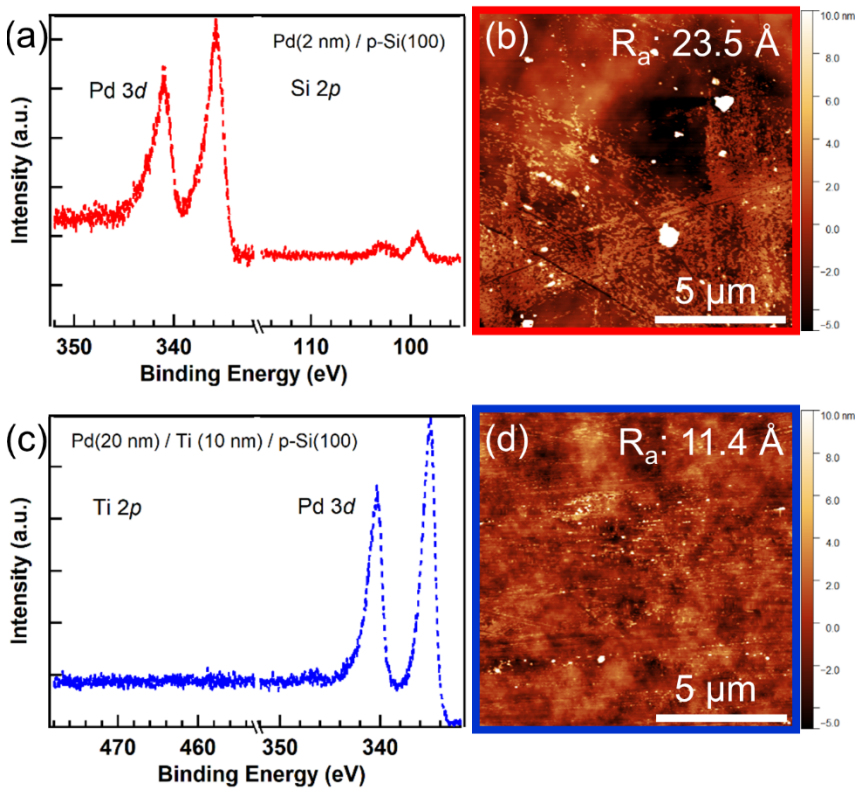

Figure 4.1. (a) Pd 3*d*, and Si 2*p* XP spectra for untreated Pd(2)/p-Si are shown with the corresponding AFM micrograph in (b). (c) Pd 3*d*, and Ti 2*p* XP spectra are shown for Pd(20)/Ti(10)/p-Si with the corresponding AFM micrograph in (d). AFM micrographs are 20×20 μm^2. The height scale is equal for both micrographs.

4.3.2. OXIDATION HALF-CYCLE: CONTROLLING PdO_x FORMATION ON Pd^0

The oxidation half-cycle of Pd^0 to PdO_x as a function of VUV exposure time is explored with Pd(2)/p-Si, where samples are co-exposed to VUV and 1 Torr O_2 at 100 °C. Pd 3*d* XP spectra for a series of co-exposure times are shown in Figure 4.2(a). Two Pd $3d_{5/2}$ XP features at 335.0 eV and 336.7 eV are clear, which are attributed to Pd^0 and Pd^{2+}, respectively. The 1.7 eV binding energy shift is a well-known characteristic of PdO_x when compared to Pd^0.[32] Results of the XP spectra of the film co-exposed to VUV and O_2 for 1 min reveals Pd^0 and Pd^{2+} are present. Pd is partially oxidized after 1 min co-exposure of VUV and O_2. When Pd(2)/p-Si is co-exposed to VUV and O_2 for 3 min, no Pd^0 remains, indicating Pd(2)/p-Si is fully oxidized.

Pd(20)/Ti(10)/p-Si is also subjected to co-exposure of VUV and O_2. Pd 3*d* XP spectra after co-exposure are shown in Figure 4.2(b). Pd(20)/10(Ti)/p-Si is partially oxidized after 3 min co-exposure of VUV and O_2. Pd^{2+} is not present after co-exposing VUV and O_2 up to 2 min, indicating a minimum VUV and O_2 co-exposure time must be surpassed to partially oxidize Pd(20)/Ti(10)/p-Si. The PdO_x thickness appears to reach a limiting value, as Pd^0 is present after a 60 min co-exposure of VUV and O_2. In the Pd 3*d* XP spectra shown in Figure 4.2(b), the Pd^{2+}/Pd^0 ratio is 1.20 and 1.52 for 3 min and 60 min exposures, respectively. The Pd^0 in Pd(2)/p-Si and Pd(20)/10(Ti)/p-Si can be partially oxidized after co-exposing VUV and O_2 for 1 min, and 3 min, respectively. Therefore, co-exposure time used herein is 1 min for Pd(2)/p-Si and 3 min for Pd(20)/Ti(10)/p-Si min in oxidation half-cycles (see below) to limit the thickness of PdO_x that forms.

It is worth noting oxidation behavior differs between Pd(2)/p-Si and Pd(20)/10(Ti)/p-Si. A minimum of 3 min is required to partially oxidize Pd(20)/Ti(10)/p-Si, while Pd(2)/p-Si is fully oxidized after 3 min. This discrepancy could be due to a difference in the exposed surface area of Pd^0. Pd(20)/10(Ti)/p-Si, with an initial surface roughness of 11.4 Å (Figure 4.1(d)), has a lower surface area compared to Pd(2)/p-Si with R_a = 23.5 Å (Figure 4.1(b)). The difference in the exposed surface area and the higher surface to volume ratio allows more oxidation to occur for Pd(2)/p-Si when compared to the continuous Pd(20)/10(Ti)/p-Si film. This could be exploited to remove material in an "over-deposition" scenario during area-selective metal ALD, as in the deposition of self-aligned vias,[34] and would add to the library allowing more ALD chemistries to be used.[35,36] Higher surface area features would be etched faster, which could remove unwanted deposition, while minimizing removal of the film in desired growth regions. This point is important in the conceptualization of the transparent conductive electrode (TCE), where ALE may be used to remove undesired catalyst deposition before electroless Cu deposition occurs. This step ensures the electrodes deposited with Cu maintain their high fidelity during growth.

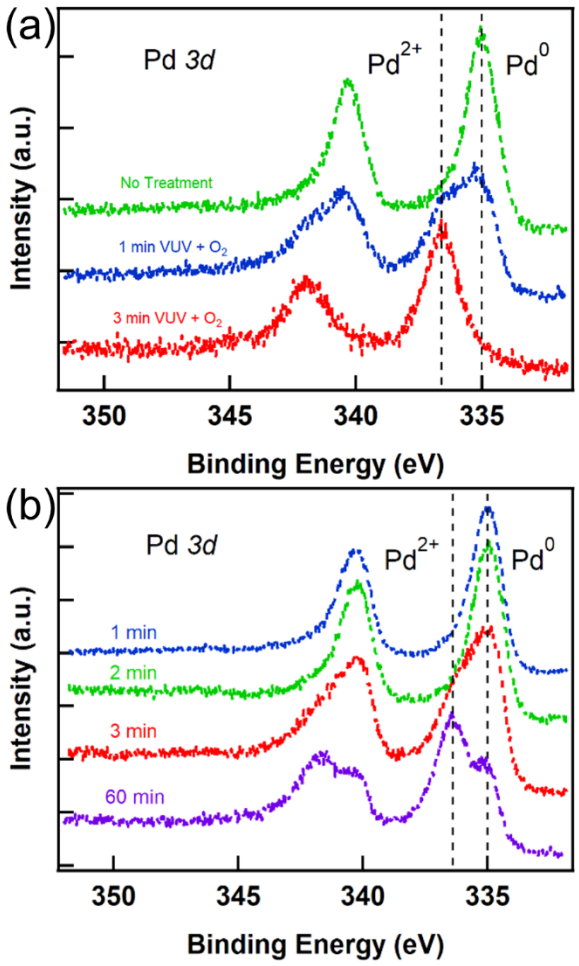

Figure 4.2. Pd 3*d* XP spectra is shown for Pd(2)/p-Si in (a), and Pd(20)/Ti(10)/p-Si in (b), which are co-exposed to O_2 and VUV light for various times. The Pd^0 and Pd^{2+} features are identified with dashed lines in both (a) and (b). All samples shown are exposed to 1 Torr O_2 at 100 °C.

The temperature dependence of PdO_x formation *via* VUV irradiation is investigated with Pd(2)/p-Si. Films are co-exposed to VUV and 1 Torr O_2 for 1 min. PdO_x formation is tracked using XPS, where Pd 3*d*, O 1*s*, and Si 2*p* XP spectra are shown in Figure 4.3(a), (b), and (c), respectively. Pd^0 and Pd^{2+} comprise the Pd $3d_{5/2}$ XP region at 335.0 eV. No Pd^0 is present after co-dosing VUV and O_2 for at 200 °C for 1 min, indicating only PdO_x is

present. This result is supported by the two oxygen chemical states in the O 1*s* XP spectra (Figure 4.3(b)): O-Si at 532.7 eV, and O-Pd at 530.5 eV.[32,33] In the Pd 3*d* XP spectra shown in Figure 4.3(a), the Pd^0/Pd^{2+} ratio is 0.90, 0.44, 0.09 for co-exposures at 100 °C, 150 °C, and 200 °C, respectively, indicating more PdO_x grows as the temperature is raised. The increase in temperature also results in a thicker SiO_2 layer on Si^0, as seen in the increase of the 103.5 eV XP feature (Si^{4+}), and attenuation of the 99.0 eV XP feature (Si^0, Figure 4.3(c)). Thus, in order to minimize oxidation (and material removed) in an ALE cycle, low temperatures should be chosen. The oxidation half-cycle temperature is 100 °C in the demonstration herein for compatibility with low-temperature applications, such as the flexible substrates in TCE fabrication as well as wearable electronics.[37]

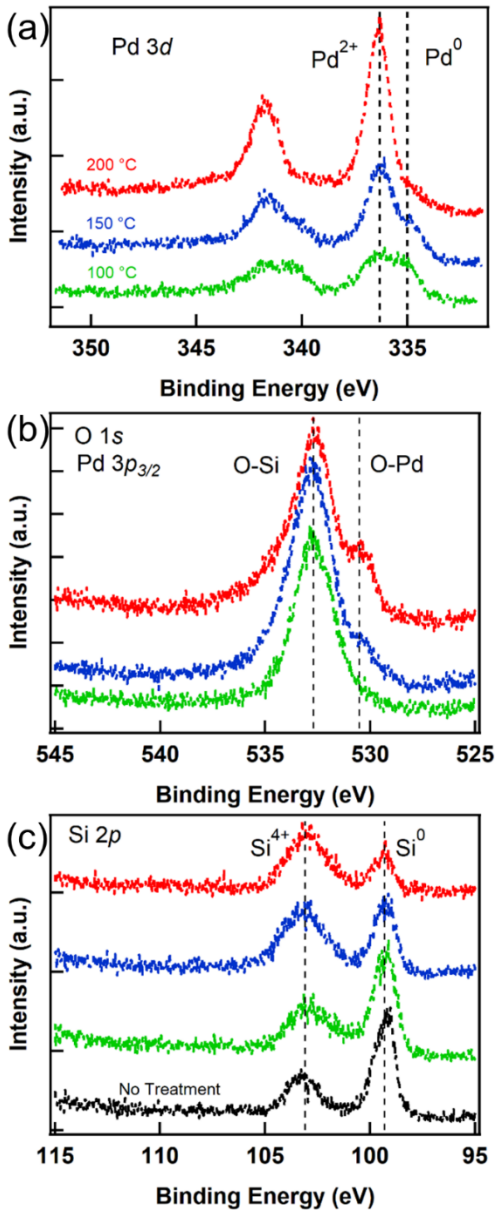

Figure 4.3. Pd 3*d* and O1*s*/Pd $3p_{3/2}$ XP spectra of Pd(2)/p-Si are shown in (a) and (b), respectively. All samples are exposed to 1 Torr O_2 with VUV light for 1 min. The temperature of the exposure ranges from 100 °C to 200 °C. Pd^0, and O-Pd XP features are shown with dashed lines in (a), while the XP features O-Pd and O-Si are shown with dashed lines in (b), and O-Si and Si^0 are indicated with dashed lines in (c). The Si 2*p* XP region before any treatment is included in (c) for comparison between Si^{4+} and Si^0 XP features.

The oxidation of continuous blanket Pd films is explored using Pd(20)/p-Si and Pd(20)/Ti(10)/p-Si. Two oxidation conditions are demonstrated: (1) exposure to 1 Torr of O_2 at 200 °C for 45 min; and (2) co-exposure to VUV and 1 Torr O_2 at 100 °C for 5 min. The Pd 3*d* XP spectra comparing the films are shown in Figure 4.4(a). Pd^0 and Pd^{2+} XP features arise, consistent with results in Figure 4.2(b). Pd $3d_{5/2}$ XP features of the film exposed to 1 Torr of O_2 at 200 °C indicates no Pd^{2+} is formed. Thus Pd^0 will not thermally oxidize in an O_2 atmosphere at 200 °C. PdO_x forms at 100 °C with co-exposure of O_2 and VUV irradiation as evidenced by the Pd^{2+} feature at 336.7 eV (Figure 4.4(a)). Pd films are likely similarly resistant to thermal oxidation with O_2 at temperatures lower than 200 °C. Thus, oxidation of Pd^0 to PdO_x can be controlled *via* VUV-light exposure, without concern of thermal oxidation with O_2.

Morphology of the thermally-treated Pd(20)/p-Si, which does not have a Ti adhesion layer, and VUV-treated Pd(20)/Ti(10)/p-Si is investigated using AFM, where 5×5 μm^2 AFM micrographs are shown in Figures 4.4(b) and 4.4(c), respectively. The R_a of Pd(20)/Ti(10)/p-Si and Pd(20)/p-Si before oxidation is 11.4 Å, and 10.9 Å, respectively. After exposing Pd(20)/p-Si to O_2 at 200 °C for 45 min the R_a is 15.3 Å. After exposing Pd(20)/Ti(10)/p-Si to VUV and O_2 for 5 min at 100 °C the R_a is 6.3 Å. Results from AFM and XPS indicate the 20 nm Pd films do not dewet for temperatures T < 200 °C. The film roughness is approximately unchanged with co-exposure of VUV and O_2 at 100 °C or O_2 at 200 °C, as the R_a values are within the variance of the starting substrates. However, there is a clear change in morphology, evidenced by the 1D linear power spectral density (PSD)

of Figures 4.4(b), and 4.4(c) (Figure F.1). A characteristic length of 2.6 nm is calculated for Figure 4.4(b), while the characteristic length is >200 nm for Figure 4.4(c). This indicates a less uniform surface results from exposure to O_2 at 200 °C for 45 min than for co-exposure of VUV and O_2 at 100 °C for 5 min.[38] A larger area AF micrograph would be required to estimate the characteristic length of Figure 4.4(c) more precisely.

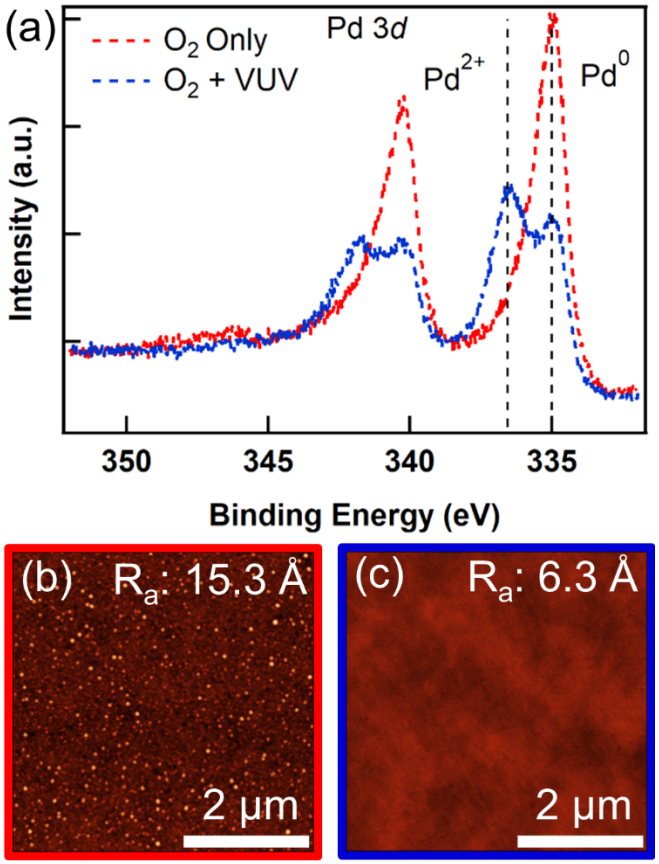

Figure 4.4. (a) Pd 3*d* XP spectra of 20 nm Pd is shown where one (Pd(20)/p-Si) is exposed to 1 Torr of O_2 at 200 °C for 45 min, and the other (Pd(20)/Ti(10)/p-Si) is co-exposed to VUV and 1 Torr of O_2 at 100 °C for 5 min. XP feature positions for Pd^0 and Pd^{2+} are shown in dashed lines. (b) and (c) Show 5×5 μm^2 AFM micrographs of Pd(20)/p-Si and Pd(20)/Ti(10)/p-Si, respectively.

4.3.3. ETCHING HALF-CYCLE: REMOVAL OF PdO_X *VIA* VAPOR EXPOSURE OF HCOOH

HCOOH has been demonstrated to etch PdO_x at 80 °C.[1] In order to keep the ALE process isothermal with the oxidation half-cycle previously discussed, the HCOOH half-cycle is kept at 100 °C. HCOOH effects on Pd(20)/Ti(10)/p-Si are investigated with XPS, AFM, and XRR (not shown). Pd(20)/Ti(10)/p-Si is exposed to HCOOH for 15 min and the only detectable change is a decrease in R_a from 11.4 Å to 8.9 Å. XRR and XPS measurements before and after HCOOH exposures are identical, indicating HCOOH vapor exposures do not etch Pd^0. HCOOH pressures between 0.50 and 5.0 Torr and exposure times between 30 s and 15 min have no effect on the removal of PdO_x. Therefore, HCOOH vapor exposure for 30 s at 0.50 Torr is sufficient to remove PdO_x as measured by XPS. The mechanism by which HCOOH etches PdO_x warrants further study and is beyond the scope of this work.

PdO_x is formed on Pd(20)/Ti(10)/p-Si by co-exposing VUV and O_2 for 180 s, which produces PdO_x (Figure 4.2(b)). PdO_x is then exposed to 30 s of HCOOH at 0.50 Torr and 100 °C. Results of the full etching cycle are shown in Figure 4.5(a) *via* the Pd 3*d* XP region. After co-exposing VUV and O_2, the Pd-O XP feature appears at 336.7 eV. After exposure to HCOOH vapor, the only Pd $3d_{5/2}$ XP feature present is at 335.0 eV, indicating the presence of Pd^0, and absence of Pd^{2+}.

Morphology is tracked through one full etching cycle using AFM in Figures 4.5(b), (c), and (d), where the surface as-deposited, after the oxidation half-cycle, and after the etching half-cycle are shown, respectively. All AFM micrographs are 5×5 μm^2. It is

important to note that Figure 4.5(b) shows a smaller area of a film equivalent to the one shown in Figure 4.1(b), and thus has an apparent larger R_a. The Pd surface is changed during the oxidation half-cycle (Figure 4.5(c)), due to the formation of PdO_x. Surface topology is retained after HCOOH exposure (Figure 4.5(d)), though the local height of surface features is reduced. The R_a of the surface as-deposited, after co-exposure of VUV and O_2, and after HCOOH exposure is, 21.2 Å, 13.4 Å, and 7.2 Å, respectively. These results are confounded with the possibility of nonuniformity of as-deposited Pd, and selection of AF analysis area. However, it is likely the overall oxidation and etching half-cycle result in a lower roughness than the as-deposited film (see below), which is consistent with known smoothing effects of repeated ALE cycles.[39]

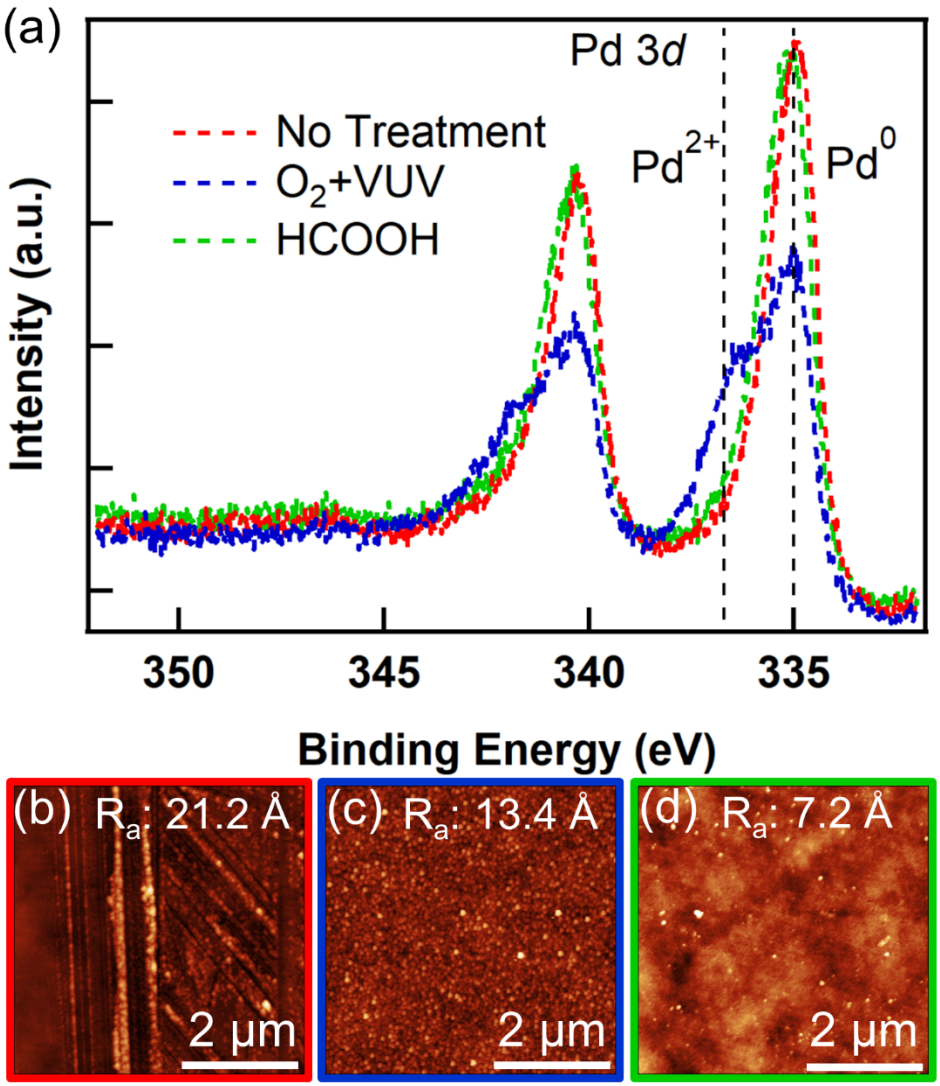

Figure 4.5. (a) Pd 3*d* XP spectra of a Pd(20)/Ti(10)/p-Si that is exposed to one ALE cycle, consisting of: co-exposing VUV and O_2 for 180 s; followed by 90 s Ar; 30 s of HCOOH; and finally 150 s Ar. The full etching cycle takes place at 1 Torr O_2, and 0.50 Torr HCOOH, at 100 °C. Pd^0 and Pd^{2+} XP features are shown with dashed lines. AFM micrographs of corresponding exposure conditions in (a) are shown in (b), (c), and (d), where the micrographs are the surface as-deposited, after oxidation, and after exposure to HCOOH, respectively. All AFM micrographs are 5×5 μm^2.

4.3.4. ATOMIC LAYER ETCHING OF PD

The etch amount per cycle for Pd(20)/Ti(10)/p-Si films is measured *ex situ*. ALE cycles are described with a shorthand indicating the time of co-exposure to VUV and O_2, followed by the Ar purge time, then the 0.50 Torr HCOOH exposure time, and finally another Ar purge time (*e.g.* 100/10/100/10 indicates 100 s of co-exposure of VUV and O_2 as well as 100 s of HCOOH with two 10 s Ar purges between oxidation and etching cycles). Films are subject to repeated 180/90/30/150 ALE cycles at 1 Torr O_2 and 100 °C. XRR is taken on all samples before and after etching (Figure 4.6(a)). AFM captures surface topology after 5, 10, and 20 etching cycles, in Figures 4.6(b), (c), and (d), respectively. Figure 4.6(a) shows before and after XRR measurements. The R_a of etched films is 6.1 Å, 9.1 Å, and 8.4 Å for 5, 10, and 20 cycles, respectively, which are all lower than the roughness before etching, 21.2 Å (Figure 4.5(b)). This indicates repeated etching cycles do not impart significant change to the morphology of the surface, and film roughness is reduced.

The amount of material removed as a function of the number of cycles is shown in Figure 4.7. Fitting of XRR spectra indicates the 5, 10, and 20 cycle film thicknesses are approximately 234 Å, 219 Å, and 223 Å before etching, and 218 Å, 187 Å, and 165 Å after etching. This yields a total thickness removed from repeated etch cycles as 15.8 Å, 32.1 Å, and 58.5 Å, for films exposed to 5, 10, and 20 cycles, respectively. The etch amount is 3.16 Å/cycle, 3.21 Å/cycle, and 2.92 Å/cycle, for 5, 10, and 20 cycles. The line of best fit has slope 2.81 ± 0.15 and a y-intercept of 2.6 ± 2.06 Å, indicating there is minimal delay in repeated ALE cycles on blanket Pd thin films. The estimate of 2.81 Å/cycle is on the order

of interplanar distances of the (111) and (100) facets of Pd (2.2 Å - 2.9 Å). Thus, oxidation of Pd *via* co-exposure of VUV and O_2, followed by exposure to HCOOH vapor, results in the etching of approximately one atomic layer of Pd, confirming ALE behavior.

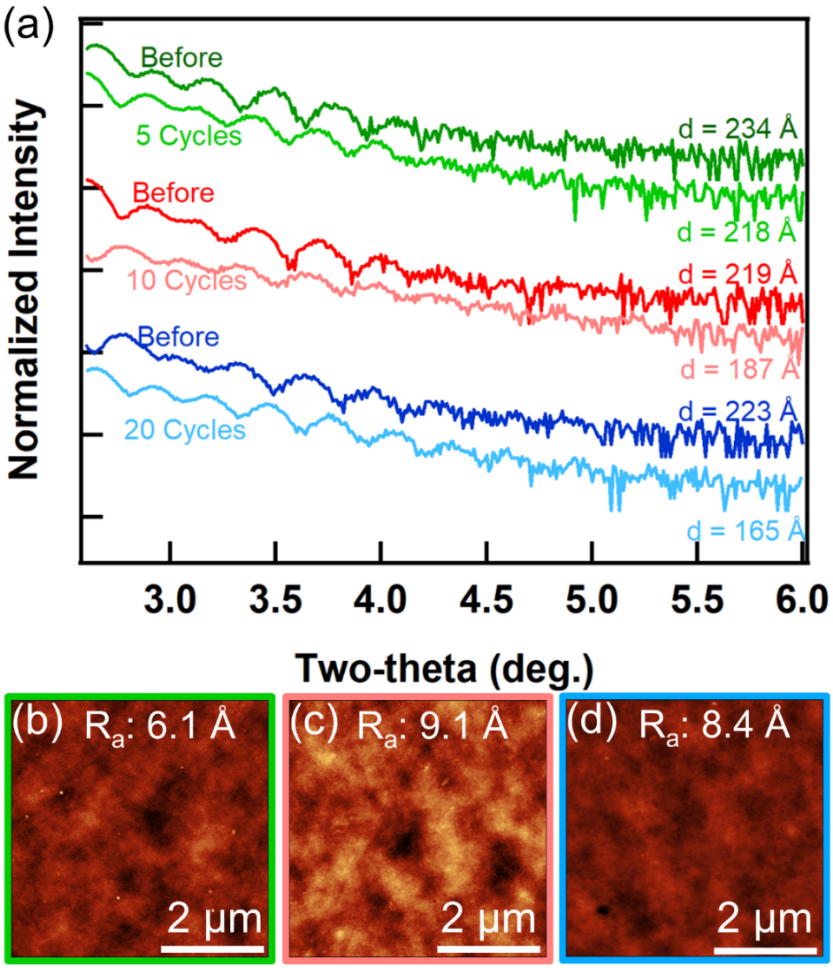

Figure 4.6. (a) XRR measurements of a Pd(20)/Ti(10)/p-Si exposed to ALE Cycles (180/90/30/150) at 1 Torr O_2 and 100 °C. Films exposed to 5, 10, and 20 atomic layer etching cycles are shown. Before and after XRR measurements are shown with the corresponding thickness indicated to the right. (b), (c), and (d) are corresponding 5×5 μm^2 AFM micrographs after 5, 10 and 20 cycles, respectively.

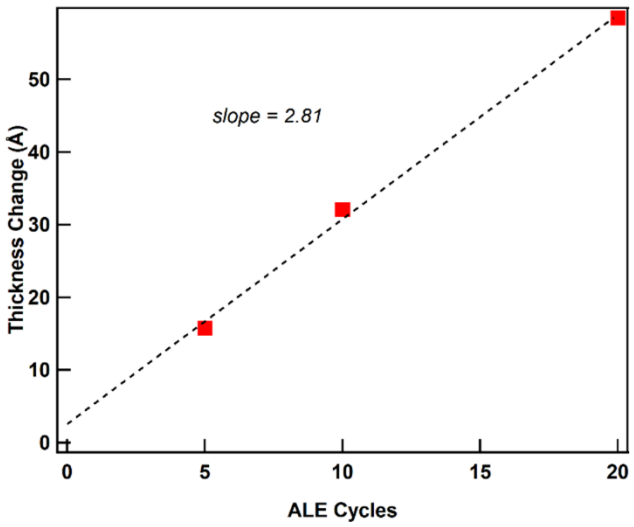

Figure 4.7. Thickness of Pd removed after 5, 10, and 20 ALE cycles (180/90/30/150) are shown. Substrates are Pd(20)/Ti(10)/p-Si exposed at 1 Torr O_2 at 100 °C The line of best fit is shown in a dashed line and extended to the origin.

VUV-enhanced ALE of Pd(2)/p-Si shows removal of Pd with repeated cycles. A film exposed to ALE cycles (60/90/30/150) at 1 Torr O_2 and 100 °C are characterized by tracking XP regions (Si 2*p*, Pd 3*d*, Pd 3*p*, and O 1*s*) and are shown in Figure 4.8, which are vertically offset for clarity. Several features are notable in the XP measurement over the course of etching. Before any ALE is performed, the Pd 3*d* XP feature has the largest intensity, with the Pd $3d_{5/2}$ and Pd $3d_{3/2}$ features visible at 335.0 eV, and 340.3 eV, respectively. The Pd $3p_{3/2}$ XP feature directly overlaps with O 1*s*. As more O is incorporated into the substrate (with repeated co-exposure to VUV and O_2) the O 1*s* XP feature grows. Two Si 2*p* XP features are present, Si^0 at 99.0 eV arising from the substrate p-Si(100), and Si^{4+} at 103.5 eV arising from the native oxide on p-Si(100). The intensity of the Si^0 XP

feature is largest before ALE cycling, and it is attenuated by the SiO_2 overlayer growing as a result of co-exposure to VUV and O_2, as discussed previously. The XP feature ~103.0 eV shifts to 103.5 eV as ALE cycles are performed due to removal of Pd, which becomes dominated by the Si-O XP feature at 103.5 eV.

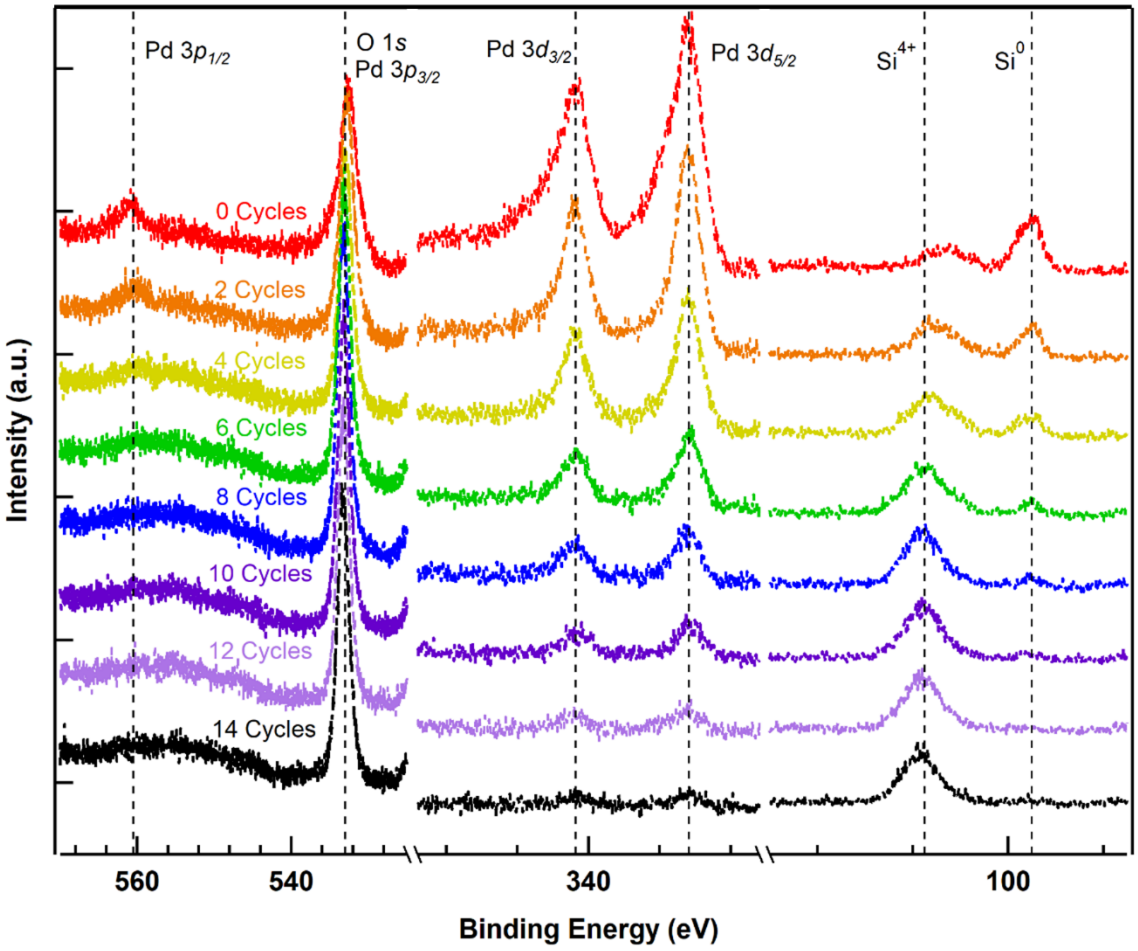

Figure 4.8. High Resolution XP spectra of Pd(2)/p-Si are shown after exposure to repeated ALE cycles (60/90/30/150) at 1 Torr O_2 and 100 °C in 2 cycle increments. The cumulative number of ALE cycles increases moving down the *y*-axis. O 1*s*/P 3*p*, Pd 3*d*, and Si 2*p* XP regions are shown with Pd $3p_{1/2}$, O 1*s*, Pd $3p_{3/2}$, Pd $3d_{5/2}$, Pd $3d_{5/2}$, Si^{4+} (overlapping with Pd 4*s*), and Si^0 XP features marked in vertical dashed lines.

High resolution XP scans are performed after ALE cycling and the integrated areas of XP features are reported in in Figure 4.9. The XP feature area after 2 cycle increments is shown for O 1*s*, Pd 3*d*, Si^{4+}, and Si^{0}. Pd 3*d* decreases monotonically with ALE cycles, consistent with Figure 4.8. The O 1*s* XP feature increases monotonically with repeated ALE cycles due to incorporation of O-Si, which can be seen in the Si^{4+} trace in Figure 4.9, as well as the Si 2*p* XP region in Figure 4.8. It is worth mentioning that after 8 cycles, the Si^{0} XP feature at 99.0 eV persists, indicating SiO_2 growth is limited after co-exposure of VUV and O_2 for 8 min at 100°C.

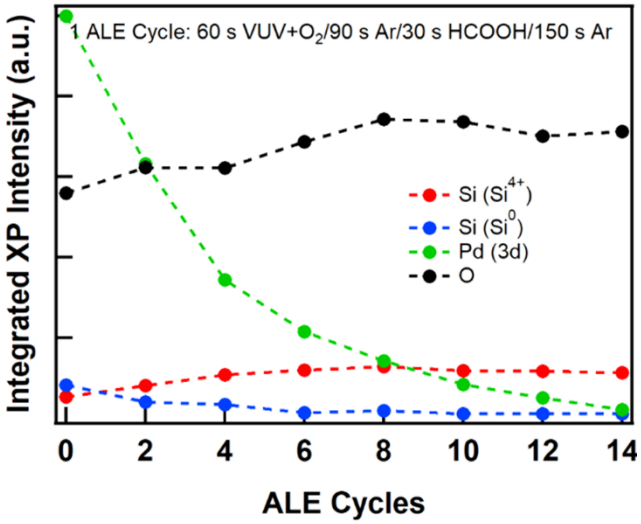

Figure 4.9. XP spectra of Pd(2)/p-Si exposed to ALE cycles (60/90/30/150) at 1 Torr O_2 and 100 °C are shown. Integrated peak areas from a given XP feature are plotted versus the number of cycles. The XP regions tracked are O 1*s*, Pd 3*d*, and Si 2*p* with contributions from the O 1*s*, Pd $3d_{5/2}$, Pd $3d_{3/2}$, Si^{4+}, and Si^{0} XP features. Traces are ordered in the legend by first appearance moving down the *y*-axis.

While Pd oxidation is observed, the exact mechanism of oxidation is not clear. Two processes could be responsible for PdO_x formation. $O(^3P)$, $O(^1D)$, and O_3 produced by VUV interacting with O_2 in the gas phase could diffuse to the Pd^0 surface, where the oxidation reaction proceeds. The oxidation reaction could also proceed by the interaction of VUV photons with oxidant species and any O_2 that are adsorbed onto the Pd^0 surface. The Pd^0 surface could also participate catalytically in the oxidation reaction Pd^0 to PdO_x.[40,41] The exact mechanism is outside the scope of this article and future work is needed to elucidate this ambiguity.

4.4. Conclusions and Summary

The first demonstration of VUV-enhanced ALE is presented, where controlling oxidation of the to-be-etched species is central to achieve ALE of Pd^0. ALE cycles are comprised of one half-cycle that oxidizes surface and near surface Pd^0, and one half-cycle that removes PdO_x via HCOOH vapor exposure. Self-limited oxidation of Pd^0 to Pd^{2+} is demonstrated via co-exposure of VUV photons ($115\ nm < \lambda < 400\ nm$) with O_2, where the thickness of the PdO_x that forms is dependent on the time of co-exposure to O_2 and VUV. The temperature of vapor etching was chosen such that the complete atomic layer etching cycle can be achieved isothermally at 100 °C, though higher temperatures would increase PdO_x thickness, and thus etch amount. Surface morphology is not strongly affected by any steps in the full ALE process, however, the surface roughness is reduced after repeated ALE cycles. Available surface area is suspected to affect the rate of Pd oxidation. Repeated cycling of continuous, blanket Pd films with an oxidation half-cycle consisting of 1 Torr

O_2 and VUV illumination for 3 min at 100 °C yields an etch rate of 2.85 Å/cycle, which is approximately one atomic layer of Pd, confirming the ALE of Pd with co-exposure of VUV and O_2.

4.5. REFERENCES

(1) Chen, J. K.-C.; Altieri, N. D.; Kim, T.; Chen, E.; Lill, T.; Shen, M.; Chang, J. P. Directional Etch of Magnetic and Noble Metals. II. Organic Chemical Vapor Etch. *J. Vac. Sci. Technol. Vac. Surf. Films* **2017**, *35* (5), 05C305.

(2) Sun, J. B.; Almquist, B. D. Interfacial Contact Is Required for Metal-Assisted Plasma Etching of Silicon. *Adv. Mater. Interfaces* **2018**, *5* (24), 1800836.

(3) Han, H.; Huang, Z.; Lee, W. Metal-Assisted Chemical Etching of Silicon and Nanotechnology Applications. *Nano Today* **2014**, *9* (3), 271–304.

(4) Huang, Z.; Geyer, N.; Werner, P.; de Boor, J.; Gosele, U. Metal-Assisted Chemical Etching of Silicon: A Review. *Adv. Mater.* **2010**, *23* (2), 285–308.

(5) Li, X.; Bohn, P. W. Metal-Assisted Chemical Etching in HF/H_2O_2 Produces Porous Silicon. *Appl. Phys. Lett.* **2000**, *77* (16), 2572–2574.

(6) Sang, X.; Chang, J. P. Physical and Chemical Effects in Directional Atomic Layer Etching. *J. Phys. Appl. Phys.* **2020**, *53* (18), 183001.

(7) Fracassi, F.; d'Agostino, R.; Cacucci, A. Dry Etching of Palladium Thin Films in Fluorine Containing Plasmas: X-ray Photoelectron Spectroscopy Investigation. *J. Vac. Sci. Technol. Vac. Surf. Films* **1998**, *13* (1), 63.

(8) Williams, K. R.; Gupta, K.; Wasilik, M. Etch Rates for Micromachining Processing-Part II. *J. Microelectromechanical Syst.* **2003**, *12* (6), 761–778.

(9) Chen, J. K.-C.; Altieri, N. D.; Kim, T.; Lill, T.; Shen, M.; Chang, J. P. Directional Etch of Magnetic and Noble Metals. I. Role of Surface Oxidation States. *J. Vac. Sci. Technol. Vac. Surf. Films* **2017**, *35* (5), 05C304.

(10) DuMont, J. W.; Marquardt, A. E.; Cano, A. M.; George, S. M. Thermal Atomic Layer Etching of SiO_2 by a "Conversion-Etch" Mechanism Using Sequential Reactions of Trimethylaluminum and Hydrogen Fluoride. *ACS Appl. Mater. Interfaces* **2017**, *9* (11), 10296–10307.

(11) Lee, Y.; George, S. M. Thermal Atomic Layer Etching of Titanium Nitride Using Sequential, Self-Limiting Reactions: Oxidation to TiO_2 and Fluorination to Volatile TiF_4. *Chem. Mater.* **2017**, *29* (19), 8202–8210.

(12) Lee, Y.; George, S. M. Atomic Layer Etching of Al_2O_3 Using Sequential, Self-Limiting Thermal Reactions with $Sn(Acac)_2$ and Hydrogen Fluoride. *ACS Nano* **2015**, *9* (2), 2061–2070.

(13) Lee, Y.; DuMont, J. W.; George, S. M. Trimethylaluminum as the Metal Precursor for the Atomic Layer Etching of Al_2O_3 Using Sequential, Self-Limiting Thermal Reactions. *Chem. Mater.* **2016**, *28* (9), 2994–3003.

(14) Johnson, N. R.; Sun, H.; Sharma, K.; George, S. M. Thermal Atomic Layer Etching of Crystalline Aluminum Nitride Using Sequential, Self-Limiting Hydrogen Fluoride and $Sn(Acac)_2$ Reactions and Enhancement by H_2 and Ar Plasmas. *J. Vac. Sci. Technol. Vac. Surf. Films* **2016**, *34* (5), 050603.

(15) Matsumoto, S.; Toguchi, M.; Takeda, K.; Narita, T.; Kachi, T.; Sato, T. Effects of a Photo-Assisted Electrochemical Etching Process Removing Dry-Etching Damage in GaN. *Jpn. J. Appl. Phys.* **2018**, *57* (12), 121001-1–7.

(16) Ko, C. H.; Su, Y. K.; Chang, S. J.; Lan, W. H.; Webb, J.; Tu, M. C.; Cherng, Y. T. Photo-Enhanced Chemical Wet Etching of GaN. *Mater. Sci. Eng. B* **2002**, *96* (1), 43–47.

(17) Lau, H. W.; Parker, G. J.; Greef, R.; Holling, M. High Aspect Ratio Submicron Silicon Pillars Fabricated by Photoassisted Electrochemical Etching and Oxidation. *Appl. Phys. Lett.* **1995**, *67* (13).

(18) Shin, H.; Zhu, W.; Donnelly, V. M.; Economou, D. J. Surprising Importance of Photo-Assisted Etching of Silicon in Chlorine-Containing Plasmas. *J. Vac. Sci. Technol. Vac. Surf. Films* **2012**, *30* (2), 021306.

(19) Ishii, M.; Meguro, T.; Sugano, T.; Gamo, K.; Aoyagi, Y. Surface Reaction Control in Digital Etching of GaAs by Using a Tunable UV Laser System: Reaction Control Mechanism in Layer-by-Layer Etching. *Appl. Surf. Sci.* **1995**, *86* (1), 554–558.

(20) Iimori, T.; Hattori, K.; Shudo, K.; Iwaki, T.; Ueta, M.; Komori, F. Laser-Induced Mono-Atomic-Layer Etching on Cl-Adsorbed Si(111) Surfaces. *Appl. Surf. Sci.* **1998**, *130–132*, 90–95.

(21) Chalker, P. R.; Marshall, P. A.; Dawson, K.; Brunell, I. F.; Sutcliffe, C. J.; Potter, R. J. Vacuum Ultraviolet Photochemical Selective Area Atomic Layer Deposition of Al_2O_3 Dielectrics. *AIP Adv.* **2015**, *5* (1), 017115.

(22) Chalker, P. R.; Marshall, P. A.; Dawson, K.; Sutcliffe, C. J.; Brunell, I. F.; Sedghi, N.; Hall, S.; Potter, R. J. Vacuum Ultraviolet Photochemical Atomic Layer Deposition of Alumina and Titania Films. *ECS Trans.* **2015**, *69* (7), 139–145.

(23) Miikkulainen, V.; Väyrynen, K.; Mizohata, K.; Räisänen, J.; Vehkamäki, M.; Ritala, M. Photoassisted Atomic Layer Deposition of Oxides Employing Alkoxides as Single-Source Precursors. *J. Vac. Sci. Technol. A* **2019**, *37* (6), 060911.

(24) Chalker, P. R. Photochemical Atomic Layer Deposition and Etching. *Surf. Coat. Technol.* **2016**, *291* (Supplement C), 258–263.

(25) Johnson, M. S.; Nilsson, E. J. K.; Svensson, E. A.; Langer, S. Gas-Phase Advanced Oxidation for Effective, Efficient in Situ Control of Pollution. *Environ. Sci. Technol.* **2014**, *48* (15), 8768–8776.

(26) Munter, R. Advanced Oxidation Processes - Current Status and Prospects. *Proc. Est. Acad. Sci. Chem.* **2008**, *50* (2), 59–80.

(27) Huffman, R. E. Absorption Cross-Sections of Atmospheric Gases for Use in Aeronomy. *Can. J. Chem.* **1969**, *47* (10), 1823–1834.

(28) Slanger, T. G.; Cosby, P. C. Oxygen Spectroscopy below 5.1 EV. *J. Phys. Chem.* **1988**, *92* (2), 267–282.

(29) Björck, M.; Andersson, G. GenX: An Extensible X-Ray Reflectivity Refinement Program Utilizing Differential Evolution. *J. Appl. Crystallogr.* **2007**, *40* (6), 1174–1178.

(30) Zhang, Z.; Nallan, H. C.; Coffey, B. M.; Ngo, T. Q.; Pramanik, T.; Banerjee, S. K.; Ekerdt, J. G. Atomic Layer Deposition of Cobalt Oxide on Oxide Substrates and Low Temperature Reduction to Form Ultrathin Cobalt Metal Films. *J. Vac. Sci. Technol. A* **2018**, *37* (1), 010903.

(31) Coffey, B. M.; Lin, E. L.; Chen, P.-Y.; Ekerdt, J. G. Area-Selective Atomic Layer Deposition of Crystalline $BaTiO_3$. *Chem. Mater.* **2019**, *31* (15), 5558–5565.

(32) Moulder, J. F.; Stickle, W. F.; Sobol, P. E.; Bomben, K. D. *Handbook of X-Ray Photoelectron Spectroscopy*; Chastain, J., Ed.; Perkin-Elmer: Eden Prarie, Minnesota, 1992.

(33) Militello, M. C.; Simko, S. J. Palladium Oxide (PdO) by XPS. *Surf. Sci. Spectra* **1998**, *3* (4), 395.

(34) Mackus, A. J. M.; Merkx, M. J. M. Fully Self-Aligned Vias: The Killer Application for Area-Selective ALD? – A Discussion of the Requirements for Implementation in High Volume Manufacturing. *Atomic Limits* **2019**, *7*.

(35) Mackus, A. J. M.; Merkx, M. J. M.; Kessels, W. M. M. From the Bottom-Up: Toward Area-Selective Atomic Layer Deposition with High Selectivity. *Chem. Mater.* **2019**, *31* (1), 2–12.

(36) Clark, R.; Tapily, K.; Yu, K.-H.; Hakamata, T.; Consiglio, S.; O'Meara, D.; Wajda, C.; Smith, J.; Leusink, G. Perspective: New Process Technologies Required for Future Devices and Scaling: APL Materials: Vol 6, No 5. *APL Mater* **2018**, No. 6, 058203.

(37) Ten Eyck, G. A.; Pimanpang, S.; Bakhru, H.; Lu, T.-M.; Wang, G.-C. Atomic Layer Deposition of Pd on an Oxidized Metal Substrate. *Chem. Vap. Depos.* **2006**, *12* (5), 290–294.

(38) Zhang, W.; Nahm, R. K.; Ma, P. F.; Engstrom, J. R. Probing Ultrathin Film Continuity and Interface Abruptness with X-Ray Photoelectron Spectroscopy and Low-Energy Ion Scattering. *J. Vac. Sci. Technol. A* **2013**, *31* (6), 061101.

(39) Kanarik, K. J.; Tan, S.; Gottscho, R. A. Atomic Layer Etching: Rethinking the Art of Etch. *J. Phys. Chem. Lett.* **2018**, *9* (16), 4814–4821.

(40) Kim, M.; Pan, L.; Weaver, J. F.; Asthagiri, A. Initial Reduction of the PdO(101) Surface: Role of Oxygen Vacancy Formation Kinetics. *J. Phys. Chem. C* **2018**, *122* (45), 26007–26017.

(41) Ouyang, L.; Tian, P.; Da, G.; Xu, X.-C.; Ao, C.; Chen, T.; Si, R.; Xu, J.; Han, Y.-F. The Origin of Active Sites for Direct Synthesis of H_2O_2 on Pd/TiO_2 Catalysts: Interfaces of Pd and PdO Domains. *J. Catal.* **2015**, *321*, 70–80.

Chapter 5: Vacuum Ultraviolet Enhanced Atomic Layer Etching of Ru Thin Films

Contents for this chapter are submitted for publication at the time of writing this dissertation.

Supporting information is found in Appendix G.

5.1. INTRODUCTION

Platinum group metals, such as Ru, are ubiquitous next generation applications, not limited to, catalysis[1,2] and nanoelectronics.[3,4] Ru is a potential interconnect material for integrated circuits as well.[5] Ru metal (and RuO_2) can also be found in dynamic random access memory devices,[6,7] and is employed for metal contacts, and barrier liners.[8–12] However, as device dimensions continue to shrink, and architectures become increasingly complex, atomic level fabrication allowing selective, low-temperature removal of metals are central to enabling next generation devices.

Ruthenium etching has been realized by oxidizing Ru and using a second chemical to remove the oxide. Thermal oxidation of Ru from O_2 is not observed until the temperature is 400 – 700 °C,[13] which exceeds the thermal budget of many devices. Lower temperature oxidation methods typically involve an O_2 plasma,[14,15] or neutral O beam,[16] which oxidizes Ru to RuO_2. Oxidized Ru is removed chemically with the aid of a second reactive species, such as CH_3OH,[14] CF_3CFH_2,[15] or C_2H_5OH.[16] Continuous etching of Ru without a plasma has also been reported, where Ru etching is accomplished using O_3, which is known to form volatile RuO_4 at temperatures above 100 – 150 °C.[17]

A self-limiting oxidation step is a likely prerequisite for Ru ALE. An electrochemical liquid ALE process has been reported for Ru, which proceeds by first forming $Ru(OH)_2$ on the surface by applying a positive voltage, and completing the etch

with Cl^- in the liquid phase.[18] We have recently demonstrated a method of ALE, vacuum ultraviolet (VUV) enhanced ALE of Pd where oxidizing species are generated by co-exposing the substrate to VUV and O_2 at temperatures of 50 – 200 °C.[19,20] VUV enhanced ALE proceeds by first oxidizing near-surface Pd layers through co-exposure of VUV/O_2 to form PdO_x. Following the oxidation half-cycle, samples are exposed to formic acid, HCOOH, vapor that completes an etch cycle. The extent of Pd oxidation is limited to the near surface region through the VUV exposure time and sample temperature. Atomic O, formed in the gas phase, is the main species responsible for oxidation of Pd under the ALE conditions. Herein we report self-limiting oxidation half-cycles using a co-exposure of VUV/O_2 and etching half-cycles using HCOOH vapor results in the ALE of Ru.

Formic acid is known to etch transition metals (e.g., Co, Fe, Ni, Pt, Pd), where the metal removed is limited to the amount of metal that is oxidized in an O_2 plasma as HCOOH does not etch the metal.[21,22] The exact etching mechanism of transition metal oxides with HCOOH is unknown. One report has suggested a bidentate $Ni(COOH)_2$ molecule etch product for etching of NiO with HCOOH.[22]

Density functional theory (DFT) complements experimental work, and can aid in addressing issues of which oxidant(s) (atomic O, O_2, and O_3) may be responsible for oxidation, and nudged elastic band (NEB) calculations can aid in addressing how the oxide front propagates through a solid film. DFT has been combined with experiments to assess adsorption and bonding of O and O_2 onto Ru(1010),[23,23–26] Ru(0001),[27–29] and Ru(100),[30] where surface configuration, surface diffusion, and competitive adsorption all have been described. Experimental and DFT reports of O on Ru surfaces have found two equilibrium surface O coverages of 0.25 monolayer (ML) O – 0.50 ML O.[23,31] The surface O loading increases to 1 ML O and 2 ML O after the temperature raised above 500 K.[31–33]

This work aims to explore VUV enhanced ALE of Ru. We show VUV/O_2 can oxidize Ru metal, that the oxidation is self-limiting, and that HCOOH is capable of etching the oxidized Ru species that are formed. We find the amount removed per cycle decreases as surface roughness decreases. This behavior is likely associated with the oxidation rate. DFT and NEB calculations are presented to provide insight into the self-limiting oxidation of Ru.

5.2. METHODS

5.2.1. EXPERIMENTAL METHODS

Ru metal films are sputtered with a >99.9% pure Ru target (Plasmaterials Inc.) at 30 mA emission current, and 4 mTorr Ar (99.999%, Matheson), yielding a deposition rate of 4 nm/min on large blanket wafers. The sputter system (EMS-Quorum, EMS300TD) is evacuated using a dual stage rotary vane mechanical pump. Substrates are single side polished p-Si(100) wafers (1 – 10 Ω cm, University Wafer Inc. and Nova Electronics Inc.), where the native oxide is present before Ru is sputtered. We have observed that other platinum group metals, such as Pd, delaminate from the Si substrate if an adhesion layer is not present. Because of this, 3 nm Ti (>99.995%, Plasmaterials Inc.) is sputtered onto the Si substrates before Ru deposition. A quartz crystal microbalance (QCM, Inficon) is used to evaluate sputtered thickness in-situ. Film thickness is measured ex-situ using X-ray reflectivity (XRR). All thicknesses reported are measured using XRR. XRR indicates that the Ru films are approximately 8 nm thick, while the Ti adhesion layer cannot be detected.

All ALE experiments take place in a custom ultra-high vacuum (UHV) stainless steel experimental and analysis facility, described elsewhere.[19,20] The UHV facility is comprised of an ALE chamber, X-ray photoelectron (XP) spectrometer, load-lock

chamber, and vacuum furnace, all connected to one another via a UHV transfer line (1×10^{-7} Torr). This allows etching and analysis to be completed without exposing samples to atmosphere.

ALE is performed in a custom stainless steel reactor as well, which is essentially a six-way cross, with a D_2 lamp (H2D2 Hamamatsu, L11798) mounted at the top of the reactor. The D_2 lamp is 110 W, with a broad emission range from $110 < \lambda < 400$ nm, and is equipped with a MgF_2 window. This gives the strongest lines at 115 and 160 nm ($6.5 < h\nu < 11.3$ eV). Exposures are performed by moving the sample along the *z*-axis of the reactor using a linear motion device with a stroke length that can span the entire length of the reactor. This allows the sample to be moved within 0.50 cm of the MgF_2 window during oxidation half-cycles, and greater than 15 cm away from the MgF_2 window during HCOOH exposure half-cycles, which is far enough away to fully attenuate VUV photons. The background pressure of the ALE reactor is maintained by introducing Ar (99.9999%, Matheson) at a total flow rate of 80 sccm, to yield a background pressure of 0.10 Torr. The sample is heated from below using a 24 V halogen light bulb (Osram), while the walls of the ALE reactor are maintained at 80 °C to minimize adsorption and pumping times.

Oxidation half-cycles are performed by first raising the sample to within 0.50 cm of the VUV light source, and then introducing O_2 (99.9999%, Matheson) into the chamber using a mass flow controller at 150 sccm. This yields an oxygen partial pressure of 1 Torr. Following the oxidation exposure, the gas is cycled off, and the sample is lowered 15 cm for the etching half-cycle, and the chamber is purged with Ar to the starting background pressure. The etching half-cycle consists of exposure to HCOOH vapor (Sigma-Aldrich, >99%) isothermally. HCOOH is introduced into the ALE chamber by opening a pneumatic valve and dosing the head space of a saturator containing liquid HCOOH at room temperature. The vapor is metered using a needle valve. This yields a HCOOH partial

pressure of 0.50 Torr. Following HCOOH exposure, the chamber is purged with Ar again. ALE cycles are indicated throughout the text with the following shorthand: VUV/O_2 co-exposure time/Ar purge/HCOOH dose time/Ar purge, where all units are in seconds (i.e., 20/10/50/30 corresponds to a 20 sec VUV/O_2 exposure, 10 sec Ar purge, 50 sec HCOOH exposure, and 30 sec Ar purge). Unless noted in the text, a new substrate is used for each experiment.

In-situ X-ray photoelectron spectroscopy (XPS) is performed by transferring samples into the XP spectrometer (PHI 5600) without exposing them to atmosphere. XPS is collected using a Mg Kα anode at 15 kV and 250 W. This yields a sample current of 40 – 50 nA. Analysis of XP spectra is performed using CasaXPS (v2.3.16).

Ex-situ analysis of the film thickness and crystallinity is performed using XRR, and X-ray diffraction (XRD). XRR and XRD are collected using a Rigaku Ultima IV Diffractometer with Cu Kα radiation. XRR patterns are fit using GenX (2.4.10)[34] to determine film thickness. Film morphology is analyzed using atomic force microscopy (AFM, Asylum Research 3DMFP), collected with Si cantilevers (HQ:NSC15/Al BS, μmasch) in tapping mode. Analysis of atomic force (AF) micrographs is completed using Gwyddion (2.47).

5.2.2. THEORETICAL METHODS

DFT is performed using the plane wave basis code QuantumEspresso (v6.4.1)[35,36] using the Perdew-Burke-Ernzerhof (PBE) functional and exchange correlation.[37,38] Ultrasoft pseudopotentials describe the valency of atoms, where the wave function, and charge density cutoff are 60 Ry, and 600 Ry, respectively. Van der Waals forces are included with the Grimme-D3 correction,[39] and Becke-Johnson damping,[40] which are needed for the accurate prediction of O_3 structures. Marzari-Vanderbilt[41] "cold-smearing"

is also employed, with a smearing width of 0.002 Ry. Spin polarized calculations are employed for free molecular oxidants.

Thick (23 nm) Ru films are deposited to identify crystalline facets that may be present in the 8 nm films used in the etching studies and to inform the surfaces to model with DFT and NEB calculations. XRD patterns for 23 and 8.7 nm Ru films are shown in Appendix G, Figure G.1. Diffraction patterns are weak for 8.7 nm Ru. Three features are present in the diffraction pattern of 23 nm Ru at 2θ of 38.54°, 42.23°, and 44.01°, which are consistent with (100), (002), and (101) reflections. These peak locations correspond to interplanar distances of 2.056, 2.135, and 2.056 ± 0.005 Å for the (100), (002), and (101) facets, respectively. While three facets are detected, the intensity of reflections at (002) and (101) are the most prominent, and therefore inform the simulations herein. The choice of (002) and (101) facets is also to align with other Ru DFT reports.

The Ru unit cell is known to be hcp with lattice constant $a = b = 2.705$ Å, and $c/a = 1.582$.[42] This structure is used to define the Ru slabs in this study, where stresses within the unit cell are minimized <2 meV/Å before slab geometries are defined. Adsorption simulations are done using (2 × 2) Ru(002) and Ru(101) surfaces, which correspond to surface coverages of 0 – 0.50 ML O. The surface coverage 0.25 – 0.50 ML O is the saturation coverage observed under most conditions and is used in this study as well. The irreducible volume of the Brillouin zone is discretized using a 5×5×1 Monkhorst-Pack grid. Periodic images normal to the slab are separated by 20 Å of vacuum to minimize periodic image interactions.

Four atomic layers of Ru are used to represent the bare Ru slab, where the top two layers are allowed to relax freely, and the bottom two layers are held at the bulk Ru position. Six atomic Ru layers are used to explore simulations with increasing O incorporation so at least two Ru layers are allowed to relax freely in between O-modified

Ru layers, and Ru layers fixed at bulk positions. O incorporation into Ru is performed by relaxing a Ru surface with 0.50 ML O coverage. The positions of O atoms corresponding to 0.50 ML O on the surface are then cumulatively propagated beneath the surface Ru layer (n = 1), between the first and second Ru layer (n = 1, and 2), and between the second and third Ru layer (n = 2, and 3). Incorporation of O on the surface layer only, on the surface and in between the first and second atomic layers, and on the surface, in between the first and second atomic layers, and in between the second and third atomic layers are denoted 1, 2, and 3 O layer structures, respectively. Convergence of atomic planes, k-points, charge density, and wave function cut off are verified by changing from 4 to 6 atomic planes, 5×5×1 points to 8×8×1, 450 to 600 Ry, and 45 to 60 Ry, respectively, which results in a change of < 2 meV/atom. All simulations are optimized until the error in energy and the force are less than 1×10^{-8} Ry, and 1×10^{-6} Ry/Å, respectively.

The NEB method[43] is used to approximate the minimum energy pathway (MEP) of O diffusion through 1, and 2, O layered Ru(002) structures, where fourteen images are used to discretize the diffusion pathway. Structures are first optimized, where a "probe" O atom is placed at the nominal starting and ending positions. Optimized structures for the starting and ending geometries are then used as the input for the NEB calculation. For the NEB calculations, the wave function and charge density cutoff values are 45, and 450 Ry, and structures are optimized until the error in energy and the force are less than 1×10^{-6} Ry, and 1×10^{-5} Ry/A, respectively. Ru structure visualization and analysis is performed using XCrysDen (Version 1.6.2).[44]

Following the procedure used in Ref. 20 (Chapter 3) adsorption energy is calculated according to Equation (5.1),

$$E_{ads} = E_{surf} + E_{Ox} - E_{Ox/surf} \quad (1)$$

where E_{surf} is the energy of the surface, E_{Ox} is the energy of the oxidant O, O_2, or O_3, and $E_{Ox/Surf}$ is the energy of the Ru surface with the oxidant adsorbed. More detail on the calculation of E_{Ox} is found in Ref. 20. Briefly, $E_{Ox,}$ references all oxidants to the calculated energy of O_2, E_{O2}. The energy of atomic O, E_O, is calculated by destabilizing the energy of E_{O2} by $\Delta E_{O-O,}$ the bond energy of an O_2 molecule (498 kJ/mol). The energy of O_3, E_{O3}, is calculated by adding in the stabilizing energy for the formation of O_3 per the reaction $O_3 \rightarrow O_2 + O$, which has a change in internal energy of 102.4 kJ/mol.[45] In this convention a positive adsorption energy indicates exothermic adsorption, while a negative value is endothermic.

5.3. RESULTS

5.3.1. RU OXIDATION USING VUV/O_2

Oxidation of 8 nm Ru thin films is explored by co-exposing substrates to VUV/O_2 at 1 Torr O_2 and 100 °C for 5, 10, and 15 min. The Ru 3*d* XP feature is shown in Figure 5.1(a). There are two clear features in the Ru 3*d* XP spectra at 280.7, and 284.8 eV, which are attributed to Ru $3d_{5/2}$ and Ru $3d_{3/2}$, respectively.[46] The 4.17 eV shift in binding energy between the 5/2, and 3/2 features as well as the asymmetry of the XP features, is characteristic of Ru metal. Evidence for Ru oxidation can be found in the broadening of the $3d_{5/2}$ and $3d_{3/2}$ XP features. This is evident in the tail towards higher binding energies, which is identified as RuO_2.[2,47,48] However, despite this increase in peak area to higher binding energies, Ru metal character remains after 5, 10, and 15 min of VUV/O_2 co-exposure. It is also worthwhile to note that the C 1*s* feature overlaps directly with the $3d_{3/2}$ XP feature, which makes oxidation state identification from the Ru 3*d* feature difficult. The Ru 3*p* XP feature is known to exhibit a shift towards higher binding energy as oxidation

proceeds.[31] There is no detectable shift for Ru 3*p* XP features in Figure 5.1(b), which indicates there is limited bulk oxidation occurring during the VUV/O_2 co-exposure.

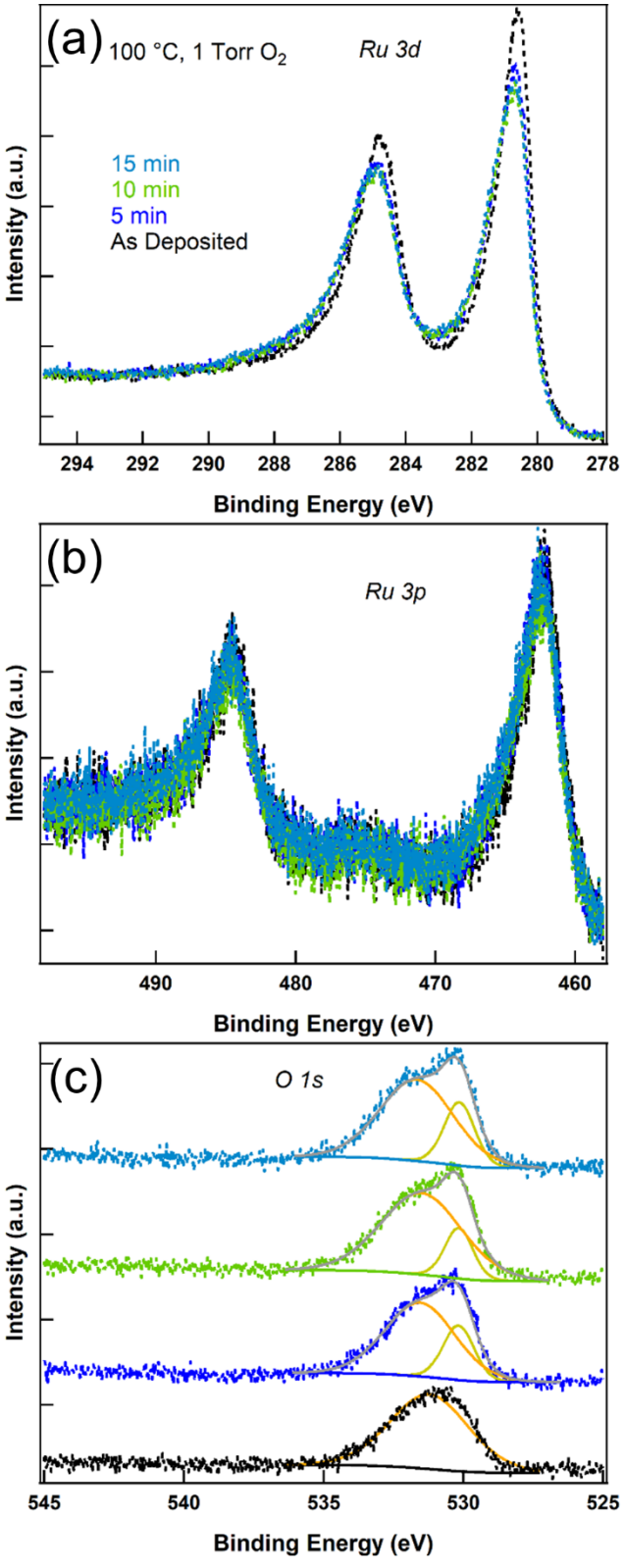
(a)
100 °C, 1 Torr O2
Ru 3d
15 min
10 min
5 min
As Deposited
Intensity (a.u.)
294
292
290
288
286
284
282
280
278
Binding Energy (eV)
(b)
Ru 3p
Intensity (a.u.)
490
480
470
460
Binding Energy (eV)
(c)
O 1s
Intensity (a.u.)
545
540
535
530
525
Binding Energy (eV)

Figure 5.1. XP Spectra of 8 nm Ru films are shown, where films are exposed to VUV/O_2 for 5, 10 and 15 min at 1 Torr O_2 at 100 °C. The Rd 3*d*, Ru 3*p* and O 1*s* XP features are shown in (a), (b), and (c), respectively. Deconvolution of the O 1*s* feature is also shown, where adsorbed oxygen (531.5 eV), and O^{2-} lattice oxygen arising from RuO_2 (530.1 eV) species are indicated in orange and yellow, respectively. The time of co-exposure to VUV/O_2 increases moving up the *y*-axis in (c).

The O 1*s* XP spectrum exhibits one clear feature at 531.5 eV for the as-deposited film (Figure 1(c)), which is indicative of an adsorbed molecular oxygen species.[32,49] This feature at 531.5 eV is removed upon Ar^+ sputtering of the as-deposited film confirming it arises from some form of adsorbed oxygen (not shown). An additional feature could be present in the as-deposited O 1*s* spectra (Figure 5.1(c), black curve) at lower binding energies ~530 eV, however, there is no statistical basis for fitting this spectrum with two peaks so we have not done so. Adsorbed molecular oxygen, evidenced by the feature at 531.5 eV, is present following all VUV/O_2 exposures (Figure 5.1(c)), as gas phase O_2 is present above the surface throughout each exposure. After 5 min of VUV/O_2 co-exposure, one feature appears at a binding energy of 530.1 eV. This is attributed to RuO_2.[31,32,49,50] XP features of RuO_2 persist after 5 min of VUV/O_2 co-exposure, however, the peak area does not appear to increase with exposure time. The fact that no further increase in RuO_2 can be detected after 10, and 15 min of VUV/O_2 co-exposure suggests self-limiting oxidation.

The effect of higher temperature on the amount of RuO_2 formed from VUV/O_2 co-exposure is explored with XPS and is shown in Figure 5.2. We note that in separate experiments (not shown) no oxidation is detected when Ru was co-exposed at 50 °C. 8 nm Ru films are co-exposed to VUV and O_2 for 5, 10, and 15 min at 150 °C. The Ru 3*d*, Ru 3*p*, and O 1*s* spectral regions are shown in (a), (b), and (c), respectively. Two features are clear in the Ru 3*d* XP spectrum at 280.7, and 284.8 eV. Relative to the XP spectra of the

as-deposited Ru, there is an increase in peak area towards higher binding energies indicative of RuO_2, however, there is negligible difference between the 100 and 150 °C exposures. Similar to oxidation at 100 °C, there is minimal bulk RuO_2 formed as indicated by the asymmetric metallic character in the $3d_{5/2}$ and $3d_{3/2}$ XP features, as well as the Ru 3*p* XP region in Figure 5.2(b).

Deconvolution of the O 1*s* feature indicates the adsorbed oxygen species is present in all samples investigated, and is shown in the orange deconvolution peak. The area of the RuO_2 oxygen XP feature at 530.1 eV is approximately constant between 100 and 150 °C. We note that it appears less RuO_2 forms at 150 °C. The ratio of the areas of the RuO_2 features at 100, and 150 °C are 1.08, 1.05, and 1.14 at 5, 10, and 15 min, respectively. This is within the 5 – 10 % error that we have similarly observed on Pd.[19,20]

Atomic O, O_2, and O_3 are present in the gas phase when O_2 is subjected to VUV photons.[51,52] We have demonstrated that atomic O is responsible for oxidation when Pd metal is co-exposed to VUV/O_2 using two different sample configurations.[20] This point is similarly explored on 8 nm Ru with two different exposure configurations. In the first configuration, Ru is illuminated by the VUV lamp during O_2 exposure, and the second configuration Ru is shadowed from the VUV lamp by mounting the Ru sample face-down. In the first (illuminated) configuration, it is likely atomic O, O_2, and O_3 oxidant species are incident on the Ru surface, while O_2, and O_3 are likely incident on the Ru surface in the second (shadowed) configuration. The ratio of the lifetime of atomic O to O_3 is approximately[53,54] 2×10^{-6}, which suggests that atomic O is consumed in gas-gas and gas-surface interactions in the shadowed configuration before diffusing to and contacting the Ru surface, while atomic O is likely not consumed in the illuminated configuration.

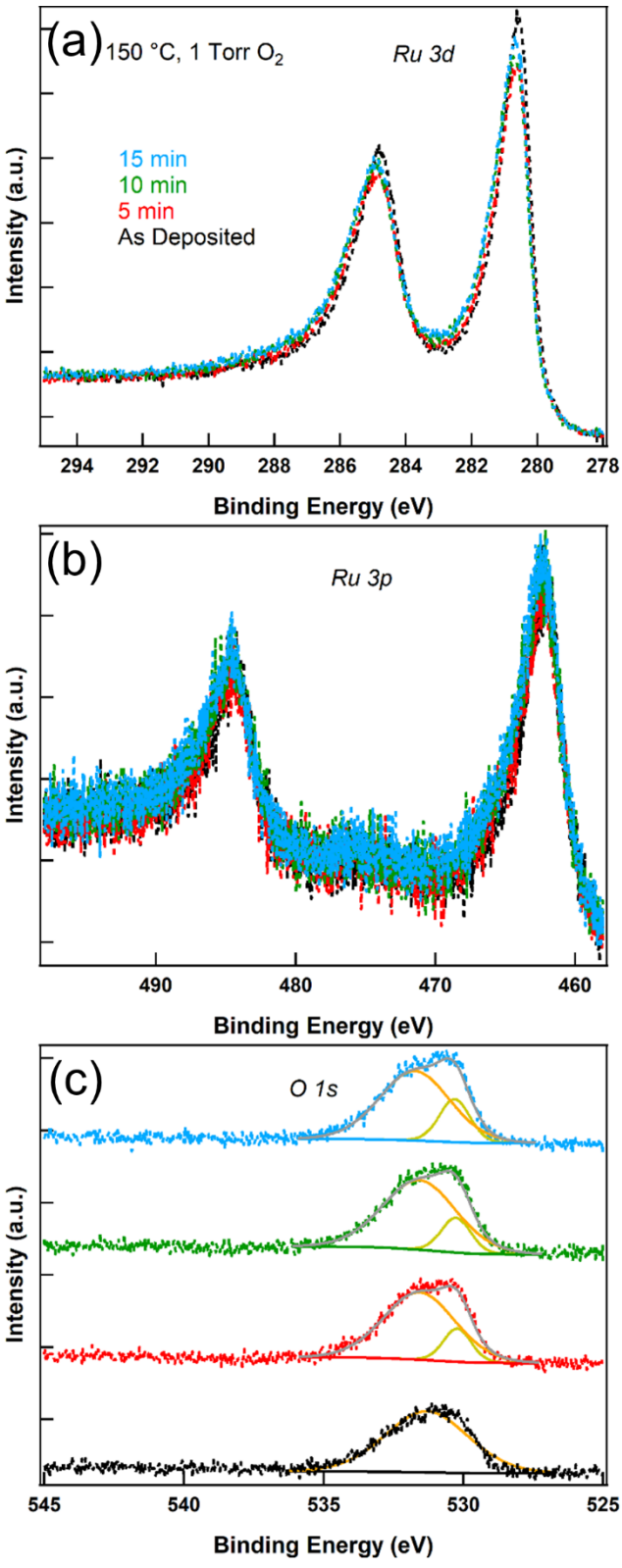
(a)
150 °C, 1 Torr O2
Ru 3d
15 min
10 min
5 min
As Deposited
Intensity (a.u.)
294
292
290
288
286
284
282
280
278
Binding Energy (eV)
(b)
Ru 3p
Intensity (a.u.)
490
480
470
460
Binding Energy (eV)
(c)
O 1s
Intensity (a.u.)
545
540
535
530
525
Binding Energy (eV)

Figure 5.2. XP Spectra of 8 nm Ru films are shown, where films are exposed to VUV/O_2 for 5, 10, and 15 min at 1 Torr O_2 at 150 °C. The Rd 3*d*, O 1*s*, and Ru 3*p* XP features are shown in (a), (b), and (c), respectively. Deconvolution of the O 1*s* XP feature is also shown, where adsorbed oxygen (531.5eV), and O^{2-} lattice oxygen arising from RuO_2 (530.1 eV) species are indicated in orange and yellow, respectively. The time of co-exposure to VUV/O_2 increases moving up the *y*-axis in (c).

Ru is co-exposed to VUV/O_2 in illuminated and shadowed configurations at 1 Torr O_2 for 5 min at 100 and 150 °C. XPS results are shown in Figure 5.3. The Ru 3*d* XP spectra in Figure 3(a) indicate that more RuO_2 is formed in illuminated configurations than shadowed configurations at 100, and 150 °C, which is revealed by the tail towards higher binding energy and reduction in feature intensity at 280.7, and 284.8 eV. Negligible difference is seen in the Ru 3*p* features at 100 or 150 °C, as seen in Figure 5.3(b). Increased RuO_2 formation is also evidenced by a larger O feature in the O 1*s* XP spectra, which is shown in Figure 5.3(c). RuO_2 features (i.e., peak at 530.1 eV in O 1*s*) are present for the illuminated configurations, while adsorbed molecular oxygen is the only statistically meaningful feature in shadowed samples. The results in Figure 5.3(c) indicate atomic O dominates the oxidation of Ru for conditions herein. This result is similar to oxidation of Pd where atomic O also dominates the oxidation reaction.[20]

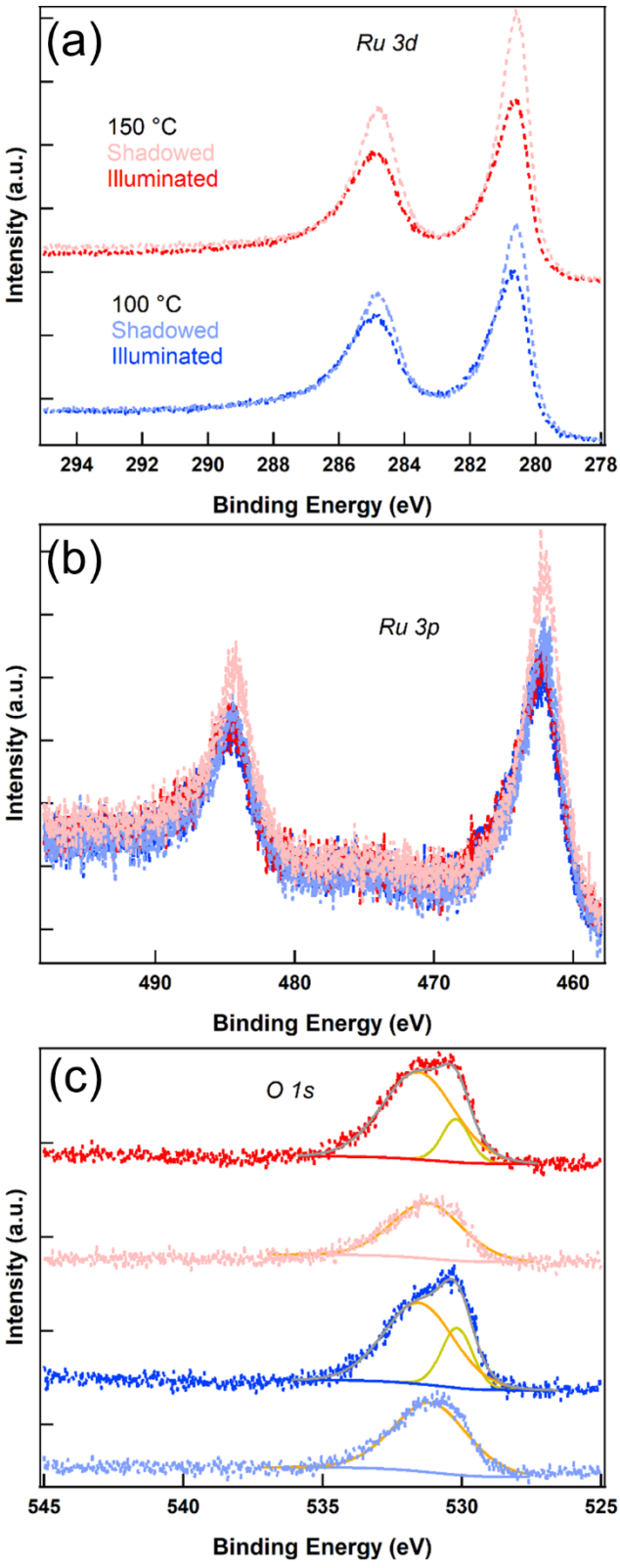
(a)
Ru 3d
150 °C
Shadowed
Illuminated
100 °C
Shadowed
Illuminated
Intensity (a.u.)
294
292
290
288
286
284
282
280
278
Binding Energy (eV)
(b)
Ru 3p
Intensity (a.u.)
490
480
470
460
Binding Energy (eV)
(c)
O 1s
Intensity (a.u.)
545
540
535
530
525
Binding Energy (eV)

Figure 5.3. XP spectra of 8 nm Ru films are shown, where films are exposed to VUV/O_2 for 5 min at 1 Torr O_2 at 100, and 150 °C, where the sample is illuminated or shadowed during VUV/O_2 co-exposure. The Rd 3*d*, Ru 3*p,* and O 1s feature are shown in (a), (b), and (c), respectively. Deconvolution of the O 1*s* feature is also shown, where adsorbed oxygen (531.5eV), and O^{2-} lattice oxygen arising from RuO_2 (530.1 eV) species are indicated in orange, and yellow, respectively. The set of 100 °C XP spectra are shown on the bottom of (a), and (c), while 150 °C XP spectra are on top. XP spectra are offset for comparison.

5.3.2. VUV ENHANCED ATOMIC LAYER ETCHING OF RU

ALE of Ru is explored by exposing 8 nm Ru thin films to an oxidation half-cycle consisting of 2 min VUV/O_2 co-exposure, followed by a 1.5 min Ar purge; and an etching half-cycle consisting of a 30 sec HCOOH exposure at 0.50 Torr, followed by a 2.5 min Ar purge. One oxidation half-cycle followed by one etching half-cycle constitutes one ALE cycle, and cycles are written in the text with the time in sec, (i.e., 120/90/30/150 for the cycle just described). XPS measurements show Ru metal and no RuO_2 following the HCOOH half-cycles (not shown). XRR of the films is shown before and after ALE cycles at 100 °C in Figure 5.4(a). XRR measurements of the Ru film before and after etching indicate a thickness change of 6, 13, and 14 ± 2 Å for 5, 10, and 15 ALE cycles, respectively. These results are presented in Figure 5.5. The slope of a line of best fit to the data at 100 °C is 0.85 ± 0.15 Å/cycle.

The XRR patterns in Figure 5.4(a) indicate all Ru surfaces are rougher as deposited compared to the surfaces after ALE is performed, which is evidenced by the lack of reflections in the range, $3° < 2\theta < 6°$ before etching, and clear reflections emerging after ALE is performed. This observation is consistent across all XRR patterns in Figure 5.4(a). 20 × 20 μm^2 atomic force (AF) micrographs of an as deposited Ru film, and Ru after 5,

and 15 ALE cycles are also shown beneath the XRR curves. The roughness, R_a, is 2.4, 0.4, and 1.0 Å, for samples as-deposited, after 5 ALE cycles, and 15 ALE cycles, respectively. We note that R_a of the as-deposited surfaces varies by 2 Å, however, the clarity in reflections in XRR curves improves for all samples. This implies that as ALE is performed, the surface roughness is reduced. This could possibly affect the oxidation rate during the oxidation half-cycle.

ALE is also performed at 150 °C with the same oxidation and etching half-cycles as described for 100 °C and the XRR and AF micrographs are shown in Figure 5.4(b). The change in thickness is 6, 12 and 16 ± 2 Å for 5, 10, and 15 ALE cycles, respectively. This results in an overall etch removal amount at 150 °C of 0.96 ± 0.15 Å/cycle (Figure 5.5). Again, the surface roughness is reduced, as evidenced by the quality of reflections in the range $3° < 2\theta < 6°$, which improve after ALE is performed. AF micrographs reveal R_a of Ru as-deposited, after 5 ALE cycles, and after 15 ALE cycles is 2.4, 1.6, and 1.2 Å, respectively, which also suggests a reduction in roughness with etching.

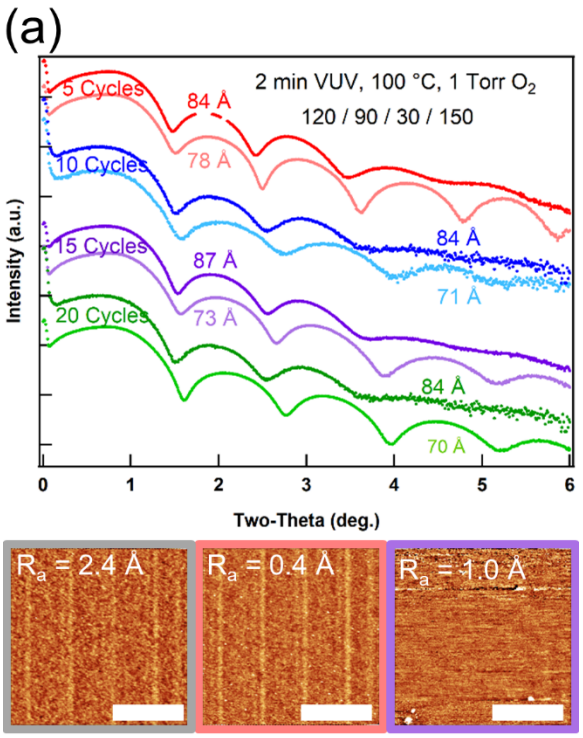
(a)
2 min VUV, 100 °C, 1 Torr O2
120 / 90 / 30 / 150
5 Cycles
84 Å
78 Å
10 Cycles
84 Å
71 Å
15 Cycles
87 Å
73 Å
20 Cycles
84 Å
70 Å
Intensity (a.u.)
Two-Theta (deg.)
Ra = 2.4 Å
Ra = 0.4 Å
Ra = 1.0 Å

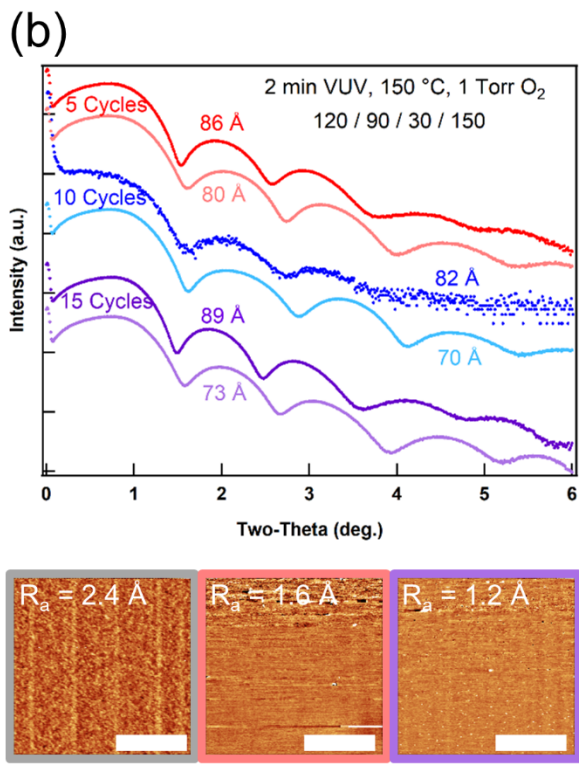
(b)
2 min VUV, 150 °C, 1 Torr O2
120 / 90 / 30 / 150
5 Cycles
86 Å
80 Å
10 Cycles
82 Å
70 Å
15 Cycles
89 Å
73 Å
Intensity (a.u.)
Two-Theta (deg.)
Ra = 2.4 Å
Ra = 1.6 Å
Ra = 1.2 Å

Figure 5.4. XRR and AF micrographs are shown for ALE cycles of 2 min VUV/O_2 co-exposure at 1 Torr O_2 followed by a 1.5 min Ar purge, followed by 30 sec of HCOOH vapor exposure at 0.50 Torr, followed by a 2.5 min Ar purge (120/90/30/150). XRR curves before and after 5, 10, and 15 ALE cycles at 100 °C are shown in (a), while XRR of films before and after 5, 10, and 15 cycles at 150 °C are shown in (b). For each set of XRR curves the top curve is the as-deposited film and the bottom curve is the film after the specified number of ALE cycles. The XXR set associated with 20 cycles in (a) corresponds to the 10 cycle-treated film, which is subjected to an additional 10 cycles. The thickness of each film is shown above each XRR curve in the same color. AF micrographs of the surface as-deposited and after 5, and 15 cycles are shown below each set of XRR curves, where the micrograph color border identifies which XRR curve is the same condition. All AF micrographs are 20 × 20 μm^2, and scale bars are 5 µm. The roughness of the AF micrograph is shown inset.

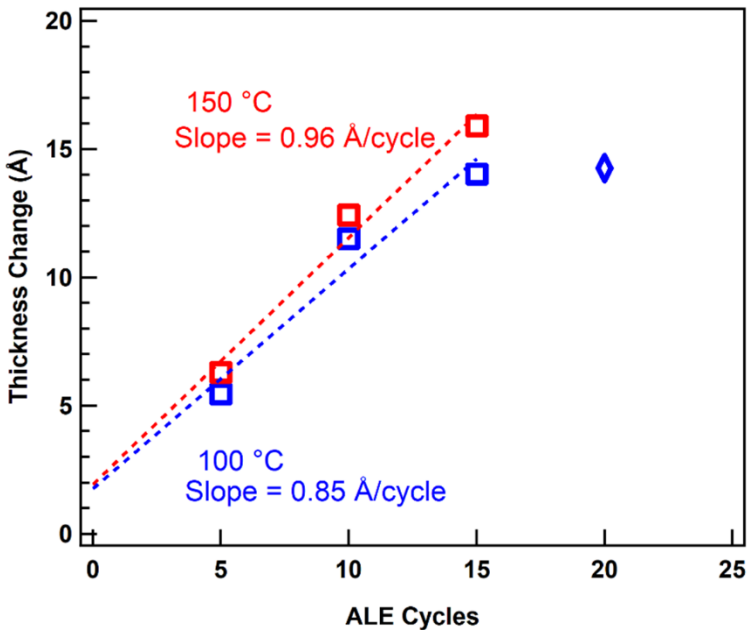

Figure 5.5. Change in thickness as determined by fits of XRR data are shown for 5, 10, and 15 ALE cycles (120/90/30/150) at 100 °C (blue), and 150 °C (red). The line of best fit for the each of the three data points is shown, where the slope of the line is indicated inset. The cumulative thickness change of a sample treated with 10 cycles (120/90/30/150, at 100 °C) and exposed to 10 additional cycles (20 cumulative ALE cycles) is shown with a diamond.

The thickness change between 10 cycles and 15 cycles at 100 °C is modest at 1 Å in comparison to 6 Å removed in the first 5 ALE cycles. Figure 5.4(a) also presents a set of XXR curves labeled 20 cycles. The 20 cycles indicated are cumulative, where the starting substrate is the sample treated with 10 cycles exposed to 10 additional cycles (i.e., 10 cycles + 10 additional cycles of 120/90/30/150). The cumulative amount of material removed is 14 Å and the incremental amount after the additional 10 ALE cycles is 1 Å. This cumulative thickness change for this sample is plotted using a diamond (◊) in Figure 5.5. The amount of Ru etched in the HCOOH half-cycle depends on the amount of RuO_2 formed in the VUV/O_2 half cycle. As previously noted, the roughness decreases with increasing numbers of ALE cycles, and we associate the reduced removal rate to a decreased rate of oxidation.

The VUV/O_2 exposure time was increased to test the hypothesis that oxidation rate slows as the roughness is reduced. The film presented in Figure 5.4(a) that is not etched after 20 cumulative ALE cycles (120/90/30/150) was exposed to 5 additional cycles (i.e., 25 cumulative cycles) using a longer oxidation half-cycle. The 5 additional cycles used 5 min VUV/O_2 co-exposures (300/90/30/150). XRR of the film after 5 additional cycles (25 cumulative ALE cycles) is shown in Figure 5.6. XRR of the samples with 10, and 20 cumulative cycles are reproduced for comparison. The cumulative amounts of Ru removed after 10, 20, and 25 cycles are 13, 14, and 19 ± 2 Å. Approximately 5 Å is removed after 5 additional 300/90/30/150 cycles, indicating the etch rate, and extent of oxidation is restored, consistent with the hypothesis that oxidation rate decreases as the film is subjected to ALE cycles.

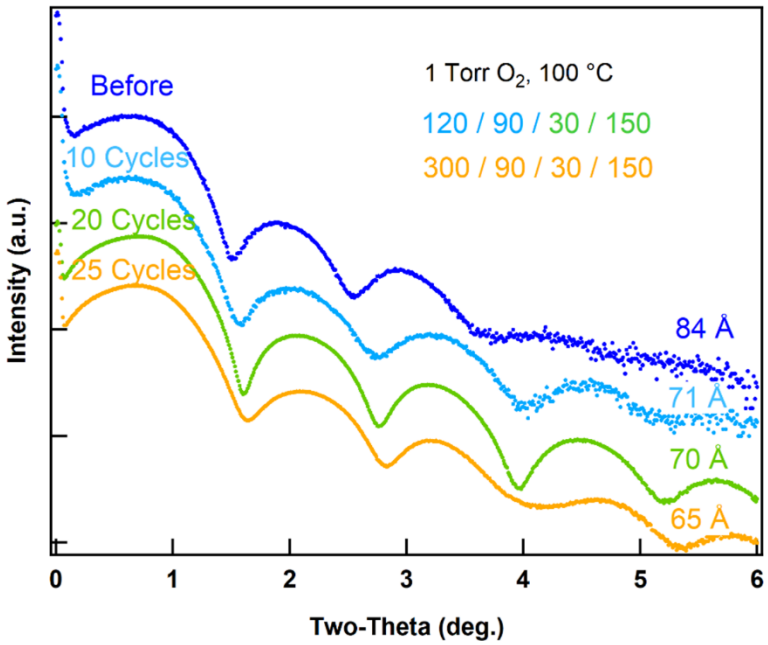

Figure 5.6. XRR of a single Ru film with 10, 20, and 25 cumulative ALE cycles at 100 °C. XRR of the Ru film before any treatment, after 10, and 20 ALE cycles (120/90/30/150) is shown. The same Ru film with 5 additional cycles (25 ALE cycles total) of a 5 min VUV/O_2 co-exposure (300/90/30/150) is also shown. The number of etch cycles increases moving down the *y*-axis. The thickness corresponding to each XRR curve is shown above each curve on the far right.

We note that etching arising from O_3 must be considered in co-exposures of VUV/O_2. Ozone has been shown to form RuO_4 at 100 – 150 °C and this forms the basis of a Ru etching process via RuO_4 sublimation.[17] The possibility that RuO_4 could have formed and contributed to the etching reported herein is explored by co-exposing Ru to VUV/O_2 at 1 Torr O_2, and 100 °C, for 30 min. Thirty min corresponds the equivalent VUV/O_2 exposure associated with 15 ALE cycles with 2 min VUV/O_2 oxidation half-cycles. XRR before and after exposure (not shown) indicate no change in Ru film thickness. The only detectable change, however, is a roughening of the surface, that is

indicated with lower quality reflections in the range $3° < 2\theta < 6°$. Roughening of the surface with co-exposure of VUV/O_2 is consistent with previous observations on Pd.[19] Additionally, ALE cycles without VUV photons (i.e., a thermal O_2 exposure at 100 °C, with 120/90/30/150 ALE cycles) result in no change in thickness (XRR not shown). This indicates ALE of Ru requires VUV/O_2 to proceed.

5.3.3. DFT Oxidant Adsorption Studies and NEB Calculations for O Diffusion

The experiments presented above illustrate that atomic O and O_3 that are incident on the Ru and oxidized Ru surfaces contribute to the formation of RuO_2 in the near surface region under VUV/O_2 exposure. There are numerous first principles studies of Ru, RuO_2, and oxygen interacting with Ru and RuO_2.[23–30] We employ DFT as well to investigate VUV-enhanced oxidation. The detailed DFT results are presented in Appendix G and are in agreement with the structural models and the energetics of atomic and molecular oxygen on Ru(101) and Ru(002). Table G.1 presents the structural results. Adsorption geometries are presented in Figure G.2 for atomic O and O_3 on (2×2) Ru(002) and Ru(101). Table G.2 presents adsorption energies predicted by DFT for O, O_2, and O_3 on (2×2) Ru(002) and Ru(101). The adsorption energy, E_{ads}, for atomic O adsorbing onto bare (101) and (002) surfaces is 5.63 eV and is 6.07 eV, respectively, which are in agreement with previous reports. Other DFT reports estimate adsorption of atomic O on Ru has an adsorption energy of 5.37 – 5.32 eV, and 5.15 – 5.26 eV on Ru(101) with 0.50, and 1.0 ML O coverage,[23,55] and 5.64–6.28 eV, and 5.52 – 5.43 eV, and 4.78 – 5.07 eV on Ru(002) with 0.25, 0.50, and 1.0 ML O coverage, respectively.[23,47,55,56]

Adsorption energetics and structures are also calculated for Ru slabs with O incorporated in between Ru atomic layers. Top and side views of the optimized O layered

Ru slabs are shown in Figure 5.7. Atomic O incorporation into Ru is performed by propagating an equivalent surface of 0.50 ML surface coverage to subsurface layers. This is done by optimizing O atom positions on the surface, noted to be one hcp site with an occupied fcc site adjacent for (002), and a "zig-zag" series of surface rows for (101) (denoted 1 O layer, Figure 5.7(a), and (b), for (002), and (101), respectively), which is consistent with other reports.[24,26,31] Atomic O is incorporated into the substrate Ru by keeping the same surface coverage, and propagating O atom positions in between the first and second Ru atomic layers (denoted 2 O layers, Figure 5.7(c), and (d), for (002), and (101), respectively), and between the first, second, and third, atomic Ru layers (denoted 3 O layers, Figure 5.7(e), and (f), for (002), and (101), respectively). Slabs with O layers are optimized, and following optimization, oxidants are adsorbed onto the surfaces.

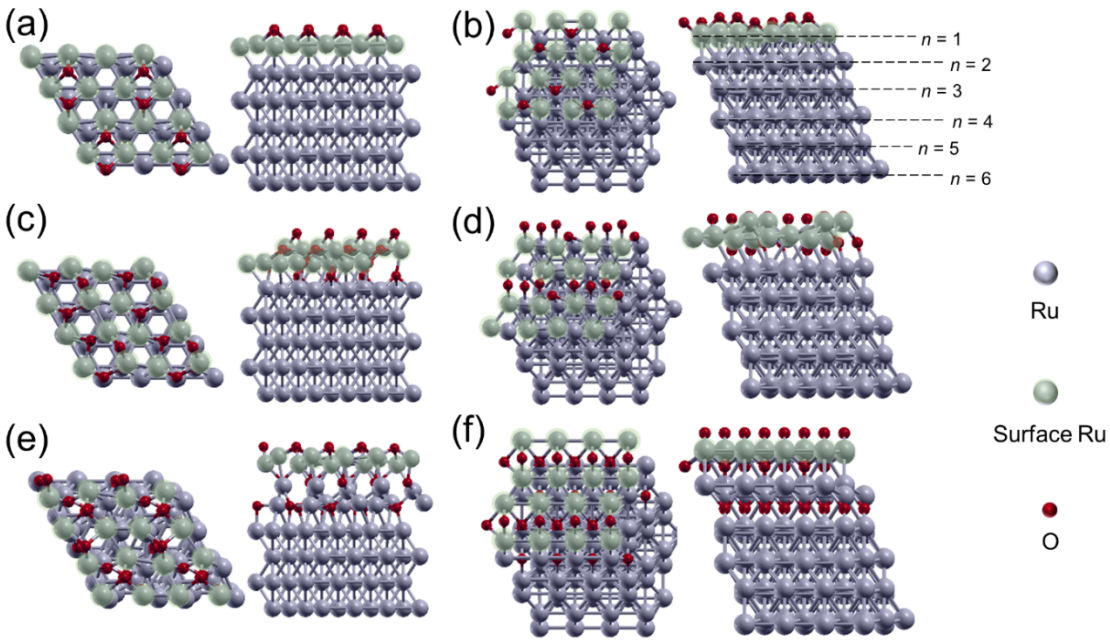

Figure 5.7. 1, 2, and 3, O layered structures are shown for (2 × 2) Ru(002) and Ru(101), and two copies of each unit cell in the *x* and *y* directions are also shown. Ru(002) and (101) slabs with 1 O layer are shown in (a), and (b), respectively. Ru(002), and Ru(101) slabs with 2 O layers are shown in (c), and (d), respectively. Ru(002), and Ru(101) slabs with 3 O layers are shown in (e), and (f), respectively. The top and side views of each structure are shown as well. Surface Ru atoms are light green circles, while O atoms are small red circles, and Ru metal atoms are silver circles. The layer number (i.e., n = 1, 2, 3… etc.) is also indicated in (b).

E_{ads} for O adsorbing onto the O layered structures is given in Table 5.1. E_{ads} for O_2, and O_3 adsorbing onto O layered structures is given in Appendix G Table G.3. E_{ads} for atomic O on Ru(002), and Ru(101) with 1 O layer is 5.32, and 5.04 eV, respectively, in line with previous reports.[23,47,55,56] This is a change of -0.75 eV, and -0.59 eV relative to bare (002), and (101). While adsorption is made less favorable by the presence of a 2D surface oxide, it is still exothermic. E_{ads} for atomic O does not monotonically decrease, however, as the trend in E_{ads} has a local minimum when 2 O layers are incorporated on Ru(002), and when 3 O layers are incorporated on Ru(101).

Table 5.1. DFT results of adsorbing O onto Ru(002), and Ru(101) are shown. The number of O layers is indicated for each Ru slab.

Species	*n* O layers	E_{ads} (eV)
Ru(002)/O	1	5.32
Ru(002)/O	2	4.23
Ru(002)/O	3	4.88
Ru(101)/O	1	5.04
Ru(101)/O	2	5.17
Ru(101)/O	3	4.49

Self-limiting behavior in the oxidation of Ru from co-exposure to VUV/O_2 is examined in more depth with the NEB method, where oxygen diffusion into a Ru surface with O incorporation is explored. NEB structures are first optimized and a "probe" O atom is placed on the surface for diffusion. The O atom is then propagated through the structures between the n = 1, and 2, layers, followed by the n = 2, and 3 layers, and finally between the n = 3, and n = 4 layers as indicated in Figure 5.7. All NEB diffusion studies, like O layered incorporation studies, are performed using Ru slabs consisting of six atomic layers. This is done to allow at least one atomic layer to relax in between the layers containing the O "probe" atom, and the layers representing the bulk Ru film. Ru(002) with 1 and 2 layers of O incorporation, as shown in Figure 5.7(a), and (c), are explored in the NEB calculation, as clean Ru is unlikely to be a relevant surface kinetically, as experiments, and simulations indicate.

The approximate minimum energy path (MEP) for Ru(002) with 1, and 2 O layers incorporated is shown in Figure 5.8 in red, and blue, respectively. For O diffusion through Ru(002) with 1 O layer on the surface, the activation energy, E_a, of O to move subsurface is 2.11 eV, and going from a subsurface location to the surface, E_a is 0.17 eV. This disparity indicates that diffusion subsurface is difficult, and requires a high O concentration on the surface to proceed. Diffusion through the n = 3, and 4 layers must overcome an overall barrier of 2.77 eV. As the trend in E_a indicates, continued O diffusion into Ru is challenging, becoming increasingly difficult for O moving past the second atomic layer of Ru. We note that for a stoichiometric RuO_2 to form from any oxidation process, Ru:O stoichiometry must be 1:2, which would correspond to a 2 O layered system in this illustration. It is also worthwhile to mention that atomic O has a calculated E_{ads} of 5.32 eV on Ru(002) with 1 O layer, which is slightly less than $|E_{max} - E_{min}|$, which is 5.46 eV. Overall, the barrier to begin to form surface RuO_2 is the activation E_a to move subsurface.

As E_a increases moving deeper into the substrate, further oxidation is not energetically favorable.

Atomic O diffusion through a 2 O layered structure is shown in Figure 5.8 as well. There is a large barrier to diffusion subsurface, E_a of 1.98 eV, which is slightly reduced compared to the 1 O layer diffusion diagram (-0.13 eV). O is at an energetic minimum when it resides in between the first and second atomic Ru layers. The calculated E_a to move subsurface is consistent with other reports of O diffusion through Ru(0001) of 1.80 ± 0.15 eV,[57] and 1.99 eV for O to move subsurface for 0.75 ML O coverage on an hcp Ru surface.[27] Continued diffusion past the second atomic Ru layer has an E_a of 5.10 eV, which we note, is larger than E_{ads} for O adsorbing onto a 2 O layered Ru(002) system (4.23 eV). Therefore, it is energetically favorable for O to remain between the n = 1, and 2 atomic Ru layers, which is consistent with the observation of self-limiting behavior from XPS, as well as ALE cycles. McCoy et al.[31] report a self-limiting oxidation of Ru from O generated by thermally cracking O_2 as well.

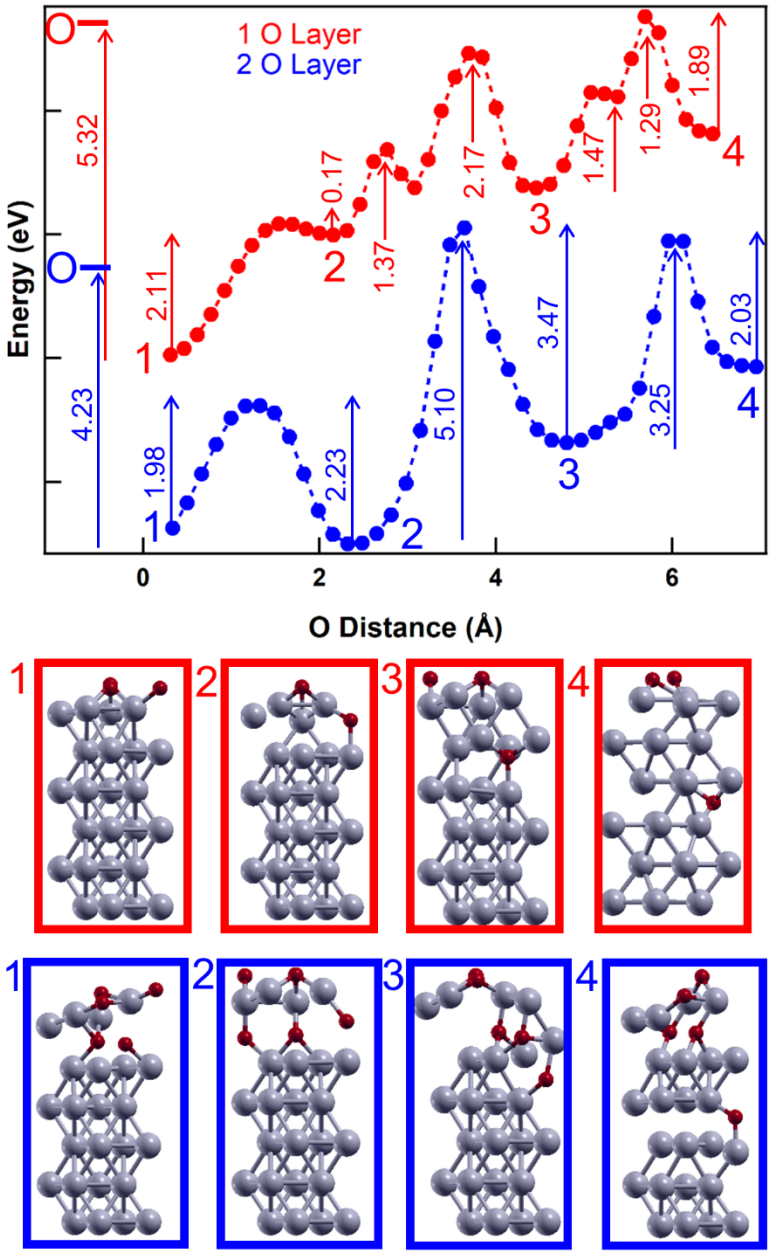
1 O Layer
2 O Layer
Energy (eV)
O Distance (Å)
5.32
4.23
2.11
0.17
1.37
2.17
1.47
1.29
1.89
1.98
2.23
5.10
3.47
3.25
2.03
1
2
3
4
0
2
4
6

Figure 5.8. Approximate MEP of Ru(002) with 1 and 2 O layers incorporated, shown in red, and blue, respectively. The activation energy for each energy maximum and minimum are shown in numbers next to arrows at the respective extrema, in text that corresponds to the color of the parent curve. The reaction coordinate is the O penetration depth, relative to the starting position that is optimized in separate calculations. Free atomic O is shown at the left of the curves for reference to adsorption energy calculations. Selected images from the NEB calculation are shown beneath the figure, where 1 O layer Ru structures are shown with red borders, and 2 O layer structures are shown with blue borders. Image labels are in the upper left next to each image, and also indicated on the MEP, where integers correspond to the E minima that are depicted in the selected images.

5.4. DISCUSSION

Chang and co-workers report,[21,22] HCOOH etching of oxidized Co, Fe, Ni, Pd, Pt metals. Our results show that HCOOH also works to etch oxidized Ru, RuO_2. The etching half cycle in a metal ALE process is relatively straightforward, however, the challenge in realizing metal ALE is to find a self-limiting oxidation processes. Through the application of VUV/O_2 at 100 to 150 °C we show that gas phase atomic O generated with a D_2 lamp produces a sufficient amount of adsorbed atomic O to drive the diffusion of this atomic O into Ru, which is in agreement with the findings of McCoy et al. over a similar temperature range.[31] We observe that atomic O is responsible for oxidation at the conditions explored herein, as shown in Figure 5.3. We also note that there is likely a competition between oxidation by atomic O and O_3 for Ru, as regimes of etch selectivity have been reported for controllable ratios of atomic O to O_3,[17] which suggests selectivity in oxidation may be achievable.

DFT is used to explore adsorption characteristics of oxidants onto Ru surfaces with increasing O content. Structures and energetics of oxidants adsorbing onto bare Ru(101), and Ru(002) are shown in Figure G.2, and Tables G.1, and G.2. Adsorption energetics for

atomic O adsorbing onto O layered Ru are presented in Table 5.1. Briefly, we find that adsorption, while still exothermic, is less favorable as more O is incorporated into the Ru slab. Atomic O adsorption is still exothermic, though there is a decrease in E_{ads} as more O is incorporated into the surface. This suggests that there is little to limit the amount of O that adsorbs onto the Ru surface, so that subsurface diffusion is likely the root of the self-limiting behavior observed in experimental studies. The NEB calculations (Figure 5.8) illustrate the energetic barrier for atomic oxygen to diffuse into the ruthenium is close to the E_{ads} of atomic O on the Ru surfaces studied in DFT (Tables 5.1, G.2, and G.3). Through a combination of substrate temperature and VUV/O_2 exposure time it is possible to realize Ru etch removal amounts of ~ 1 Å/cycle (Figure 5.5). It is this removal amount per cycle, and the self-limiting oxidation shown in Figures 1, and 2, that lead us to describe the work reported herein as an ALE process.

The oxidation rate is observed to decrease as ALE is performed, which indicates that oxidation, and etch amount, depend on the surface characteristics. We have shown the extent of Pd oxidation, and in turn the amount of Pd etched, using VUV/O_2 is greater for discontinuous Pd films than it is for void-free films.[19] The AFM and XRR results illustrate the Ru films are rougher at the outset and become smoother after treated with only 5 ALE cycles (Figure 4).

It is important to note that, while atomically smooth facets are used to understand adsorption characteristics in DFT and NEB calculations, it is not expected that this reflects the true mechanism of oxidation on Ru films owing to different diffusion pathways on the surface, and through the Ru film, and the existence of higher order facets on the surface. Higher order facets undoubtedly accompany the roughness of as deposited Ru thin films. As etching proceeds, the roughness, along with prevalence of higher order facets, is reduced. This has the effect of reducing the exposed surface area, and number of surface

configurations, available during oxidant adsorption, likely reducing the oxidation rate. We explore this by increasing the time of VUV/O_2 co-exposure during oxidation half-cycles for a 10 ALE cycle-treated substrate that is observed to experience minimal (i.e., 1 Å) etching with 10 additional ALE cycles (120/90/30/150). The film thickness is reduced after increasing the VUV/O_2 co-exposure time from 2 min to 5 min (i.e., ALE cycles of 300/90/30/150), suggesting that oxidation kinetics are a limiting factor in allowing ALE to proceed. The existence of higher order facets likely is responsible for the difference in oxidation kinetics on Ru.

5.5. CONCLUSIONS

VUV enhanced ALE of Ru metal is demonstrated. ALE is accomplished with a half-cycle that oxidizes near surface Ru in a self-limiting manner, followed by a half-cycle that etches oxidized Ru metal. Oxidation half-cycles consist of co-exposure of VUV/O_2 for 2 min at 1 Torr O_2, while etching half-cycles consist of exposure to HCOOH vapor at 0.50 Torr for 30 sec. Ar is used to purge the reactor between oxidation and etching half-cycles for 1.5, and 2.5 min, respectively. This yields controllable oxidation of the Ru, and yields an etch rate that decreases with ALE cycles if co-exposure time is held constant. The differential removal amount for 5 cycles (i.e., material removed between 0 and 5 cycles) at 100, and 150 °C is 1.10, and 1.20 Å/cycle, respectively, indicating a slight increase in etch rate with temperature. DFT results suggest that all oxidants (O, O_2, and O_3) adsorb strongly to the bare Ru surface, and equilibrate at a surface coverage between 0.50 and 0.75 ML O. Subsurface O diffusion is probed using the NEB method, which demonstrates a large activation energy, E_a, barrier to diffusion for an O atom to move beneath the subsurface layers (i.e., beyond n = 2 atomic layers of Ru). These findings suggest self-limiting

behavior is due to the inability of the RuO_2 front to propagate through bulk Ru. We use this reasoning to suggest that the decrease in etch rate as ALE is performed is likely due to a slowing oxidation rate, which tend towards self-limiting behavior with longer VUV/O_2 co-exposure times. This hypothesis is substantiated using a Ru sample exposed to 10 additional ALE cycles with 2 min VUV/O_2 oxidation half-cycles, which is observed to be only minimally etched. The same film is then exposed to 5 ALE cycles with 5 min VUV/O_2 oxidation half-cycles. This increased time of oxidation half-cycles restores the etch rate that is observed for few ALE cycles.

5.6. REFERENCES

(1) Rajkumar, C.; Thirumalraj, B.; Chen, S.-M.; Veerakumar, P.; Liu, S.-B. Ruthenium Nanoparticles Decorated Tungsten Oxide as a Bifunctional Catalyst for Electrocatalytic and Catalytic Applications. *ACS Appl. Mater. Interfaces* **2017**, *9* (37), 31794–31805.

(2) Bianchi, C. L.; Ragaini, V.; Cattania, M. G. An XPS Study on Ruthenium Compounds and Catalysts. *Mater. Chem. Phys.* **1991**, *29* (1), 297–306.

(3) Naota, T.; Takaya, H.; Murahashi, S.-I. Ruthenium-Catalyzed Reactions for Organic Synthesis. *Chem. Rev.* **1998**, *98* (7), 2599–2660.

(4) Popovici, M.; Groven, B.; Marcoen¶, K.; Phung, Q. M.; Dutta, S.; Swerts, J.; Meersschaut, J.; van den Berg, J. A.; Franquet, A.; Moussa, A.; Vanstreels, K.; Lagrain, P.; Bender, H.; Jurczak¶, M.; Van Elshocht, S.; Delabie, A.; Adelmann, C. Atomic Layer Deposition of Ruthenium Thin Films from (Ethylbenzyl) (1-Ethyl-1,4-Cyclohexadienyl) Ru: Process Characteristics, Surface Chemistry, and Film Properties. *Chem. Mater.* **2017**, *29* (11), 4654–4666.

(5) Wen, L. G.; Roussel, P.; Pedreira, O. V.; Briggs, B.; Groven, B.; Dutta, S.; Popovici, M. I.; Heylen, N.; Ciofi, I.; Vanstreels, K.; Østerberg, F. W.; Hansen, O.; Petersen, D. H.; Opsomer, K.; Detavernie, C.; Wilson, C. J.; Elshocht, S. V.; Croes, K.; Bömmels, J.; Tőkei, Z.; Adelmann, C. Atomic Layer Deposition of Ruthenium with TiN Interface for Sub-10 Nm Advanced Interconnects beyond Copper. *ACS Appl. Mater. Interfaces* **2016**, *8* (39), 26119–26125.

(6) Kim, S. K.; Popovici, M. Future of Dynamic Random-Access Memory as Main Memory. *MRS Bull.* **2018**, *43* (5), 334–339.

(7) Schaekers, M.; Capon, B.; Detavernier, C.; Blasco, N. The Deposition of Ru and RuO_2 Films for DRAM Electrode. *ECS Trans.* **2010**, *33* (2), 135.

(8) Popovici, M.; Swerts, J.; Redolfi, A.; Kaczer, B.; Aoulaiche, M.; Radu, I.; Clima, S.; Everaert, J.-L.; Van Elshocht, S.; Jurczak, M. Low Leakage Ru-Strontium Titanate-Ru Metal-Insulator-Metal Capacitors for Sub-20 Nm Technology Node in Dynamic Random Access Memory. *Appl. Phys. Lett.* **2014**, *104* (8), 082908.

(9) Kim, S. K.; Kim, W.-D.; Kim, K.-M.; Hwang, C. S.; Jeong, J. High Dielectric Constant TiO2 Thin Films on a Ru Electrode Grown at 250 °C by Atomic-Layer Deposition. *Appl. Phys. Lett.* **2004**, *85* (18), 4112–4114.

(10) Kwon, O. J.; Cha, S. H.; Kim, J. J. Ruthenium Bottom Electrode Prepared by Electroplating for a High Density DRAM Capacitor. *J. Electrochem. Soc.* **2004**, *151* (2), C127.

(11) Suh, Y.-S.; Lazar, H.; Chen, B.; Lee, J.-H.; Misra, V. Electrical Characteristics of HfO_2 Dielectrics with Ru Metal Gate Electrodes. *J. Electrochem. Soc.* **2005**, *152* (9), F138.

(12) Misra, V.; Huicai Zhong; Lazar, H. Electrical Properties of Ru-Based Alloy Gate Electrodes for Dual Metal Gate Si-CMOS. *IEEE Electron Device Lett.* **2002**, *23* (6), 354–356.

(13) Jelenkovic, E. V.; Tong, K. Y. Thermally Grown Ruthenium Oxide Thin Films. *J. Vac. Sci. Technol. B Microelectron. Nanometer Struct. Process. Meas. Phenom.* **2004**, *22* (5), 2319–2325.

(14) Hwang, S. M.; Garay, A. A.; Lee, W. I.; Chung, C. W. High Density Plasma Reactive Ion Etching of Ru Thin Films Using Non-Corrosive Gas Mixture. *Thin Solid Films* **2015**, *587*, 28–33.

(15) Pan, W.; Desu, S. B. Reactive Ion Etching of RuO_2 Thin Films Using the Gas Mixture O_2/CF_3CFH_2. *J. Vac. Sci. Technol. B Microelectron. Nanometer Struct. Process. Meas. Phenom.* **1994**, *12* (6), 3208–3213.

(16) Gu, X.; Kikuchi, Y.; Nozawa, T.; Samukawa, S. A New Metallic Complex Reaction Etching for Transition Metals by a Low-Temperature Neutral Beam Process. *J. Phys. Appl. Phys.* **2014**, *47* (32), 322002.

(17) Nakahara, M.; Tsunekawa, S.; Watanabe, K.; Arai, T.; Yunogami, T.; Kuroki, K. Etching Technique for Ruthenium with a High Etch Rate and High Selectivity Using Ozone Gas. *J. Vac. Sci. Technol. B Microelectron. Nanometer Struct. Process. Meas. Phenom.* **2001**, *19* (6), 2133–2136.

(18) Gong, Y.; Akolkar, R. Electrochemical Atomic Layer Etching of Ruthenium. *J. Electrochem. Soc.* **2020**, *167* (6), 062510.

(19) Coffey, B. M.; Nallan, H. C.; Engstrom, J. R.; Lam, C. H.; Ekerdt, J. G. Vacuum Ultraviolet Enhanced Oxidation - A Route to the Atomic Layer Etching of Palladium Metal. *Chem. Mater.* **2020**, *32* (14), 6035–6042.

(20) Coffey, B. M.; Nallan, H. C.; Engstrom, J. R.; Ekerdt, J. G. Vacuum Ultraviolet Enhanced Oxidation Mechanism for Pd - Near Surface Oxidation for Atomic Layer Etching. *ACS Appl. Mater. Interfaces* **2020**, *Accepted*.

(21) Chen, J. K.-C.; Altieri, N. D.; Kim, T.; Chen, E.; Lill, T.; Shen, M.; Chang, J. P. Directional Etch of Magnetic and Noble Metals. II. Organic Chemical Vapor Etch. *J. Vac. Sci. Technol. Vac. Surf. Films* **2017**, *35* (5), 05C305.

(22) Sang, X.; Chen, E.; Chang, J. P. Patterning Nickel for Extreme Ultraviolet Lithography Mask Application I. Atomic Layer Etch Processing. *J. Vac. Sci. Technol. A* **2020**, *38* (4), 042603.

(23) Schwegmann, S.; Seitsonen, A. P.; De Renzi, V.; Dietrich, H.; Bludau, H.; Gierer, M.; Over, H.; Jacobi, K.; Scheffler, M.; Ertl, G. Oxygen Adsorption on the Ru(10$\bar{1}$0) Surface: Anomalous Coverage Dependence. *Phys. Rev. B* **1998**, *57* (24), 15487–15495.

(24) Baraldi, A.; Lizzit, S.; Paolucci, G. Identification of Atomic Adsorption Site by Means of High-Resolution Photoemission Surface Core-Level Shift: Oxygen on Ru(10$\bar{1}$0). *Surf. Sci.* **2000**, *457* (1), L354–L360.

(25) Zhang, H. J.; Lu, B.; Li, H. Y.; Bao, S. N.; He, P. Scanning Tunneling Microscopy and Ultraviolet Photoemission Spectroscopy Studies of Oxygen Adsorption on Ru(10$\bar{1}$0). *Surf. Sci.* **2004**, *556* (1), 63–68.

(26) Zhang, H. J.; Lu, B.; Lu, Y. H.; Xu, Y. F.; Li, H. Y.; Bao, S. N.; He, P. Growth of RuO_2 Thin Layer on Ru(10$\bar{1}$0) Studied by Scanning Tunneling Microscopy. *Surf. Sci.* **2007**, *601* (11), 2297–2301.

(27) Cai, J.-Q.; Luo, H.-J.; Tao, X.-M.; Tan, M.-Q. Initial Subsurface Incorporation of Oxygen into Ru(0001): A Density Functional Theory Study. *Chem Phys Chem* **2015**, *16* (18), 3937–3948.

(28) Stampfl, C.; Scheffler, M. Theoretical Study of O Adlayers on Ru(0001). *Phys. Rev. B* **1996**, *54* (4), 2868–2872.

(29) Scheffler, M.; Stampfl, C. Theory of Adsorption on Metal Substrates. In *Handbook of Surface Science*; 2000; Vol. 2, pp 285–357.

(30) Yakovkin, I. N. Hydrogen-Induced Mitigation of O on Ru(100): A Density-Functional Study. *Phys. Chem. Chem. Phys.* **2009**, *11* (27), 5695–5702.

(31) McCoy, A. P.; Bogan, J.; Brady, A.; Hughes, G. Oxidation of Ruthenium Thin Films Using Atomic Oxygen. *Thin Solid Films* **2015**, *597*, 112–116.

(32) Chan, H. Y. H.; Takoudis, C. G.; Weaver, M. J. High-Pressure Oxidation of Ruthenium as Probed by Surface-Enhanced Raman and X-Ray Photoelectron Spectroscopies. *J. Catal.* **1997**, *172* (2), 336–345.

(33) Herd, B.; Goritzka, J. C.; Over, H. Room Temperature Oxidation of Ruthenium. *J. Phys. Chem. C* **2013**, *117* (29), 15148–15154.

(34) Björck, M.; Andersson, G. GenX: An Extensible X-Ray Reflectivity Refinement Program Utilizing Differential Evolution. *J. Appl. Crystallogr.* **2007**, *40* (6), 1174–1178.

(35) Giannozzi, P.; Baroni, S.; Bonini, N.; Calandra, M.; Car, R.; Cavazzoni, C.; Ceresoli, D.; Chiarotti, G. L.; Cococcioni, M.; Dabo, I.; Corso, A. D.; Gironcoli, S. de; Fabris, S.; Fratesi, G.; Gebauer, R.; Gerstmann, U.; Gougoussis, C.; Kokalj, A.; Lazzeri, M.; Martin-Samos, L.; Marzari, N.; Mauri, F.; Mazzarello, R.; Paolini, S.; Pasquarello, A.; Paulatto, L.; Sbraccia, C.; Scandolo, S.; Sclauzero, G.; Seitsonen, A. P.; Smogunov, A.; Umari, P.; Wentzcovitch, R. M. QUANTUM ESPRESSO: A Modular and Open-Source Software Project for Quantum Simulations of Materials. *J. Phys. Condens. Matter* **2009**, *21* (39), 395502.

(36) Giannozzi, P.; Andreussi, O.; Brumme, T.; Bunau, O.; Nardelli, M. B.; Calandra, M.; Car, R.; Cavazzoni, C.; Ceresoli, D.; Cococcioni, M.; Colonna, N.; Carnimeo, I.; Corso, A. D.; Gironcoli, S. de; Delugas, P.; DiStasio, R. A.; Ferretti, A.; Floris, A.; Fratesi, G.; Fugallo, G.; Gebauer, R.; Gerstmann, U.; Giustino, F.; Gorni, T.; Jia, J.; Kawamura, M.; Ko, H.-Y.; Kokalj, A.; Küçükbenli, E.; Lazzeri, M.; Marsili, M.; Marzari, N.; Mauri, F.; Nguyen, N. L.; Nguyen, H.-V.; Otero-de-la-Roza, A.; Paulatto, L.; Poncé, S.; Rocca, D.; Sabatini, R.; Santra, B.; Schlipf, M.; Seitsonen, A. P.; Smogunov, A.; Timrov, I.; Thonhauser, T.; Umari, P.; Vast, N.; Wu, X.; Baroni, S. Advanced Capabilities for Materials Modelling with Quantum ESPRESSO. *J. Phys. Condens. Matter* **2017**, *29* (46), 465901.

(37) Perdew, J. P.; Burke, K.; Ernzerhof, M. Generalized Gradient Approximation Made Simple. *Phys. Rev. Lett.* **1996**, *77* (18), 3865–3868.

(38) Perdew, J. P.; Burke, K.; Ernzerhof, M. Generalized Gradient Approximation Made Simple. *Phys. Rev. Lett.* **1997**, *78* (7), 1396–1396.

(39) Grimme, S.; Antony, J.; Ehrlich, S.; Krieg, H. A Consistent and Accurate Ab Initio Parametrization of Density Functional Dispersion Correction (DFT-D) for the 94 Elements H-Pu. *J. Chem. Phys.* **2010**, *132* (15), 154104.

(40) Grimme, S.; Ehrlich, S.; Goerigk, L. Effect of the Damping Function in Dispersion Corrected Density Functional Theory. *J. Comput. Chem.* **2011**, *32* (7), 1456–1465.

(41) Marzari, N.; Vanderbilt, D.; De Vita, A.; Payne, M. C. Thermal Contraction and Disordering of the Al(110) Surface. *Phys. Rev. Lett.* **1999**, *82* (16), 3296–3299.

(42) Song, C.; Sakata, O.; Kumara, L. S. R.; Kohara, S.; Yang, A.; Kusada, K.; Kobayashi, H.; Kitagawa, H. Size Dependence of Structural Parameters in Fcc and Hcp Ru Nanoparticles, Revealed by Rietveld Refinement Analysis of High-Energy X-Ray Diffraction Data. *Sci. Rep.* **2016**, *6* (1), 31400.

(43) Henkelman, G.; Uberuaga, B. P.; Jónsson, H. A Climbing Image Nudged Elastic Band Method for Finding Saddle Points and Minimum Energy Paths. *J. Chem. Phys.* **2000**, *113* (22), 9901–9904.

(44) Kokalj, A. XCrySDen—a New Program for Displaying Crystalline Structures and Electron Densities. *J. Mol. Graph. Model.* **1999**, *17* (3), 176–179.

(45) Taniguchi, N.; Takahashi, K.; Matsumi, Y.; Dylewski, S. M.; Geiser, J. D.; Houston, P. L. Determination of the Heat of Formation of O_3 Using Vacuum Ultraviolet Laser-Induced Fluorescence Spectroscopy and Two-Dimensional Product Imaging Techniques. *J. Chem. Phys.* **1999**, *111* (14), 6350–6355.

(46) Moulder, J. F.; Stickle, W. F.; Sobol, P. E.; Bomben, K. D. *Handbook of X-Ray Photoelectron Spectroscopy*; Chastain, J., Ed.; Perkin-Elmer: Eden Prarie, Minnesota, 1992.

(47) Kim, Y. D.; Seitsonen, A. P.; Wendt, S.; Wang, J.; Fan, C.; Jacobi, K.; Over, H.; Ertl, G. Characterization of Various Oxygen Species on an Oxide Surface: RuO_2(110). *J. Phys. Chem. B* **2001**, *105* (18), 3752–3758.

(48) Morgan, D. J. Resolving Ruthenium: XPS Studies of Common Ruthenium Materials. *Surf. Interface Anal.* **2015**, *47* (11), 1072–1079.

(49) Shen, J. Y.; Adnot, A.; Kaliaguine, S. An ESCA Study of the Interaction of Oxygen with the Surface of Ruthenium. *Appl. Surf. Sci.* **1991**, *51* (1), 47–60.

(50) Ananth, A.; Gandhi, M. S.; Mok, Y. S. A Dielectric Barrier Discharge (DBD) Plasma Reactor: An Efficient Tool to Prepare Novel RuO_2 nanorods. *J. Phys. Appl. Phys.* **2013**, *46* (15), 155202.

(51) Slanger, T. G.; Cosby, P. C. Oxygen Spectroscopy below 5.1 EV. *J. Phys. Chem.* **1988**, *92* (2), 267–282.

(52) Huffman, R. E. Absorption Cross-Sections of Atmospheric Gases for Use in Aeronomy. *Can. J. Chem.* **1969**, *47* (10), 1823–1834.

(53) Bakhtchadjian, R. *Bimodal Oxidation: Coupling of Heterogeneous and Homogeneous Reactions*; CRC Press, 2019.

(54) Dessler, A. *Chemistry and Physics of Stratospheric Ozone*; Elsevier, 2000.

(55) Petrova, N. V.; Yakovkin, I. N. Binding Energies for Oxygen on Transition Metal Surfaces. *Surf. Rev. Lett.* **2012**.

(56) Materzanini, G.; Tantardini, G. F.; Lindan, P. J. D.; Saalfrank, P. Water Adsorption at Metal Surfaces: A First-Principles Study of the p($\sqrt{3}\times\sqrt{3}$) R30° H_2O Bilayer on Ru(0001). *Phys. Rev. B* **2005**, *71* (15), 155414.

(57) Bonn, M.; Funk, S.; Hess, C.; Denzler, D. N.; Stampfl, C.; Scheffler, M.; Wolf, M.; Ertl, G. Phonon- Versus Electron-Mediated Desorption and Oxidation of CO on Ru(0001). *Science* **1999**, *285* (5430), 1042–1045.

Chapter 6: Area Selective Atomic Layer Deposition of $BaTiO_3$ for Photonic Devices

Contents for this chapter are published as: B. M. Coffey, E. L. Lin, P. Y. Chen, J. G. Ekerdt, Area-Selective Atomic Layer Deposition of Crystalline $BaTiO_3$. Chemistry of Materials, 2019, 31, 5558-5565.

Supporting information is found in Appendix H.

6.1. Introduction

Epitaxial crystalline oxides have received interest for their ferroelectricity, piezoelectricity, high permittivity, electro-optic effect, and ferromagnetism.[1–10] Of particular interest are $BaTiO_3$ (BTO),[1] $SrTiO_3$ (STO),[4,11] and $Ba_xSr_{(1-x)}TiO_3$.[12] BTO has received attention due to its potential applications in ferroelectric field effect transistors,[13–16] negative-capacitance devices,[17] and nanophotonic devices.[18–20] Devices using crystalline perovskites such as BTO require patterning and monolithic integration with semiconducting substrates. BTO patterns have been defined using sacrificial SiO_2 lift-off procedures,[14] or Cl etching.[15] However, build-up of Ti-containing etch products on the surface,[21,22] and decreasing nanofeature dimensions, make monolithic integration of patterned perovskites difficult using existing techniques. A potential solution to the challenges in defining crystalline BTO patterns is bottom-up area-selective (AS) patterning.

Typically, BTO is deposited using pulsed laser deposition,[7] chemical vapor deposition,[23] molecular beam epitaxy (MBE),[24] RF Sputtering,[25] or atomic layer deposition

(ALD),[1,2] however, ALD is the most amenable to AS patterning in next generation device fabrication. ALD is a well-known self-limiting, low temperature, conformal deposition technique, which offers precise thickness control over nanofeature dimensions via chemical surface reactions. Additionally, low temperature ALD growth of BTO makes it compatible with organic blocking layers that may be thermally sensitive. Area selectivity has been accomplished by locally catalyzing surface reactions,[26] or using tone reversal methods involving sacrificial amorphous carbon structures.[27] Area selectivity can also be accomplished by changing surface reactivity with methods such as hydrogen depassivation lithography,[28] or thermochemical surface modification of PMMA as a resist layer,[29] where modification of the PMMA resist layer restricts surface adsorption by defining hydrophobic organic regions. Controlling adsorption of precursors with hydrophobicity is amenable to BTO ALD, as AS-ALD on oxygen-rich hydrophilic surfaces is well known.[2,30,31] AS-ALD can be performed using self-assembled monolayers,[32,33] directed self-assembly of di-block copolymers,[34,35] photolithographic exposure of polystyrene (PS),[36] and electron beam induced deposition.[37] While these techniques have been shown to enable AS-ALD, we are unaware of any report on AS-ALD growth of films leading to a single crystal layer, such as epitaxial BTO.

Depositing epitaxial films on surfaces with a process history is a major challenge, as growth of functional perovskite films and epitaxy are sensitive to the deposition surface. Furthermore, patterning for AS-ALD is typically implemented by subjecting the surface to chemical treatments. As a result, it is important to understand if the patterning process

alters the surface cleanliness, and if there is any effect on deposition. We find ALD of BTO is generally amorphous as-grown if the substrate is not a pristine template layer prepared in ultra-high vacuum.[1,2] Subsequent crystallization of the perovskite film requires epitaxy, using the substrate as a crystalline template. To the extent epitaxy is dependent on the quality of the interface, it is important to understand if the interface quality is retained throughout the AS process.

Herein we explore the effect of surface treatment in the AS-ALD of crystalline BTO. ALD of BTO is investigated after subjecting a crystalline STO(001) surface to PS deposition and removal. Subsequent crystallization behavior is also probed. BTO crystallizes after using photolithographic exposure of PS and solvent-based removal of uncrosslinked PS to define the active area. STO(001) is used for epitaxial crystallization in this demonstration for convenience and similarity between prior demonstrations that showed monolithic integration of BTO onto Si(001) using a ~2 nm-thick STO template layer.[2,38] AS-ALD is shown to be a promising technique to enable epitaxial structures with potential uses in a variety of photonic devices.

6.2. Experimental Methods

A 2 wt% PS solution was made by mixing propylene glycol monomethyl ether acetate with polystyrene (Sigma-Aldrich, 200,000 Da). 10 × 10 mm^2 STO(001) single crystal substrates (MTI corporation) were cleaned by sonicating for 10 min in acetone (99%, Fisher Scientific), followed by 2-propanol (99%, Fisher Scientific), and finally with 18.2 MΩ·cm water (Millipore). STO(001) substrates were then placed in a UV-ozone

generator, which produces light at 185 nm and 254 nm, (Novascan PSD Digital UV Ozone System) for 15 min. Substrates were subsequently placed on a spin coating system (Smart Coater 100, Weinview), had the 2 wt% PS solution pipetted onto the surface, and spun for 1 min at 2000 rpm. Substrates were immediately placed on a heated surface at 100 °C to allow the propylene glycol monomethyl ether acetate to evaporate. This produced PS films that were 45 nm thick.

Crosslinking of the PS was performed in a UV-ozone generator, where N_2 (Airgas, 99.999%) was used to continually purge the system of oxygen. Following the procedure in Ref. 39, the shadow mask was placed on top of the substrate before purging. The shadow mask was a SiO_2 mask that consisted of a grid of squares that decreased in size from 250 μm to 50 μm. The UV-exposure enclosure was purged with N_2 for 30 min before the UV lamp ($\lambda < 254$ nm) was turned on. The exposed PS was crosslinked during UV exposure, while the PS beneath the shadow mask was left uncrosslinked. Uncrosslinked PS was removed by rinsing with toluene (99%, Fisher Scientific) for 1 min. The complete process of PS deposition, ALD of BTO, removal of PS, and crystallization of BTO can be seen in Figure 7.1.

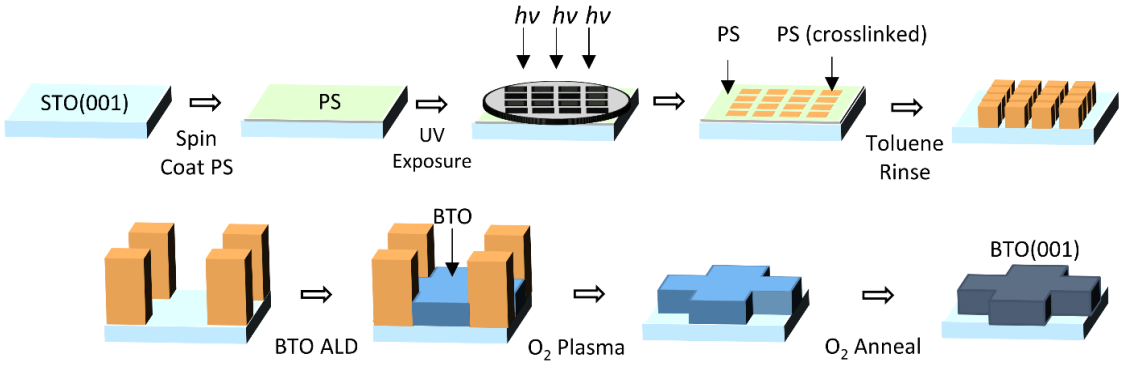

Figure 6.1. The process flow for creating patterned PS and subsequent BTO ALD. PS is spun onto the STO(001) surface. A shadow mask is then placed on top of the PS layer, which blocks areas of the surface from UV exposure ($\lambda < 254$ nm). The areas of the PS layer that are exposed to UV light are crosslinked, while the areas beneath the shadow mask are uncrosslinked. Toluene is used to remove the uncrosslinked PS, which exposes the STO(001) surface. BTO ALD then takes place, and grows on the exposed substrate. After ALD growth, crosslinked PS is removed using an O_2 plasma. Finally, surface crystalline order is monitored with RHEED, and the substrate is annealed to 50 °C above the temperature at which crystallization is observed. Crystallization is performed in an O_2 atmosphere of 1×10^{-6} Torr.

BTO growth, X-ray photoelectron spectroscopy (XPS) analysis, and reflective high energy electron diffraction (RHEED) analysis take place in a system comprised of a custom-built ALD reactor connected via a UHV transfer line. A more detailed description can be found elsewhere.[1,4,40] The ALD reactor is a stainless steel chamber operating at a background pressure of ~1 Torr during deposition. Ar is used as both carrier and purge gas in the ALD chamber. The precursors are vaporized thermally and introduced into the ALD reactor via a gas manifold. ALD growth of BTO has been reported previously.[2,41,42] Barium bis(triisopropylcyclopentadienyl) [$Ba(^{i}Pr_3Cp)_2$], and titanium tetraisopropoxide[$(Ti(O\text{-}^{i}Pr)_4$] (TTIP) were used as the Ba and Ti precursors, respectively, while deionized water was used as the oxidant. The Ba and Ti precursors were kept at 150 °C, and 37 °C,

respectively, while deionized water was kept at room temperature. The number of unit cycles for each element is adjusted to obtain a near-stoichiometric composition (*i.e.*, ABO_3).[1] ALD-grown BTO was amorphous as deposited at 225 °C. BTO films were annealed in 1×10^{-6} Torr partial pressure of O_2 by ramping the temperature to 600 °C at a rate of 20 °C/min. The temperature was raised an additional 50 °C greater than the crystallization temperature by ramping at a rate of 10 °C/min and held at the final temperature for 10-15 min to allow for complete crystallization. The onset of crystallization is established using reflective high-energy electron diffraction (RHEED), and observed between 770 °C and 850 °C. Blanket films are used to calibrate the stoichiometry and crystallization parameters, which were repeated over on PS-patterned substrates.

RHEED and XPS are used *in situ* to monitor the surface order, and composition of the sample, respectively, without risk of contamination. XPS uses a monochromated Al $K\alpha$ X-ray source with a photon energy of 1486.6 eV and a VG Scienta R3000 analyzer. After deposition, and sometimes after UHV post-deposition annealing, X-ray diffraction (XRD) and X-ray reflectivity (XRR) are used to characterize the film crystalline structure and thickness. XRD and XRR are performed using a Rigaku Ultima IV diffractometer with a Cu $K\alpha$ X-ray source. XRR is taken without any monochromator in the beam path, while XRD was taken using a Ge monochromator. BTO film thickness was determined by fitting the XRR data using GenX.[43]

Crosslinked PS is removed *ex situ* in a capactively coupled plasma etching chamber (Oxford PlasmaLab). The plasma etching chamber was purged three times by

flowing 20 sccm of Ar to maintain a pressure of 30 mTorr within the chamber for 1 min. The chamber is then evacuated to 1×10^{-6} Torr. This procedure is repeated twice before etching takes place. An O_2 plasma is used to remove crosslinked PS, which has an etch rate of ~13 nm/min using 20 sccm of O_2 at 100 W RF power and no ICP power applied. Crosslinked and uncrosslinked PS is measured *ex situ* using spectroscopic ellipsometry (J.A. Woolam), and fit using a Cauchy model (CompleteEase, J.A. Woolam).

Atomic force microscopy (AFM, Asylum Research) is obtained in tapping mode, and height images are obtained using Si cantilevers (HQ:NSC15/Al BS, μmasch). Images are analyzed using Gwyddion (v2.47). Top view scanning electron microscopy (SEM, FEI Quanta 650 ESEM) is obtained using a 30 kV electron beam.

Chemical spatial mapping is obtained with time of flight secondary ion mass spectroscopy (TOF-SIMS) using a TOF.SIMS 5 instrument (ION-TOF GmbH, 2010). A short (100 ns) pulsed primary ion beam (Bi^+, 30 keV energy, ~3.1 pA measured sample current) is rastered either over a 200 μm × 200 μm or 100 μm × 100 μm area on the sample surface to collect surface chemical maps. Depth profiling is done using a shorter primary ion beam pulse (~18 ns) in a 100 μm × 100 μm area focused within a 250 μm × 250 μm area that was sputtered by a secondary ion beam (Cs^+, 500 eV energy, ~50 pA measured sample current). Depth profiles are acquired within the UHV system, which has a base pressure of $\sim 5 \times 10^{-10}$ Torr in noninterlaced mode (*i.e.*, sequential data acquisition and sputtering) and with the primary ion beam in high current bunched mode. All detected secondary ions have positive polarity with mass resolution >13,000 ($m/\delta m$).

6.3. Results and Discussion

6.3.1. Passivating Ability of Polystyrene to BTO ALD

PS was used as a blocking material in this work, thus its resistance to BTO ALD was probed first. Figure 7.2 presents X-ray photoelectron (XP) spectra after 200 ALD cycles on crosslinked PS and on a STO(001) surface that had spincoated PS removed with a toluene rinse. 200 ALD cycles corresponds to a BTO thickness of ~12 nm on a bare STO(001) surface that was not exposed to PS. Figures 2(a) and (b) show the Ba 3*d* and Ti 2*p* XP spectra, respectively. The Ba 3*d* XP signal is significantly reduced and the Ti 2*p* signal is undetectable by XPS after 200 ALD cycles on crosslinked PS compared to the STO(001) substrate. Some Ba precursor adsorption occurred on crosslinked PS as indicated by the presence of Ba 3*d* XP signal in Figure 7.2(a). The crosslinked PS surface before BTO deposition has a weak O 1*s* XP signal at 534.1 eV, indicating PS incorporated oxygen during crosslinking (Figure 7.2(c). This is expected with a non-air tight UV generator, which can allow residual oxygen into the enclosure during crosslinking.[36] After 200 ALD cycles, the O 1*s* signal shifts to lower binding energy, 529.5 eV. Oxygen present during the UV exposure is typically incorporated as a carbonyl oxygen in PS.[44] Carbonyl oxygen in the crosslinked PS surface is likely the adsorption site for the Ba precursor. In separate control experiments uncrosslinked PS is subjected to 200 ALD cycles. The Ba 3*d*, Ti 2*p*, O 1*s,* and C 1*s* XP spectral signals do not change after 200 ALD cycles (not shown) from the spectra recorded before ALD. Uncrosslinked PS is inert to BTO ALD so it is expected that crosslinked PS would be inert with more effective purging of the UV exposure chamber.

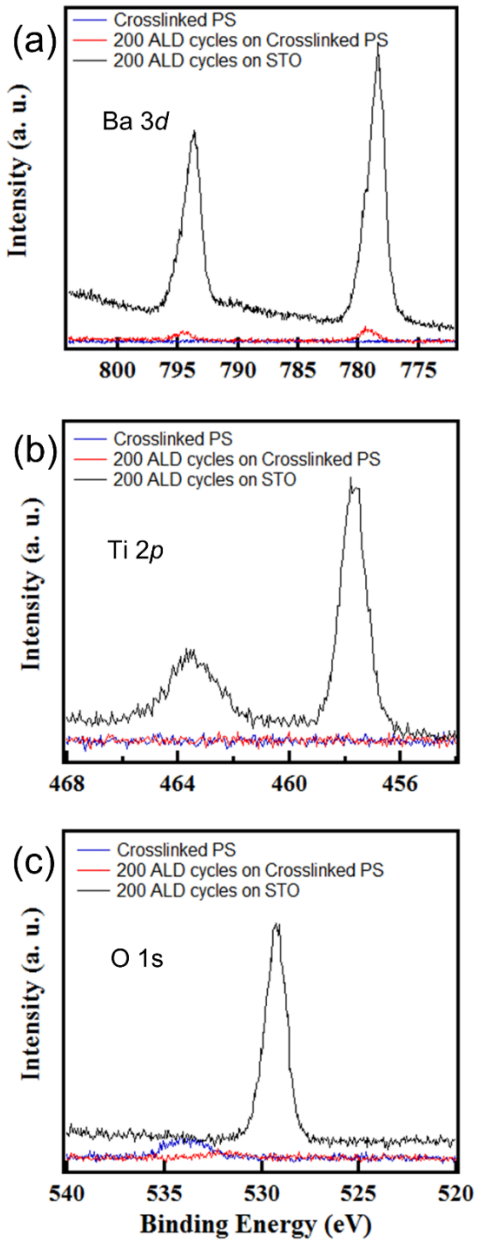

Figure 6.2. (a) Ba 3*d* and (b) Ti 2*p* XP spectra of a crosslinked PS film, a crosslinked PS film exposed to 200 ALD cycles at 225 °C, and 200 ALD cycles on a STO(001) substrate that had PS deposited and removed by rinsing with toluene (c) O 1*s* XP spectra for a crosslinked PS surface, and 200 ALD cycles at 225 °C on STO(001) that had PS deposited and removed by rinsing with toluene.

The morphology of the STO surface is investigated after PS deposition and removal. The process of depositing/removing PS should leave the surface of STO unchanged, so as to allow ALD growth and BTO crystallization in subsequent steps (Figure 7.1). The AFM image of a STO(001) surface exposed to PS deposition and removal with toluene is seen in Figure 7.3(a). For reference we measure the roughness (R_a) of an as-received STO(001) crystal is ~2 Å, while the roughness (R_a) of an ALD-grown BTO film on a cleaned STO(001) crystal not exposed to PS is ~7 Å. The roughness of the surface shown in Figure 7.3(a) is the same as the as-received STO crystal. BTO ALD is performed on surfaces similar to the one presented in Figure 7.3(a). The deposition and removal of PS does however introduce sparse particles onto the surface, which are the bright spots seen in the AFM image. Despite the introduction of particles to the surface, the surface roughness change is undetectable by AFM, signifying restoration of the STO(001) surface to its initial condition.

Removal of crosslinked PS, which is performed after BTO ALD (Figure 7.1), should leave the surface unaffected as well to allow for further processing in device fabrication. Crosslinked PS is removed using an O_2 plasma etch. Optimal conditions for crosslinked PS removal are found by varying the RF power applied and the Ar/O_2 gas flow rate. The final parameters (20 sccm O_2, 0 sccm Ar, 100 W RF power, 0 V bias) are found to yield the best results. The STO surface after crosslinked PS removal can be seen in Figure 7.3(b). Crosslinked PS etching left more particles on the surface compared to uncrosslinked PS removal with toluene; the roughness after O_2 plasma etching was 4.2 Å.

Light redeposition of BTO occurred during this O_2 plasma etching step as probed by TOF-SIMS (discussed below) and may have contributed to the increased roughness.

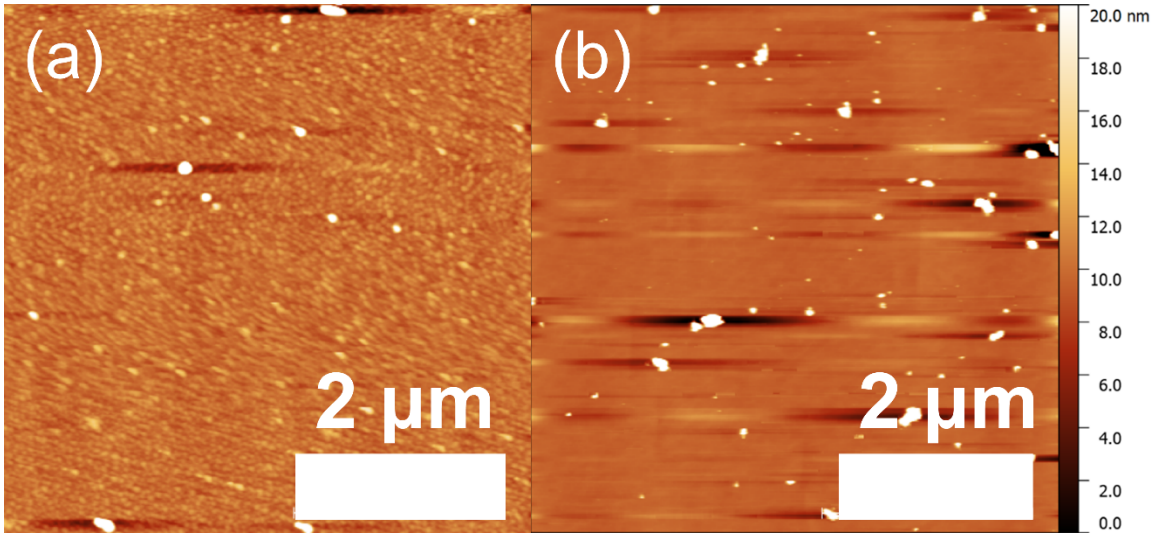

Figure 6.3. (a) AFM image of an STO(001) surface that had PS spincoated on and subsequently rinsed off with toluene. The roughness of the film is 2.2 Å. (b) AFM image of an STO(001) surface that had PS spincoated on and crosslinked by exposure to UV light. PS was then removed in an O_2 plasma etch. The roughness of the surface after plasma exposure is 4.2 Å. Both images are 5 µm × 5 µm.

6.3.2. Growth of Epitaxial BTO

A bare STO(001) surface was subjected to PS deposition without crosslinking and the PS was subsequently removed with a toluene rinse. Additional solvents and methods were investigated to find the optimal rinse for removal of PS. Isopropanol, acetone, and n-hexane all partially removed the PS, while toluene was the most effective at removing

uncrosslinked PS to allow for both BTO ALD and epitaxy.[39] The resulting toluene-rinsed surface is then exposed to 200 ALD cycles and RHEED is used to determine the onset of crystallization. Crystallization of the ALD-grown BTO film is strongly dependent on composition of the film. The stoichiometry of Ba:Ti that yielded the lowest crystallization temperature is 1:1, with crystallization observed at 770 °C at an oxygen partial pressure of 1×10^{-6} Torr. Ba:Ti ratios that deviate from 1:1 result in higher crystallization temperatures. Nonstoichiometric Ba:Ti films resulted in crystallites forming that are only observable as a secondary pattern in RHEED images, likely due to a Ti-rich surface region that exhibited different surface order than the bulk perovskite.[45] All BTO films reported herein are stoichiometric in Ba:Ti unless otherwise noted.

XRD is used to confirm the single crystalline nature of the BTO, which is seen in Figure 7.4(a) and 4(c). Two features are observed: a higher intensity feature at 46.5° is attributed to the substrate STO(002) peak, and a lower intensity feature located at 45.1° is attributed to BTO(002). No other peaks are observed for BTO. A wide-angle scan is also presented in Figure 7.4(c). The wide-angle scan shows three main features at ~22°, ~46°, and ~72°, which are the (00*l* =1, 2, 3) STO substrate peaks. Additionally, at the ~22°, and ~46° peak locations, two features are present due to the registry between BTO and STO. The feature at ~22° is comprised of STO(001) at 22.8° and BTO(001) at 22.1°. The ~46° feature is the same shown in Figure 7.4(a), which arises from STO(002) and BTO(002) located at 46.5° and 45.1°, respectively. The feature at 72.6° is attributed to STO(003). BTO(003) could not be resolved by XRD as the BTO(003) feature is not expected to have

a large intensity. The *d*-spacing for the BTO film is 4.02 Å ± 0.02 Å. The out-of-plane lattice constant is close to the bulk value for tetragonal *c*-axis BTO, 4.036 Å,[2] which indicates crystalline BTO is not strained to STO(001). The rocking curve on the BTO(002) peak can be seen in Figure 7.4(b). The FWHM of the 002 rocking curve is 0.085°, which suggests the ALD-grown BTO is a high quality single crystal, with low mosaicity, and has epitaxially crystallized to STO(001).

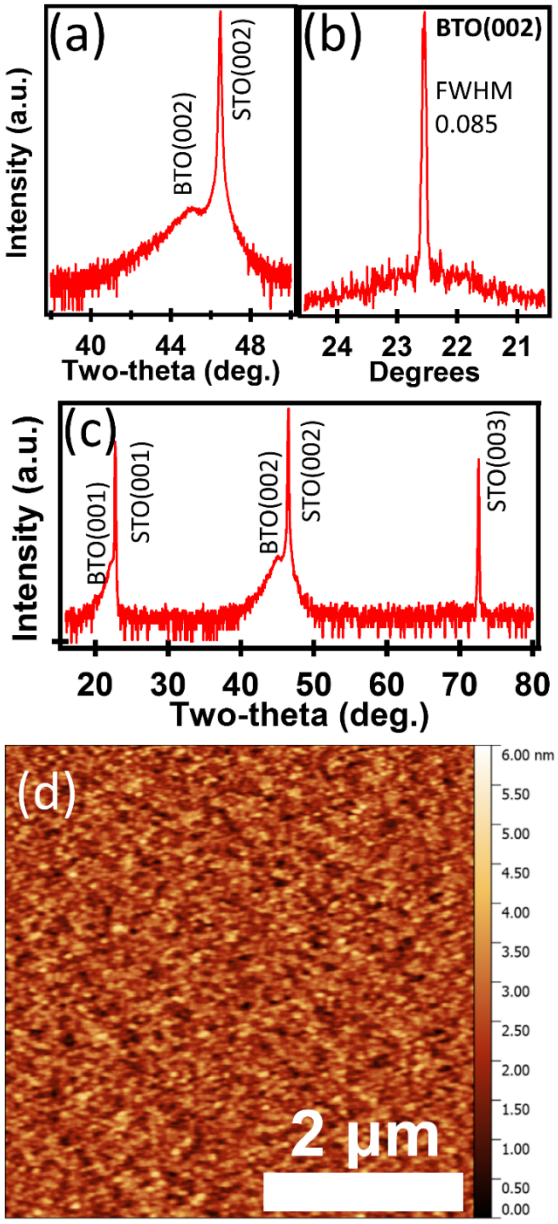

Figure 6.4. (a) Two-theta omega XRD scan of a 12 nm crystallized BTO sample, centered on the STO(002) and BTO(002) feature. (b) Rocking curve of the BTO(002) feature. The FWHM of the rocking curve is 0.085. (c) Two-theta omega XRD scan of (00*l* =1, 2, 3) peaks (d) AFM image showing the surface of the crystallized BTO sample. The AFM image is 5 µm × 5 µm, with a surface roughness of 5.5 Å.

Film roughness was investigated using AFM, which is seen in Figure 7.4(d). The AFM image shows a 5 μm × 5 μm area with an average surface roughness of 5.5 Å compared to 2 Å for a STO(001) surface. This is in good agreement with the roughness we have observed for ALD-grown BTO films, which ranges 5-7 Å on a bare STO(001) surface, not subjected to the AS process. In summary, the BTO is single crystalline and has epitaxially crystallized on STO(001) that had been exposed to the PS deposition and toluene removal procedure.

6.3.3. AREA-SELECTIVE ALD OF CRYSTALLINE BTO

Area-selective deposition is investigated by crosslinking PS on STO(001) surfaces with exposure to UV light (Figure 7.1). After rinsing uncrosslinked PS away with toluene, the patterned substrates are exposed to 200 ALD cycles. After BTO growth, crosslinked PS is removed by exposure to an O_2 plasma, as discussed previously. The BTO film is then annealed in UHV under an O_2 partial pressure of 1×10^{-6} Torr to allow crystallization. Crystallization is observed at 790 °C for the film shown in Figure 7.5. TOF-SIMS is used to obtain surface chemical maps, where the pattern was defined using a shadow mask (Figure 7.5(a)). Ba^+ and Sr^+ ion signals were chosen to represent the Ba-rich and Sr-rich regions, respectively, where Ba^+ is continuous and shown in red, and Sr^+ is discontinuous, shown in purple.

A scanning electron micrograph of a wider area of the same region is shown in Figure 7.5(b). The dark regions in the scanning electron micrograph are STO, and correspond to the purple regions in Figure 7.5(a), while the bright regions are ALD-grown

BTO and correspond to the continuous red regions in Figure 7.5(a). The corresponding area of the patterned BTO seen in Figure 7.5(a) is indicated in a red square in Figure 7.5(b). Sr^+ chemical maps showed Sr^+ was contained to the STO(001) substrate region beneath the crosslinked PS as expected, while Ba^+ was seen in the continuous region with some signal on the Sr-rich regions. The Ba^+ observed on the Sr-rich region is likely due to redeposition of Ba during the O_2 plasma etching step to remove crosslinked PS. Ba^+ is observed throughout the STO(001) substrate region as well as in the BTO ALD-growth regions. The STO(001) substrate has 0.86 wt% Ba impurity per the manufacturer, which leads to the background signal observed in TOF-SIMS.

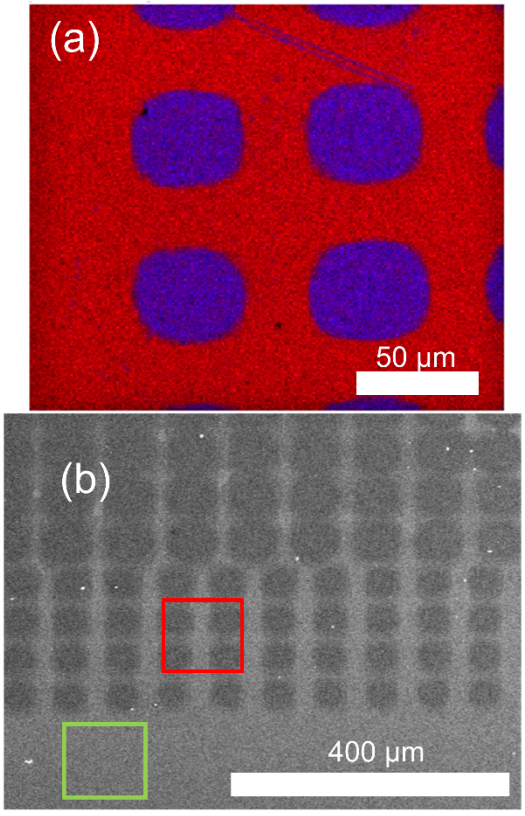

Figure 6.5. (a) TOF-SIMS chemical map of the pattern after 200 ALD cycles and PS removal. The continuous (red) region corresponds to Ba^+, which originated from BTO, while the discontinuous (purple) region corresponds to Sr^+, which originated from the STO substrate. The TOF-SIMS data was collected in a 200 μm × 200 μm region. (b) Scanning electron micrograph after 200 ALD cycles and PS removal on STO(001). Dark regions are the STO(001) substrate, while bright regions are ALD-grown BTO, which are purple and red, respectively, in Figure 7.5(a). The red square in Figure 7.5(b) is a representative area that is shown in Figure 7.5(a) and a representative of the area analyzed with TOF-SIMS, while the green square shows the representative area used for XRD and AFM analysis.

Redeposition and composition of the BTO features are investigated using TOF-SIMS as shown in Figure 7.6. It is worth noting that TOF-SIMS records a 2-D image as it sputters, so that features smaller than ~300 μm on a planar surface will appear as a 2-D projection in the TOF-SIMS image due to the negligible difference in ions' time of flight to reach the detector. Thus the BTO pattern appears sunk into the STO substrate in Figure 7.6. The Sr^+ signal can be seen in Figure 7.6(a), where the background is indicated as dark blue on the top of the pads at the four corners and at the bottom of the trenches and is limited to the STO substrate. Ba^+, as seen in Figure 7.6(b), is most concentrated in the middle region, where BTO deposition occurred due to AS-ALD. There is some Ba^+ localized onto the surface of the STO pads, which is most likely due to redeposition during O_2 plasma etching. Surface Ba^+ is removed with light sputtering, as indicated by the Ba^+ signal dropping to the background level associated with the 0.86 wt% Ba impurity in STO. The ultrathin surface Ba^+ on the Sr-rich region is not continuous, and unlikely to have originated during ALD growth, as once nucleation occurs, growth persists. The overlay of the Sr^+ and Ba^+ TOF-SIMS maps can be seen in Figure 7.6(c). Both species, STO and BTO,

are confined to the regions defined during PS crosslinking. The interface of STO/BTO is seen at the bottom of the trenches in Figure 7.6(a). A carbon C^+ signal, due to adventitious C or PS sources from the toluene rinse, would be visible in this location, however, the C^+ TOF-SIMS signal intensity at the interface was not different than the background C^+ signal throughout the STO/BTO (not shown).

AFM is used to investigate feature fidelity of the BTO patterns, which is seen in Figure 7.7(a), which again corresponds to the red square in Figure 7.5(b). Horizontal lines correspond to extracted height profiles shown in Figure 7.7(b). The low regions in Figure 7.7(a) correspond to the substrate, STO(001), where the PS is crosslinked during exposure. Figure 7.7(c) shows the TOF-SIMS chemical map, where the STO substrate is discontinuous and visible in the corners (purple), while the ALD-grown BTO is the continuous (red) raised region. The raised regions correspond to PS areas that are blocked during UV exposure and removed with the toluene rinse, which is where BTO growth takes place. The smallest opening on the shadow mask is 50 μm × 50 μm, while the line width is approximately 25 μm. AFM height profiles indicate the line width is approximately 25 μm in Figure 7.7, while the holes are approximately 45 μm × 45 μm in Figure 7.5(a) within the red square region in Figure 7.5(b). The hole and line widths are in good agreement with nominal hole and line widths of the shadow mask, which are 50 μm × 50 μm, 25 μm, respectively. 200 ALD cycles is expected to deposit ~12 nm of BTO, consistent with the extracted height profiles in Figure 7.7(b). BTO typically has roughness of ~5-7 Å on bare STO(001) and toluene-rinsed blanket STO(001) surfaces, while STO(001) has a roughness

of ~2 Å, which is consistent with the visibly rougher BTO compared to STO in Figure 7.7(a). Good agreement between the ALD-grown BTO and the shadow mask dimensions demonstrates reliable patterning from the crosslinked PS to the deposited BTO film. Large scale patterning can be seen in the scanning electron micrograph in Figure 7.5(b).

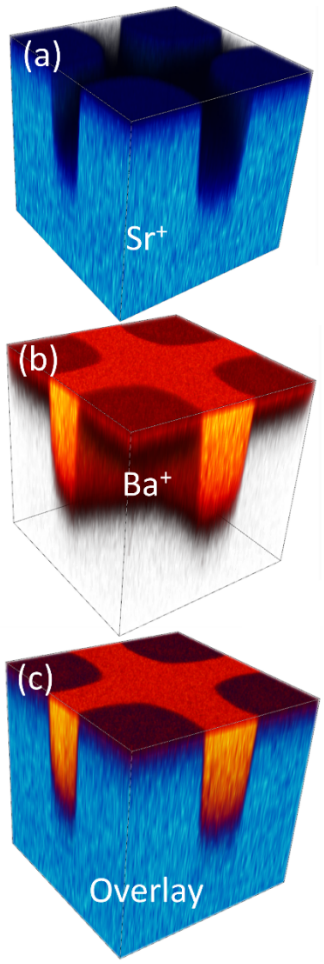

Figure 6.6. Depth profiling in TOF-SIMS of (a) Sr^+, (b) Ba^+, and (c) the overlay of Sr^+ and Ba^+. The sample was sputtered using Cs^+ ions at 500 eV on the same region that is presented in the red square in Figure 7.5(b). Higher ion signals of both Sr^+ and Ba^+ are indicated by brighter regions and dark regions indicate low ion signals. The height of the BTO film is 12 nm and the analysis area for TOF-SIMS was 100 μm × 100 μm.

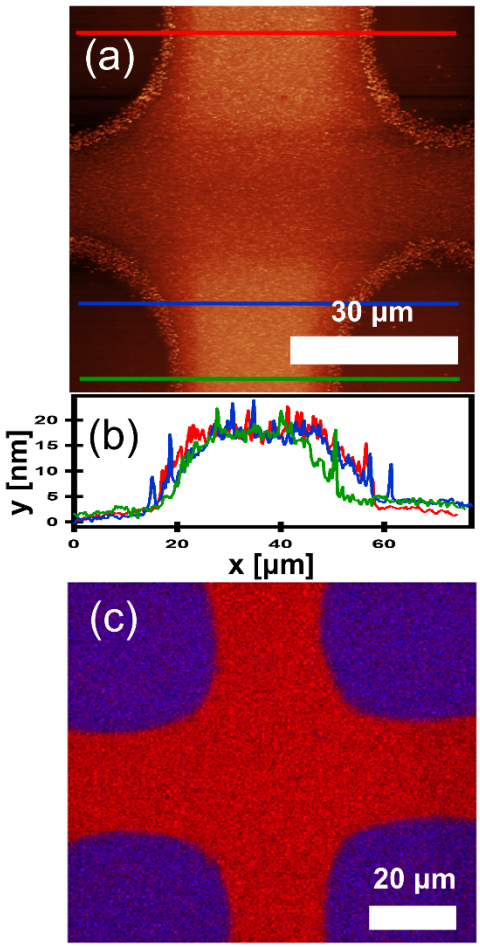

Figure 6.7. (a) Tapping mode AFM image of 200 BTO ALD cycles on STO(001) where crosslinked and uncrosslinked PS has been removed. The BTO film was annealed in an oxygen atmosphere to allow crystallization. Horizontal lines correspond to the height profile and color in the AFM image correspond to the same color in the extracted height profile in (b). (c) TOF-SIMS chemical surface map of a similar area, where the substrate STO is seen in the corners (purple), while the continuous region is ALD-grown BTO (red). The representative area is indicated by the red square in Figure 7.5(b). The analysis area for TOF-SIMS was 100 µm × 100 µm.

Patterning is successful over the entire shadow mask indicating the process of depositing, crosslinking, and removing PS can be used to deposit BTO selectively. Large shadow mask features are not transferred with the same fidelity as the smaller features in the process herein due to poor contact between the shadow mask and the substrate. Feature fidelity is improved at the smaller holes in the shadow mask, which is likely due to a non-optimized photo-transfer process in exposing the PS to UV light. Minimizing the gap between shadow mask and substrate or collimating the UV-light would likely improve feature fidelity.

To examine physical sputtering of BTO with oxygen ions during the crosslinked PS removal step, a PS patterned STO(001) substrate is subjected to 150 ALD cycles (~9 nm thick BTO). The patterned BTO with PS removed is then annealed in oxygen to allow the film to crystallize. The surface morphology of the BTO within the green square indicated in Figure 7.5(b) is investigated after O_2 plasma etching. The roughness of the ALD-grown BTO film does not change, indicating that O_2 plasma etching does not introduce morphological changes into the film, even though it is likely some particles were left over as seen in Figure 7.3(b). XRR before and after O_2 plasma etching and before and after O_2 annealing confirm this, as film thickness was ~9 nm in all measurements (not shown). TOF-SIMS is the only technique that detected a change with O_2 etching, which shows a weak Ba^+ signal. Thus, damage to BTO is not appreciable in any of the AS-process steps.

The patterned BTO films are then crystallized and probed for epitaxy. The onset of crystallization is observed at 790 °C, which is monitored *in situ* with RHEED. The Ba:Ti stoichiometry was 49.3:50.7. The streak-like diffraction pattern in the RHEED inset in Figure 7.8(a) is due to the registry between BTO and STO, indicating a smooth crystalline BTO surface. The representative BTO area investigated with XRD is shown in the green square in Figure 7.5(b). The shoulder at two-theta values 45.1° is BTO(002). A wide-angle XRD scan is shown in Figure 7.8(b), where three features, arising from the substrate STO/BTO(00*l*) peaks, can be observed. XRD for the patterned BTO film and the blanket BTO film deposited on PS treated STO(001) are identical (Figure 7.4). The sole presence of {00*l*} reflections indicates a preferred orientation to the crystalline films expected for surface phase epitxay. The patterned BTO film (Figure 7.8) has an out-of-plane lattice constant of 4.02 Å ± 0.02 Å, which is the same as the out-of-plane lattice constant for the blanket BTO film exposed to PS (Figure 7.4). Considering the uncertainty of this value, it is consistent with 4.036 Å expected for an out-of-plane *c*-axis oriented and relaxed BTO film. STO is cubic with a = 3.905 Å[46] and tetragonal BTO has a = 3.966 Å.[47] If the BTO(001) films are strained to STO(001) the out-of-plane spacing would be greater than the bulk BTO *c* value of 4.036 Å. Previous studies have examined the effect of annealing on crystallization, and have shown that low enough temperature ramp rates (5 °C/min) will retain a strained film throughout the annealing process.[2] AFM indicates deposition thickness is approximately 9 nm, and the thickness after crystallization is also approximately 9 nm, which is close to the thickness calculated using XRR, 8.8 nm (not shown).

Thus in this proof of concept the AS-ALD process can be used to grow crystalline BTO films through solid phase epitaxy. In this work 45 μm patterns in PS are explored and smaller features are likely possible. Five to six μm features have been demonstrated using UV-crosslinked PS,[39,48] and 20-30 nm features have been demonstrated with a PS-based self-assembled diblock polymer film.[39] We expect this technique can be implemented on other crystalline surfaces than the STO(001) substrates used herein that have a 2-3 nm-thick STO template layer on them, such as STO on Si(001),[2] or STO on Ge(001),[1] which would enable monolithic integration of patterned BTO into semiconductor devices, such as negative capacitance FETs,[17] ferroelectric FETs,[13] or multiferroic FETs incorporating BTO.[49] Such applications could include the Si ring resonator, which is nearing its theoretical smallest diameter of 3 μm,[50] or ferroelectric BTO waveguides, which can have feature sizes up to 100 μm.[19]

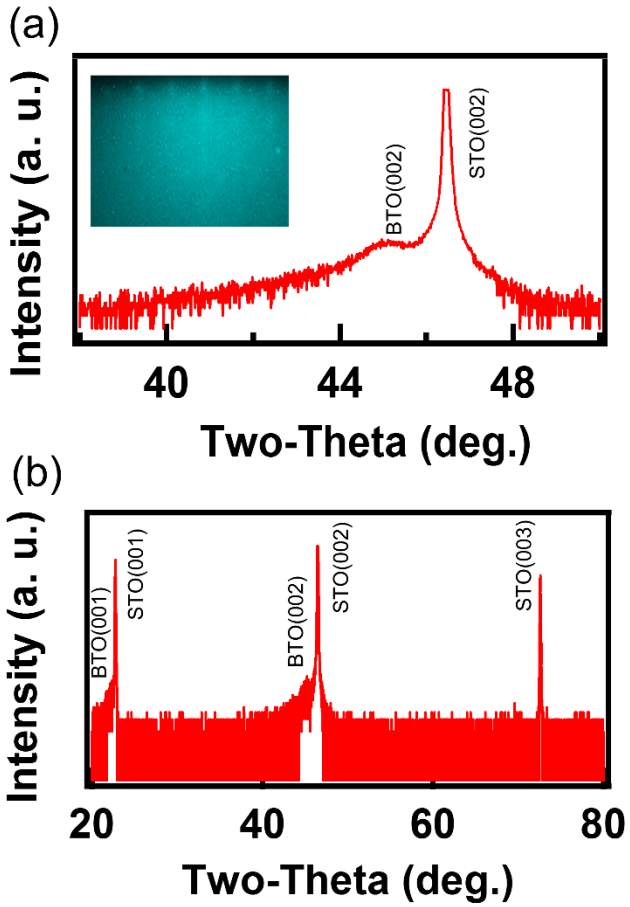

Figure 6.8. (a) Two-theta omega XRD scan of 150 ALD cycles on PS-patterned STO(001) that was annealed at an oxygen partial pressure of 1×10^{-6} Torr by ramping to 600 °C at a rate of 20 °C/min, followed by a second ramp to 850 °C at a rate of 10 °C/min and held at 850 °C for 10 min. The crystallization area is representative of the area shown in the green square in Figure 7.5(b). The narrow-angle two-theta omega XRD scan is focused on STO(002). Inset is the RHEED image showing the crystallization diffraction pattern of the film. (b) Wide-angle two-theta omega XRD scan showing the single-crystalline nature of the ALD-grown BTO on STO(001), which has epitaxially crystallized.

6.4. Conclusions and Summary

Area-selective ALD of BTO is demonstrated on a STO(001) surface. Area-selective patterns are defined by crosslinking PS through exposure to UV light ($\lambda < 254$ nm). Uncrosslinked PS is removed by rinsing the surface with toluene. BTO growth is blocked on uncrosslinked PS up to at least 200 cycles. Residual oxygen in the UV exposure enclosure likely introduces impurities into the PS film, which behave as nucleation sites during BTO ALD growth. Even though some Ba adsorbs on top of the crosslinked PS, uncrosslinked PS is expected to have high selectivity to BTO ALD. The PS deposition procedure does not inhibit BTO growth on STO(001), as the procedure for removing crosslinked and uncrosslinked PS restore the STO(001) surface to allow for epitaxial crystallization. BTO is single crystalline after annealing in O_2, and it is suspected Ba:Ti stoichiometry is the main parameter to be controlled for crystallizing BTO. Future work is needed extending this technique to smaller features, and using AS-ALD to produce BTO films strained to the substrate. The effect of the BTO/STO interface on crystallization and examining electro-optic performance after AS-ALD also require further study.

6.5. References

(1) Lin, E. L.; Posadas, A. B.; Wu, H. W.; Smith, D. J.; Demkov, A. A.; Ekerdt, J. G. Epitaxial Growth of Barium Titanate Thin Films on Germanium via Atomic Layer Deposition. *J. Cryst. Growth* **2017**, *476*, 6–11.

(2) Ngo, T. Q.; Posadas, A. B.; McDaniel, M. D.; Hu, C.; Bruley, J.; Yu, E. T.; Demkov, A. A.; Ekerdt, J. G. Epitaxial c-Axis Oriented $BaTiO_3$ Thin Films on $SrTiO_3$-Buffered Si(001) by Atomic Layer Deposition. *Appl. Phys. Lett.* **2014**, *104* (8), 082910.

(3) Abel, S.; Stöferle, T.; Marchiori, C.; Rossel, C.; Rossell, M. D.; Erni, R.; Caimi, D.; Sousa, M.; Chelnokov, A.; Offrein, B. J.; et al. A Strong Electro-Optically Active Lead-Free Ferroelectric Integrated on Silicon. *Nat. Commun.* **2013**, *4*, 1671.

(4) McDaniel, M. D.; Hu, C.; Lu, S.; Ngo, T. Q.; Posadas, A.; Jiang, A.; Smith, D. J.; Yu, E. T.; Demkov, A. A.; Ekerdt, J. G. Atomic Layer Deposition of Crystalline $SrHfO_3$ Directly on Ge (001) for High-K Dielectric Applications. *J. Appl. Phys.* **2015**, *117* (5), 054101.

(5) Dubourdieu, C.; Bruley, J.; Arruda, T. M.; Posadas, A.; Jordan-Sweet, J.; Frank, M. M.; Cartier, E.; Frank, D. J.; Kalinin, S. V.; Demkov, A. A.; et al. Switching of Ferroelectric Polarization in Epitaxial $BaTiO_3$ Films on Silicon without a Conducting Bottom Electrode. *Nat. Nanotechnol.* **2013**, *8* (10), 748–754.

(6) Posadas, A.; Berg, M.; Seo, H.; de Lozanne, A.; Demkov, A. A.; Smith, D. J.; Kirk, A. P.; Zhernokletov, D.; Wallace, R. M. Epitaxial Integration of Ferromagnetic Correlated Oxide $LaCoO_3$ with Si (100). *Appl. Phys. Lett.* **2011**, *98* (5), 053104.

(7) Niu, G.; Yin, S.; Saint-Girons, G.; Gautier, B.; Lecoeur, P.; Pillard, V.; Hollinger, G.; Vilquin, B. Epitaxy of $BaTiO_3$ Thin Film on Si(001) Using a $SrTiO_3$ Buffer Layer for Non-Volatile Memory Application. *Microelectron. Eng.* **2011**, *88* (7), 1232–1235.

(8) Wang, Y.; Ganpule, C.; Liu, B. T.; Li, H.; Mori, K.; Hill, B.; Wuttig, M.; Ramesh, R.; Finder, J.; Yu, Z.; et al. Epitaxial Ferroelectric $Pb(Zr,Ti)O_3$ Thin Films on Si Using $SrTiO_3$ Template Layers. *Appl. Phys. Lett.* **2002**, *80* (1), 97–99.

(9) Kormondy, K. J.; Abel, S.; Fallegger, F.; Popoff, Y.; Ponath, P.; Posadas, A. B.; Sousa, M.; Caimi, D.; Siegwart, H.; Uccelli, E.; et al. Analysis of the Pockels Effect in Ferroelectric Barium Titanate Thin Films on Si(001). *Microelectron. Eng.* **2015**, *147*, 215–218.

(10) Ponath, P.; Fredrickson, K.; Posadas, A. B.; Ren, Y.; Wu, X.; Vasudevan, R. K.; Baris Okatan, M.; Jesse, S.; Aoki, T.; McCartney, M. R.; et al. Carrier Density Modulation in a Germanium Heterostructure by Ferroelectric Switching. *Nat. Commun.* **2015**, *6*, 6067.

(11) McDaniel, M. D.; Posadas, A.; Ngo, T. Q.; Dhamdhere, A.; Smith, D. J.; Demkov, A. A.; Ekerdt, J. G. Epitaxial Strontium Titanate Films Grown by Atomic Layer Deposition on $SrTiO_3$-Buffered Si(001) Substrates. *J. Vac. Sci. Technol. A* **2012**, *31* (1), 01A136.

(12) Li, J.; Jin, D.; Zhou, L.; Cheng, J. Dielectric Properties of Barium Strontium Titanate (BST) Ceramics Synthesized by Using Mixed-Phase Powders Calcined at Varied Temperatures. *Mater. Lett.* **2012**, *76*, 100–102.

(13) Mathews, S.; Ramesh, R.; Venkatesan, T.; Benedetto, J. Ferroelectric Field Effect Transistor Based on Epitaxial Perovskite Heterostructures. *Science* **1997**, *276* (5310), 238–240.

(14) Ponath, P.; Posadas, A. B.; Ren, Y.; Wu, X.; Lai, K.; Demkov, A.; Schmidt, M.; Duffy, R.; Hurley, P.; Wang, J.; et al. Advances of the Development of a

Ferroelectric Field-Effect Transistor on Ge(001). In *2017 IEEE International Conference on IC Design and Technology (ICICDT)*; 2017; pp 1–3.

(15) Shoron, O. F.; Raghavan, S.; Freeze, C. R.; Stemmer, S. $BaTiO_3/SrTiO_3$ Heterostructures for Ferroelectric Field Effect Transistors. *Appl. Phys. Lett.* **2017**, *110* (23), 232902.

(16) Wang, X.; Liu, C.; Chen, Y.; Wu, G.; Yan, X.; Huang, H.; Wang, P.; Tian, B.; Zhenchen Hong; Wang, Y.; et al. Ferroelectric FET for Nonvolatile Memory Application with Two-Dimensional $MoSe_2$ Channels. *2D Mater.* **2017**, *4* (2), 025036.

(17) Khan, A. I.; Chatterjee, K.; Wang, B.; Drapcho, S.; You, L.; Serrao, C.; Bakaul, S. R.; Ramesh, R.; Salahuddin, S. Negative Capacitance in a Ferroelectric Capacitor. *Nat. Mater.* **2015**, *14* (2), 182–186.

(18) Wang, C.; Zhang, M.; Stern, B.; Lipson, M.; Lončar, M. Nanophotonic Lithium Niobate Electro-Optic Modulators. *Opt. Express* **2018**, *26* (2), 1547–1555.

(19) Xiong, C.; Pernice, W. H. P.; Ngai, J. H.; Reiner, J. W.; Kumah, D.; Walker, F. J.; Ahn, C. H.; Tang, H. X. Active Silicon Integrated Nanophotonics: Ferroelectric $BaTiO_3$ Devices. *Nano Lett.* **2014**, *14* (3), 1419–1425.

(20) Eltes, F.; Caimi, D.; Fallegger, F.; Sousa, M.; O'Connor, E.; Rossell, M. D.; Offrein, B.; Fompeyrine, J.; Abel, S. Low-Loss $BaTiO_3$–Si Waveguides for Nonlinear Integrated Photonics. *ACS Photonics* **2016**, *3* (9), 1698–1703.

(21) Dai, L.; Wang, S.; Shu, P.; Zhong, Z.; Wang, G.; Zhang, G. Etching Mechanism of Barium Strontium Titanate (BST) Thin Films in CHF_3/Ar Plasma. *Chin. Sci. Bull.* **2011**, *56* (21), 2267–2271.

(22) Li, Y.; Wang, C.; Yao, Z.; Kim, H.-K.; Kim, N.-Y. Comparative Analysis of Barium Titanate Thin Films Dry Etching Using Inductively Coupled Plasmas by Different Fluorine-Based Mixture Gas. *Nanoscale Res. Lett.* **2014**, *9* (1), 530.

(23) Kwak, B. S.; Zhang, K.; Boyd, E. P.; Erbil, A.; Wilkens, B. J. Metalorganic Chemical Vapor Deposition of $BaTiO_3$ Thin Films. *J. Appl. Phys.* **1991**, *69* (2), 767–772.

(24) Mazet, L.; Yang, S. M.; Kalinin, S. V.; Schamm-Chardon, S.; Dubourdieu, C. A Review of Molecular Beam Epitaxy of Ferroelectric $BaTiO_3$ Films on Si, Ge and GaAs Substrates and Their Applications. *Sci. Technol. Adv. Mater.* **2015**, *16* (3), 036005.

(25) Park, K.-I.; Xu, S.; Liu, Y.; Hwang, G.-T.; Kang, S.-J. L.; Wang, Z. L.; Lee, K. J. Piezoelectric $BaTiO_3$ Thin Film Nanogenerator on Plastic Substrates. *Nano Lett.* **2010**, *10* (12), 4939–4943.

(26) Singh, J. A.; Thissen, N. F. W.; Kim, W.-H.; Johnson, H.; Kessels, W. M. M.; Bol, A. A.; Bent, S. F.; Mackus, A. J. M. Area-Selective Atomic Layer Deposition of

Metal Oxides on Noble Metals through Catalytic Oxygen Activation. *Chem. Mater.* **2018**, *30* (3), 663–670.

(27) Stevens, E.; Tomczak, Y.; Chan, B. T.; Altamirano Sanchez, E.; Parsons, G. N.; Delabie, A. Area-Selective Atomic Layer Deposition of TiN, TiO_2, and HfO_2 on Silicon Nitride with Inhibition on Amorphous Carbon. *Chem. Mater.* **2018**, *30* (10), 3223–3232.

(28) Ballard, J. B.; Sisson, T. W.; Owen, J. H. G.; Owen, W. R.; Fuchs, E.; Alexander, J.; Randall, J. N.; Von Ehr, J. R. Multimode Hydrogen Depassivation Lithography: A Method for Optimizing Atomically Precise Write Times. *J. Vac. Sci. Technol. B* **2013**, *31* (6), 06FC01.

(29) Hua, Y.; King, W. P.; Henderson, C. L. Nanopatterning Materials Using Area Selective Atomic Layer Deposition in Conjunction with Thermochemical Surface Modification via Heated AFM Cantilever Probe Lithography. *Microelectron. Eng.* **2008**, *85* (5), 934–936.

(30) Torgersen, J.; Acharya, S.; Dadlani, A. L.; Petousis, I.; Kim, Y.; Trejo, O.; Nordlund, D.; Prinz, F. B. Relating Electronic and Geometric Structure of Atomic Layer Deposited $BaTiO_3$ to Its Electrical Properties. *J. Phys. Chem. Lett.* **2016**, *7* (8), 1428–1433.

(31) Chen, Z.; Wang, H.; Wang, X.; Chen, P.; Liu, Y.; Zhao, H.; Zhao, Y.; Duan, Y. Low-Temperature Remote Plasma Enhanced Atomic Layer Deposition of ZrO_2/zircone Nanolaminate Film for Efficient Encapsulation of Flexible Organic Light-Emitting Diodes. *Sci. Rep.* **2017**, *7*, 40061.

(32) Hong, J.; Porter, D. W.; Sreenivasan, R.; McIntyre, P. C.; Bent, S. F. ALD Resist Formed by Vapor-Deposited Self-Assembled Monolayers. *Langmuir* **2007**, *23* (3), 1160–1165.

(33) Chopra, S. N.; Zhang, Z.; Kaihlanen, C.; Ekerdt, J. G. Selective Growth of Titanium Nitride on HfO_2 across Nanolines and Nanopillars. *Chem. Mater.* **2016**, *28* (14), 4928–4934.

(34) Bates, C. M.; Maher, M. J.; Janes, D. W.; Ellison, C. J.; Willson, C. G. Block Copolymer Lithography. *Macromolecules* **2014**, *47* (1), 2–12.

(35) Lee, T.; Yao, N.; Aksay, I. A. Nanoscale Patterning of Barium Titanate on Block Copolymers. *Langmuir* **1997**, *13* (14), 3866–3870.

(36) Zhang, Z.; Nallan, H. C.; Coffey, B. M.; Ngo, T. Q.; Pranamik, T.; Ekerdt, J. G.; Banerjee, S. Atomic Layer Deposition of Cobalt Oxide on Oxide Substrates and Low Temperature Reduction to Form Ultrathin Cobalt Metal Films. *J. Vac. Sci. Technol. A* **2019**, *37* (1), 010903.

(37) Mackus, A. J. M.; Mulders, J. J. L.; van de Sanden, M. C. M.; Kessels, W. M. M. Local Deposition of High-Purity Pt Nanostructures by Combining Electron Beam

Induced Deposition and Atomic Layer Deposition. *J. Appl. Phys.* **2010**, *107* (11), 116102.

(38) Lin, E. L.; Hu, S.; Ekerdt, J. G. Monolithic Integration of Metal-Ferroelectric-Semiconductor Heterostructure Using Atomic Layer Deposition. In *Oxide-based Materials and Devices VIII*; International Society for Optics and Photonics, 2017; Vol. 10105, p 1010519.

(39) Zhang, Z.; Dwyer, T.; Sirard, S. M.; Ekerdt, J. G. Area-Selective Atomic Layer Deposition of Cobalt Oxide to Generate Patterned Cobalt Films. *J. Vac. Sci. Technol. A* **2019**, *37* (2), 020905.

(40) Choi, M.; Posadas, A. B.; Rodriguez, C. A.; O'Hara, A.; Seinige, H.; Kellock, A. J.; Frank, M. M.; Tsoi, M.; Zollner, S.; Narayanan, V.; et al. Structural, Optical, and Electrical Properties of Strained La-Doped $SrTiO_3$ Films. *J. Appl. Phys.* **2014**, *116* (4), 043705.

(41) Vehkamäki, M.; Hatanpää, T.; Ritala, M.; Leskelä, M.; Väyrynen, S.; Rauhala, E. Atomic Layer Deposition of $BaTiO_3$ Thin Films—Effect of Barium Hydroxide Formation. *Chem. Vap. Depos.* **2007**, *13* (5), 239–246.

(42) Lee, S. W.; Choi, B. J.; Eom, T.; Han, J. H.; Kim, S. K.; Song, S. J.; Lee, W.; Hwang, C. S. Influences of Metal, Non-Metal Precursors, and Substrates on Atomic Layer Deposition Processes for the Growth of Selected Functional Electronic Materials. *Coord. Chem. Rev.* **2013**, *257* (23), 3154–3176.

(43) Björck, M.; Andersson, G. GenX: An Extensible X-Ray Reflectivity Refinement Program Utilizing Differential Evolution. *J. Appl. Crystallogr.* **2007**, *40* (6), 1174–1178.

(44) Powell, C. J.; Jablonski, A. *NIST Electron Effective-Attenuation-Length Database Version 1.3*; National Institute of Standards and Technology: Gaithersburg, MD, 2011.

(45) Morgan, T. Self-Assembled Barium Titanate Nanoscale Films by Molecular Beam Epitaxy. *Theses Diss.* **2018**.

(46) Schmidbauer, M.; Kwasniewski, A.; Schwarzkopf, J. High-Precision Absolute Lattice Parameter Determination of $SrTiO_3$, $DyScO_3$ and $NdGaO_3$ Single Crystals. *Acta Crystallogr. B* **2012**, *68* (1), 8–14.

(47) Wang, J. J.; Meng, F. Y.; Ma, X. Q.; Xu, M. X.; Chen, L. Q. Lattice, Elastic, Polarization, and Electrostrictive Properties of $BaTiO_3$ from First-Principles. *J. Appl. Phys.* **2010**, *108* (3), 034107.

(48) Palacios, M.; García, O.; Rodríguez-Hernández, J. Constructing Robust and Functional Micropatterns on Polystyrene Surfaces by Using Deep UV Irradiation. *Langmuir* **2013**, *29* (8), 2756–2763.

(49) Mangalam, R. V. K.; Ray, N.; Waghmare, U. V.; Sundaresan, A.; Rao, C. N. . Multiferroic Properties of Nanocrystalline $BaTiO_3$. *Solid State Communications* **2009**, *149*, 1–5.

(50) Xu, Q.; Fattal, D.; Beausoleil, R. G. Silicon Microring Resonators with 1.5-μm Radius. *Opt. Express* **2008**, *16* (6), 4309–4315.

Chapter 7: Conclusions and Recommendations for Future Work

Methods in nanofabrication motivated by implementation of metal assisted chemical etching (MACE), electroless Cu deposition, and area-selective (AS) deposition are presented. Specifically, the first demonstration of vacuum ultraviolet (VUV) enhanced atomic layer etching (ALE) is presented. VUV enhanced ALE is shown on the catalyst metals Pd, and Ru, used in both MACE and electroless Cu deposition. VUV enhanced ALE is used to remove catalyst from nanofeatures, and remove catalyst material area-selectively for electrode fabrication in flexible display applications. AS atomic layer deposition (ALD) of functional materials is also presented, as a method to circumvent post-deposition etching/patterning entirely.

7.1. Vacuum Ultraviolet Enhanced Atomic Layer Etching

VUV enhanced ALE is presented, where ALE cycles are comprised of one oxidation half-cycle, an Ar purge, one etching half-cycle, followed by a second Ar purge. All films are monitored using in situ X-ray photoelectron spectroscopy (XPS). Oxidation half-cycles are performed by co-exposing Pd and Ru substrates to VUV and O_2 at 1 torr O_2, and temperatures 50 – 150 °C. Etching half-cycles are performed by exposing oxidized substrates to formic acid, HCOOH, at 0.50 Torr, for 30 sec, isothermally. ALE rates for Pd and Ru are found to be 2.8, and 1.2 Å/cycle, respectively, as characterized from ex situ X-ray reflectivity (XRR) measurements. Atomic O is the main species responsible for oxidation from VUV/O_2 co-exposure. This is demonstrated in experiments where substrates are illuminated and shadowed during VUV/O_2 co-exposure, where illuminated substrates are oxidized, and shadowed substrates are not. This point suggests selectivity in oxidation, and thus etching, may be possible with VUV enhanced ALE. Oxidation of near surface layers is not self-limiting on Pd, despite the difficulty for O to diffuse through bulk

Pd layers, as determined from density functional theory (DFT), and nudged elastic band (NEB) calculations. The amount of PdO_x formed in the near surface region can be controlled via time and temperature of co-exposure to VUV/O_2. Non-self-limiting behavior of oxidation on Pd is contrasted against oxidation of Ru, which is self-limiting. It is shown that oxidation half-cycle exposure times greater than 5 min do not form more RuO_x. The temperature of exposure has an effect on the amount of oxide formed, as O atoms can more easily overcome energetic barriers to diffusion. This is shown in more detail with DFT and NEB calculations, where a large energetic barrier to diffusion exists for O to move between subsurface atomic planes. This gives rise to self-limiting behavior, and also explains the increasing amount of oxide forming with increasing temperature, as characterized experimentally with in situ XPS, and ex situ XRR thickness measurements.

Oxidation kinetics of the VUV/O_2 co-exposure are found to be surface area dependent as well. 2 nm discontinuous Pd films (R_a = 2.3 Å) oxidize more rapidly than 20 nm continuous Pd films (R_a = 11 Å). This is particularly important for the area-selectivity required for fabrication of electrodes using electroless Cu deposition, where it is required to remove undesired Pd deposition while leaving desired Pd deposition unchanged. More rapid oxidation of high surface area features is also verified on Ru, where the differential etch rate (i.e., amount of material removed between 0 to 5 cycles, 5 to 10 cycles, and 10 to 15 cycles, etc.) decreases as ALE is performed when Ru is co-exposed to VUV/O_2 for 2 min. This is attributed to a decrease in surface roughness, as characterized using XRR, and AFM ex situ. Decreased surface roughness requires longer VUV/O_2 co-exposure to oxidize the metal. This result is consistent with results on Pd as well. Ru that is not etched with 2 min VUV/O_2 co-exposure is shown to be etched with 5 min VUV/O_2 co-exposure.

7.2. Area-Selective Atomic Layer Deposition

AS-ALD, is also presented for $BaTiO_3$ (BTO), which is a functional oxide of importance to photonic devices. AS methods consist of spin-coating polystyrene (PS) onto STO(001), and defining a pattern by exposing PS to UV light through a shadowmask. PS is crosslinked in the UV illuminated regions, whereas PS is uncrosslinked in shadowed regions. Uncrosslinked PS is then rinsed away with toluene. PS patterns are hydrophobic, and thus resist BTO ALD up to 200 cycles (equivalent to 12 nm thick BTO), whereas ALD nucleates without any delay in exposed STO regions. In this way BTO patterns are defined with one lithographic step. BTO (12 and 9 nm) is deposited at 225 °C. BTO films grown on PS patterned substrates demonstrate pattern transfer, where dimensions are verified using atomic force microscopy (AFM), scanning electron microscopy (SEM), and time of flight secondary ion mass spectroscopy (TOF-SIMS). Chemical composition of films is verified using in situ XPS, and ex situ TOF-SIMS depth profiling. Crystallization of AS-patterned BTO is achieved with post-deposition annealing films in 1×10^{-6} Torr O_2. Crystallization is monitored in situ with reflective high energy electron diffraction (RHEED), and verified ex situ with X-ray diffraction (XRD). Epitaxial crystallization of BTO is observed, where the temperature of the onset of crystallization is 775 °C. Thus patterns are transferred using AS patterning methods, which does not limit the epitaxial crystallization of the oxide that is deposited.

7.3. Future Work and Recommendations

The first demonstration of VUV enhanced ALE is presented, as well as the first demonstration of AS-ALD to pattern functional oxides with Si photonic applications in mind. Thus, future work can be split into two categories – recommendations for VUV enhanced ALE and recommendations for AS – ALD.

As VUV enhanced ALE is a nascent technique, there are several directions to investigate further. Oxidation of Pd, and Ru with co-exposure of VUV and O_2 is demonstrated herein, however, it is expected these methods can be similarly applied to a variety of materials, and co-exposure of a variety of reactive gases. Of particular interest are materials, such as Co, Fe, Ni, Mg, Ti, W, Pt. Continuous co-exposure to O_2 is used to oxidize materials, however, it is reasonable to suspect that an exposure to adsorb a monolayer of a reactive species may also be used. The VUV exposure step could cause decomposition/reaction on the surface, and thus offer truly self-limiting behavior. Some gases to consider are, NO_2, H_2O, H_2O_2. Use of these species, if conditions are tuned to allow a monolayer to adsorb, may be decomposed locally on the surface, thus creating reactive species locally. Additionally, many gas molecules have large adsorption coefficients in the VUV spectral range. This implies VUV enhancement does not necessarily have to proceed by O containing species. It is therefore reasonable to explore other gases, for example, fluorinating gases (SF_6, CHF_3, HF, NF_3, CF_4, etc.), nitriding gases (NH_3, N_2, etc.), chlorinating gases (Cl_2, BCl_3, etc.), phosphiding gases (PH_3), or other gases typically used in semiconductor processing (e.g., H_2). The production of fluorides, nitrides, phosphides, or chlorides could also extend methods of VUV enhanced ALE to etching of SiN, TiN, GaN, etc. if combined with, for instance, an etch step consisting of vapor exposure of $Sn(acac)_2$.

Additionally, as VUV/O_2 is shown to produce atomic O, it is worthwhile to explore selectivity from VUV enhancement. Exposure of a substrate through a shadow/hard mask could offer selectivity in oxidation, and thus etching, for any combination of the aforementioned gas phase species. As atomic O is the main species responsible for oxidation, it is also worthwhile to explore VUV/O_2 co-exposure for any applications that require an O_2 plasma, such as defect, or oxygen vacancy repair.

The mechanism of etching of transition metals using HCOOH is yet to be elucidated. Future work should carry out more in depth theoretical studies to offer insight into the interaction of molecules on the surface of various transition metal oxides, PdO_x, and RuO_x, specifically. Careful DFT, ab initio molecular dynamics (AIMD), and molecular dynamics (MD) simulations can be used to offer insight into, for example, the structure of the etch product, geometries of adsorption or geoemtries in the gas phase, bonding character, oxidation state of the metal center, etc. While it was not completed in this body of work, some possible etch products from RuO_x etching with HCOOH are indicated in Figure 8.1. Part of the difficulty in predicting the Ru^{x+} etch product is the oxidation state of Ru is known to vary between x = -2 … +8. This suggests many geometries may arise from HCOOH etching of RuO_x. Additional work is recommended to analyze etch products from the HCOOH etching reaction using either FTIR, or monitoring effluent gas streams with SIMS or quadrupole mass spectroscopy (QMS) with a large mass range (i.e., 300 amu). One may be able to elucidate this information with carefully designed QCM studies, however, they will likely need to be complemented with FTIR, QMS, or SIMS.

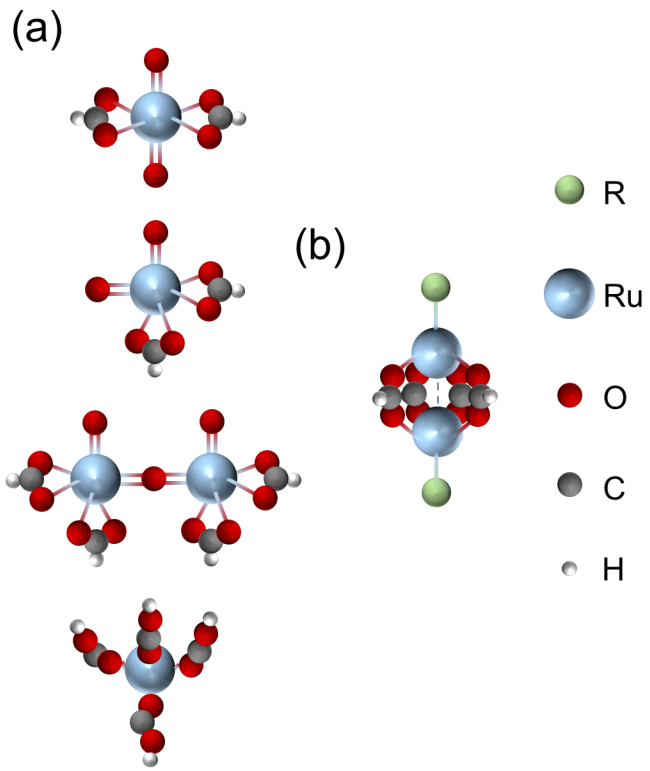

Figure 7.1. Possible products of HCOOH etched RuO_x. (a) shows Ru products where the metal center is Ru^{4+}, where several conformations are shown, from a bidentate structure in the top half of the column, to a double-coordinated Ru center with two bidentate HCOO ligands, the last entry in the column shows a monodentate structure, where the conformation is tetrahedral. (b) shows a potential etch product where Ru is in a lower oxidation state. The atoms are indicated on the right of the figure, where green spheres are a generic "R" group, pale blue spheres are Ru, red spheres are O, dark gray spheres are C, and white spheres are H.

Finally, as it is briefly demonstrated in this work, VUV enhanced ALE for fabrication of FinFETs or 3D NAND structures fabricated with MACE is worth exploring further. Effects on device performance manufactured using a standard O_2 plasma, and VUV enhancement are worth investigating as well. The fabrication of the transparent conductive electrode is also worthwhile to explore further, as selective etching based on surface area

is demonstrated and suggested as a method to ameliorate any issues with undesired deposition for any nanofabrication process.

AS-ALD is presented to pattern BTO, that is epitaxially registered to the substrate, STO(001). Future work will involve fabricating a Si waveguide from the AS-ALD process, and characterizing its function. It is also worthwhile to explore other perovskite materials, as BTO can be doped with other rare earth metals to enhance its conductivity, and thus applicability to a variety of devices, such as negative capacitance FETs, or Si wave guides.

Appendices

APPENDIX A

Samples within the etching system has been engineered to optimize the number of samples that are allowed in the system at once. It is also designed to minimize the potential to drop samples either during transfer, or while transporting them down the length of the transfer line. This is accomplished through careful machining of the sample holders (called "pucks"), as well as the forks used to transfer samples. The puck and the locking plate are shown in Figure A.1(a). Samples are mounted on pucks, which are 1" diameter cylinders, with two grooves cut into the sides, where forks make contact with the sample during transfer. Samples are 10×10 mm^2 for compatibility between the etching and deposition UHV systems. Samples are mounted by placing them in the square groove, which is recessed 1mm, and open beneath the sample so as to allow sample heating from radiation below the sample. Once placed in the groove, a plate is installed to compress the sample between the top plate and the puck. The plate is then rotated counter-clockwise, where grooves in the top plate catch four flat head 2-56 screws, and lock the top plate, and thus the sample, into place.

Forks are designed to have the minimum diameter to accept a puck, and are mounted on magnetic linear motion devices in at all sample transfer points within the UHV system, where gimbals are installed on all linear motion transfer arms to facilitate ease of transfer. Forks also have a groove cut into one side, which captures the puck when it is held on a fork. This groove, and the tolerance that the puck grooves are machined to, minimize the chance for random motion and shaking to dislodge a puck from a fork.

The transfer line cart is shown in Figure A.1. The transfer line cart is equipped with eight of the above designed forks, where they are mounted back to back to maximize the

density of samples, and minimize the overall length of the transfer line cart. The cart is moved through the transfer line on a platform with shallow rails that spans the entire length of the transfer line (20'). A drive chain is secured to both ends of the transfer line cart, where the chain traverses the length of the transfer line around two gears at both ends of the transfer line. There is an electric motor that controls motion (clock-wise and counter clock-wise rotation) mounted at the end of the transfer line nearest the ALE chamber. Samples are transferred using the bottom groove on the transfer line cart, and the top groove on all magnetic transfer arms. The transfer line cart is designed such that the bottom groove is aligned with the transfer line cart fork when the alignment is correct.

Figure A.1. The universal puck with the locking top plate is shown in (a), while the transfer line cart with several (old style) pucks is shown in (b). The transfer line cart is shown. There are eight forks total on the cart, where they are mounted back to back in groups of two. (old style) pucks are seen on four of the eight forks. The guide rail can also be seen beneath the transfer line cart, where the chain that controls the motion of the cart along the length of the reactor can be seen above the transfer line cart, and anchored to both sides of the cart. Numbers are stamped on both sides of the cart to help with sample identification and bookkeeping.

APPENDIX B

The valve control circuit has been redesigned to mitigate any risk associated with turning a channel on or off, and allowing too much current to pass through the National Instruments Data Acquisition Controller (NI-6525). The old circuit is shown in Figure B.1(a), while the new circuit is shown in Figure B.1(b), and the circuit housing with all internal ancillary equipment is shown in Figure B.1(c).

The circuit shown in Figure B.1(a) is driving two solenoid valves (Parker 3-way, and ALD Valve), with +24 V. The maximum power that has been observed in firing these two solenoid valves is approximately 0.5 A. The risk with the circuit shown in Figure B.1(a) arises when shutting the solenoid valves off, as the induced current can be large enough to exceed the maximum rating on the NI 6525 DAQ, which is 500 mA, and cause the connected channel to over-current and be destroyed. The upgraded circuit mitigates this risk. The upgraded circuit, shown in Figure B.1.(b), has the same four components, an LED, snubbing diode, and two solenoid valves, however, the current from the component part of the circuit is no longer sunk to ground through the NI-6525. This is accomplished by placing the NI-6525 upstream of a BJT, which when turned on, allows the components to actuate. When removing power from the BJT, current is sunk to ground, avoiding the NI-6525. The valve control box is also upgraded as shown in Figure B.1(c), where a project box houses the circuit, NI-6525, and +24 V power supply. LEDs are mounted on the right wall for indication on which valve is opened at a given time. The current rating for the power supply is 5 A, so all solenoids may be actuated concurrently, if so desired. A further upgrade would include a third component slot, so that three solenoid valves may be fired

on one channel. This may be useful if a shutter, or motion of something internal to the vacuum system is required during a half-cycle.

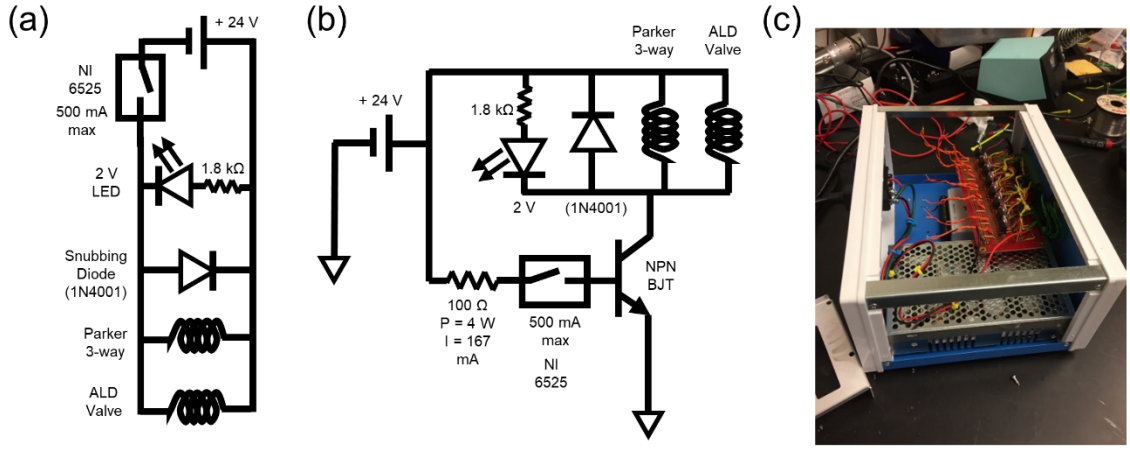

Figure B.1. Circuit diagrams are shown for the valve control circuit in (a), and (b), respectively, where (a) is the second version of the valve circuit, and (b) is the third version of the circuit. The actual housing with all components is shown in (c), where the project box houses the DAQ, power supply, and circuit. Front panel display from the LEDs indicates which valve is actuated at a given time.

APPENDIX C

The ALE chamber used in this dissertation has allowed the study of VUV-enhanced ALE of Pd and Ru, however, some upgrades are recommended. Upgrades fall into two categories, the ALE reactor, and the precursor manifold. The current design of the ALE reactor (version 2) is shown in Figure C.1(a). The current design utilizes a main chamber that is a custom six-way stainless steel cross, that has one 8", one 4.5", one 6", and one 2.75" CF flange centered at the middle plane of the system. It also has four oblique 2.75" CF ports around the middle-plane 6" CF flange, as shown in Figure C.1(a). However, many of these flanges are unused in VUV/O_2 and remote plasma experiments. It is also beneficial to modify the reactor so that VUV-enhanced ALD may be an option for further research projects, which requires more careful design of the internal geometry to minimize dead volume, and gas mixing for nominal ALD behavior.

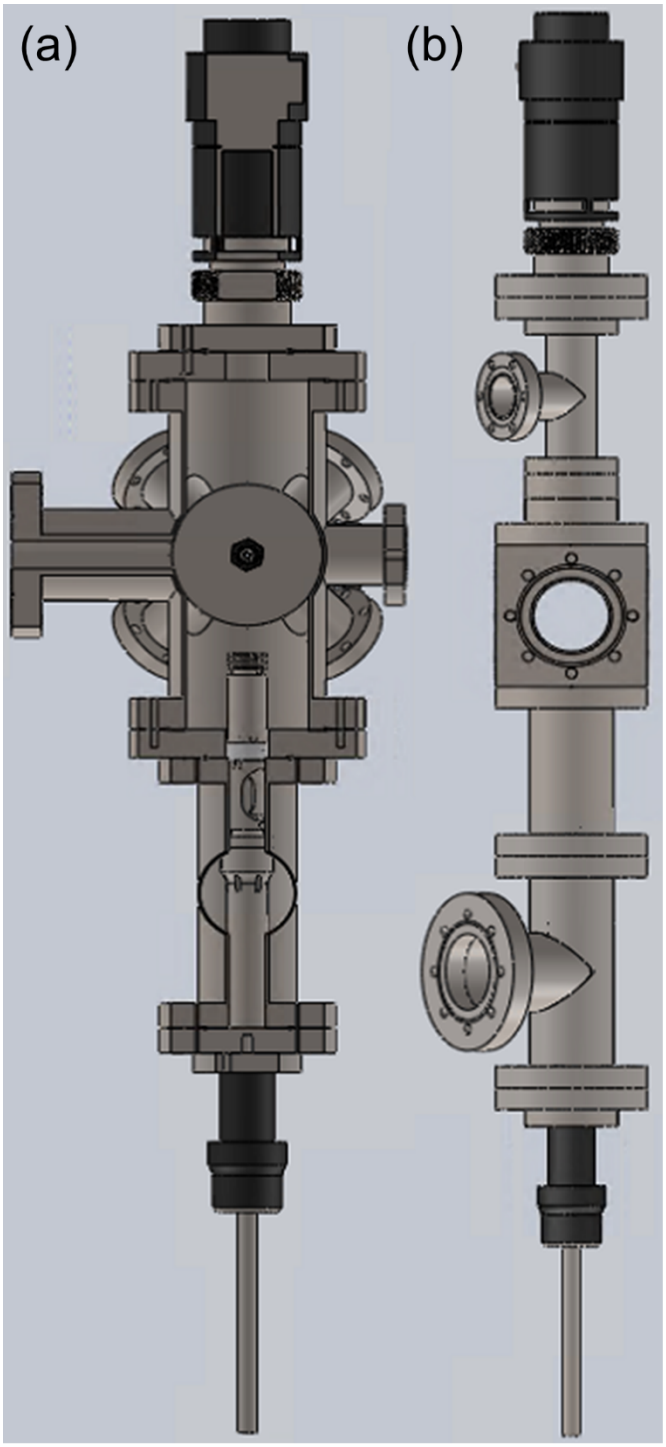

Figure C.1. CAD drawings of (a) version 2 of the ALE reactor, and (b), the suggested configuration and changes for version 3 of the ALE reactor.

The ALE reactor version 3 is modified in several ways to minimize the volume in the chamber, make it such that a shutter can be used to control dosing of the VUV lamp, and eventual exploration of VUV enhanced ALD is feasible. Version 3 of the ALE reactor is a redesign along the lines of the high vacuum (i.e., non-UHV) standalone ALD reactor, where a "shotgun" pulse of precursors enters the reactor, and it is designed such that it is a straight flow path to the exhaust with as few obstructions and additions along the way as possible. Version 3 of the ALE reactor is essentially another "shotgun" allowing precursor molecules to immediately enter the system in the vicinity of the substrate. The custom six-way cross is recommended to be replaced with a 4.5" CF tee or nipple, where the Langmuir probe with no modifications, is mounted on the bottom of a second 4.5" CF tee, the same way it currently is. The exhaust is down the axial length of the Langmuir probe, and exits on the third half nipple that is unused on the 4.5" CF tee. On the exhaust line, two valves are present where one isolates a turbomolecular pump for UHV (with a UHV pressure gauge behind the valve), and a second roughing line that is used during ALD/ALE. A further modification would be to add another valve to isolate exhaust to the commercial gas scrubber, which can be used for reactive fluorinated gases (NF_3, SF_6, etc.).

The D_2 lamp is still recommended to be mounted on the top of the reactor, where a 4.5" CF nipple is used for the gas feedthroughs in the vicinity of the VUV lamp. This is chosen to minimize volume of the ALE reactor, and simplify the gas path to the substrate, and the exhaust. The 4.5" CF nipple must be thick enough to accommodate a 1.33" CF flange, that is directly opposite a 0.25" VCR connection as an additional gas feedthrough (O_2, other). Separating the gas inlets is to maintain the ability to avoid mixing certain gases in the manifold, otherwise it may be used as an Ar purge line to sweep the ALE reactor section more efficiently. The 1.33" CF flange is the manifold connection, where the manifold is discussed later on. The D_2 lamp is behind a MgF_2 window to allow

transparency of VUV photons into the ALE chamber. The D_2 lamp is in its own differentially pumped section, where a turbomolecular pump (or 15 L/s ion pump) evacuates the photon column. A pneumatic shutter is placed in the photon column, so that dosing of the VUV photons can be accomplished using the shutter as opposed to the attenuation length of photons in a Ar gas environment, as the way it is in version 1 of the ALE reactor. This has an added benefit of adding distance between the D_2 lamp connection flange (which is a compression connection), and cannot be exposed to temperatures above 100 °C, safely. Due to this benefit, the ALE reactor can be held at an elevated temperature in a hot-wall scenario, which may be important to performing ALD in the reactor.

The manifold is shown in Figure C.2. The manifold is carefully designed to maximize the number of precursors that occupy a given area, so that in a smaller distance, eight precursors can be used, while only six could be used before. This also is accompanied by a slight redesign of the saturator, where two-way ALD valves are used instead of three-way valves, which allows each precursor assembly to be planar. The only modification that must be made are new weldments to make the elbow connection leaving the saturator going to the ALD valve, and shorter male-to-male VCR fittings for the straight connection from the parker 3-way valve to the ALD valve tee. The center of the manifold is a custom 1.33” CF nipple, that has eight 0.25” VCR glands welded at an even spacing on one side, where that same pattern is repeated on the opposite side, and shifted by half the pitch. Split nuts are added onto the glands based on whichever connection should be made, typically female connections. The large diameter of the manifold allows for a relatively low surface area to volume ratio, and the short length is amenable to fast purge times. This manifold design has been verified on the low-vacuum Standalone ALD reactor, known as Stan. Another benefit of the 1.33” CF nipple base for the manifold is the use of a main channel flow mass flow controller. A mass flow controller can be used to drive the flow rate down the main

channel so that sweep rates for each precursor can be tuned independently, and give rise to more accessible reaction parameters (i.e., flow, pressure, residence time, etc.).

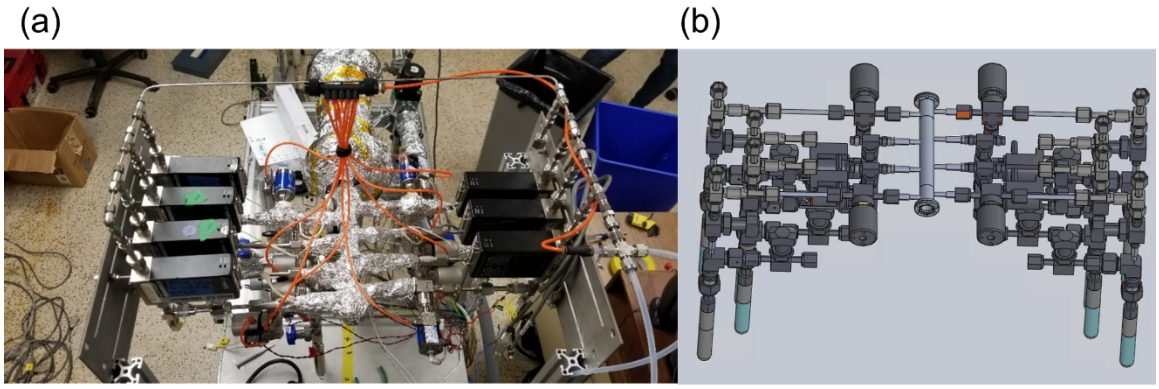

Figure C.2. (a) Top down view of the upgraded manifold, as installed on the low-vacuum standalone ALD reactor (Stan). (b) CAD drawing of the manifold version 2, with eight precursors installed, four of the saturators are of the old-style, to maxize the use of the non-planar ALD valves.

APPENDIX D

The DFT description of Pd and Ru is chosen by evaluating several exchange correlations, functionals, dispersion effects, and pseudopotentials. Quantum Espresso allows for combining different functionals, exchange correlations, and dispersion corrections, in addition to the choice of pseudopotential, all within the generalized gradient approximation (GGA). As van der Waals forces are non-negligible in this investigation, the functional, choice of dispersion, exchange correlation, and pseudopotential are all evaluated. The functionals and exchange correlations considered are: Perdew-Berke-Ernzerhof (PBE) both the functional and exchange correlation; the Perdew-Wang 91 (PW91) functional and PBE exchange correlation, slater determinant and vdW1 (sla+pw+pbe+vdw1); PBE for solids (PBEsol) functional and exchange correlation, which is corrected to yield better equilibrium values for solids when compared to PBE; the

Perdew-Wang 91 (PW91) functional and PBE exchange correlation slater determinant and vdW2 (sla+pw+pbe+vdw2); and the Cooper09 (c09x) functional and exchange correlation, slater determinant and vdW1 (sla+pw+c09x+vdw1). The choice of vdw1 or vdw2, as well as c09x, or PBEsol, is to use a functional with dispersion forces built-in. This is distinctly different than the corrections to the atomic orbitals that are employed in other dispersion treatments, such as with the Grimme-D1, D2, and D3, corrections. The dispersion corrections investigated that are not built into the functional are chosen between the Grimme-D3 correction with second order damping, or Becke-Johnson (BJ) damping. These are chosen as they have a strong record of offering good treatment of dispersion forces for systems in non van der Waals-functionals. In addition to the treatment of dispersion forces and exchange functional and correlation terms, the choice of pseudopotential is also investigated. The pseudopotentials investigated are: projector augmented wave (PAW) pseudopotentials; ultrasoft pseudopotentials (USPP); optimized norm conserving (ONCV) pseudopotentials; and standard solid state pseudopotentials (SSSP). Relativistic effects are not considered, as they are negligible for Pd and Ru, which have mass 106.42, and 101.07 amu, respectively.

The choice of functional, exchange correlation, treatment of dispersion effects, and pseudopotential is made by comparing geometric and energetic results with accepted literature values. As energetic calculations are usually only correct within the context of the simulations, the weight given to the energetic values is lower than those for which experimental measurements exist. Each model is scored on how close the calculated values are to the reference values, and then normalized to the number of parameters that are normalized to. This is quality parameter calculation shown in Equation D.1,

$$f(x) = \frac{1}{N}\sum_{j=1}^{N} f_i(x_i) = \frac{1}{N}\sum_{i=1}^{N}\left(\frac{x_i}{x_i^0} - 1\right)^2 w_i \qquad \text{(D.1)}$$

where f is the quality parameter, f_i is the i-th quality parameter, N is the number of parameters for a given set of simulation conditions, x_i is the calculated value of parameter i from simulations, x_i^0 is the reference value for parameter i, and w_i is the weight associated with the given parameter. The weights are selected to weight the simulation towards values that are known in the literature, or equivalently, to put less emphasis on values that are not known precisely. The parameters used to qualify the models are shown in Table D1.

Table D.1. A list of the parameters used to validate the choice of DFT model.

w_i	Parameter	x_i^0	Unit	Reference
0.1	Pd(111) O_2 E_{ads}	2.12	eV	[1]
0.1	Pd(100) O_2 E_{ads}	2.38	eV	[2]
0.1	Pd(111) O E_{ads}	3.90	eV	[3]
0.1	Pd(100) O E_{ads}	3.90	eV	[3]
1	ΔU_r ($2O \rightarrow O_2$)	5.16	eV/molecule	
1	ΔU_r ($3O \rightarrow O_3$)	4.61	eV/molecule	
1	O_2 $d_{O\text{-}O}$	1.208	Å	
1	O_3 $d_{O\text{-}O}$	1.277	Å	
1	O_3 $d_{\angle}$	116.8	deg	
1	Pd(111) $d_{Pd\text{-}Pd}$	2.75	Å	
1	Pd(100) $d_{Pd\text{-}Pd}$	2.75	Å	

The value of each f_i is shown in Figure D1 for combinations as discussed above. Overall, all of the functions are close to the reference values for geometric calculations, with the majority of the variation coming from energetic calculations (i.e., bond energy,

adsorption energy). Therefore, the quality parameter is biased towards functions that exhibit adsorption or bond energies that are in good agreement with the reference and do not over-predict adsorption energetics. This essentially reflects how well each functional can predict the bond energy of O_2, and O_3, as well as the adsorption energy of O_2, and atomic O on various surfaces. The functional that has the lowest f is the PBE exchange functional and correlation, using ultrasoft pseudopotentials with dispersion accounted for using the Grimme-D3 correction with Becke-Johnson damping. Choice of pseudopotential does not appear to have a strong effect on the result for the system investigated, so USPP is chosen for comparison with other DFT reports.

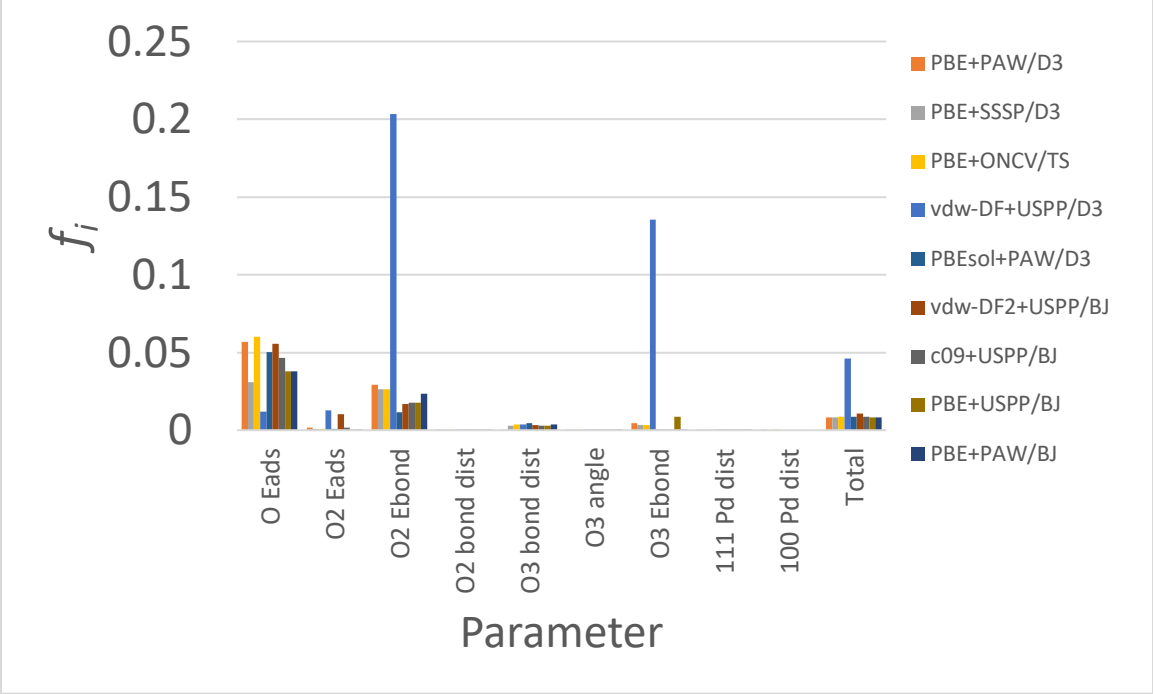

Figure D.1. Calculations for the quality metric, f_i, where each functional is shown on the right side of the graph, and the value of f_i is shown on the left.

A sample input file for quantum espresso to run a Ru simulation (DFT) is found below. Note that comments are followed by the "!" character, as the code is compiled in Fortran.

```
&CONTROL
   calculation   = "relax"
   max_seconds   =  1.72800e+05
   nstep         = 1001
   pseudo_dir    = "/work/07346/bmctacc/lonestar/projects/pseudopotentials"
   outdir        = "./outdir"
   prefix        = "pwscf"
         etot_conv_thr = 1e-6
         forc_conv_thr = 1e-5
   verbosity     = "high"
/

&SYSTEM
   a     =  5.41310e+00
   c     =  4.63685e+01
   degauss               =  0.002
   ecutrho               =  600
   ecutwfc               =  60
   ibrav                 = 4
   nat                   = 31
   nspin                 = 1
```

```
            ! tot_magnetization        = 2 ! Double check for Ru calculations, none that I have
seen use
            ntyp                  = 2
            occupations             = "smearing"
            smearing                = "marzari-vanderbilt" ! methfessel-paxton is other option
but gives (possibly) bad Ef values
            nosym                 = .TRUE. ! Not using this for vc-relax calcs
            vdw_corr                = "dft-d3" ! Grimme d3 correction keep for o3 adsorption
studies later
            dftd3_version           = 4 ! BJ-damping
           ! input_dft                        = "sla+pw+c09x+vdw1" ! vdw-df2 with pbe
exchange/correlation
         /

         &ELECTRONS
            conv_thr        =  1.00000e-08
            electron_maxstep = 1000
            mixing_beta     =  4.00000e-01
            startingpot     = "atomic+random"
            startingwfc     = "atomic+random"
            mixing_mode     = "local-TF"       !For anisotropy, local dependency allowed
         /

         &IONS
            ion_dynamics = "bfgs"
```

/

K_POINTS {automatic}

5 5 1 0 0 0

ATOMIC_SPECIES

Ru 101.07000 Ru.pbe-spn-rrkjus_psl.1.0.0.UPF

O 15.99940 O.pbe-n-rrkjus_psl.1.0.0.UPF

ATOMIC_POSITIONS {angstrom}

Ru 0.199360952 1.673714482 30.902936835

Ru -1.416916484 3.665774079 30.557647217

Ru 3.244514790 1.635271968 31.813196205

Ru 1.365328201 4.126466863 30.806746282

Ru 1.201472270 0.820853826 28.342351915

Ru -0.061572057 2.922450800 28.219713696

Ru 4.107550836 0.844348765 28.342270373

Ru 2.610502665 3.189822903 28.366139606

Ru -0.038963509 1.486506796 26.195157471

Ru -1.396117140 3.915832656 26.232935017

Ru 2.660428390 1.601139196 26.221738977

Ru 1.313264305 3.936829281 26.222097627

Ru 1.355111257 0.788978559 24.149643930

Ru -0.009823577 3.115175938 24.174968723

Ru 4.033126243 0.792540268 24.150191325

Ru	2.697255770	3.146473141	24.161572937			
Ru	-0.000000000	1.577858000	22.156961000	0	0	0
Ru	-1.353275000	3.921799000	22.156961000	0	0	0
Ru	2.706550000	1.577858000	22.156961000	0	0	0
Ru	1.353275000	3.921799000	22.156961000	0	0	0
Ru	1.366465000	0.788929000	20.000000000	0	0	0
Ru	0.013190000	3.132870000	20.000000000	0	0	0
Ru	4.073015000	0.788929000	20.000000000	0	0	0
Ru	2.719740000	3.132870000	20.000000000	0	0	0
O	1.587281568	2.816776342	32.183639888			
O	1.538401640	0.344391428	31.866668824			
O	2.392377137	1.886093945	29.820871398			
O	2.754134737	-0.224843018	29.352044848			
O	-0.661808264	0.238649342	33.654140868	0	0	0
O	-0.870088209	1.739792453	33.201650414	0	0	0
O	0.507209195	-0.053914071	33.944534957	0	0	0

A sample input NEB file is found below as well.

```
BEGIN
BEGIN_PATH_INPUT
&PATH
   restart_mode      = "from_scratch"
   string_method     = "neb"
   nstep_path        = 150
   ds                = 1
   opt_scheme        = "broyden"
   num_of_images     = 14
   path_thr          = 0.01 ! The norm of the force orthogonal to the path in eV/A
   CI_scheme         = "no-CI" ! Other option is "auto" to auto generate CI points
   first_last_opt    = .TRUE.
```

```
/
END_PATH_INPUT
BEGIN_ENGINE_INPUT
&CONTROL
   calculation   = "relax"
   max_seconds   =  1.72800e+05
   nstep         = 1001
   pseudo_dir    = "/work/07346/bmctacc/lonestar/projects/pseudopotentials"
   outdir        = "./outdir"
   prefix        = "pwscf"
         etot_conv_thr = 1e-6
         forc_conv_thr = 1e-5
/

&SYSTEM
   a     =  5.41310e+00
   c     =  4.63685e+01
   degauss                =  0.002
   ecutrho                =  600
   ecutwfc                =  60
   ibrav                  = 4
   nat                    = 29
   nspin                  = 1
```

```
            ! tot_magnetization        = 2 ! Double check for Ru calculations, none that I have
seen use
            ntyp                  = 2
            occupations             = "smearing"
            smearing                = "marzari-vanderbilt" ! methfessel-paxton is other option
but gives (possibly) bad Ef values
            nosym                 = .TRUE. ! Not using this for vc-relax calcs
            vdw_corr                = "dft-d3" ! Grimme d3 correction keep for o3 adsorption
studies later
            dftd3_version           = 4 ! BJ-damping
           ! input_dft                        = "sla+pw+c09x+vdw1" ! vdw-df2 with pbe
exchange/correlation
         /

         &ELECTRONS
            conv_thr        =  1.00000e-08
            electron_maxstep = 1000
            mixing_beta     =  4.00000e-01
            startingpot     = "atomic+random"
            startingwfc     = "atomic+random"
            mixing_mode     = "local-TF"       !For anisotropy local dependency allowed
         /

         &IONS
            ion_dynamics = "bfgs"
```

/

K_POINTS {automatic}

5 5 1 0 0 0

ATOMIC_SPECIES

Ru 101.07000 Ru.pbe-spn-rrkjus_psl.1.0.0.UPF

O 15.99940 O.pbe-n-rrkjus_psl.1.0.0.UPF

BEGIN_POSITIONS

FIRST_IMAGE

ATOMIC_POSITIONS {angstrom}

Ru 0.071683674 1.445535095 31.500836089

Ru -1.403388163 3.434700953 30.898571475

Ru 3.069480893 1.522094365 32.230453929

Ru 1.389457359 3.970336187 31.327126396

Ru 1.323839501 0.800831721 28.450779531

Ru -0.081438483 3.060538243 28.527594710

Ru 4.158559780 0.820130832 28.622182520

Ru 2.733900979 3.126958736 28.582704286

Ru -0.011210252 1.571659484 26.395841210

Ru -1.375718277 3.910594499 26.424715847

Ru 2.729316597 1.578324579 26.427056464

Ru 1.351746294 3.925183113 26.413682592

Ru 1.354214964 0.800480309 24.269208884

Ru -0.004079581 3.141562559 24.278360545

Ru 4.061605833 0.802529840 24.276046380

Ru 2.712482006 3.140712392 24.278877481

Ru 0.000000000 1.577858000 22.156961000

Ru -1.353275000 3.921799000 22.156961000

Ru 2.706550000 1.577858000 22.156961000

Ru 1.353275000 3.921799000 22.156961000

Ru 1.366465000 0.788929000 20.000000000

Ru 0.013190000 3.132870000 20.000000000

Ru 4.073015000 0.788929000 20.000000000

Ru 2.719740000 3.132870000 20.000000000

O 1.489647715 2.557814599 32.671953379

O 1.541729830 0.173762191 32.154216024

O 1.273364979 2.368381982 30.009605298

O 2.812140182 0.015737250 29.870073861

O -0.920613305 0.447743597 32.876427853

LAST_IMAGE

ATOMIC_POSITIONS {angstrom}

Ru -0.097630995 1.185253902 32.310969132

Ru -1.354017322 3.358693016 31.752263206

Ru 2.803151821 1.185393851 32.311143715

Ru 1.352532356 3.574447937 31.746295040

Ru 1.352976761 0.803828747 28.498942812

Ru	0.053796639	3.092140565	28.509594448
Ru	4.059485135	0.781421260	28.560624090
Ru	2.651615958	3.092054374	28.509398385
Ru	-0.002955198	1.570768035	26.434633296
Ru	-1.353881028	3.938210444	26.397897672
Ru	2.708771012	1.570612558	26.434572011
Ru	1.352707944	3.922770030	26.423877260
Ru	1.352683981	0.805577065	24.273053116
Ru	0.000929570	3.135369122	24.288796285
Ru	4.059215988	0.806472824	24.258173671
Ru	2.704033215	3.135445308	24.288688866
Ru	0.000000000	1.577858000	22.156961000
Ru	-1.353275000	3.921799000	22.156961000
Ru	2.706550000	1.577858000	22.156961000
Ru	1.353275000	3.921799000	22.156961000
Ru	1.366465000	0.788929000	20.000000000
Ru	0.013190000	3.132870000	20.000000000
Ru	4.073015000	0.788929000	20.000000000
Ru	2.719740000	3.132870000	20.000000000
O	1.352535264	2.260738130	33.200323989
O	1.352809669	-0.097246641	33.133294135
O	1.352606024	2.591894479	30.002823318
O	1.352786402	-0.830939699	29.829715161
O	-1.353969248	0.632214623	30.712357208

```
END_POSITIONS
END_ENGINE_INPUT
END
```

APPENDIX E

Supplementary information for the DFT and experimental investigation of oxidation of Pd using VUV/O_2

Energy of Oxidants

The energy per O atom is shown in Figure E.1. The energy of O is calculated from E_{O2} by subtracting the O-O bond energy (5.16 eV, or 498 kJ/mol) and dividing by the number of oxygen atoms, 2. The energy of O_3 is calculated from E_{O2} by adding the energy of an O atom, E_O, calculated previously, and accounting for the energy change of the reaction according to $O_3 \rightarrow O_2 + O$, which has a ΔH_r of 1.06 eV (102.4 kJ/mol). We define these oxidant energies to standardize all calculations herein, and to allow comparison between other DFT reports. All energies are referenced to the energy of a free O_2 molecule, which is 0.

The initial state of O, O_2, and O_3 is in the gas phase, indicated by the "free" column in Figure E.1, while the intermediate state, "adsorbed", is shown in the middle column, and the "final" energy of a given configuration is shown in the last column. The adsorbed column is only relevant for systems where an adsorption event takes place, as O adsorption onto Pd(111) or Pd(100) cannot be identified in the electronic energy optimization. Molecular O_2 and O_3 adsorb, and thus indicate an energy of adsorption in an intermediate state. However, further decomposition may or may not occur, which is observed in the decomposition products, O_2* + O and O + O, resulting from O_3 and O_2 decomposition, respectively. Repulsive effects on the surface clearly influence decomposition behavior, as the energetic minimum of O_2 on Pd(100) is observed for O_2*, and dissociation to two surface O species results in a net increase in energy. No dissociation for O_3 on Pd(100) is observed due to repulsive effects on the surface. Thus O_3* on Pd(100) is the final state for

that system. To compare this diagram to the main text, the energy difference indicated in Figure E.1 is equal to $n \times \Delta E$, where n is the number of O atoms on the surface.

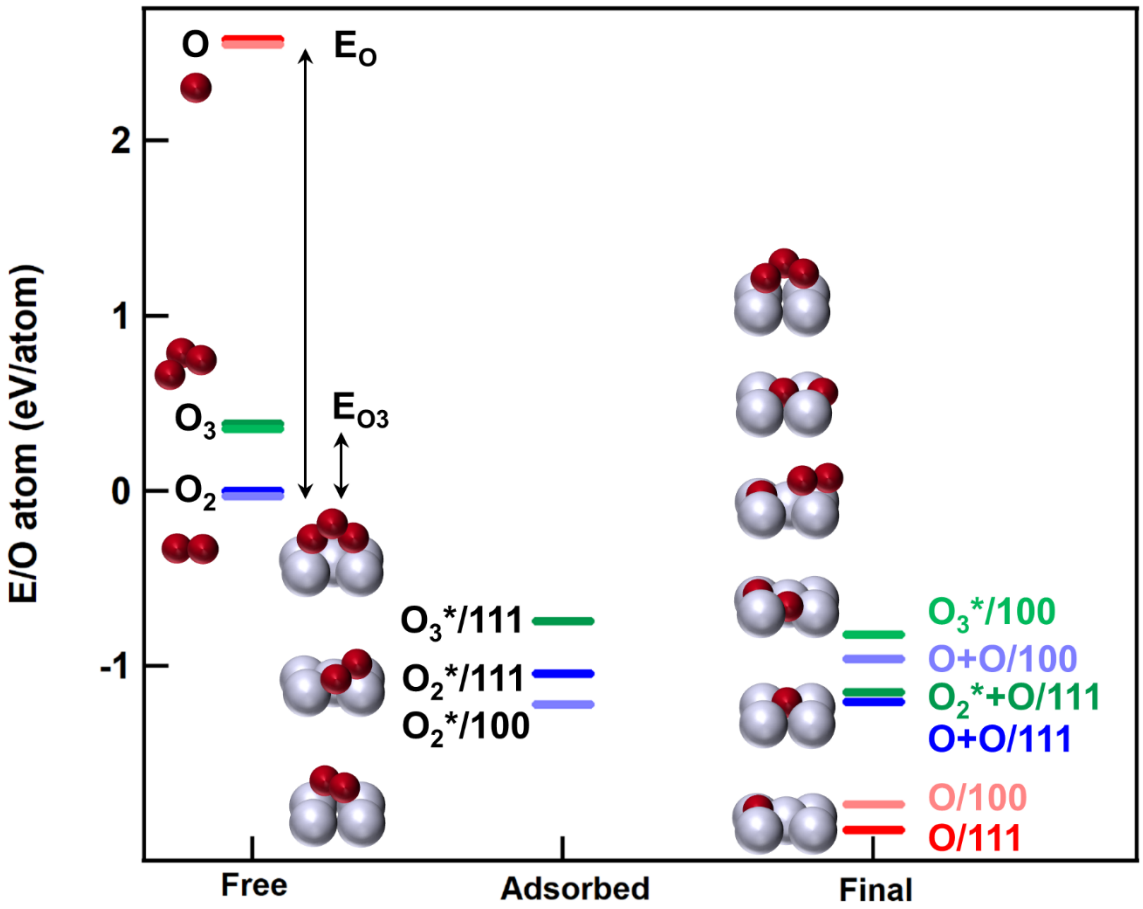

Figure E.1. Energetics per O atom of O, O_2 and O_3 are shown adsorbed onto clean Pd(111) and Pd(100) in three different states: the "free" molecule state, the "adsorbed" state, if it exists, and the "final" state, which represents the final step in the decomposition and adsorption reaction pathway. Geometric configurations are shown to the left of the "adsorbed" and "final" states, stacked according to the energy rows in a column.

Structural Results from DFT

Results of DFT calculations (interplanar Pd distances between the nth and (n + 1)th layer, $d_{n(n+1),}$ Pd-O distances, $d_{Pd\text{-}O}$, O-O distances, $d_{O\text{-}O}$, and adsorbed O height, z) of clean Pd(111) and Pd(100) slabs are listed in Table S1. The interplanar Pd spacing, d_{111} and $d_{100,}$ are calculated to be 2.247 Å and 1.946 Å, compared to measured values of d_{111} = 2.248 ± 0.001 Å and d_{100} = 1.955 ± 0.003 Å, respectively. For Pd(111), the interplanar distance between the first (n = 1) and second (n = 2) Pd atom layers, $d_{12,}$ expands by +0.2%, and relaxes back to the bulk interplanar distance gradually as d_{23} is +0.15%. A similar result is observed for Pd(100). This is consistent with other reports showing gradual expansion of interplanar distances as the surface-vacuum interface is approached.[1] Simulations of free molecular oxidants result in a bond distance, $d_{O\text{-}O}$ = 1.22 Å for O_2, and $d_{O\text{-}O}$, of 1.27 Å and bond angle, $d_{\angle}$, of 117.6°, for O_3, as shown in Table E.1. The experimental bond distances (and angle for O_3) are $d_{O\text{-}O}$ = 1.24 Å and $d_{O\text{-}O}$ = 1.27 Å (angle $d_{\angle}$ of 116.8°), for O_2 and O_3, respectively.[2]

Structural parameters after adsorption of O_x onto Pd(111) and Pd(100) slabs are also presented in Table S1. It is important to note that while O_2 will dissociate on clean Pd(111) at temperatures, T > 160 K, O_3 dissociatively adsorbs for all T based on the simulations herein. Because of this, values reported for O_3 are for the intermediate state unless stated otherwise. Further optimization of the intermediate state results in O_3 decomposition to O and O_2.

Table E.1. DFT structural results for (2×2) unit cells of Pd(100), and Pd(111), with O, O_2, and O_3 adsorbed onto the surfaces. Letter subscripts indicate the distance between the two species indicated. Number subscripts indicate distance associated with the nth atomic layer (i.e., d_{12} indicates the distance between the n = 1, and n = 2 atomic Pd layers).

Species	Surface	$d_{O\text{-}O}$ (Å)	$d_{Pd\text{-}O}$ (Å)	^1z (Å)	d_{12} (Å)	d_{23} (Å)	d_{34} (Å)
O_2		1.22					
O_3		1.27 ($d_\angle = 117.6°$)					
Pd	100				1.951	1.950	1.947
Pd/O	100		2.071	0.707	2.097	1.957	1.947
Pd/O_2	100	1.387	2.130	1.476	1.961	1.992	1.947
Pd/O_3	100	1.398	2.123	1.602	1.938	2.002	1.947
Pd	111				2.284	2.256	2.248
Pd/O	111		1.986	1.134	2.245	2.241	2.248
Pd/O_2	111	1.370	2.001	1.843	2.209	2.237	2.248
Pd/O_3	111	1.357	2.132	2.127	2.265	2.321	2.248

^1z refers to the equilibrium height of the adsorbed species relative to the surface plane of Pd atoms; for O_2 and O_3, this is the height of the O closest to the surface

O_3 adsorbed onto Pd(111) and Pd(100) is shown in Figure 4 in the main text, while structures of adsorbed O and O_2 onto Pd(111) and Pd(100) are shown in below. Atomic O, O_2 and O_3 adsorb to the hcp site at a height of 1.134 Å, 1.84 Å and 2.12 Å, respectively, on Pd(111), and 0.70 Å, 1.47 Å, and 1.60 Å, respectively, on Pd(100). When O_2 and O_3 adsorb to Pd(100), the interplanar distances d_{12} and d_{23} are +0.72%, and +2.31%, respectively, for O_2, and -0.46%, and +2.82%, respectively, for O_3. Similarly, for Pd(111), d_{12} and d_{23} for O_2 and O_3 adsorption are -1.73%, and -0.49%, respectively, for O_2, and -0.75%, and +3.24%, respectively, for O_3, indicating subsurface Pd atoms and electrons have a role in adsorption. Molecular O_2 and O_3 introduce additional repulsive steric effects on the surface, which causes the adsorbed height to increase by 108.5%, and 126.5%,

respectively, on Pd(100), and 62.5%, and 87.5%, respectively, on Pd(111), relative to O. Estimates for adsorption equilibrium heights, z, for O and O_2 are consistent with previous reports on Pd(100) as well as Pd(111).[3,4]

The adsorption height for O is lower than O_2 and O_3 due to the formation of Pd-O bonds associated with a 2D surface oxide. This surface oxide (O on Pd surfaces in Table E.1) has nominal bond distances of $1.96 < d_{Pd\text{-}O} < 1.98$ Å. A surface 2D oxide, Pd_5O_4, has been reported on Pd(111),[5] and a Pd-O bond distance of $d_{Pd\text{-}O} = 1.98$ Å has been reported for O adsorbed onto Pd(111) in a separate study.[6] The 2D oxide Pd_5O_4 is reported on Pd(111) at temperatures as low at 158 °C and does not have the spectral $3d_{5/2}$ feature at 336.7 eV that we observe is needed for ALE of Pd,[7] rather Pd_5O_4 has a $3d_{5/2}$ feature at 335.5 eV.[5]

Adsorbed structures of O and O_2 are shown in Figure E.2, where each image shows two unit cells in the x and y dimensions. Pd(111) structures are shown in the left column, while Pd(100) structures are shown in the right column. Atomic O, O_2, and O_3 are shown adsorbed onto each surface in the first, second, and third rows, respectively. Atomic O adsorbed onto Pd(111) and Pd(100) are similar, however, the adsorbed height of O is lower on the (100) surface compared to the (111) surface. This is due to the size of the hollow site available for adsorption. Molecular O_2 adsorbs to the same site that O does on both surfaces, however, the surface O_2 species is twisted, as indicated in Figure E.2(c), and S2(d). Minimal subsurface restructuring also occurs, where subsurface Pd atoms are slightly perturbed. Molecular O_3 adsorption structures are shown in Figure E.2(e), and (f). Again, O_3 adsorbs to the same hollow site, and O_3 is twisted on the surface, elongating compared to the free O_3 species. It is important to note that the structure shown for O_3 adsorbing onto Pd(111) is for an intermediate adsorption step. Continued optimization of the energy of the O_3/Pd(111) slab results in dissociation of O_3 to O and O_2. Dissociative

adsorption of O_3 is not observed on Pd(100), likely due to the smaller unit cell, when compared to Pd(111). However, it is likely to suspect that O_3 would dissociatively adsorb on a larger, 3×3, or 4×4, (100) unit cell.

Interestingly, larger oxidants (O_2 and O_3), which do not directly incorporate themselves into the Pd lattice, do not cause all interplanar distances to monotonically decrease into the bulk film (i.e. $d_{12} > d_{23} > d_{34}$). When O_2 and O_3 adsorb to Pd(100), the interplanar distances d_{12} and d_{23} are +0.72%, and +2.31% for O_2 and -0.46%, and +2.82% for O_3. Similarly, for Pd(111), d_{12} and d_{23} for O_2 and O_3 adsorption are -1.73%, and -0.49% for O_2, and -0.75%, and +3.24% for O_3. This is likely due to the contribution of subsurface Pd electrons to adsorption.

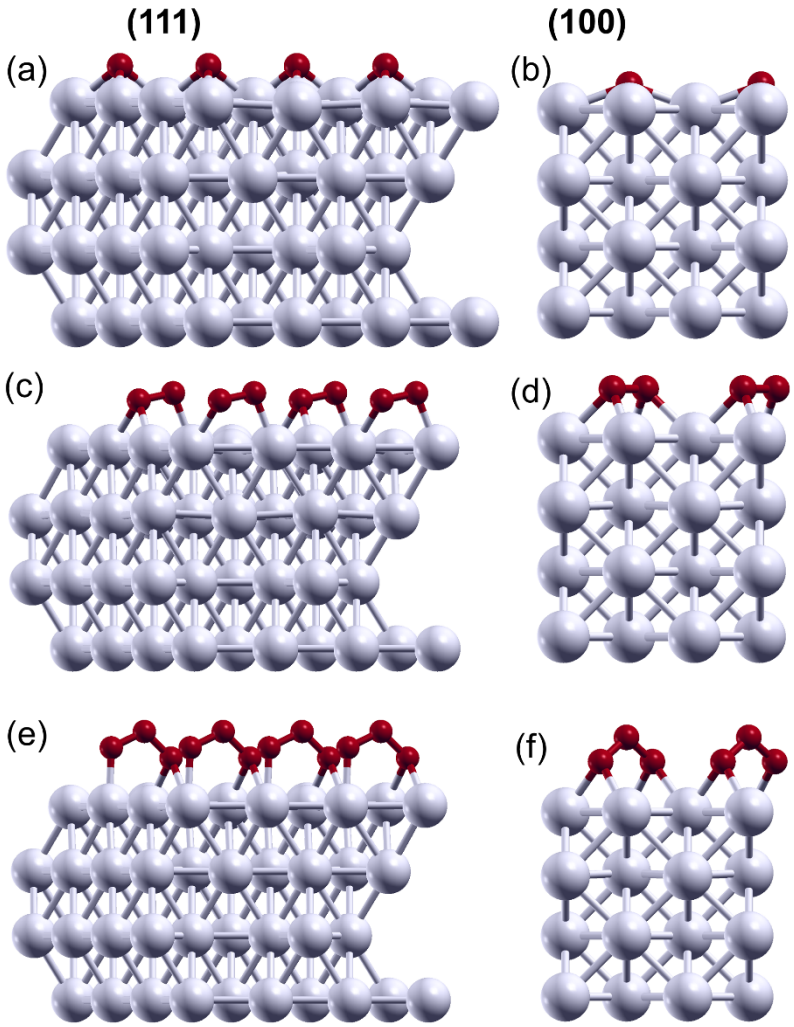

Figure E.2. O, O_2 and O_3 is shown adsorbed onto clean Pd(111) and Pd(100) in the left(a, c, and e), and right columns (b, d, f), respectively. The oxidants O, O_2 and O_3, are shown in the first (a, and b), second (c, and d), and third (e, and f) rows as well. The structure for O_3 adsorbed onto Pd(111) is an intermediate step, as continued optimization of the energy of the system results is dissociative adsorption. All structures shown are two unit cells in the *x* and *y* directions of the slab.

Optimized Pd structures with O placed in between Pd atomic planes are shown in Figure E.3. Structures are indicated by listing the number of O layers contained within Pd atomic planes. A single O layer is equivalent to a surface oxide (the same structure shown in Figure E.2(a) and (b)), while 2 O layers indicates O is on the surface as well as in between the $n = 1$ and $n = 2$ atomic Pd planes. Similarly, 3 O layers indicates O is on the surface, in between the $n = 1$, and $n = 2$ atomic planes, as well as between the $n = 2$, and $n = 3$ atomic planes. Structures with more O incorporated approximate a PdO(101) surface, which is observed to grow in oxidation experiments of Pd(111) and Pd(100).[8] This is most easily observed in the Pd(111) structure. There is significant perturbation by incorporating O into the structures, and the optimal O-Pd distance, $d_{\text{Pd-O}}$ is 1.98 Å, which agrees well with other reports.[6]

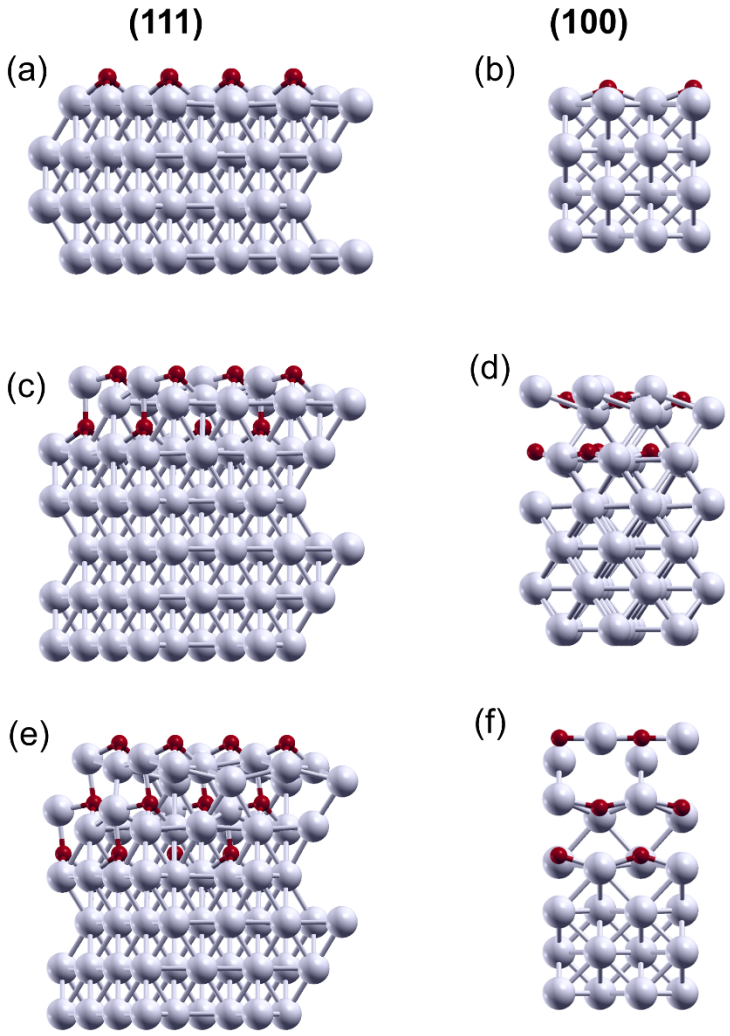

Figure E.3. Pd structures with optimized placement of O throughout the layers. Structures with 1 O layer have four Pd atomic planes, where the bottom two are fixed at the bulk position. Structures with 2 and 3 O layers have six Pd atomic layers, where the bottom two are again fixed at the bulk position. Pd(111) structures are shown on the left (a, c, and e), while Pd(100) is shown on the right (b, d, and f). 1, 2, and 3 O layers are shown in the first (a, and b), second (c, and d), and third (e, and f) rows, respectively. All structures shown depict 2 unit cells in the *x* and *y* directions (in plane) of the surface.

ALE cycles with O_2 only and VUV/O_2

ALE employs VUV/O_2 co-exposure to cause PdO_x to form, which is etched by HCOOH exposure.[7] Figure E.4 shows XRR before and after exposure to 5 ALE cycles where the oxidation half-cycle is accomplished with co-exposure of VUV/O_2 for 3 min at 1 Torr and 100 °C in the blue curve, and exposure of O_2 for 3 min at 1 Torr and 100 °C in the red curve. Etching half-cycles are 30 s exposures to HCOOH at 0.5 Torr in both samples. A figure depicting the stack of the substrate is shown inset in Figure E.4. The thickness before and after 5 VUV/O_2 ALE cycles is 234, and 218 Å, respectively. The thickness before and after etching with 5 thermal O_2 ALE cycles is the same (224 Å). There is a clear shift in reflections for the VUV/O_2 oxidized sample, where there is no discernable difference between the sample before and after etching for thermal O_2 exposure. Clearly the 2D oxide that forms on the surface of Pd from O_2 alone is unable to be removed by HCOOH exposure, indicating that Pd^{2+} must be formed for etching to take place.

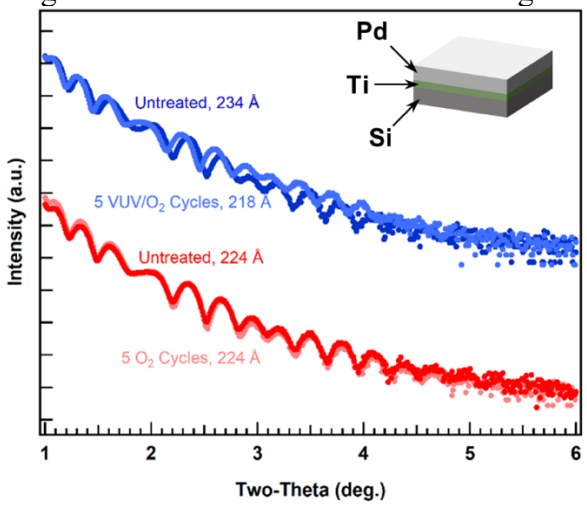

Figure E.4. XRR before and after 5 ALE cycles where 20 nm Pd is exposed to O_2 at 1 Torr and 100 °C for 3 min either with VUV light (top, blue curve), or no VUV light (bottom, red curve). Etching half cycles are 30 s exposures to 0.5 Torr of HCOOH at 100 °C as well. The XRR corresponding to the sample before any treatment is shown as well as the thickness, obtained from fitting the XRR curve. The Pd/Ti/Si heterostructure is shown inset for context.

Projected Density of State Analysis

Bonding of O_3 onto the resulting surface for incorporating O into Pd(111) can be seen in Figure E.5. PDOS and $\Delta\rho$ are seen in the left and right columns, respectively, where the rows show 1, 2, and 3 O layers, respectively, as well. Recruitment of deep electrons are observed in all three cases of O layer incorporation. These are seen in the O p states between 6-8 eV below E_f. These electrons likely do not participate in adsorption (as they are evident in Figure E.5(a)), however, they likely contribute to better charge transfer from subsurface atoms. This is evidenced in the differential charge density accompanying each adsorption scenario, where electrons are easily seen to be perturbed from deep Pd atomic layers.

The Pd surface that is most active towards O_3 bonding (i.e., the strongest covalent bond) is shown in the Fermi energy plot, in Figure E.5(g). 3 O layers allow the most covalent character to be seen in adsorbed O_3, which is clear from the greater charge transfer in Figure E.5(f), complemented by larger number of O p states 6 eV below E_f. This is consistent with the observation that O_3 is predicted to dissociatively adsorb onto the 3 O layer structure, due to the ease with which O can be incorporated into the surface. The same behavior is not observed on Pd(100). The structure with the most available states is clear Pd with 3 O layers, however, the difference in DOS between 1, 2, and 3 O layers is minimal, when compared against a bare Pd(111) or Pd(100) surface.

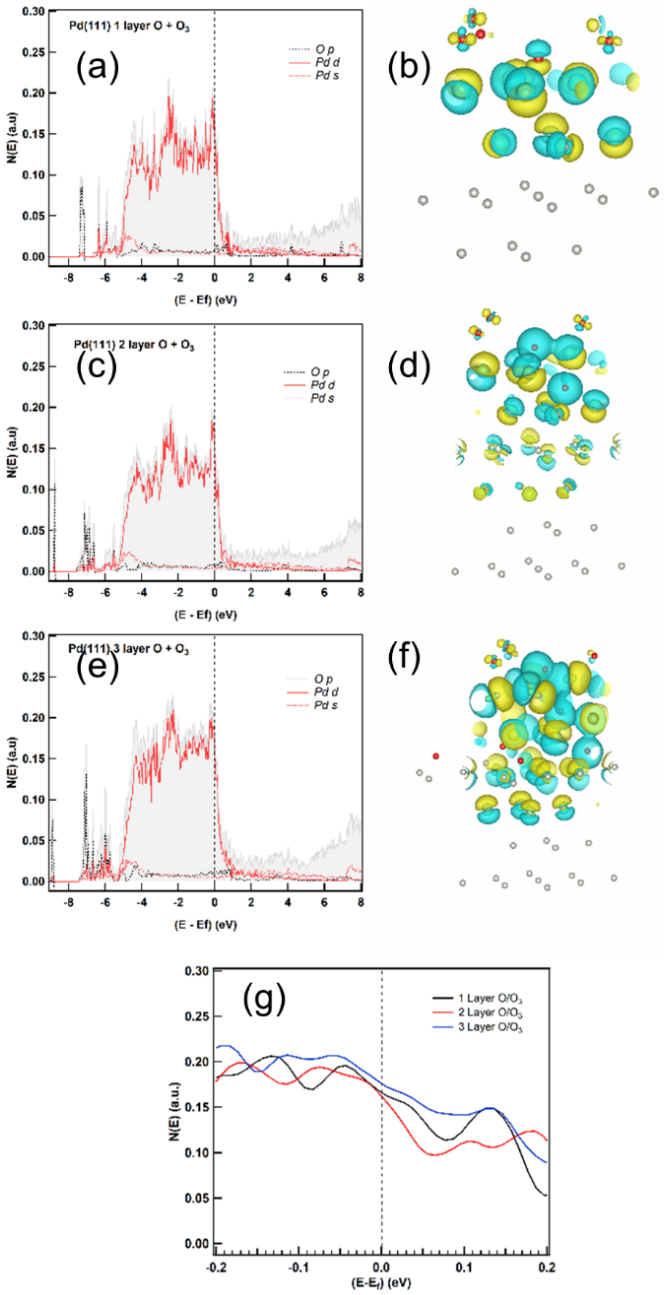

Figure E.5. Varying levels of O incorporation into the Pd(111) surface and the effect on the DOS, PDOS and Δρ for O_3/Pd(111). (a), (c), and (e), show the PDOS for O_3 adsorbing onto Pd(111) with 1, 2, and 3 O layers incorporated, where (b), (d), and (f), are the corresponding differential charge density diagrams (Δρ = 0.031e/bohr^3). Panel (g) shows the total DOS for the 1, 2, and 3 O layered systems.

O_3 adsorbing onto Pd(100) with varying levels of O incorporation is shown in Figure E.6, where 1, 2, and 3 O layers are seen in (a), (c), and (d), respectively, with accompanying differential charge density plots shown in (b), (d), and (f). The total DOS in the vicinity of E_f is shown in (g). A similar case as that observed on the Pd(111) surface is seen for Pd(100), where the most covalent bonds are formed with adsorption of O_3 onto the highest O content surfaces (3 O layers). Increasing the number of O layers also has a large effect on $\Delta\rho$, where charge transfer is propagated from deep substrate layers to the surface. This indicates an effective potential is induced with the more PdO_x character in the substrate. The effective potential appears to facilitate charge transfer, and aid in adsorption.

Comparing to the total DOS for Pd(111), there is also a large disparity between the total DOS for 3 O layers and 2 O layers, where 3 O layers exhibits a greater enhancement in the total number of states of Pd(100) compared to Pd(111). Overall, decomposition of O_3 on Pd surfaces is inhibited for 1 and 2 O layers of incorporation, and enhanced for 3 layers of O incorporation. This indicates a "sticking point" exists, where and energetic barrier must be overcome in order to PdO_x to continue growing if O_3 were to be responsible for PdO_x formation.

Molecular O_2 is shown bonding onto Pd(100) and Pd(111), where the PDOS and $\Delta\rho$ are shown for 1, 2, and 3 O layers incorporated in Figures S7, and S8, respectively. On Pd(100), covalent bonds are formed easily for all layers of incorporation, as evidenced by the total DOS in Figure E.7(g). However, bonding appears to be less favored as the amount of O increases to 2 and 3 O layers. Interestingly, there is a large increase in Pd *d*-band resonance for 1 and 3 O layers of incorporation, indicating favorable hybridization between O_2 and the substrate, which is also evidenced by the charge difference shown with each respective adsorption condition. For Pd(111), there is not much difference in covalent

bonding or charge transfer for 1 or 2 O layers incorporated. When 3 O layers are incorporated, it is accompanied by a large increase in Pd *d*-band resonance. This indicates favorable bonding, which is substantiated by the total DOS shown in (g). This also suggests that further decomposition of O_2 is predicted on Pd(111) for 3 O layers, which is similar to the predicted behavior of O_3 on Pd(111) with 3 O layers as well.

PDOS and $\Delta\rho$ for O adsorbed onto Pd(100) and Pd(111) is shown in Figures S9, and S10, respectively. The largest effect on PDOS is seen in O adsorbing onto 3 O layers for both Pd(100) and Pd(111), where the Pd *d*-band resonance is large as well as the total number of states in the *d*-band region. This is clear from the differential charge density figures in shown in (f) for both Pd(111) and Pd(100).

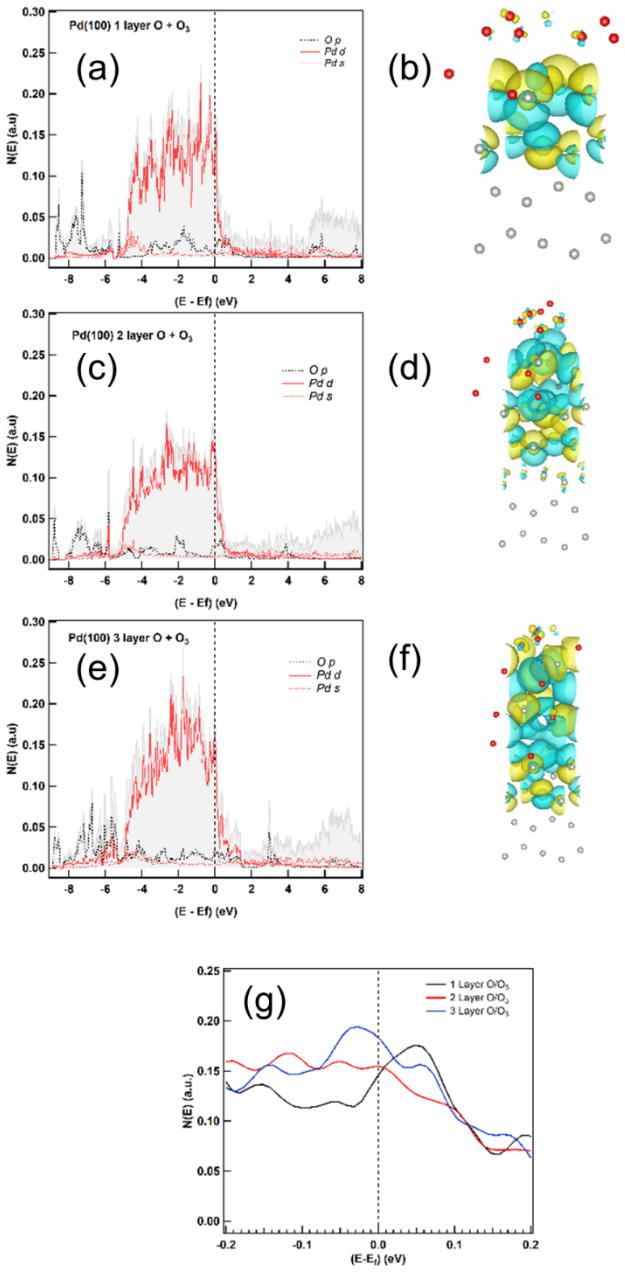

Figure E.6. Varying levels of O incorporation into the Pd(100) surface and the effect on the DOS, PDOS and Δρ for O_3/Pd(100). (a), (c), and (e), show the PDOS for O_3 adsorbing onto Pd(100) with 1, 2, and 3 O layers incorporated, where (b), (d), and (f), are the corresponding differential charge density diagrams (Δρ = 0.031e/bohr^3). Panel (g) shows the total DOS for the 1, 2, and 3 O layered systems.

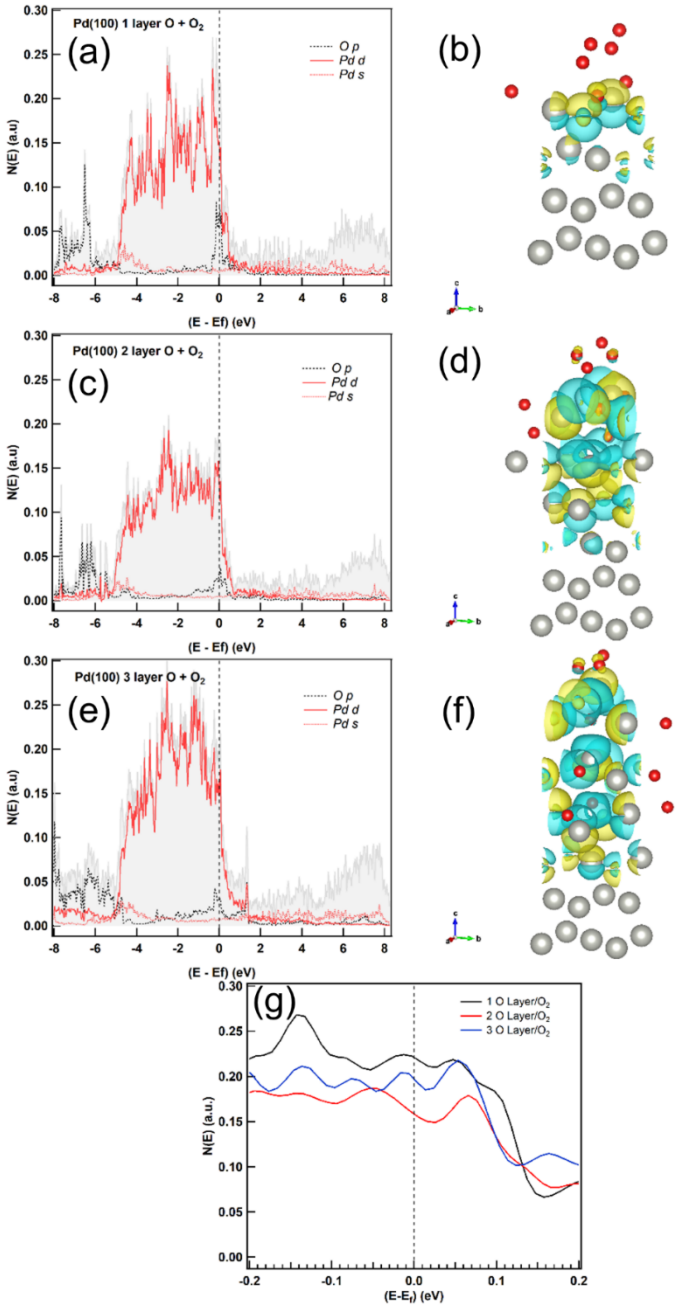

Figure E.7. Varying levels of O incorporation into the Pd(100) surface and the effect on the DOS, PDOS and Δρ for O_2/Pd(100). (a), (c), and (e), show the PDOS for O_2 adsorbing onto Pd(100) with 1, 2, and 3 O layers incorporated, where (b), (d), and (f), are the corresponding differential charge density diagrams (Δρ = 0.031e/bohr^3). Panel (g) shows the total DOS for the 1, 2, and 3 O layered systems.

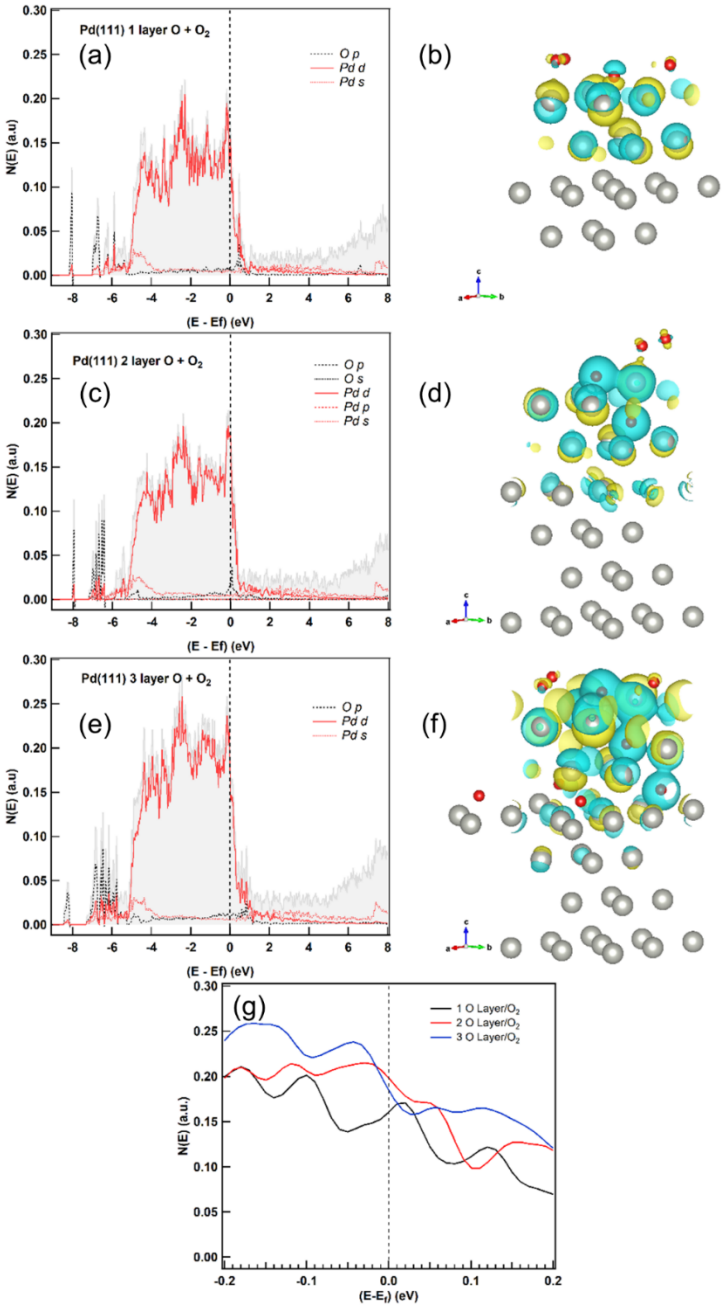

Figure E.8. Varying levels of O incorporation into the Pd(111) surface and the effect on the DOS, PDOS and Δρ for O_2/Pd(111). (a), (c), and (e), show the PDOS for O_2 adsorbing onto Pd(111) with 1, 2, and 3 O layers incorporated, where (b), (d), and (f), are the corresponding differential charge density diagrams (Δρ = 0.031e/bohr^3). Panel (g) shows the total DOS for the 1, 2, and 3 O layered systems.

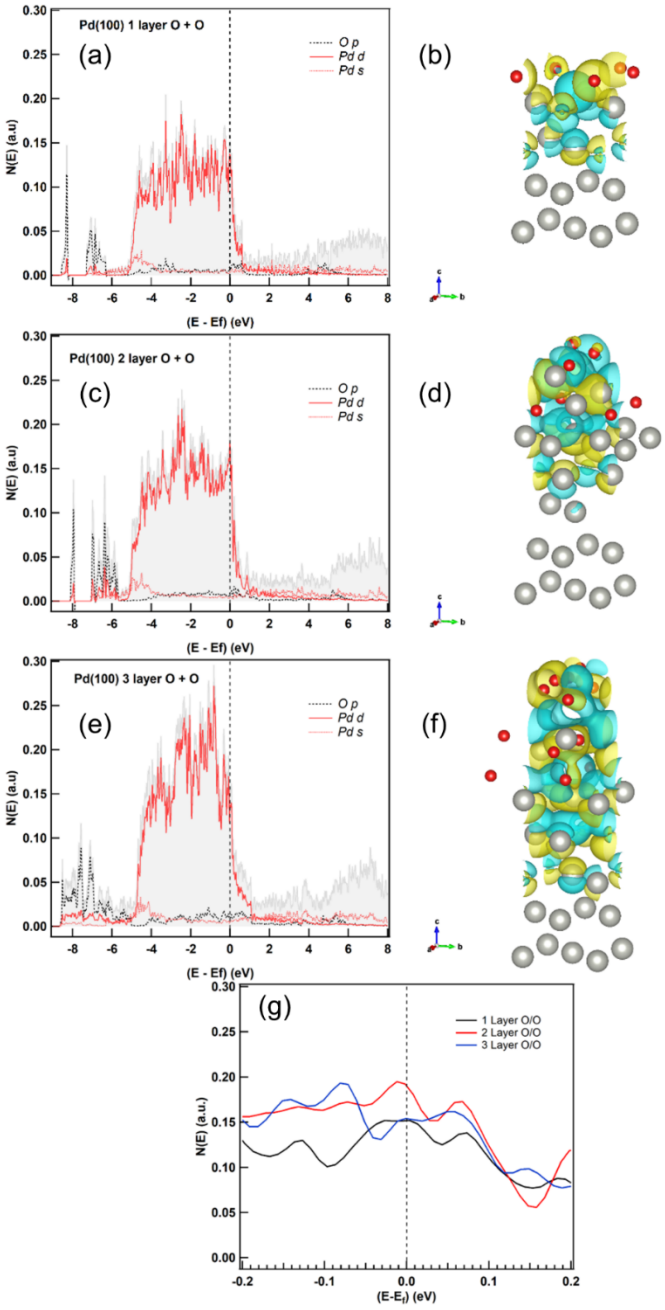

Figure E.9. Varying levels of O incorporation into the Pd(100) surface and the effect on the DOS, PDOS and Δρ for O/Pd(100). (a), (c), and (e), show the PDOS for O adsorbing onto Pd(100) with 1, 2, and 3 O layers incorporated, where (b), (d), and (f), are the corresponding differential charge density diagrams (Δρ = 0.031e/bohr^3). Panel (g) shows the total DOS for the 1, 2, and 3 O layered systems.

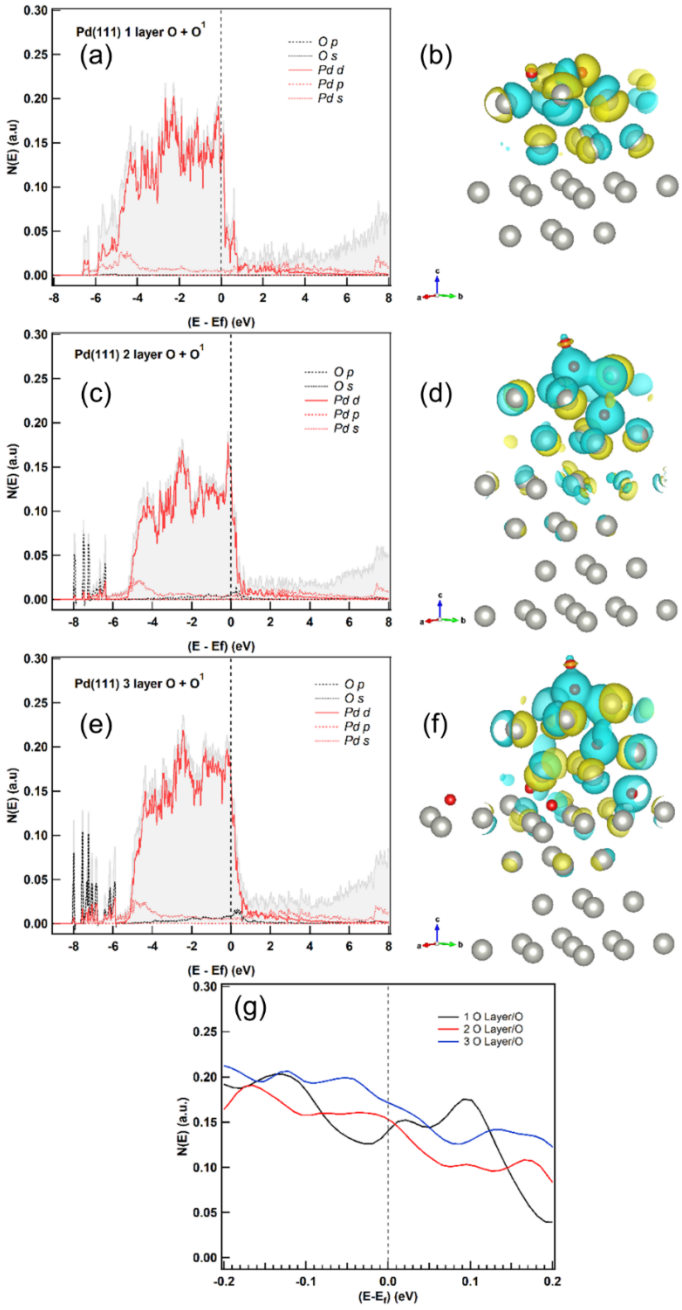

Figure E.10. Varying levels of O incorporation into the Pd(111) surface and the effect on the DOS, PDOS and Δρ for O/Pd(111). (a), (c), and (e), show the PDOS for O adsorbing onto Pd(111) with 1, 2, and 3 O layers incorporated, where (b), (d), and (f), are the corresponding differential charge density diagrams (Δρ = 0.031e/bohr^3). Panel (g) shows the total DOS for the 1, 2, and 3 O layered systems.

REFERENCES

(1) Todorova, M.; Reuter, K.; Scheffler, M. Oxygen Overlayers on Pd(111) Studied by Density Functional Theory. *J. Phys. Chem. B* **2004**, *108* (38), 14477–14483.

(2) Linstrom, P. NIST Chemistry WebBook, NIST Standard Reference Database 69, 1997.

(3) Honkala, K.; Laasonen, K. Ab Initio Study of O2 Precursor States on the Pd(111) Surface. *J. Chem. Phys.* **2001**, *115* (5), 2297–2302.

(4) Naito, K.; Nakamura, M.; Sakata, O.; Hoshi, N. Surface X-Ray Scattering of Pd(111) and Pd(100) Electrodes during the Oxygen Reduction Reaction. *Electrochemistry* **2011**, *79* (4), 256–260.

(5) Gabasch, H.; Unterberger, W.; Hayek, K.; Klötzer, B.; Kleimenov, E.; Teschner, D.; Zafeiratos, S.; Hävecker, M.; Knop-Gericke, A.; Schlögl, R.; Han, J.; Ribeiro, F. H.; Aszalos-Kiss, B.; Curtin, T.; Zemlyanov, D. In Situ XPS Study of Pd(111) Oxidation at Elevated Pressure, Part 2: Palladium Oxidation in the 10−1mbar Range. *Surf. Sci.* **2006**, *600* (15), 2980–2989.

(6) Plauck, A.; Stangland, E. E.; Dumesic, J. A.; Mavrikakis, M. Active Sites and Mechanisms for H_2O_2 Decomposition over Pd Catalysts. *Proc. Natl. Acad. Sci.* **2016**, *113* (14), E1973–E1982.

(7) Coffey, B. M.; Nallan, H. C.; Engstrom, J. R.; Lam, C. H.; Ekerdt, J. G. Vacuum Ultraviolet Enhanced Oxidation - A Route to the Atomic Layer Etching of Palladium Metal. *Chem. Mater.* **2020**, 32, 14, 6035–6042.

(8) Seriani, N.; Harl, J.; Mittendorfer, F.; Kresse, G. A First-Principles Study of Bulk Oxide Formation on Pd(100). *J. Chem. Phys.* **2009**, *131* (5), 054701.

APPENDIX F

Supplementary information experimental investigation of ALE of Pd (2 and 20 nm Pd).

Power spectral density analysis of topography

The morphology changes due to thermal sources (i.e., dewetting) and changes incurred during the VUV oxidation process are explored using one Pd(20)/p-Si film and another Pd(20)/Ti(10)/p-Si film. Pd(20)/p-Si is exposed to 1 Torr of O_2 at 200 °C for 45 min, while Pd(20)/Ti(10)/p-Si is co-exposed to VUV and 1 Torr O_2 at 100 °C for 5 min (Figure F.1(a) and F.1(b), respectively). Height profiles indicated by dashed lines are shown beneath each AF micrograph (Figure F.1(c) and F.1(d)). While the height profiles show much variation between the two oxidation conditions, the roughness is minimally changed, where the O_2 thermal exposure and co-exposure to VUV and O_2 have R_a values of 15.3 A and 6.3 A, respectively. For a self-affine surface, which these are expected to be, plotting the 1D linear power spectral density (PSD) against the spatial frequency yields two regions: (1) a horizontal region due to the absence of correlation, and (2) region with negative slope, indicating the self-affine nature of the film.[1] The intersection of these two curves provides a correlation length for the film. The correlation length for O_2 thermal exposure is 0.381 nm^{-1} (Figure F.1(e)) , whose reciprocal is 2.6 nm. The intersection of the two regions in the PSD shown in Figure F.1(f) indicates a characteristic length > 200 nm. A larger AF micrograph would need to be obtained to present this value more precisely. The results from the PSD's indicates Pd(20) exposed to O_2 at 200 °C results in a less uniform surface when compared to oxidation via VUV.

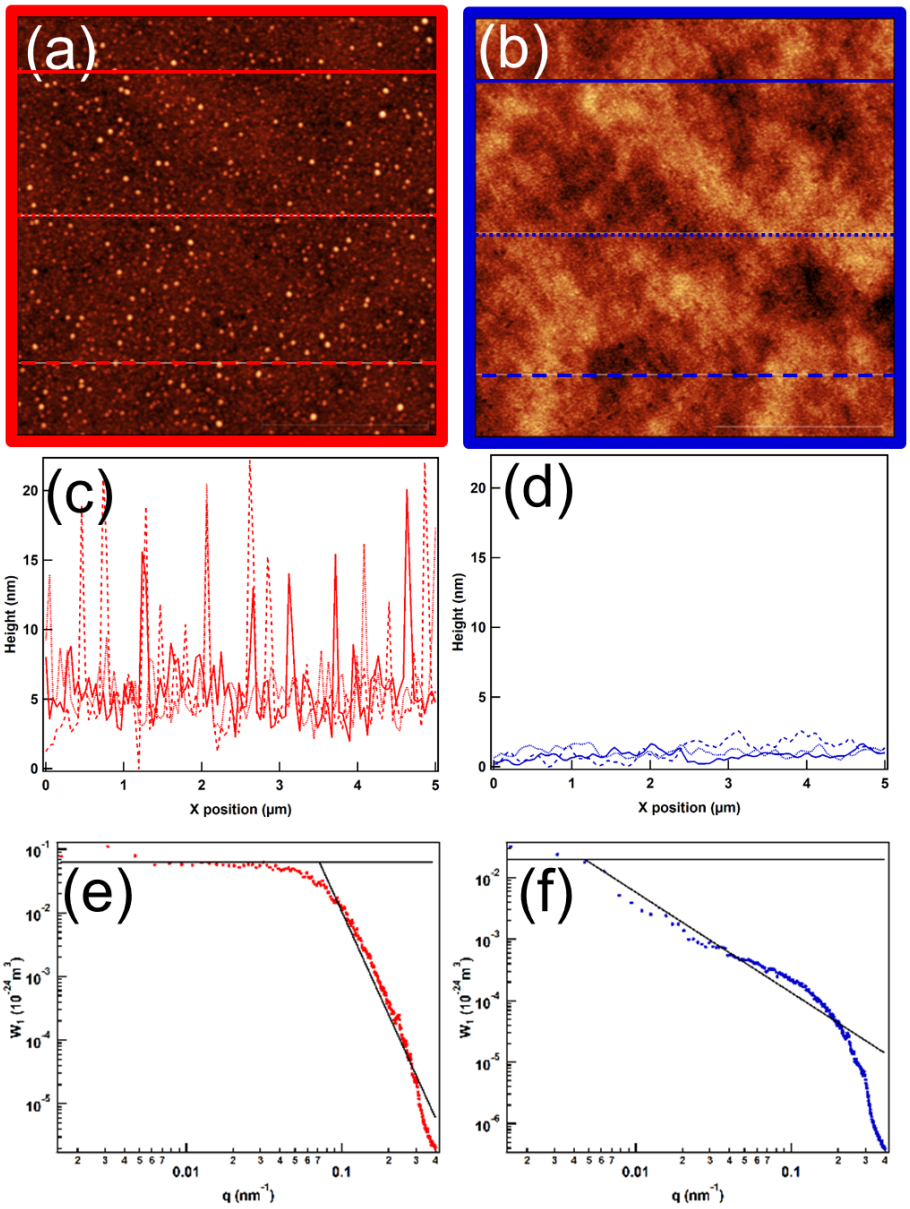

Figure F.1. The same two AF micrographs are shown in Figure 4 of the main text are shown here with line scan profiles, as well as 1D linear PSD curves. (a) is of Pd(20)/p-Si that has been exposed to 1 Torr of O_2 at 200 °C for 45 min, while (b) is of Pd(20)/Ti(10)/p-Si that has been exposed to VUV/O_2 at 100 °C for 5 min. (c) and (e) correspond to height profiles shown in (a) and the 1D linear PSD of the AF micrograph shown in (a), respectively. Similarly, (d) and (f) are the height profiles and 1D linear PSD of (b). AF micrographs have the same height scale and are 5×5 μm^2.

APPENDIX G

Supplementary information for the ALE of Ru.

XRD Informing the DFT Model

Three features in the 2θ-ω scan are show in Figure G.1. The three Ru features are located at 38.54°, 42.23°, and 44.008°, which correspond to Ru(100), Ru(002), and Ru(101), respectively. These positions correspond to interplanar spacing, d_{hkl}, of the (002) and (101) facets of 2.155, and 2.048 Å, respectively.

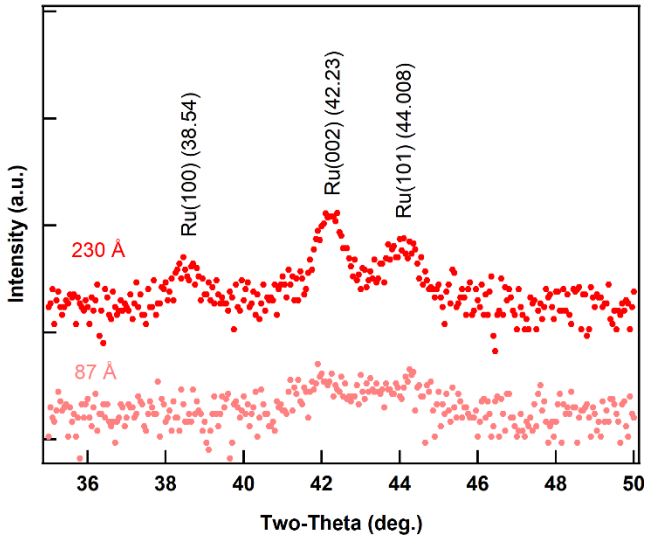

Figure G.1. XRD pattern of Ru as sputtered, where the sputtered thickness is measured using XRR, and indicated in the figure, above the curve on the left. Three Ru features are indicated, Ru(100), Ru(002), and Ru(101), with the respective position of the Gaussian fit shown with each label.

Structural Results from DFT

Structural results of DFT calculations (interplanar Ru distances between the *n*th and (*n* + 1)th layer, $d_{n(n+1),}$ Ru-O distances, $d_{Ru\text{-}O}$, O-O distances, $d_{O\text{-}O}$, and adsorbed O height, *z*) of clean Ru(101) and Ru(002) slabs are listed in Table G.1. Clean Ru(101) and Ru(002) exhibit a similar expansion of the lattice as the vacuum/surface interface is approached. The interplanar distances contract by -4.68%, and -1.43% for d_{12}, and d_{23}, respectively, for Ru(002). This trend is not monotonic for Ru(101), most likely due the fact that the unit cell is more complicated. For Ru(101), d_{12}, and d_{23} change by -4.39%, and 2.68%, respectively. This is in agreement with other DFT reports as well.[1–4] Bulk (101), and (002) interplanar spacing are modeled to be 2.048, and 2.156 Å, respectively. The interplanar spacing of the (101), and (002) facet` is measured experimentally as 2.055, and 2.138 ± 0.005 Å, respectively.

Structural results after oxidant adsorption onto Ru are also seen in Table G.1. It is important to note that for oxidants that are predicted to dissociatively adsorb (O_2, and O_3), the structural adsorption geometries and energies are calculated from optimization of the Ru slab around the initial adsorption event, while freezing all O atoms. This is done as continued energy optimization results in dissociation. Examining Ru(002), the adsorption height of O decreases with the number of O atoms on the surface, consistent with increased repulsion from more O atoms on the surface.

Adsorbing atomic O onto either the (002) or (101) surface results in expansion of near surface layers to accommodate surface O. This is indicated by $d_{12,}$and d_{23} changing by 0.1%, and -0.5%, respectively for Ru(002). Similarly, d_{12} and d_{23} change by 0.9% and 1.6% when atomic O adsorbs onto Ru(101). This is consistent with restructuring, and expansion of the lattice, to accommodate O, and facilitate formation of RuO_x in the near surface region. The distance of the Ru-O bond, $d_{Ru\text{-}O}$, is 2.01, and 1.90 Å, for (002), and

(101) surfaces, respectively. The distance of an Ru-O bond, $d_{Ru\text{-}O}$, in RuO_2 is calculated to be between $1.96 < d_{Ru\text{-}O} < 2.005$ Å. All of which are similar to other DFT reports.[5]

All oxidants have a similar effect on surface restructuring, with O_2 exhibiting a larger subsurface expansion to accommodate the adsorbing molecule. The interplanar spacing d_{23} is largest at 2.26 for O_2 adsorbing onto Ru(002), compared to 2.144, and 2.181 Å, for O, and O_3, respectively. Ru-O bond distances are estimated to be 2.014, 2.019, and 1.995 for O, O_2, and O_3, respectively. This is approximately the estimated equilibrium Ru-O distance for RuO_2, which has distances ranging from $1.96 < d_{Ru\text{-}O} < 2.005$ Å.[4,5]

O_3 adsorption restructures the surface, where the (002) interplanar spacing changes by -0.2%, and 1.15%, and the (101) interplanar spacing changes by 2.7%, and 4.0%. The final equilibrium height for O adsorbed onto Ru(002) and Ru(101) is calculated to be 1.15, and 1.18 Å, respectively, while for O_3 it is 1.77, and 1.82 Å, respectively. While there are no reports of O_3 adsorbing onto Ru surfaces, the results for atomic O adsorption are in good agreement with previous reports.[1,5,6] We wish to note that, while this report is not meant to be an in-depth study of all aspects of the oxidation mechanism of thin Ru films with co-exposure to VUV/O_2 (i.e., configuration, surface diffusion, adsorption sites, stepped surfaces, etc.), it is worthwhile to note that O adsorbs to the fcc site on bare Ru(002) surfaces, where subsequent O adsorption occurs at the hcp site. A similar case is observed for the Ru(101) surface, where rows of ordered O adsorption are predicted rather than uniform occupation of surface sites, which is observed experimentally in other reports as well.[7–9]

Table G.1. Results of DFT calculations of oxidants O, O_2, and O_3 adsorbing onto Ru(101), and Ru(002). Distances are indicated by letters when the instance is indicated between two atoms, and numbers when the distance is between planes of a Ru slab. The numbers indicate between which two atom layers the spacing refers (i.e., d_{12} refers to the distance between the n = 1, and 2, atomic layers).

Species	Surface	$d_{O\text{-}O}$ (Å)	$d_{Ru\text{-}O}$ (Å)	^1z (Å)	d_{12} (Å)	d_{23} (Å)	d_{34} (Å)
O_2		1.223					
O_3		1.278 ($d_{\angle} = 117.6°$)					
Ru	002				2.055	2.125	2.156
Ru/O	002		2.014	1.157	2.156	2.144	2.156
Ru/O_2	002	1.352	2.019	1.533	2.174	2.260	2.156
Ru/O_3	002	1.551-1.353 ($d_{\angle} = 107.3°$)	1.995	1.777	2.151	2.181	2.156
Ru	101				1.958	2.103	2.048
Ru/O	101		1.903	1.184	2.068	2.082	2.048
Ru/O_2	101	1.514	1.972	1.845	1.995	2.073	2.048
Ru/O_3	101	1.461-1.560 ($d_{\angle} = 99.7°$)	2.046	1.827	2.104	2.131	2.048
	^1z refers to the equilibrium height of the adsorbed species relative to the surface plane of Pd atoms; for O_2 and O_3, this is the height of the O closest to the surface						

Adsorption Energetics onto Bare Ru(101), and Ru(002)

Adsorption energies of atomic O, O_2, and O_3 on Ru(002) and Ru(101) are reported in Table G.2, and O and O_3 adsorption is shown in Figure G.2. Other DFT reports estimate adsorption of atomic O on Ru has an adsorption energy of 5.32 –5.37 eV, and 5.15 – 5.26 eV on Ru(101) with 0.50, and 1.0 ML O coverage,[1,3] and 5.64 – 6.28 eV, and 5.52 – 5.43 eV, and 4.78 – 5.07 eV on Ru(002) with 0.25, 0.50, and 1.0 ML O coverage, respectively.[1,3,4,10] We find E_{ads} for atomic O on the bare (002) and (101) surfaces is 6.07, and 5.63 eV, respectively, in agreement with previous reports. Adsorption is favored on the (002) surface, as the hcp site is favored for adsorption with minimal surface reconstruction, also observed in results of structural calculations. Adsorption of O_2 and O_3 is exothermic, as E_{ads} is 2.40, and 4.67 eV, respectively, on Ru(002), and 3.61, and 3.48 eV, respectively, on Ru(101). While both molecular species adsorb strongly to both Ru surfaces in this study, dissociative adsorption on bare Ru surfaces is energetically favored for both O_2, and O_3, where a surface with 0.50 ML O coverage is predicted for all O_2 adsorption calculations, and a surface with 0.75 ML O coverage is predicted for all O_3 adsorption calculations. E_{ads} of optimized O locations for complete dissociative adsorption on Ru(002) is 5.94, and 6.38 eV, for O_2, and O_3, respectively, and 6.46. and 10.15 eV for O_2, and O_3, respectively, on Ru(101). This indicates, while adsorption precedes decomposition, that the Ru surface is efficient at dissociating both O_2, and O_3, and the formation of surface RuO_x is facile.

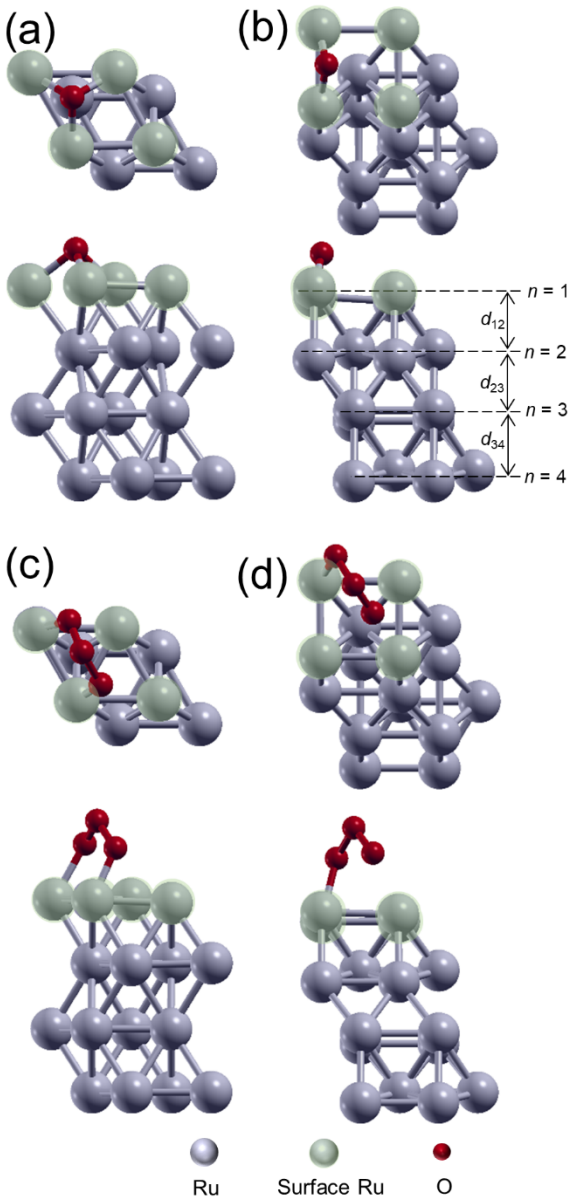

Figure G.2. Top and views of Ru(002), and Ru(101) 2×2 unit cells with atomic O is adsorbed are seen in (a), and (b), respectively. O_3 adsorbed onto Ru(002), and Ru(101) are seen in (c), and (d), respectively. Surface Ru atoms are indicated in both top and side views with a light green spheres, while O atoms are smaller red spheres. Silver spheres are Ru atoms. Relevant interplanar distances are indicated in (b), which correspond to the discussion in the text.

It appears the Ru surface can uptake O and this likely results in saturation after a short time, which we note is needed for ALE to proceed. This is consistent with other reports that demonstrate RuO_2 formation with O_2 at temperatures > 400 °C,[11] and motivates the requirement for atomic O to facilitate oxidation of Ru at low temperatures.

Table G.2. DFT results for adsorption of O, O_2, and O_3 on 2×2 Ru(002), and 2×2 Ru(101). The adsorption energy is shown with the energy normalized to number of O atoms shown parenthetically to the right. The reactions are indicated in the far right column. Subscripts on O indicate the equilibrium site

Species	Surface	Cell	E_{ads} (eV)	Reaction
Ru/O	002	2×2	6.07	O-g + Ru(002) → O/ Ru(002)
[1]Ru/O_2	002	2×2	2.40 (1.20)	O_2-g + Ru(002) → O_2*/ Ru(002)
Ru/O + O	002	2×2	5.94 (2.97)	O_2-g + Ru(002) → O_{hcp} + O_{fcc} / Ru(002)
[1]Ru/O_3	002	2×2	4.67 (1.55)	O_3-g + Ru(002) → O_3*/ Ru(002)
Ru/O_3	002	2×2	6.38 (2.12)	O_3-g + Ru(002) → 3O/ Ru(002)
Ru/O	101	2×2	5.63	O-g + Ru(101) → O/ Ru(101)
[1]Ru/O_2	101	2×2	3.61 (1.80)	O_2-g + Ru(101) → O_2*/ Ru(101)
Ru/O + O	101	2×2	6.46 (3.23)	O_2-g + Ru(101) →O_{br} + O_{fcc}/ Ru(101)
[1]Ru/O_3	101	2×2	3.48 (1.16)	O_3-g + Ru(101) → O_3*/ Ru(101)
Ru/O_3	101	2×2	10.15 (3.38)	O_3-g + Ru(101) → 3O/ Ru(101)

[1]Adsorbed molecular oxidants are indicated, distinct from the energetically favorable dissociation to oxygen atoms

*Indicates an adsorbed species

Adsorption Energetics and Structures for O layered Ru systems

E_{ads} for O_2, and O_3 adsorbing onto the O layered structures are given in Table G.3, where E_{ads} per O atom are shown parenthetically next to E_{ads}. While adsorption is made less favorable by the presence of a 2D surface oxide, it is still exothermic, likely owing to the tendency to form an Ru surface with 0.75 ML coverage that is observed when O_3 dissociatively adsorbs to clean Ru surfaces (Table G.2). E_{ads} does not monotonically decrease, however, as the trend in E_{ads} has a local minimum when 2 O layers are incorporated on Ru(002), and when 3 O layers are incorporated on Ru(101). Adsorption of O_3 is exothermic for all amounts of O layer incorporation, where E_{ads} decreases for higher O incorporation. This is likely due to repulsive effects on the surface.

Table G.3. DFT Results of adsorbing O, O_2, and O_3 onto Ru(002), and Ru(101) are shown. The number of O layers is indicated for each Ru slab. Adsorption energy, E_{ads}, is shown normalized to the number of O atoms in parentheses as well.

	Ru(101)		Ru(002)	
Species	*n* O layers	E_{ads} (eV)	*n* O layers	E_{ads} (eV)
Ru/O_2	1	1.72 (0.86)	1	1.60 (0.80)
Ru/O_3	1	2.66 (0.88)	1	2.55 (0.85)
Ru/O_2	2	3.13 (1.56)	2	1.95 (0.97)
Ru/O_3	2	2.58 (0.86)	2	2.31 (0.77)
Ru/O_2	3	1.41 (0.70)	3	1.81 (0.90)
Ru/O_3	3	1.75 (0.58)	3	1.39 (.46)

It is also worthwhile to note that, while O_3 adsorbs to clean Ru to form a surface with 0.75 ML O surface coverage, this appears to be the largest O loading predicted. This is evidenced by the dissociative adsorption of O_3 to form adsorbed O_2 and O. Thus it appears that O_3 is likely a good source of O for oxidation of Ru, which is consistent with other reports of etching of Ru via formation of RuO_4,[12] however, we note that Ru is not etched via RuO_4 formation with VUV/O_2, so there is likely a pressure or temperature dependence of O_3 to facilitate RuO_4 formation.

References

(1) Schwegmann, S.; Seitsonen, A. P.; De Renzi, V.; Dietrich, H.; Bludau, H.; Gierer, M.; Over, H.; Jacobi, K.; Scheffler, M.; Ertl, G. Oxygen Adsorption on the Ru(10$\bar{1}$0) Surface: Anomalous Coverage Dependence. *Phys. Rev. B* **1998**, *57* (24), 15487–15495.

(2) Stampfl, C.; Scheffler, M. Theoretical Study of O Adlayers on Ru(0001). *Phys. Rev. B* **1996**, *54* (4), 2868–2872.

(3) Petrova, N. V.; Yakovkin, I. N. Binding Energies for Oxygen on Transition Metal Surfaces. *Surf. Rev. Lett.* **2012**.

(4) Kim, Y. D.; Seitsonen, A. P.; Wendt, S.; Wang, J.; Fan, C.; Jacobi, K.; Over, H.; Ertl, G. Characterization of Various Oxygen Species on an Oxide Surface: RuO_2(110). *J. Phys. Chem. B* **2001**, *105* (18), 3752–3758.

(5) Cai, J.-Q.; Luo, H.-J.; Tao, X.-M.; Tan, M.-Q. Initial Subsurface Incorporation of Oxygen into Ru(0001): A Density Functional Theory Study. *ChemPhysChem* **2015**, *16* (18), 3937–3948.

(6) Wang, H.; Schneider, W. F. Effects of Coverage on the Structures, Energetics, and Electronics of Oxygen Adsorption on RuO_2(110). *J. Chem. Phys.* **2007**, *127* (6), 064706.

(7) Baraldi, A.; Lizzit, S.; Paolucci, G. Identification of Atomic Adsorption Site by Means of High-Resolution Photoemission Surface Core-Level Shift: Oxygen on Ru(10$\bar{1}$0). *Surf. Sci.* **2000**, *457* (1), L354–L360.

(8) Zhang, H. J.; Lu, B.; Lu, Y. H.; Xu, Y. F.; Li, H. Y.; Bao, S. N.; He, P. Growth of RuO_2 Thin Layer on Ru(10$\bar{1}$0)Studied by Scanning Tunneling Microscopy. *Surf. Sci.* **2007**, *601* (11), 2297–2301.

(9) McCoy, A. P.; Bogan, J.; Brady, A.; Hughes, G. Oxidation of Ruthenium Thin Films Using Atomic Oxygen. *Thin Solid Films* **2015**, *597*, 112–116.

(10) Materzanini, G.; Tantardini, G. F.; Lindan, P. J. D.; Saalfrank, P. Water Adsorption at Metal Surfaces: A First-Principles Study of the p(√3×√3) R30° H_2O Bilayer on Ru(0001). *Phys. Rev. B* **2005**, *71* (15), 155414.

(11) Jelenkovic, E. V.; Tong, K. Y. Thermally Grown Ruthenium Oxide Thin Films. *J. Vac. Sci. Technol. B Microelectron. Nanometer Struct. Process. Meas. Phenom.* **2004**, *22* (5), 2319–2325.

(12) Nakahara, M.; Tsunekawa, S.; Watanabe, K.; Arai, T.; Yunogami, T.; Kuroki, K. Etching Technique for Ruthenium with a High Etch Rate and High Selectivity Using Ozone Gas. *J. Vac. Sci. Technol. B Microelectron. Nanometer Struct. Process. Meas. Phenom.* **2001**, *19* (6), 2133–2136.

APPENDIX H

Supplementary information for the area-selective atomic layer deposition of $BaTiO_3$.

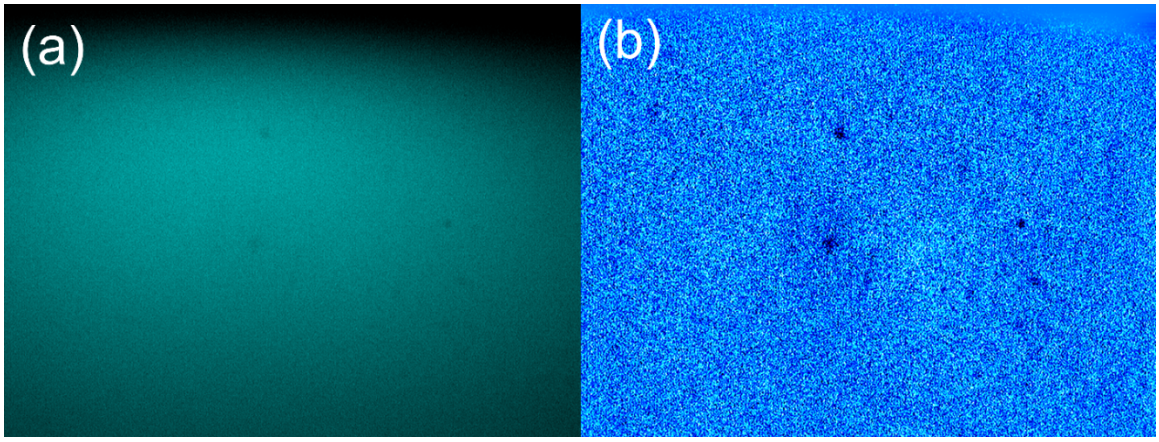

Figure H.1. (a) RHEED image of the as-deposited $BaTiO_3$ ALD film grown using 200 ALD cycles. The stoichiometry observed was 51.5:48.5 Ba:Ti. (b) Image processing on (a) to remove background camera blur.

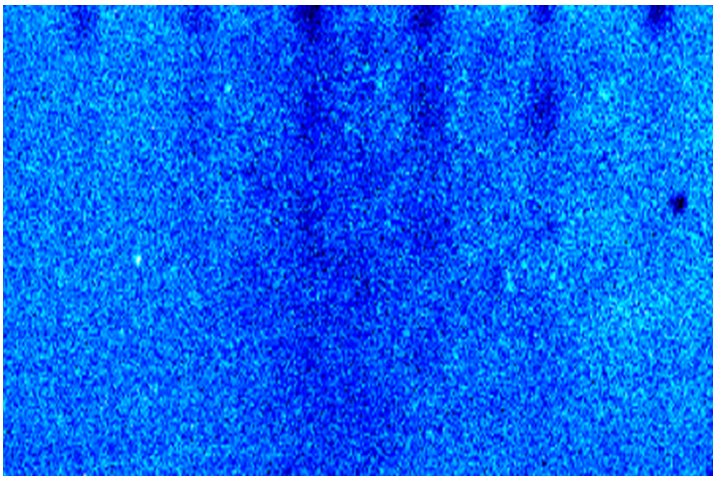

Figure H.2. RHEED image of a $BaTiO_3$ film that was grown using 150 ALD cycles and annealed in oxygen at a partial pressure of 1×10^{-6} Torr by ramping to 600 °C at a rate of 20 °C/min, followed by a second ramp to 850 °C at a rate of 10 °C/min and held at 850 °C for 10 min.

APPENDIX I

First authored publications (*Denotes equal contribution)

1. B. M. Coffey, H. C. Nallan, J. R. Engstrom, J. G. Ekerdt. Vacuum Ultraviolet Enhanced Atomic Layer Etching of Ru Metal. *Submitted*. **2020**
2. B. M. Coffey, H. C. Nallan, J.R. Engstrom, J. G. Ekerdt, Vacuum Ultraviolet Enhanced Oxidation Mechanism for Pd – Near Surface Oxidation for Atomic Layer Etching. *Accepted*. **2020**
3. B. M. Coffey, H. C. Nallan, J. R. Engstrom, C. H. Lam, J. G. Ekerdt, Vacuum Ultraviolet Photon-Enhanced Atomic Layer Etching of Pd Metal. *Chemistry of Materials*, **2020**, 32, 14, 6035-6042
4. B. M. Coffey*, E. L. Lin*, P. Chen, J. G. Ekerdt. Area-Selective Atomic Layer Deposition of Crystalline $BaTiO_3$. *Chemistry of Materials*, **2019**, 31 15, 5558-5565

Co-authored publications

1. E. L. Lin, A. B. Posadas, L. Zheng, H. Wu, P. Y. Chen, B. M. Coffey, K. Lai, A. A. Demkov, D. J. Smith, J. G. Ekerdt. Epitaxial Integration of Ferroelectric and Conductive Perovskites on Silicon. *Journal of Vacuum Science & Technology A*, **2020**, 38, 0224403.
2. Z. Zhang, H. C. Nallan, B. M. Coffey, T. Q. Ngo, T. Pramanik, S. K. Banerjee, J. G. Ekerdt. Atomic Layer Deposition of Cobalt Oxide on Oxide Substrates and Low Temperature Reduction to Form Ultrathin Cobalt Metal Films. *Journal of Vacuum Science & Technology A,* **2019**, 37, 010903

Technical Presentations

1. B. M. Coffey,* H. C. Nallan,* X. Yang, J. G. Ekerdt. *Low-Temperature Deposition and Etching of Pd*. AVS ASD, Stanford CA, April **2020** (Cancelled due to COVID-19)
2. E. Lin, B. M. Coffey, Z. Zhang, P. Y. Chen, B. Edmondson, J. G. Ekerdt. *Area-Selective Deposition of Crystalline Perovskites*. AVS 65, Long Beach CA, October, **2018**
3. B.M. Coffey, E. Lin, Z. Zhang, J. G. Ekerdt, *Metallic Sn as an Etch Mask*. MRS, Boston, MA. November, **2017**

Bibliography

Abel, S., Eltes, F., Ortmann, J. E., Messner, A., Castera, P., Wagner, T., Urbonas, D., Rosa, A., Gutierrez, A. M., Tulli, D., Ma, P., Baeuerle, B., Josten, A., Heni, W., Caimi, D., Czornomaz, L., Demkov, A. A., Leuthold, J., Sanchis, P., & Fompeyrine, J. (2019). Large Pockels effect in micro- and nanostructured barium titanate integrated on silicon. *Nature Materials*, *18*(1), 42–47. https://doi.org/10.1038/s41563-018-0208-0

Abel, S., & Fompeyrine, J. (2015). Electro-Optically Active Oxides on Silicon for Photonics. In *Thin Films on Silicon: Vol. Volume 8* (pp. 455–501). WORLD SCIENTIFIC. https://doi.org/10.1142/9789814740487_0010

Abel, S., Stöferle, T., Marchiori, C., Rossel, C., Rossell, M. D., Erni, R., Caimi, D., Sousa, M., Chelnokov, A., Offrein, B. J., & Fompeyrine, J. (2013). A strong electro-optically active lead-free ferroelectric integrated on silicon. *Nature Communications*, *4*, 1671. https://doi.org/10.1038/ncomms2695

Agha, I., Davanço, M., Thurston, B., & Srinivasan, K. (2012). Low-noise chip-based frequency conversion by four-wave-mixing Bragg scattering in SiN_x waveguides. *Optics Letters*, *37*(14), 2997–2999. https://doi.org/10.1364/OL.37.002997

Ameta, R., Solanki, M. S., Benjamin, S., & Ameta, S. C. (2018). Chapter 6—Photocatalysis. In *Advanced Oxidation Processes for Waste Water Treatment* (pp. 135–175). Academic Press. https://doi.org/10.1016/B978-0-12-810499-6.00006-1

Ananth, A., Gandhi, M. S., & Mok, Y. S. (2013). A dielectric barrier discharge (DBD) plasma reactor: An efficient tool to prepare novel RuO2nanorods. *Journal of Physics D: Applied Physics*, *46*(15), 155202. https://doi.org/10.1088/0022-3727/46/15/155202

Bakhtchadjian, R. (2019). *Bimodal Oxidation: Coupling of Heterogeneous and Homogeneous Reactions*. CRC Press.

Ballard, J. B., Sisson, T. W., Owen, J. H. G., Owen, W. R., Fuchs, E., Alexander, J., Randall, J. N., & Von Ehr, J. R. (2013). Multimode hydrogen depassivation lithography: A method for optimizing atomically precise write times. *Journal of Vacuum Science & Technology B*, *31*(6), 06FC01. https://doi.org/10.1116/1.4823756

Baraldi, A., Lizzit, S., & Paolucci, G. (2000). Identification of atomic adsorption site by means of high-resolution photoemission surface core-level shift: Oxygen on Ru(10$\bar{1}$0). *Surface Science*, *457*(1), L354–L360. https://doi.org/10.1016/S0039-6028(00)00394-0

Bates, C. M., Maher, M. J., Janes, D. W., Ellison, C. J., & Willson, C. G. (2014). Block Copolymer Lithography. *Macromolecules*, *47*(1), 2–12. https://doi.org/10.1021/ma401762n

Bianchi, C. L., Ragaini, V., & Cattania, M. G. (1991). An XPS study on ruthenium compounds and catalysts. *Materials Chemistry and Physics*, *29*(1), 297–306. https://doi.org/10.1016/0254-0584(91)90025-P

Björck, M., & Andersson, G. (2007). GenX: An extensible X-ray reflectivity refinement program utilizing differential evolution. *Journal of Applied Crystallography*, *40*(6), 1174–1178. https://doi.org/10.1107/S0021889807045086

Cai, J.-Q., Luo, H.-J., Tao, X.-M., & Tan, M.-Q. (2015). Initial Subsurface Incorporation of Oxygen into Ru(0001): A Density Functional Theory Study. *ChemPhysChem*, *16*(18), 3937–3948. https://doi.org/10.1002/cphc.201500681

Chalker, P. R. (2016). Photochemical atomic layer deposition and etching. *Surface and Coatings Technology*, *291*(Supplement C), 258–263. https://doi.org/10.1016/j.surfcoat.2016.02.046

Chalker, P. R., Marshall, P. A., Dawson, K., Brunell, I. F., Sutcliffe, C. J., & Potter, R. J. (2015). Vacuum ultraviolet photochemical selective area atomic layer deposition of Al_2O_3 dielectrics. *AIP Advances*, *5*(1), 017115. https://doi.org/10.1063/1.4905887

Chalker, P. R., Marshall, P. A., Dawson, K., Sutcliffe, C. J., Brunell, I. F., Sedghi, N., Hall, S., & Potter, R. J. (2015). Vacuum Ultraviolet Photochemical Atomic Layer Deposition of Alumina and Titania Films. *ECS Transactions*, *69*(7), 139–145. https://doi.org/10.1149/06907.0139ecst

Chan, H. Y. H., Takoudis, C. G., & Weaver, M. J. (1997). High-Pressure Oxidation of Ruthenium as Probed by Surface-Enhanced Raman and X-Ray Photoelectron Spectroscopies. *Journal of Catalysis*, *172*(2), 336–345. https://doi.org/10.1006/jcat.1997.1841

Chen, C.-Y., Wei, T.-C., Lin, C.-T., & Li, J.-Y. (2017). Enhancing formation rate of highly-oriented silicon nanowire arrays with the assistance of back substrates. *Scientific Reports*, *7*(1), 3164. https://doi.org/10.1038/s41598-017-03498-y

Chen, J. K.-C., Altieri, N. D., Kim, T., Chen, E., Lill, T., Shen, M., & Chang, J. P. (2017). Directional etch of magnetic and noble metals. II. Organic chemical vapor etch. *Journal of Vacuum Science & Technology A: Vacuum, Surfaces, and Films*, *35*(5), 05C305. https://doi.org/10.1116/1.4983830

Chen, J. K.-C., Altieri, N. D., Kim, T., Lill, T., Shen, M., & Chang, J. P. (2017). Directional etch of magnetic and noble metals. I. Role of surface oxidation states. *Journal of Vacuum Science & Technology A: Vacuum, Surfaces, and Films*, *35*(5), 05C304. https://doi.org/10.1116/1.4983829

Chen, X., Guo, W., Xie, L., Wei, C., Zhuang, J., Su, W., & Cui, Z. (2017). Embedded Ag/Ni Metal-Mesh with Low Surface Roughness As Transparent Conductive Electrode for Optoelectronic Applications. *ACS Applied Materials & Interfaces*, *9*(42), 37048–37054. https://doi.org/10.1021/acsami.7b11779

Chen, Y. (2015). Nanofabrication by electron beam lithography and its applications: A review. *Microelectronic Engineering*, *135*, 57–72. https://doi.org/10.1016/j.mee.2015.02.042

Chen, Z., Wang, H., Wang, X., Chen, P., Liu, Y., Zhao, H., Zhao, Y., & Duan, Y. (2017). Low-temperature remote plasma enhanced atomic layer deposition of ZrO_2/zircone nanolaminate film for efficient encapsulation of flexible organic light-emitting diodes. *Scientific Reports*, *7*, 40061. https://doi.org/10.1038/srep40061

Chen, Z.-X., Neyman, K. M., Lim, K. H., & Rösch, N. (2004). CH_3O Decomposition on PdZn(111), Pd(111), and Cu(111). A Theoretical Study. *Langmuir*, *20*(19), 8068–8077. https://doi.org/10.1021/la049377z

Choi, M., Posadas, A. B., Rodriguez, C. A., O'Hara, A., Seinige, H., Kellock, A. J., Frank, M. M., Tsoi, M., Zollner, S., Narayanan, V., & Demkov, A. A. (2014). Structural, optical, and electrical properties of strained La-doped SrTiO3 films. *Journal of Applied Physics*, *116*(4), 043705. https://doi.org/10.1063/1.4891225

Chopra, S. N., Zhang, Z., Kaihlanen, C., & Ekerdt, J. G. (2016). Selective Growth of Titanium Nitride on HfO2 across Nanolines and Nanopillars. *Chemistry of Materials*, *28*(14), 4928–4934. https://doi.org/10.1021/acs.chemmater.6b01036

Clark, R., Tapily, K., Yu, K.-H., Hakamata, T., Consiglio, S., O'Meara, D., Wajda, C., Smith, J., & Leusink, G. (2018). Perspective: New process technologies required for future devices and scaling: APL Materials: Vol 6, No 5. *APL Mater.*, *6*, 058203.

Coffey, B. M., Lin, E. L., Chen, P.-Y., & Ekerdt, J. G. (2019). Area-Selective Atomic Layer Deposition of Crystalline $BaTiO_3$. *Chemistry of Materials*, *31*(15), 5558–5565. https://doi.org/10.1021/acs.chemmater.9b01271

Coffey, B. M., Nallan, H. C., Engstrom, J. R., & Ekerdt, J. G. (2020). *Vacuum Ultraviolet Enhanced Oxidation Mechanism for Pd—Near Surface Oxidation for Atomic Layer Etching*. *Accepted*.

Coffey, B. M., Nallan, H. C., Engstrom, J. R., Lam, C. H., & Ekerdt, J. G. (2020). *Vacuum Ultraviolet Enhanced Oxidation—A Route to the Atomic Layer Etching of Palladium Metal*. *32*(14), 6035–6042. https://doi.org/10.1021/acs.chemmater.0c01379

Dai, L., Wang, S., Shu, P., Zhong, Z., Wang, G., & Zhang, G. (2011). Etching mechanism of barium strontium titanate (BST) thin films in CHF_3/Ar plasma. *Chinese Science Bulletin*, *56*(21), 2267–2271. https://doi.org/10.1007/s11434-011-4561-5

Deckert, C. A. (1995). *Electroless Copper Plating A Review: Part I*. 48–55.

Dessler, A. (2000). *Chemistry and Physics of Stratospheric Ozone*. Elsevier.

Dimaggio, E., Narducci, D., & Pennelli, G. (2018). Fabrication of Silicon Nanowire Forests for Thermoelectric Applications by Metal-Assisted Chemical Etching. *Journal of*

Materials Engineering and Performance, *27*(12), 6279–6285. https://doi.org/10.1007/s11665-018-3605-2

Dubourdieu, C., Bruley, J., Arruda, T. M., Posadas, A., Jordan-Sweet, J., Frank, M. M., Cartier, E., Frank, D. J., Kalinin, S. V., Demkov, A. A., & Narayanan, V. (2013). Switching of ferroelectric polarization in epitaxial $BaTiO_3$ films on silicon without a conducting bottom electrode. *Nature Nanotechnology*, *8*(10), 748–754. https://doi.org/10.1038/nnano.2013.192

DuMont, J. W., Marquardt, A. E., Cano, A. M., & George, S. M. (2017). Thermal Atomic Layer Etching of SiO_2 by a "Conversion-Etch" Mechanism Using Sequential Reactions of Trimethylaluminum and Hydrogen Fluoride. *ACS Applied Materials & Interfaces*, *9*(11), 10296–10307. https://doi.org/10.1021/acsami.7b01259

Eltes, F., Caimi, D., Fallegger, F., Sousa, M., O'Connor, E., Rossell, M. D., Offrein, B., Fompeyrine, J., & Abel, S. (2016). Low-Loss $BaTiO_3$–Si Waveguides for Nonlinear Integrated Photonics. *ACS Photonics*, *3*(9), 1698–1703. https://doi.org/10.1021/acsphotonics.6b00350

Falkenstein, Z. (2001). *Surface cleaning mechanisms utilizing VUV radiation in oxygen-containing gaseous environments* (E.-B. Kley & H. P. Herzig, Eds.; pp. 246–255). https://doi.org/10.1117/12.448055

Fracassi, F., d'Agostino, R., & Cacucci, A. (1998). Dry etching of palladium thin films in fluorine containing plasmas: X-ray photoelectron spectroscopy investigation. *Journal of Vacuum Science & Technology A: Vacuum, Surfaces, and Films*, *13*(1), 63–66. https://doi.org/10.1116/1.579444

Gabasch, H., Unterberger, W., Hayek, K., Klötzer, B., Kleimenov, E., Teschner, D., Zafeiratos, S., Hävecker, M., Knop-Gericke, A., Schlögl, R., Han, J., Ribeiro, F. H., Aszalos-Kiss, B., Curtin, T., & Zemlyanov, D. (2006). In situ XPS study of Pd(111) oxidation at elevated pressure, Part 2: Palladium oxidation in the 10−1mbar range. *Surface Science*, *600*(15), 2980–2989. https://doi.org/10.1016/j.susc.2006.05.029

Giannozzi, P., Andreussi, O., Brumme, T., Bunau, O., Nardelli, M. B., Calandra, M., Car, R., Cavazzoni, C., Ceresoli, D., Cococcioni, M., Colonna, N., Carnimeo, I., Corso, A. D., Gironcoli, S. de, Delugas, P., DiStasio, R. A., Ferretti, A., Floris, A., Fratesi, G., … Baroni, S. (2017). Advanced capabilities for materials modelling with Quantum ESPRESSO. *Journal of Physics: Condensed Matter*, *29*(46), 465901. https://doi.org/10.1088/1361-648X/aa8f79

Giannozzi, Paolo, Baroni, S., Bonini, N., Calandra, M., Car, R., Cavazzoni, C., Ceresoli, D., Chiarotti, G. L., Cococcioni, M., Dabo, I., Corso, A. D., Gironcoli, S. de, Fabris, S., Fratesi, G., Gebauer, R., Gerstmann, U., Gougoussis, C., Kokalj, A., Lazzeri, M., … Wentzcovitch, R. M. (2009). QUANTUM ESPRESSO: A modular and open-source software project for quantum simulations of materials. *Journal of*

Physics: Condensed Matter, *21*(39), 395502. https://doi.org/10.1088/0953-8984/21/39/395502

Gong, Y., & Akolkar, R. (2020). Electrochemical Atomic Layer Etching of Ruthenium. *Journal of The Electrochemical Society*, *167*(6), 062510. https://doi.org/10.1149/1945-7111/ab864b

Grimme, S., Antony, J., Ehrlich, S., & Krieg, H. (2010). A consistent and accurate ab initio parametrization of density functional dispersion correction (DFT-D) for the 94 elements H-Pu. *The Journal of Chemical Physics*, *132*(15), 154104. https://doi.org/10.1063/1.3382344

Grimme, S., Ehrlich, S., & Goerigk, L. (2011). Effect of the damping function in dispersion corrected density functional theory. *Journal of Computational Chemistry*, *32*(7), 1456–1465. https://doi.org/10.1002/jcc.21759

Gu, X., Kikuchi, Y., Nozawa, T., & Samukawa, S. (2014). A new metallic complex reaction etching for transition metals by a low-temperature neutral beam process. *Journal of Physics D: Applied Physics*, *47*(32), 322002. https://doi.org/10.1088/0022-3727/47/32/322002

Han, H., Huang, Z., & Lee, W. (2014). Metal-assisted chemical etching of silicon and nanotechnology applications. *Nano Today*, *9*(3), 271–304. https://doi.org/10.1016/j.nantod.2014.04.013

Harwell, J., Burch, J., Fikouras, A., Gather, M. C., Di Falco, A., & Samuel, I. D. W. (2019). Patterning Multicolor Hybrid Perovskite Films via Top-Down Lithography. *ACS Nano*, *13*(4), 3823–3829. https://doi.org/10.1021/acsnano.8b09592

Henkelman, G., Uberuaga, B. P., & Jónsson, H. (2000). A climbing image nudged elastic band method for finding saddle points and minimum energy paths. *The Journal of Chemical Physics*, *113*(22), 9901–9904. https://doi.org/10.1063/1.1329672

Herd, B., Goritzka, J. C., & Over, H. (2013). Room Temperature Oxidation of Ruthenium. *The Journal of Physical Chemistry C*, *117*(29), 15148–15154. https://doi.org/10.1021/jp404239y

Hong, J., Porter, D. W., Sreenivasan, R., McIntyre, P. C., & Bent, S. F. (2007). ALD Resist Formed by Vapor-Deposited Self-Assembled Monolayers. *Langmuir*, *23*(3), 1160–1165. https://doi.org/10.1021/la0606401

Honkala, K., & Laasonen, K. (2001). Ab initio study of O2 precursor states on the Pd(111) surface. *The Journal of Chemical Physics*, *115*(5), 2297–2302. https://doi.org/10.1063/1.1384009

Hsu, C. C., Coburn, J. W., & Graves, D. B. (2005). Etching of ruthenium coatings in O2- and Cl2-containing plasmas. *Journal of Vacuum Science & Technology A*, *24*(1), 1–8. https://doi.org/10.1116/1.2121751

Hu, S., McDaniel, M. D., Posadas, A., Hu, C., Wu, H., Yu, E. T., Smith, D. J., Demkov, A. A., & Ekerdt, J. G. (2016). Monolithic integration of perovskites on Ge(001) by atomic layer deposition: A case study with $SrHf_xTi_{1-x}O_3$. *MRS Communications*, *6*(3), 125–132. https://doi.org/10.1557/mrc.2016.36

Hua, Y., King, W. P., & Henderson, C. L. (2008). Nanopatterning materials using area selective atomic layer deposition in conjunction with thermochemical surface modification via heated AFM cantilever probe lithography. *Microelectronic Engineering*, *85*(5), 934–936. https://doi.org/10.1016/j.mee.2008.01.105

Huang, Z., Geyer, N., Werner, P., de Boor, J., & Gosele, U. (2010). *Metal-Assisted Chemical Etching of Silicon: A Review*. *23*(2), 285–308. https://doi.org/10.1002/adma.201001784

Huffman, R. E. (1969). Absorption cross-sections of atmospheric gases for use in aeronomy. *Canadian Journal of Chemistry*, *47*(10), 1823–1834. https://doi.org/10.1139/v69-298

Hwang, S. M., Garay, A. A., Lee, W. I., & Chung, C. W. (2015). High density plasma reactive ion etching of Ru thin films using non-corrosive gas mixture. *Thin Solid Films*, *587*, 28–33. https://doi.org/10.1016/j.tsf.2014.12.031

Iimori, T., Hattori, K., Shudo, K., Iwaki, T., Ueta, M., & Komori, F. (1998). Laser-induced mono-atomic-layer etching on Cl-adsorbed Si(111) surfaces. *Applied Surface Science*, *130–132*, 90–95. https://doi.org/10.1016/S0169-4332(98)00031-2

Ishii, M., Meguro, T., Sugano, T., Gamo, K., & Aoyagi, Y. (1995). Surface reaction control in digital etching of GaAs by using a tunable UV laser system: Reaction control mechanism in layer-by-layer etching. *Applied Surface Science*, *86*(1), 554–558. https://doi.org/10.1016/0169-4332(94)00464-1

Ishikawa, K., Karahashi, K., Ichiki, T., Chang, J. P., George, S. M., Kessels, W. M. M., Lee, H. J., Tinck, S., Um, J. H., & Kinoshita, K. (2017). Progress and prospects in nanoscale dry processes: How can we control atomic layer reactions? *Japanese Journal of Applied Physics*, *56*(6S2), 06HA02. https://doi.org/10.7567/JJAP.56.06HA02

Ishikawa, K., Karahashi, K., Ishijima, T., Cho, S. I., Elliott, S., Hausmann, D., Mocuta, D., Wilson, A., & Kinoshita, K. (2018). Progress in nanoscale dry processes for fabrication of high-aspect-ratio features: How can we control critical dimension uniformity at the bottom? *Japanese Journal of Applied Physics*, *57*(6S2), 06JA01. https://doi.org/10.7567/JJAP.57.06JA01

Janthon, P., Luo, S. (Andy), Kozlov, S. M., Viñes, F., Limtrakul, J., Truhlar, D. G., & Illas, F. (2014). Bulk Properties of Transition Metals: A Challenge for the Design of Universal Density Functionals. *Journal of Chemical Theory and Computation*, *10*(9), 3832–3839. https://doi.org/10.1021/ct500532v

Jelenkovic, E. V., & Tong, K. Y. (2004). Thermally grown ruthenium oxide thin films. *Journal of Vacuum Science & Technology B: Microelectronics and Nanometer Structures Processing, Measurement, and Phenomena*, *22*(5), 2319–2325. https://doi.org/10.1116/1.1783319

Johnson, M. S., Nilsson, E. J. K., Svensson, E. A., & Langer, S. (2014). Gas-Phase Advanced Oxidation for Effective, Efficient in Situ Control of Pollution. *Environmental Science & Technology*, *48*(15), 8768–8776. https://doi.org/10.1021/es5012687

Johnson, N. R., Sun, H., Sharma, K., & George, S. M. (2016). Thermal atomic layer etching of crystalline aluminum nitride using sequential, self-limiting hydrogen fluoride and $Sn(acac)_2$ reactions and enhancement by H_2 and Ar plasmas. *Journal of Vacuum Science & Technology A: Vacuum, Surfaces, and Films*, *34*(5), 050603. https://doi.org/10.1116/1.4959779

Jovanović, V., Suligoj, T., Poljak, M., Civale, Y., & Nanver, L. K. (2010). Ultra-high aspect-ratio FinFET technology. *Solid-State Electronics*, *54*(9), 870–876. https://doi.org/10.1016/j.sse.2010.04.021

Kanarik, K. J., Tan, S., & Gottscho, R. A. (2018). *Atomic Layer Etching: Rethinking the Art of Etch*. *9*(16), 4814–4821. https://doi.org/10.1021/acs.jpclett.8b00997

Khan, A. I., Chatterjee, K., Wang, B., Drapcho, S., You, L., Serrao, C., Bakaul, S. R., Ramesh, R., & Salahuddin, S. (2015). Negative capacitance in a ferroelectric capacitor. *Nature Materials*, *14*(2), 182–186. https://doi.org/10.1038/nmat4148

Kim, H. W., Ju, B.-S., & Kang, C.-J. (2003). Patterning of Ru electrode in O2/Cl2 gas using reactive ion etcher. *Vacuum*, *71*(4), 481–486. https://doi.org/10.1016/S0042-207X(03)00047-2

Kim, M., Pan, L., Weaver, J. F., & Asthagiri, A. (2018). Initial Reduction of the PdO(101) Surface: Role of Oxygen Vacancy Formation Kinetics. *The Journal of Physical Chemistry C*, *122*(45), 26007–26017. https://doi.org/10.1021/acs.jpcc.8b08226

Kim, S. K., Kim, W.-D., Kim, K.-M., Hwang, C. S., & Jeong, J. (2004). High dielectric constant TiO2 thin films on a Ru electrode grown at 250 °C by atomic-layer deposition. *Applied Physics Letters*, *85*(18), 4112–4114. https://doi.org/10.1063/1.1812832

Kim, S. K., & Popovici, M. (2018). Future of dynamic random-access memory as main memory. *MRS Bulletin*, *43*(5), 334–339. https://doi.org/10.1557/mrs.2018.95

Kim, Y. D., Seitsonen, A. P., Wendt, S., Wang, J., Fan, C., Jacobi, K., Over, H., & Ertl, G. (2001). Characterization of Various Oxygen Species on an Oxide Surface: RuO2(110). *The Journal of Physical Chemistry B*, *105*(18), 3752–3758. https://doi.org/10.1021/jp003213j

Ko, C. H., Su, Y. K., Chang, S. J., Lan, W. H., Webb, J., Tu, M. C., & Cherng, Y. T. (2002). Photo-enhanced chemical wet etching of GaN. *Materials Science and Engineering: B*, *96*(1), 43–47. https://doi.org/10.1016/S0921-5107(02)00323-9

Kokalj, A. (1999). XCrySDen—A new program for displaying crystalline structures and electron densities. *Journal of Molecular Graphics and Modelling*, *17*(3), 176–179. https://doi.org/10.1016/S1093-3263(99)00028-5

Kormondy, K. J., Abel, S., Fallegger, F., Popoff, Y., Ponath, P., Posadas, A. B., Sousa, M., Caimi, D., Siegwart, H., Uccelli, E., Czornomaz, L., Marchiori, C., Fompeyrine, J., & Demkov, A. A. (2015). Analysis of the Pockels effect in ferroelectric barium titanate thin films on Si(001). *Microelectronic Engineering*, *147*, 215–218. https://doi.org/10.1016/j.mee.2015.04.041

Kwak, B. S., Zhang, K., Boyd, E. P., Erbil, A., & Wilkens, B. J. (1991). Metalorganic chemical vapor deposition of BaTiO3 thin films. *Journal of Applied Physics*, *69*(2), 767–772. https://doi.org/10.1063/1.347362

Kwon, O. J., Cha, S. H., & Kim, J. J. (2004). Ruthenium Bottom Electrode Prepared by Electroplating for a High Density DRAM Capacitor. *Journal of The Electrochemical Society*, *151*(2), C127. https://doi.org/10.1149/1.1637900

Lai, R., A., Hymel, T., M., Narasimhan, V., K., & Cui, Y. (2016). *Schottky Barrier Catalysis Mechanism in Metal-Assisted Chemical Etching of Silicon | ACS Applied Materials & Interfaces*. *8*(14), 8875–8879. https://doi.org/10.1021/acsami.6b01020

Lau, H. W., Parker, G. J., Greef, R., & Holling, M. (1995). *High aspect ratio submicron silicon pillars fabricated by photoassisted electrochemical etching and oxidation*. *67*(13), 1877–1879.

Lee, S. W., Choi, B. J., Eom, T., Han, J. H., Kim, S. K., Song, S. J., Lee, W., & Hwang, C. S. (2013). Influences of metal, non-metal precursors, and substrates on atomic layer deposition processes for the growth of selected functional electronic materials. *Coordination Chemistry Reviews*, *257*(23), 3154–3176. https://doi.org/10.1016/j.ccr.2013.04.010

Lee, T., Yao, N., & Aksay, I. A. (1997). Nanoscale Patterning of Barium Titanate on Block Copolymers. *Langmuir*, *13*(14), 3866–3870. https://doi.org/10.1021/la960774m

Lee, Y., DuMont, J. W., & George, S. M. (2016). Trimethylaluminum as the Metal Precursor for the Atomic Layer Etching of Al_2O_3 Using Sequential, Self-Limiting Thermal Reactions. *Chemistry of Materials*, *28*(9), 2994–3003. https://doi.org/10.1021/acs.chemmater.6b00111

Lee, Y., & George, S. M. (2015). Atomic Layer Etching of Al_2O_3 Using Sequential, Self-Limiting Thermal Reactions with $Sn(acac)_2$ and Hydrogen Fluoride. *ACS Nano*, *9*(2), 2061–2070. https://doi.org/10.1021/nn507277f

Lee, Y., & George, S. M. (2017). Thermal Atomic Layer Etching of Titanium Nitride Using Sequential, Self-Limiting Reactions: Oxidation to TiO_2 and Fluorination to Volatile TiF_4. *Chemistry of Materials*, *29*(19), 8202–8210. https://doi.org/10.1021/acs.chemmater.7b02286

Lejaeghere, K., Speybroeck, V. V., Oost, G. V., & Cottenier, S. (2014). Error Estimates for Solid-State Density-Functional Theory Predictions: An Overview by Means of the Ground-State Elemental Crystals. *Critical Reviews in Solid State and Materials Sciences*, *39*(1), 1–24. https://doi.org/10.1080/10408436.2013.772503

Li, J., Jin, D., Zhou, L., & Cheng, J. (2012). Dielectric properties of Barium Strontium Titanate (BST) ceramics synthesized by using mixed-phase powders calcined at varied temperatures. *Materials Letters*, *76*, 100–102. https://doi.org/10.1016/j.matlet.2012.02.045

Li, X., & Bohn, P. W. (2000). Metal-assisted chemical etching in HF/H_2O_2 produces porous silicon. *Applied Physics Letters*, *77*(16), 2572–2574. https://doi.org/10.1063/1.1319191

Li, Y., Wang, C., Yao, Z., Kim, H.-K., & Kim, N.-Y. (2014). Comparative analysis of barium titanate thin films dry etching using inductively coupled plasmas by different fluorine-based mixture gas. *Nanoscale Research Letters*, *9*(1), 530. https://doi.org/10.1186/1556-276X-9-530

Lin, E. L. (2018). *Atomic Layer Deposition of Epitaxial Perovskites for Electronic and Photonic Applications*.

Lin, E. L., Hu, S., & Ekerdt, J. G. (2017). Monolithic integration of metal-ferroelectric-semiconductor heterostructure using atomic layer deposition. *Oxide-Based Materials and Devices VIII*, *10105*, 1010519. https://doi.org/10.1117/12.2254196

Lin, E. L., Posadas, A. B., Wu, H. W., Smith, D. J., Demkov, A. A., & Ekerdt, J. G. (2017). Epitaxial growth of barium titanate thin films on germanium via atomic layer deposition. *Journal of Crystal Growth*, *476*, 6–11. https://doi.org/10.1016/j.jcrysgro.2017.08.003

Linstrom, P. (1997). *NIST Chemistry WebBook, NIST Standard Reference Database 69* [Data set]. National Institute of Standards and Technology. https://doi.org/10.18434/T4D303

Mack, C. A. (2011). Fifty Years of Moore's Law. *IEEE Transactions on Semiconductor Manufacturing*, *24*(2), 202–207. https://doi.org/10.1109/TSM.2010.2096437

Mackus, A. J. M., & Merkx, M. J. M. (2019). *Fully self-aligned vias: The killer application for area-selective ALD? – A discussion of the requirements for implementation in high volume manufacturing*. *7*. https://www.atomiclimits.com/2019/07/18/fully-self-aligned-vias-the-killer-application-for-area-selective-ald-a-discussion-of-the-requirements-for-implementation-in-high-volume-manufacturing/

Mackus, A. J. M., Mulders, J. J. L., van de Sanden, M. C. M., & Kessels, W. M. M. (2010). Local deposition of high-purity Pt nanostructures by combining electron beam induced deposition and atomic layer deposition. *Journal of Applied Physics*, *107*(11), 116102. https://doi.org/10.1063/1.3431351

Mackus, Adriaan J. M., Merkx, M. J. M., & Kessels, W. M. M. (2019). From the Bottom-Up: Toward Area-Selective Atomic Layer Deposition with High Selectivity. *Chemistry of Materials*, *31*(1), 2–12. https://doi.org/10.1021/acs.chemmater.8b03454

Mallavarapu, A., & Sreenivasan, S. V. (2020). *Metal Assisted Chemical Etching of Ru for Si nanowires*.

Mangalam, R. V. K., Ray, N., Waghmare, U. V., Sundaresan, A., & Rao, C. N. R. (2009). *Multiferroic properties of nanocrystalline $BaTiO_3$*. *149*, 1–5.

Martin, L. W., & Rappe, A. M. (2016). Thin-film ferroelectric materials and their applications. *Nature Reviews Materials*, *2*(2), 1–14. https://doi.org/10.1038/natrevmats.2016.87

Materzanini, G., Tantardini, G. F., Lindan, P. J. D., & Saalfrank, P. (2005). Water adsorption at metal surfaces: A first-principles study of the $p(\sqrt{3}\ifmmode\times\else\texttimes\fi{}\sqrt{3})R30\ifmmode^\circ\else\textdegree\fi{}$ ${\mathrm{H}}_{2}\mathrm{O}$ bilayer on Ru(0001). *Physical Review B*, *71*(15), 155414. https://doi.org/10.1103/PhysRevB.71.155414

Mathews, S., Ramesh, R., Venkatesan, T., & Benedetto, J. (1997). Ferroelectric Field Effect Transistor Based on Epitaxial Perovskite Heterostructures. *Science*, *276*(5310), 238–240. https://doi.org/10.1126/science.276.5310.238

Matsumoto, S., Toguchi, M., Takeda, K., Narita, T., Kachi, T., & Sato, T. (2018). *Effects of a photo-assisted electrochemical etching process removing dry-etching damage in GaN*. *57*(12), 121001-1–7.

Matthey, J. (n.d.). *Tin-Palladium Catalysts for Electroless Plating*. Johnson Matthey Technology Review. Retrieved September 24, 2020, from https://www.technology.matthey.com/article/26/2/58-64/

Mazet, L., Yang, S. M., Kalinin, S. V., Schamm-Chardon, S., & Dubourdieu, C. (2015). A review of molecular beam epitaxy of ferroelectric BaTiO3 films on Si, Ge and GaAs substrates and their applications. *Science and Technology of Advanced Materials*, *16*(3), 036005. https://doi.org/10.1088/1468-6996/16/3/036005

McCoy, A. P., Bogan, J., Brady, A., & Hughes, G. (2015). Oxidation of ruthenium thin films using atomic oxygen. *Thin Solid Films*, *597*, 112–116. https://doi.org/10.1016/j.tsf.2015.11.024

McCrory, C. C. L., Jung, S., Peters, J. C., & Jaramillo, T. F. (2013). Benchmarking Heterogeneous Electrocatalysts for the Oxygen Evolution Reaction. *Journal of the*

American Chemical Society, *135*(45), 16977–16987. https://doi.org/10.1021/ja407115p

McDaniel, M. D., Hu, C., Lu, S., Ngo, T. Q., Posadas, A., Jiang, A., Smith, D. J., Yu, E. T., Demkov, A. A., & Ekerdt, J. G. (2015). Atomic layer deposition of crystalline SrHfO3 directly on Ge (001) for high-k dielectric applications. *Journal of Applied Physics*, *117*(5), 054101. https://doi.org/10.1063/1.4906953

McDaniel, M. D., Posadas, A., Ngo, T. Q., Dhamdhere, A., Smith, D. J., Demkov, A. A., & Ekerdt, J. G. (2012). Epitaxial strontium titanate films grown by atomic layer deposition on SrTiO3-buffered Si(001) substrates. *Journal of Vacuum Science & Technology A*, *31*(1), 01A136. https://doi.org/10.1116/1.4770291

Miikkulainen, V., Väyrynen, K., Mizohata, K., Räisänen, J., Vehkamäki, M., & Ritala, M. (2019). Photoassisted atomic layer deposition of oxides employing alkoxides as single-source precursors. *Journal of Vacuum Science & Technology A*, *37*(6), 060911. https://doi.org/10.1116/1.5124100

Militello, M. C., & Simko, S. J. (1998). Palladium Oxide (PdO) by XPS. *Surface Science Spectra*, *3*(4), 395–401. https://doi.org/10.1116/1.1247784

Misra, V., Huicai Zhong, & Lazar, H. (2002). Electrical properties of Ru-based alloy gate electrodes for dual metal gate Si-CMOS. *IEEE Electron Device Letters*, *23*(6), 354–356. https://doi.org/10.1109/LED.2002.1004233

Momma, K., & Izumi, F. (2011). VESTA 3 for three-dimensional visualization of crystal, volumetric and morphology data. *Journal of Applied Crystallography*, *44*(6), 1272–1276. https://doi.org/10.1107/S0021889811038970

Morgan, D. J. (2015). Resolving ruthenium: XPS studies of common ruthenium materials. *Surface and Interface Analysis*, *47*(11), 1072–1079. https://doi.org/10.1002/sia.5852

Morgan, T. (2018). Self-Assembled Barium Titanate Nanoscale Films by Molecular Beam Epitaxy. *Theses and Dissertations*. https://scholarworks.uark.edu/etd/2817

Moulder, J. F., Stickle, W. F., Sobol, P. E., & Bomben, K. D. (1992). *Handbook of X-ray Photoelectron Spectroscopy* (J. Chastain, Ed.). Perkin-Elmer.

Munter, R. (2008). Advanced Oxidation Processes—Current status and prospects. *Proceedings from the Estonian Academy of Sciences, Chemistry*, *50*(2), 59–80.

Nagy, D., Indalecio, G., GarcíA-Loureiro, A. J., Elmessary, M. A., Kalna, K., & Seoane, N. (2018). FinFET Versus Gate-All-Around Nanowire FET: Performance, Scaling, and Variability. *IEEE Journal of the Electron Devices Society*, *6*, 332–340. https://doi.org/10.1109/JEDS.2018.2804383

Naito, K., Nakamura, M., Sakata, O., & Hoshi, N. (2011). Surface X-ray Scattering of Pd(111) and Pd(100) Electrodes during the Oxygen Reduction Reaction. *Electrochemistry*, *79*(4), 256–260. https://doi.org/10.5796/electrochemistry.79.256

Nakahara, M., Tsunekawa, S., Watanabe, K., Arai, T., Yunogami, T., & Kuroki, K. (2001). Etching technique for ruthenium with a high etch rate and high selectivity using ozone gas. *Journal of Vacuum Science & Technology B: Microelectronics and Nanometer Structures Processing, Measurement, and Phenomena*, *19*(6), 2133–2136. https://doi.org/10.1116/1.1415517

Naota, T., Takaya, H., & Murahashi, S.-I. (1998). Ruthenium-Catalyzed Reactions for Organic Synthesis. *Chemical Reviews*, *98*(7), 2599–2660. https://doi.org/10.1021/cr9403695

Ngo, T. Q., Posadas, A. B., McDaniel, M. D., Hu, C., Bruley, J., Yu, E. T., Demkov, A. A., & Ekerdt, J. G. (2014). Epitaxial c-axis oriented BaTiO3 thin films on SrTiO3-buffered Si(001) by atomic layer deposition. *Applied Physics Letters*, *104*(8), 082910. https://doi.org/10.1063/1.4867469

Nian, Q., Callahan, M., Look, D., Efstathiadis, H., Bailey, J., & Cheng, G. J. (2015). Highly transparent conductive electrode with ultra-low HAZE by grain boundary modification of aqueous solution fabricated alumina-doped zinc oxide nanocrystals. *APL Materials*, *3*(6), 062803. https://doi.org/10.1063/1.4915489

Niu, G., Yin, S., Saint-Girons, G., Gautier, B., Lecoeur, P., Pillard, V., Hollinger, G., & Vilquin, B. (2011). Epitaxy of BaTiO3 thin film on Si(001) using a SrTiO3 buffer layer for non-volatile memory application. *Microelectronic Engineering*, *88*(7), 1232–1235. https://doi.org/10.1016/j.mee.2011.03.028

Ouyang, L., Tian, P., Da, G., Xu, X.-C., Ao, C., Chen, T., Si, R., Xu, J., & Han, Y.-F. (2015). The origin of active sites for direct synthesis of H2O2 on Pd/TiO2 catalysts: Interfaces of Pd and PdO domains. *Journal of Catalysis*, *321*, 70–80. https://doi.org/10.1016/j.jcat.2014.10.003

Palacios, M., García, O., & Rodríguez-Hernández, J. (2013). Constructing Robust and Functional Micropatterns on Polystyrene Surfaces by Using Deep UV Irradiation. *Langmuir*, *29*(8), 2756–2763. https://doi.org/10.1021/la304931x

Pan, W., & Desu, S. B. (1994). Reactive ion etching of RuO2 thin films using the gas mixture O2/CF3CFH2. *Journal of Vacuum Science & Technology B: Microelectronics and Nanometer Structures Processing, Measurement, and Phenomena*, *12*(6), 3208–3213. https://doi.org/10.1116/1.587501

Park, K.-I., Xu, S., Liu, Y., Hwang, G.-T., Kang, S.-J. L., Wang, Z. L., & Lee, K. J. (2010). Piezoelectric BaTiO3 Thin Film Nanogenerator on Plastic Substrates. *Nano Letters*, *10*(12), 4939–4943. https://doi.org/10.1021/nl102959k

Parker, D. H., & Koel, B. E. (1990). Chemisorption of high coverages of atomic oxygen on the Pt(111), Pd(111), and Au(111) surfaces. *Journal of Vacuum Science & Technology A*, *8*(3), 2585–2590. https://doi.org/10.1116/1.576675

Parsons, G. N., George, S. M., & Knez, M. (2011). Progress and future directions for atomic layer deposition and ALD-based chemistry. *MRS Bulletin*, *36*(11), 865–871. https://doi.org/10.1557/mrs.2011.238

Perdew, J. P., Burke, K., & Ernzerhof, M. (1996). Generalized Gradient Approximation Made Simple. *Physical Review Letters*, *77*(18), 3865–3868. https://doi.org/10.1103/PhysRevLett.77.3865

Perdew, J. P., Burke, K., & Ernzerhof, M. (1997). Generalized Gradient Approximation Made Simple [Phys. Rev. Lett. 77, 3865 (1996)]. *Physical Review Letters*, *78*(7), 1396–1396. https://doi.org/10.1103/PhysRevLett.78.1396

Peter, M., Adamovsky, S., Camacho, J. M. F., & Schauermann, S. (2013). Energetics of elementary reaction steps relevant for CO oxidation: CO and O_2 adsorption on model Pd nanoparticles and Pd(111). *Faraday Discussions*, *162*(0), 341–354. https://doi.org/10.1039/C3FD00001J

PETROVA, N. V., & YAKOVKIN, I. N. (2012). BINDING ENERGIES FOR OXYGEN ON TRANSITION METAL SURFACES. *Surface Review and Letters*. https://doi.org/10.1142/S0218625X09012615

Philipsen, H., Mouwen, N., Teck, S., Monnens, W., Le, Q. T., Holsteyns, F., & Struyf, H. (2019). Wet-chemical etching of metals for advanced semiconductor technology nodes: Ru etching in acidic Ce4+ solutions. *Electrochimica Acta*, *306*, 285–298. https://doi.org/10.1016/j.electacta.2019.03.065

Plauck, A., Stangland, E. E., Dumesic, J. A., & Mavrikakis, M. (2016). Active sites and mechanisms for H2O2 decomposition over Pd catalysts. *Proceedings of the National Academy of Sciences*, *113*(14), E1973–E1982. https://doi.org/10.1073/pnas.1602172113

Ponath, P., Posadas, A. B., Ren, Y., Wu, X., Lai, K., Demkov, A., Schmidt, M., Duffy, R., Hurley, P., Wang, J., Young, C., Vasudevan, R. K., Okatan, M. B., Jesse, S., & Kalinin, S. V. (2017). Advances of the development of a ferroelectric field-effect transistor on Ge(001). *2017 IEEE International Conference on IC Design and Technology (ICICDT)*, 1–3. https://doi.org/10.1109/ICICDT.2017.7993524

Ponath, Patrick, Fredrickson, K., Posadas, A. B., Ren, Y., Wu, X., Vasudevan, R. K., Baris Okatan, M., Jesse, S., Aoki, T., McCartney, M. R., Smith, D. J., Kalinin, S. V., Lai, K., & Demkov, A. A. (2015). Carrier density modulation in a germanium heterostructure by ferroelectric switching. *Nature Communications*, *6*, 6067. https://doi.org/10.1038/ncomms7067

Popovici, M., Swerts, J., Redolfi, A., Kaczer, B., Aoulaiche, M., Radu, I., Clima, S., Everaert, J.-L., Van Elshocht, S., & Jurczak, M. (2014). Low leakage Ru-strontium titanate-Ru metal-insulator-metal capacitors for sub-20 nm technology node in dynamic random access memory. *Applied Physics Letters*, *104*(8), 082908. https://doi.org/10.1063/1.4866860

Popovici, Mihaela, Groven, B., Marcoen¶, K., Phung, Q. M., Dutta, S., Swerts, J., Meersschaut, J., van den Berg, J. A., Franquet, A., Moussa, A., Vanstreels, K., Lagrain, P., Bender, H., Jurczak¶, M., Van Elshocht, S., Delabie, A., & Adelmann, C. (2017). Atomic Layer Deposition of Ruthenium Thin Films from (Ethylbenzyl) (1-Ethyl-1,4-cyclohexadienyl) Ru: Process Characteristics, Surface Chemistry, and Film Properties. *Chemistry of Materials*, *29*(11), 4654–4666. https://doi.org/10.1021/acs.chemmater.6b05437

Posadas, A., Berg, M., Seo, H., de Lozanne, A., Demkov, A. A., Smith, D. J., Kirk, A. P., Zhernokletov, D., & Wallace, R. M. (2011). Epitaxial integration of ferromagnetic correlated oxide LaCoO3 with Si (100). *Applied Physics Letters*, *98*(5), 053104. https://doi.org/10.1063/1.3549301

Powell, C. J., & Jablonski, A. (2011). *NIST Electron Effective-Attenuation-Length Database Version 1.3*. National Institute of Standards and Technology.

Rajkumar, C., Thirumalraj, B., Chen, S.-M., Veerakumar, P., & Liu, S.-B. (2017). Ruthenium Nanoparticles Decorated Tungsten Oxide as a Bifunctional Catalyst for Electrocatalytic and Catalytic Applications. *ACS Applied Materials & Interfaces*, *9*(37), 31794–31805. https://doi.org/10.1021/acsami.7b07645

Rose, M. K., Borg, A., Dunphy, J. C., Mitsui, T., Ogletree, D. F., & Salmeron, M. (2003). Chemisorption and dissociation of O_2 on Pd(111) studied by STM. *Surface Science*, *547*(1), 162–170. https://doi.org/10.1016/j.susc.2003.08.057

Sang, X., & Chang, J. P. (2020). Physical and chemical effects in directional atomic layer etching. *Journal of Physics D: Applied Physics*, *53*(18), 183001. https://doi.org/10.1088/1361-6463/ab6d94

Sang, X., Chen, E., & Chang, J. P. (2020). Patterning nickel for extreme ultraviolet lithography mask application I. Atomic layer etch processing. *Journal of Vacuum Science & Technology A*, *38*(4), 042603. https://doi.org/10.1116/6.0000190

Sard, R. (1970). The Nucleation, Growth, and Structure of Electroless Copper Deposits. *Journal of The Electrochemical Society*, *117*(7), 864. https://doi.org/10.1149/1.2407658

Schaekers, M., Capon, B., Detavernier, C., & Blasco, N. (2010). The Deposition of Ru and RuO2 Films for DRAM Electrode. *ECS Transactions*, *33*(2), 135. https://doi.org/10.1149/1.3485250

Scheffler, M., & Stampfl, C. (2000). Theory of Adsorption on Metal Substrates. *ArXiv:Cond-Mat/0011217*. http://arxiv.org/abs/cond-mat/0011217

Schmidbauer, M., Kwasniewski, A., & Schwarzkopf, J. (2012). High-precision absolute lattice parameter determination of $SrTiO_3$, $DyScO_3$ and $NdGaO_3$ single crystals. *Acta Crystallographica Section B: Structural Science*, *68*(1), 8–14. https://doi.org/10.1107/S0108768111046738

Schwegmann, S., Seitsonen, A. P., De Renzi, V., Dietrich, H., Bludau, H., Gierer, M., Over, H., Jacobi, K., Scheffler, M., & Ertl, G. (1998). Oxygen adsorption on the Ru(101\ifmmode\bar\else\textasciimacron\fi{}0) surface: Anomalous coverage dependence. *Physical Review B*, *57*(24), 15487–15495. https://doi.org/10.1103/PhysRevB.57.15487

Seriani, N., Harl, J., Mittendorfer, F., & Kresse, G. (2009). A first-principles study of bulk oxide formation on Pd(100). *The Journal of Chemical Physics*, *131*(5), 054701. https://doi.org/10.1063/1.3187935

Sha, Y., Yu, T. H., Merinov, B. V., & Goddard, W. A. (2014). DFT Prediction of Oxygen Reduction Reaction on Palladium–Copper Alloy Surfaces. *ACS Catalysis*, *4*(4), 1189–1197. https://doi.org/10.1021/cs4009623

Shen, J. Y., Adnot, A., & Kaliaguine, S. (1991). An ESCA study of the interaction of oxygen with the surface of ruthenium. *Applied Surface Science*, *51*(1), 47–60. https://doi.org/10.1016/0169-4332(91)90061-N

Shin, H., Zhu, W., Donnelly, V. M., & Economou, D. J. (2012). Surprising importance of photo-assisted etching of silicon in chlorine-containing plasmas. *Journal of Vacuum Science & Technology A: Vacuum, Surfaces, and Films*, *30*(2), 021306. https://doi.org/10.1116/1.3681285

Shoron, O. F., Raghavan, S., Freeze, C. R., & Stemmer, S. (2017). $BaTiO_3/SrTiO_3$ heterostructures for ferroelectric field effect transistors. *Applied Physics Letters*, *110*(23), 232902. https://doi.org/10.1063/1.4985014

Singh, J. A., Thissen, N. F. W., Kim, W.-H., Johnson, H., Kessels, W. M. M., Bol, A. A., Bent, S. F., & Mackus, A. J. M. (2018). Area-Selective Atomic Layer Deposition of Metal Oxides on Noble Metals through Catalytic Oxygen Activation. *Chemistry of Materials*, *30*(3), 663–670. https://doi.org/10.1021/acs.chemmater.7b03818

Sjövall, P., & Uvdal, P. (1998). Adsorption of oxygen on Pd(111): Precursor kinetics and coverage-dependent sticking. *Journal of Vacuum Science & Technology A: Vacuum, Surfaces, and Films*, *16*(3), 943. https://doi.org/10.1116/1.581216

Slanger, T. G., & Cosby, P. C. (1988). Oxygen spectroscopy below 5.1 eV. *The Journal of Physical Chemistry*, *92*(2), 267–282. https://doi.org/10.1021/j100313a008

Song, C., Sakata, O., Kumara, L. S. R., Kohara, S., Yang, A., Kusada, K., Kobayashi, H., & Kitagawa, H. (2016). Size dependence of structural parameters in fcc and hcp Ru nanoparticles, revealed by Rietveld refinement analysis of high-energy X-ray diffraction data. *Scientific Reports*, *6*(1), 31400. https://doi.org/10.1038/srep31400

Stampfl, C., & Scheffler, M. (1996). Theoretical study of O adlayers on Ru(0001). *Physical Review B*, *54*(4), 2868–2872. https://doi.org/10.1103/PhysRevB.54.2868

Stevens, E., Tomczak, Y., Chan, B. T., Altamirano Sanchez, E., Parsons, G. N., & Delabie, A. (2018). Area-Selective Atomic Layer Deposition of TiN, TiO_2, and HfO_2 on

Silicon Nitride with inhibition on Amorphous Carbon. *Chemistry of Materials*, *30*(10), 3223–3232. https://doi.org/10.1021/acs.chemmater.8b00017

Suh, Y.-S., Lazar, H., Chen, B., Lee, J.-H., & Misra, V. (2005). Electrical Characteristics of HfO2 Dielectrics with Ru Metal Gate Electrodes. *Journal of The Electrochemical Society*, *152*(9), F138. https://doi.org/10.1149/1.1992467

Sun, J. B., & Almquist, B. D. (2018). Interfacial Contact is Required for Metal-Assisted Plasma Etching of Silicon. *Advanced Materials Interfaces*, *5*(24), 1800836. https://doi.org/10.1002/admi.201800836

Tamarov, K., Swanson, J. D., Unger, B. A., Kolasinski, K. W., Ernst, A. T., Aindow, M., Lehto, V.-P., & Riikonen, J. (2020). Controlling the Nature of Etched Si Nanostructures: High- versus Low-Load Metal-Assisted Catalytic Etching (MACE) of Si Powders. *ACS Applied Materials & Interfaces*, *12*(4), 4787–4796. https://doi.org/10.1021/acsami.9b20514

Taniguchi, N., Takahashi, K., Matsumi, Y., Dylewski, S. M., Geiser, J. D., & Houston, P. L. (1999). Determination of the heat of formation of O3 using vacuum ultraviolet laser-induced fluorescence spectroscopy and two-dimensional product imaging techniques. *The Journal of Chemical Physics*, *111*(14), 6350–6355. https://doi.org/10.1063/1.479939

Ten Eyck, G. A., Pimanpang, S., Bakhru, H., Lu, T.-M., & Wang, G.-C. (2006). Atomic Layer Deposition of Pd on an Oxidized Metal Substrate. *Chemical Vapor Deposition*, *12*(5), 290–294. https://doi.org/10.1002/cvde.200506456

Todorova, M., Reuter, K., & Scheffler, M. (2004). Oxygen Overlayers on Pd(111) Studied by Density Functional Theory. *The Journal of Physical Chemistry B*, *108*(38), 14477–14483. https://doi.org/10.1021/jp040088t

Torgersen, J., Acharya, S., Dadlani, A. L., Petousis, I., Kim, Y., Trejo, O., Nordlund, D., & Prinz, F. B. (2016). Relating Electronic and Geometric Structure of Atomic Layer Deposited BaTiO3 to its Electrical Properties. *The Journal of Physical Chemistry Letters*, *7*(8), 1428–1433. https://doi.org/10.1021/acs.jpclett.6b00393

Toyoshima, I., & Somorjai, G. A. (1979). *Heats of Chemisorption of O_2, H_2, CO, CO_2, and N_2 on Polycrystalline and Single Crystal Transition Metal Surfaces*. *19*(1), 105–159.

Uzunlar, E., Wilson, Z., & Kohl, P. A. (2013). Electroless Copper Deposition Using Sn/Ag Catalyst on Epoxy Laminates. *Journal of The Electrochemical Society*, *160*(12), D3237. https://doi.org/10.1149/2.039312jes

Vehkamäki, M., Hatanpää, T., Ritala, M., Leskelä, M., Väyrynen, S., & Rauhala, E. (2007). Atomic Layer Deposition of $BaTiO_3$ Thin Films—Effect of Barium Hydroxide Formation. *Chemical Vapor Deposition*, *13*(5), 239–246. https://doi.org/10.1002/cvde.200606538

Vukmirovic, M. B., Bliznakov, S. T., Sasaki, K., Wang, J. X., & Adzic, R. R. (2011). Electrodeposition of Metals in Catalyst Synthesis: The Case of Platinum Monolayer Electrocatalysts. *The Electrochemical Society Interface*, *20*(2), 33. https://doi.org/10.1149/2.F04112if

Wan, D., Paolillo, S., Rassoul, N., Kotowska, B. K., Blanco, V., Adelmann, C., Lazzarino, F., Ercken, M., Murdoch, G., Bömmels, J., Wilson, C. J., & Tökei, Z. (2018). Subtractive Etch of Ruthenium for Sub-5nm Interconnect. *2018 IEEE International Interconnect Technology Conference (IITC)*, 10–12. https://doi.org/10.1109/IITC.2018.8454841

Wang, C., Zhang, M., Stern, B., Lipson, M., & Lončar, M. (2018). Nanophotonic lithium niobate electro-optic modulators. *Optics Express*, *26*(2), 1547–1555. https://doi.org/10.1364/OE.26.001547

Wang, D., & Flanagan, T. B. (2005). Diffusion of oxygen in Pd. *Scripta Materialia*, *52*(7), 599–601. https://doi.org/10.1016/j.scriptamat.2004.11.027

Wang, H., & Schneider, W. F. (2007). Effects of coverage on the structures, energetics, and electronics of oxygen adsorption on RuO2(110). *The Journal of Chemical Physics*, *127*(6), 064706. https://doi.org/10.1063/1.2752501

Wang, J. J., Meng, F. Y., Ma, X. Q., Xu, M. X., & Chen, L. Q. (2010). Lattice, elastic, polarization, and electrostrictive properties of $BaTiO_3$ from first-principles. *Journal of Applied Physics*, *108*(3), 034107. https://doi.org/10.1063/1.3462441

Wang, X., Liu, C., Chen, Y., Wu, G., Yan, X., Huang, H., Wang, P., Tian, B., Zhenchen Hong, Wang, Y., Sun, S., Shen, H., Lin, T., Hu, W., Tang, M., Zhou, P., Wang, J., Jinglan Sun, Meng, X., … Li, Z. (2017). Ferroelectric FET for nonvolatile memory application with two-dimensional MoSe 2 channels. *2D Materials*, *4*(2), 025036. https://doi.org/10.1088/2053-1583/aa5c17

Wang, Y., Ganpule, C., Liu, B. T., Li, H., Mori, K., Hill, B., Wuttig, M., Ramesh, R., Finder, J., Yu, Z., Droopad, R., & Eisenbeiser, K. (2002). Epitaxial ferroelectric Pb(Zr,Ti)O3 thin films on Si using SrTiO3 template layers. *Applied Physics Letters*, *80*(1), 97–99. https://doi.org/10.1063/1.1428413

Wen, L. G., Roussel, P., Pedreira, O. V., Briggs, B., Groven, B., Dutta, S., Popovici, M. I., Heylen, N., Ciofi, I., Vanstreels, K., Østerberg, F. W., Hansen, O., Petersen, D. H., Opsomer, K., Detavernie, C., Wilson, C. J., Elshocht, S. V., Croes, K., Bömmels, J., … Adelmann, C. (2016). Atomic Layer Deposition of Ruthenium with TiN Interface for Sub-10 nm Advanced Interconnects beyond Copper. *ACS Applied Materials & Interfaces*, *8*(39), 26119–26125. https://doi.org/10.1021/acsami.6b07181

Williams, K. R., Gupta, K., & Wasilik, M. (2003). Etch rates for micromachining processing-Part II. *Journal of Microelectromechanical Systems*, *12*(6), 761–778. https://doi.org/10.1109/JMEMS.2003.820936

Xiang, C., Kung, S.-C., Taggart, D. K., Yang, F., Thompson, M. A., Güell, A. G., Yang, Y., & Penner, R. M. (2008). Lithographically Patterned Nanowire Electrodeposition: A Method for Patterning Electrically Continuous Metal Nanowires on Dielectrics. *ACS Nano*, *2*(9), 1939–1949. https://doi.org/10.1021/nn800394k

Xiong, C., Pernice, W. H. P., Ngai, J. H., Reiner, J. W., Kumah, D., Walker, F. J., Ahn, C. H., & Tang, H. X. (2014). Active Silicon Integrated Nanophotonics: Ferroelectric BaTiO3 Devices. *Nano Letters*, *14*(3), 1419–1425. https://doi.org/10.1021/nl404513p

Xu, Q., Fattal, D., & Beausoleil, R. G. (2008). Silicon microring resonators with 1.5-μm radius. *Optics Express*, *16*(6), 4309–4315. https://doi.org/10.1364/OE.16.004309

Yae, S., Morii, Y., Fukumuro, N., & Matsuda, H. (2012). Catalytic activity of noble metals for metal-assisted chemical etching of silicon. *Nanoscale Research Letters*, *7*(1), 352. https://doi.org/10.1186/1556-276X-7-352

Yakovkin, I. N. (2009). Hydrogen-induced mitigation of O on Ru(100): A density-functional study. *Physical Chemistry Chemical Physics*, *11*(27), 5695–5702. https://doi.org/10.1039/B903099A

Zhang, H. J., Lu, B., Li, H. Y., Bao, S. N., & He, P. (2004). Scanning tunneling microscopy and ultraviolet photoemission spectroscopy studies of oxygen adsorption on Ru(10$\bar{1}$0). *Surface Science*, *556*(1), 63–68. https://doi.org/10.1016/j.susc.2004.03.012

Zhang, H. J., Lu, B., Lu, Y. H., Xu, Y. F., Li, H. Y., Bao, S. N., & He, P. (2007). Growth of RuO2 thin layer on Ru(101$\bar{}$0) studied by scanning tunneling microscopy. *Surface Science*, *601*(11), 2297–2301. https://doi.org/10.1016/j.susc.2007.03.014

Zhang, W., Nahm, R. K., Ma, P. F., & Engstrom, J. R. (2013). Probing ultrathin film continuity and interface abruptness with x-ray photoelectron spectroscopy and low-energy ion scattering. *Journal of Vacuum Science & Technology A*, *31*(6), 061101. https://doi.org/10.1116/1.4812695

Zhang, Z., Dwyer, T., Sirard, S. M., & Ekerdt, J. G. (2019). Area-selective Atomic Layer Deposition of Cobalt Oxide to Generate Patterned Cobalt Films. *Journal of Vacuum Science & Technology A*, *37*(2), 020905. https://doi.org/10.1116/1.5066437

Zhang, Z., Nallan, H. C., Coffey, B. M., Ngo, T. Q., Pramanik, T., Banerjee, S. K., & Ekerdt, J. G. (2018). Atomic layer deposition of cobalt oxide on oxide substrates and low temperature reduction to form ultrathin cobalt metal films. *Journal of Vacuum Science & Technology A*, *37*(1), 010903. https://doi.org/10.1116/1.5063669

Zhang, Z., Nallan, H. C., Coffey, B. M., Ngo, T. Q., Pranamik, T., Ekerdt, J. G., & Banerjee, S. (2019). Atomic Layer Deposition of Cobalt Oxide on Oxide Substrates and Low Temperature Reduction to Form Ultrathin Cobalt Metal Films. *Journal of*

Vacuum Science & Technology A, *37*(1), 010903. https://doi.org/10.1116/1.5063669

Zhukov, V., Popova, I., & Yates, J. T. (2000). Delivery of pure ozone in ultrahigh vacuum. *Journal of Vacuum Science & Technology A*, *18*(3), 992–994. https://doi.org/10.1116/1.582288

Vita

Brennan Muir Coffey was born and raised in Boulder, Colorado. He has sought to broaden his expertise through several summer internships. From 2011, 2012, and 2013, he worked at NASA's Jet Propulsion Laboratory at the California Institute of Technology, working on various aspects of the Orbiting Carbon Observatory – 2 (OCO-2), which is in orbit as of 7/2014. In the summers of 2014, and 2015, he was involved in internships with Lawrence Berkeley National Laboratory, and ExxonMobil, respectively. He attended the University of Colorado Boulder for his undergraduate B.S. degrees in Chemical Engineering and Applied Mathematics, which he graduated *summa cum laude* in both in 2015. He began his studies at The University of Texas at Austin the same year.

Brennan joined Prof. John Ekerdt's research group in 2015, where he designed, and built several systems focused on nanofabrication methods of atomic layer deposition and atomic layer etching (ALE), where he endeavored to demonstrate vacuum ultraviolet enhanced ALE for the first time. He was awarded an NSF graduate research fellowship in 2017 to support these aims. Brennan has authored seven peer-reviewed journal articles (five of which he is the first-author), six technical presentations, and one patent. At the time of the writing of this dissertation there are two additional publications in preparation.

Permanent email address: bcoffey@utexas.edu

This dissertation was typed by the author.